

Toughening mechanisms for the attachment of architected materials: The mechanics of the tendon enthesis

Mikhail Golman

Submitted in partial fulfillment of the
requirements for the degree of
Doctor of Philosophy
under the Executive Committee
of the Graduate School of Arts and Sciences

COLUMBIA UNIVERSITY

2021

© 2021

Mikhail Golman

All Rights Reserved

Abstract

Toughening mechanisms for the attachment of architected materials: The mechanics of the tendon enthesis

Mikhail Golman

Use of load-bearing materials whose functionality arises from architected microstructures, so called architected materials, has been hindered by the challenge of connecting them. A solution in nature is found at the tendon enthesis, a tissue that connects tendon and bone, two vastly different natural architected materials. The tendon enthesis provides stability and allows for mobility of a joint though effective transfer of muscle forces from tendon to bone, while exhibiting toughness across a wide range of loadings. Unfortunately, many painful and physically debilitating conditions occur at or near this interface when the enthesis architecture is compromised due to injury or degeneration. Surgical and natural repairs do not reconstitute the natural toughening mechanisms of the enthesis and often fail. Hence, understanding the architectural mechanisms by which healthy and pathologic tendon entheses achieve strength and toughness would inform the development of both biological and engineered attachments.

Integrating biomechanical analyses, failure characterizations, numerical simulations, and novel imaging, this thesis presents architectural mechanisms of enthesis toughening in a mouse model. Imaging uncovered fibrous architecture within the enthesis, which controlled trade-offs between strength and toughness. *Ex vivo* enthesis failure modes exhibited nanoscale differences in damage, milliscale differences in fiber load-sharing, and macroscale differences in energy absorption that depended on structure, composition, and the nature of loading. The elastic and failure responses of

the tendon enthesis also varied with the direction of loading. This variation was due to the fibrous nature of the tendon enthesis, with a clear role for bony anatomy and fiber recruitment in enthesis toughening behavior.

In vivo, the loss of toughening mechanisms at the enthesis due to pathologic loading was evaluated by either increased (i.e., overuse) loading via downhill treadmill running or decreased (i.e., underuse) loading via botulinum toxin A induced paralysis. These loading environments led to changes in the mineralization and architecture at the tendon enthesis. These micro-architectural adaptations compromised the trade-offs between strength and toughness; overuse loading prompted active reinforcement and stiffening of the underlying trabeculae, leading a maintenance of strength and a compromise in overall toughness, whereas underloading prompted active resorption of the underlying trabecular architecture, leading to a compromise in both strength and toughness.

The mouse models of the tendon enthesis failure revealed a correlation between tendon enthesis architecture and injury prevention (i.e., toughening) mechanisms. To test this concept in a clinical setting, an injury classification system was developed for patellar tendinopathy and partial patellar tendon tears. This classification system identified the stages of tear progression and prognosis by tracking changes to patellar tendon architecture. Results revealed a relationship between patellar tendon thickness and likelihood of improvement with nonoperative treatment.

Taken together, this dissertation revealed how fibrous architecture can be tailored to toughen attachments between vastly different materials. This understanding can have prognostic value: tracking changes to enthesis architecture can be used as a tool for identifying candidates for various treatment options, as we showed for the patellar tendon clinical example. Furthermore, the toughening mechanisms identified here provide guidance for enhancing enthesis surgical repair and designing enthesis tissue engineered scaffolds, as well as motivating biomimetic approaches for attachment of architected engineering material systems.

Table of Contents

List of Tables	ix
List of Figures	x
Acknowledgments	xxv
Dedication	xxix
Chapter 1: Introduction	1
1.1 Architectured materials	1
1.1.1 Key motivation: Competing for performance requirements of modern materials	1
1.1.2 Architectured materials: General characteristics	1
1.1.3 Architectured materials in nature	3
1.2 The Dilemma: Attaching two architected materials	7
1.3 The Solution: The mechanics of the healthy tendon enthesis	7
1.3.1 The tendon enthesis as a guide to designing bi-material attachments	7
1.3.2 Multi-scale mechanisms reduce stress-concentrations at the tendon enthesis	8
1.3.3 Gap in knowledge: Limited understanding of strength and toughness mechanisms	15
1.4 The clinical significance: Injured enthesis does not regenerate toughening mechanisms, resulting in failure of repairs	15

1.4.1	Prevalence of tendon and tendon enthesis injuries	15
1.4.2	Characteristics of tendon enthesis injury and repair	16
1.4.3	Compromised enthesis architecture is not regenerated during healing after surgical and natural repair	19
1.5	The final piece of the puzzle: understanding toughening mechanisms	20
1.6	Scope and procedure of the dissertation	22
1.6.1	Specific Aims	22
Chapter 2: Attachment at the enthesis relies on a fibrous architected material system . . .		26
2.1	Introduction	26
2.2	Methods	27
2.2.1	Sample Preparation and Study Workflow	27
2.2.2	Contrast enhanced and conventional micro computed tomography (microCT) imaging	28
2.2.3	Tendon cross-sectional area, mineralized fibrocartilage area, footprint area, insertion area, and failure area determination	28
2.2.4	Scanning Electron Microscopy (SEM)	29
2.2.5	Histological Analysis	30
2.2.6	Mechanical Testing	30
2.2.7	Statistical Analysis	31
2.3	Results	31
2.3.1	The tendon enthesis exhibits fibrous architected material system	31
2.3.2	The tendon enthesis fails via bony avulsion at its primary insertion site . . .	34
2.4	Discussion	38
2.5	Conclusion	45

Chapter 3: Multiscale toughening mechanisms enable the tendon entheses to exhibit distinct failure modes under varying loading conditions	46
3.1 Introduction	46
3.2 Methods	47
3.2.1 Sample Preparation and Study Workflow	47
3.2.2 Mechanical testing	48
3.2.3 Contrast enhanced and conventional micro computed tomography (microCT) imaging	49
3.2.4 Collagen damage visualization	50
3.2.5 Statistical Analysis	51
3.3 Results	51
3.3.1 Macroscale: tendon enthesis mechanical failure depends on its loading history	51
3.3.2 Nanoscale: the tendon enthesis toughening mechanism to resist cyclical loading	52
3.4 Discussion	52
3.5 Conclusion	61
Chapter 4: Differential recruitment of collagen fibers and the shape of the bony attachment endows toughness to the tendon enthesis across loading directions	62
4.1 Introduction	62
4.2 Methods	65
4.2.1 <i>Ex vivo</i>	65
4.2.1.1 Sample preparation and study workflow	65
4.2.1.2 Mechanical testing	66
4.2.1.3 Imaging	66

4.2.1.4	Failure mode and failure area characterization	67
4.2.2	<i>In silico</i>	67
4.2.2.1	Positional-recruitment model	67
4.2.2.2	Numerical experiments	73
4.2.3	Statistical Analysis	74
4.3	Results	74
4.3.1	<i>Ex vivo</i>	74
4.3.1.1	Orientation and engagement of tendon enthesis fibers depends on joint position	74
4.3.1.2	Tendon enthesis failure behavior depended strongly on the angle of abduction	75
4.3.2	<i>In silico</i>	77
4.3.2.1	<i>Positional-recruitment model</i> simulation successfully reproduced experimentally observed enthesis mechanics as a function of abduction angle	77
4.3.2.2	The balance between tendon enthesis strength, toughness, and stiffness varies across loading directions	78
4.3.2.3	Fiber packing density influences joint position-dependent tendon enthesis mechanics	79
4.3.2.4	Energy storing tendons prioritize toughness over strength, while positional tendons prioritize consistent stiffness	80
4.3.2.5	The bony anatomy onto which the tendon attaches influences fiber recruitment patterns and resulting enthesis mechanics	81
4.4	Discussion	83
4.5	Conclusion	87
Chapter 5: Mineral content is crucial for tendon enthesis strength		88

5.1	Introduction	88
5.2	Methods	89
5.2.1	Sample Preparation and Study Workflow	89
5.2.2	<i>Ex vivo</i> removal of chemical constituents of the tendon enthesis	90
5.2.3	Contrast Enhanced and Conventional Micro-computed tomography (microCT) Imaging	91
5.2.4	Mechanical Testing	92
5.2.5	Statistical Analysis	92
5.3	Results	93
5.3.1	Removal of Extracellular Matrix Components	93
5.4	Discussion	95
5.5	Conclusion	99
Chapter 6:	The tendon enthesis actively adapts its architecture <i>in vivo</i> in response to loading by controlling its mineral composition and microarchitecture	100
6.1	Introduction	100
6.2	Methods	102
6.2.1	Sample preparation and study workflow	102
6.2.2	<i>In vivo</i> degeneration models	102
6.2.3	Contrast enhanced and conventional micro-computed tomography (microCT) imaging	103
6.2.4	Bone morphometry and individual trabecula segmentation (ITS) analysis	104
6.2.5	Determining tendon cross-sectional area (TCSA), mineralized fibrocartilage (MFC) area, and failure area	105
6.2.6	Mechanical testing	107

6.2.7	Enthesis fracture model	107
6.2.8	Statistical analysis	109
6.3	Results	109
6.3.1	Mechanical and failure properties	109
6.3.2	Bone morphology and trabecular microarchitecture	110
6.3.3	Modeling entheses fractures <i>in silico</i>	116
6.3.4	Connecting entheses morphology and trabecular microarchitecture to its mechanical and failure behavior	119
6.4	Discussion	119
6.4.1	<i>In vivo</i> overuse and underuse lead to distinct changes to mechanical behavior	120
6.4.2	<i>In vivo</i> overuse and underuse induced diverging failure behavior	121
6.4.3	Loading-induced architectural adaptations to the mineralized bony base underlying the entheses dictate the extent of entheses failure	122
6.4.4	Overuse and underuse led to diverging adaptations to local trabecular microarchitectural network underlying the tendon entheses	124
6.4.5	Entheses strength correlated with underlying bony architecture, while entheses toughness correlated with entheses geometry	126
6.4.6	Pathological loading conditions induce distinct microarchitectural adaptations that compromised tendon entheses toughness	127
6.5	Conclusion	130
Chapter 7: Clinical Example:		
Rethinking Patellar Tendinopathy and Partial Patellar Tendon Tears		
A Novel Classification System		
7.1	Introduction	131
7.2	Methods	133
7.2.1	Study Subjects	133

7.2.2	Determination of Partial Patellar Tendon Characteristics	134
7.2.3	Statistical Methods	135
7.2.4	Histological Evaluation of Healthy Patellar Tendon	137
7.3	Results	137
7.3.1	Study Subjects and Presence of Partial Tears	137
7.3.2	Patellar Tendon Size	138
7.3.3	PPTT Location and Size	140
7.3.4	Comparison of Partial Tear Size and Proposed Tear Size Classification System	140
7.3.5	Robustness of the Proposed PPTT Classification System	144
7.3.6	Histological Evaluation of Healthy Patellar Tendon	145
7.4	Discussion	148
7.5	Conclusion	153
Chapter 8: Conclusions and future directions		154
8.1	Summary of the dissertation	154
8.2	Limitations	158
8.3	Conclusions and outlook	159
References		162
Appendix A: Enhanced Tendon-to-Bone Healing via IKK β Inhibition in a Rat Rotator Cuff Model		190
A.1	Abstract	190
A.2	Introduction	191
A.3	Materials and Methods	192

A.3.1	Cell culture	192
A.3.2	Rotator cuff animal model	194
A.3.3	Gene expression	194
A.3.4	Bone morphometry	195
A.3.5	Biomechanics	195
A.3.6	Histological analysis	197
A.3.7	Statistical Analysis	197
A.4	Results	197
A.4.1	Cell culture model of tendinopathy	197
A.4.2	Gene expression	198
A.4.3	Biomechanics	199
A.4.4	Bone morphometry	199
A.4.5	Histology	202
A.5	Discussion	202
A.6	Conclusion	208
A.7	Acknowledgments	208

List of Tables

2.1	Enthesis Footprint, Insertion, and Failure Area	37
4.1	Supraspinatus tendon enthesis 2D measurements and selected model parameters	73
6.1	Definition of ITS-Based Microarchitectural Parameters	106
7.1	Patient Sport/Activity Distributions	139
7.2	Patellar Tendon Geometry	139
7.3	Partial Patellar Tendon Tear Geometry (N = 56 Patients)	141
7.4	Distribution of PPTTs According to Proposed Popkin-Golman MRI Grading	144
7.5	Intra- and Inter- observer Reliability Analysis: Popkin-Golman (PG) MRI Grading	148
A.1	Names of Genes, Associated Categories and Sequences	196
A.2	Tendon-to-Bone Histological Scores.	204

List of Figures

1.1	<i>Architectural features at the micro- and meso-scales can lead to unique behavior at the full length scale of the material.</i> Architected materials lie in the intermediate length scale between the microstructure and the superstructure. This allows architected materials to obtain high morphological control over the material microstructure and achieve optimal mechanical performance that meets a specific function (i.e., the engineering end-application). Here, the application of lightweight and damage-tolerant architected materials used for creating a fan in an airplane engine is shown. The images are adapted, with permission, from Pham <i>et. al.</i> [9].	2
1.2	<i>Bio-inspired engineered architected materials break typical performance trade-offs.</i> (A) Hybrid designs of 3D printed engineered architected materials containing hierarchies and functional gradients. (B) Visualizing performance of engineered architected materials using a radar plot. (C) The overall performance comparisons between different designs of architected materials. Adapted, with permission, from Jia <i>et. al.</i> [7] under the terms of the Creative Commons Attribution-NonCommercial-No Derivatives License.	4
1.3	<i>Bone derives its toughening mechanisms through a hierarchical architecture.</i> Bone is primarily composed of collagen type I and hydroxyapatite mineral crystals that arrange into an intricate hierarchical structure. The origins of strength and toughness of bone result from a number of mechanisms that operate throughout its hierarchical architecture. Adapted, with permission, from Wegst <i>et. al.</i> [3].	5
1.4	<i>Hierarchical architecture of tendon.</i> Here, the nomenclature for the human Achilles tendon hierarchy is shown. MG refers to medial gastrocnemius and LG refers to lateral gastrocnemius sub-tendons. Adapted, with permission, from Handsfield <i>et. al.</i> [37].	6

- 1.5 *The healthy tendon enthesis presents multiscale solutions to the problem of attaching two dissimilar materials under physiologic loading conditions.* At the millimeter scale, allometric scaling of the attachment footprint area and the splaying shape of the attachment site were shown to effectively reduce stress concentrations. At the micrometer scale, strong attachment at the tendon enthesis arises from a zone of compliant transitional tissue that mitigates stress concentrations through functional gradation in fiber orientation, biomolecular composition, and mineral concentrations. Furthermore, the interdigitations at mineralized and unmineralized tissues leads to a balance between attachment strength and toughness. At the nanometer scale, the particular arrangement of mineral crystal relative to the collagen fibril dictate the stiffening of the matrix. It is also suggested that, at this scale, non-collagenous proteins (NCPs) interact with the tendon enthesis fibers and mineral crystals to aid effective load transfer. Adapted under the terms of the Creative Commons Attribution-NonCommercial-No Derivatives License from Schwartz *et al.* [56]. Adapted, with permission, from Hu *et al.* [57] and Alexander *et al.* [30]. 9
- 1.6 *Tendon enthesis collagen composition changes from type I to type II before attaching to bone.* **(A)** Confocal image of representative the porcine Achilles tendon enthesis, immunostained for collagen type I (magenta) and type II (cyan). Scale is 300 μ m. **(B)** Fluorescence intensities plotted over the tendon enthesis (0.0 - bone and 2.0 - tendon). Adapted, with permission, from Rossetti *et al.* [61]. 10
- 1.7 *The tendon enthesis attachment area increases isometrically with muscle size, maintaining constant interfacial stress concentrations across animal species.* Modeling results revealed that the stress concentration factor (SCF) does not vary across animals whose mass varies as much as three orders of magnitude. Adapted, with permission, from Saadat *et al.* [66]. 11
- 1.8 *The tendon enthesis contains a high compliance region near the mineralized gradient that is optimized to reduce stress concentrations at the attachment.* **(A)** Micro-mechanical testing of the mouse tendon enthesis confirmed the existence of a compliant region near the mineralization gradient within the tendon enthesis. **(B)** Numerical modelling showed that the biomimetic gradation in material properties containing a region that is more compliant than both tendon and bone, is optimized to reduce stress concentrations at the attachment. Adapted, with permission, from Deymier *et al.* [64] and Liu *et al.* [67]. 12
- 1.9 *Tendon entheses often fail due to injury or degeneration.* Clinically, bone avulsion fractures or tendon mid-substance ruptures are commonly seen in high-impact injuries and in pediatric patients, while insertion failures are prominent for the degenerated rotator cuff in adult patients. Arrows indicate failure locations. HH - humeral head; G - glenoid; Ac - acromion; C - clavicle. Adapted, with permission, from Jeong *et al.* [101], Godin *et al.* [102], and Ghazanfari *et al.* [103]. 17

1.10 *Tendon enthesis architecture is not regenerated after healing.* Histological sections stained with heamotoxylin and eosin of intact and healing canine flexor digitorum profundus tendon viewed under (**top**) bright-field and (**bottom**) polarized light. Highly aligned collagen architecture is evident in healthy, while disorganized scar tissue is apparent in healing tendon enthesis after injury-and-repair. Adapted, with permission, from Silva *et al.* [127]. 21

2.1 *Mercury (II) chloride-stained contrast enhanced high-resolution microCT imaging revealed that, hidden within the well-known larger apparent attachment footprint area, is a smaller, much denser primary insertion site where tendon fibers insert directly into the bone.* (A), Three-dimensional volume rendering of representative intact enthesis. (B), Magnified cross sectional view of yellow box in (A); within blue dotted lines outline apparent enthesis and within green dotted lines outline dense primary insertion. (scale: 200 μm). (C), Representative image of pentachrome-stained coronal section of the tendon enthesis, where red stain shows mature collagen fibers, yellow stain shows mineralized tissue and connective tissue. (scale: 200 μm) 32

2.2 *The newly visualized fibrous primary insertion site was only 32% of the overall footprint area and slightly larger than that of tendon bulk cross-sectional area.* (A) Intact images of tendon enthesis obtained by conventional and contrast enhanced high resolution micro computed tomography (microCT) technique. The location of images shown in the transverse view are represented as a line within orange arrow heads in the coronal view imaging. The 3D view was generated using MATLAB from volume contouring and rendering. 2D image scaling is 800 μm for all images. 3D representations are not to scale. (B) Minimal tendon cross-sectional area and (C) enthesis apparent footprint, true footprint, and insertion area obtained from microCT images of tendon enthesis. Gray shaded measurement was obtained using conventional microCT technique, while all other measurements were obtained using contrast enhanced microCT technique. (** $p < 0.01$, *** $p < 0.001$, repeated measures ANOVA followed by the Tukey’s multiple comparison test) 33

2.3 *Tendon enthesis samples failed catastrophically, creating failure craters at the attachment site.* (A) Tendon enthesis force-displacement curve indicates a nonlinear loading response of the tissue when enthesis samples were pulled uniaxially, quasi-statically to failure. Enthesis samples fail catastrophically upon reaching maximum loading. Mean failure load and failure displacement is represented by a blue dot, crossheads represent errors. (B) Representative murine tendon enthesis sample pictures before and after mechanical testing (scale: 2 mm). While majority of the primary insertion was avulsed, peritenon tissue surrounding the primary insertion site was still attached post failure (blue arrow). (C) MicroCT imaging from before and after testing revealed that all samples exhibited failure craters at the attachment site (outlined in orange dotted line). 35

2.4	<i>Histology of intact and failed entheses show that the avulsed fragment contained mineralized fibrocartilage and bone tissue. (Top), Toluidine blue staining of intact and failed tendon enthesis highlights the enthesis fibrocartilage. The avulsed fragment contains interdigitations where the trabecular bone integrates into fibrocartilage. (Bottom), Polarized light images corresponding to above images, with a color map overlay indicating the local collagen fiber alignment. Scale is 200 μm.</i>	36
2.5	<i>Contrast enhanced microCT imaging of failed enthesis revealed that the majority of the primary insertion was avulsed, while some tendon enthesis fibers were still attached at the time of failure. Intact dense primary insertion fibers are outlined in green. Avulsed bony fragment at primary insertion site, outlined with a red dotted line. Scale is 200 μm. Three-dimensional representation of avulsed fragment showing portions of trabeculae at the failure site (red arrow).</i>	37
2.6	<i>Contrast enhanced microCT images of the failure site suggest crack propagation around the avulsion site. (A) Bone avulsion site visualized via contrast enhance microCT in coronal, sagittal, and transverse view. Scale is 500 μm.(B) Coronal slices from the edge of the failure site to the center of avulsed fragment. Scale is 100 μm.</i>	38
2.7	<i>Scanning electron microscopy of the failure site shows crack propagation around the avulsion site. Crack propagation around the avulsion site is outlined in red circle, with zoomed in images following the crack propagation site. Images were obtained in BSE mode.</i>	39
2.8	<i>Tendon entheses failed either at the interface between mineralized fibrocartilage and bone (MF-B failure type), or in the underlying trabecular bone (B-T failure type). Conventional microCT imaging of post-failure humeral head samples (3D rendering and 2D sagittal view) and 3D visualization of avulsed fragment. Orange outline and orange arrows represent site of entheses attachments (humeral head post failure crater). Red arrows represent fracture (failure) surfaces. Scale is 500 μm.</i>	40
3.1	<i>Experimental set up. To examine effect of loading on failure mode, samples were loaded (A) across a range of loading rates to simulate acute injuries or (B) loaded cyclically to simulate degenerative loading. (C) 3D printed securable guide bars and 3D printed fixtures were used for interrupted testing. The gripping system allowed for enthesis samples to be secured and recovered post-testing at their loading levels or failure displacements.</i>	48

3.2	<i>There were three distinct failure modes, depending on the loading regime: bone avulsion, tendon mid-substance failure, and fibrocartilage interface. Under monotonic loading, most samples failed by bony avulsion. Under “high” cyclical loading (20%-70% failure force), all samples failed at the insertion. Under “low” cyclical loading (1%-20% failure force) samples did not fail, even after 100,000 cycles. Scale is 500μm</i>	52
3.3	<i>Mechanical responses of tendon enthesis were largely strain-rate insensitive, with increases in strength and toughness when loaded at higher strain rates. (A) Representative strength (force)-displacement curves for monotonic loadings. (B) Stiffness was not affected by increase in strain rates. However, (C) enthesis strength (i.e., failure load) and (D) enthesis toughness (i.e., energy absorption) increased with the loading rate.</i>	53
3.4	<i>The enthesis stored enough energy, even at high loading rates, to shift the fracture away from the attachment and towards the bone. (A) Representative contrast enhanced images of failed samples after increases in loading rate. Scale is 250μm. (B) Avulsed (failed/fractured) area increased with loading rate, with bimodal distribution at high loading rates (10x and 100x). (C) The number of avulsed (fractured) pieces increased with an increase in loading rate. (D) The failure interface (MF-B vs. B-T) did not significantly change with an increase in loading rate, although trending towards B-T failure type with an increase in loading rate.</i>	54
3.5	<i>F-CHP fluorescence intensity, indicative of collagen molecule damage accumulation, increased with the level of applied load and with the number of cycles. Representative whole-sample images of mouse entheses that were subjected to quasi-static (top), or cyclic loading (bottom). For quasi-statically loaded samples (top), there was little to no fluorescent signal in the low force group (1N-2N), followed by increased staining near the attachment site at higher loads (3N and failure). For cyclically loaded samples (bottom), F-CHP staining was initially concentrated in a few fibers near the tendon mid-substance (10K-40K cycles) and ultimately propagated down the entire tendon in concentrated bands Dotted lines represent outline of bone (white) and tendon (yellow). Solid line represents failure surface. Scale is 500μm.</i>	55
3.6	<i>Multiscale toughening mechanisms enable the entheses to exhibit distinct failure modes under varying loading conditions. This chapter revealed key aspects of energy absorption by the fibrous nature of tendon enthesis: when the attachment was pulled monotonically to failure, the energy stored in the enthesis was sufficient to fracture and avulse the mineralized tissue; however, when the attachment was pulled cyclically, energy was dissipated in the enthesis and damage accumulated in the tendon followed by tendon rupture. Hence, the enthesis contains fiber-level toughening mechanisms to resist monotonic loading and an underlying nanoscale mechanism to resist cyclical loading.</i>	59

4.1 *Range of motion (ROM) for supraspinatus, Achilles, and patellar tendon with corresponding contrast enhanced images of murine rotator cuff (supraspinatus tendon), ankle (Achilles tendon), and knee (patellar tendon) joints at flexion, straight, and extension.* Green dashed lines outline tendons at each position. HH-humeral head; G-glenoid. 64

4.2 *Positional-recruitment model.* (A) Coronal section of high resolution contrast-enhanced microCT image of a murine supraspinatus tendon attached to the humeral head. (B) Tendon enthesis fibers are shown in green, the bone is shown in gray, and the black arrow represents the direction of loading. (C) At rest, the length of the outer fibers is larger than the length of the inner fibers. When a fiber is engaged and oriented so that it contacts the bone ridge, it tightens until it reaches the tangent to the humeral head curvature (blue arrow) and the tangent point to the tendon fiber (purple arrow). (D) To approximate the distribution of fibers at the enthesis, with middle fibers being more numerous and storing more energy, fiber density was varied across the attachment. Specifically, (D, top) the distance between fibers was increased at the outer edges and (D, bottom) fiber stiffness K was increased for middle fibers. 68

4.3 *Initial rest state.* At rest length, the outer fibers are larger than the inner fibers. The grip (black points) is placed so that the innermost fiber is not in tension when tendon is oriented horizontally ($\theta = 0$ and fibers aligned with the \hat{i} direction). x_3^0 is the gauge length and was defined as constant for all fibers of energy storing tendons. 70

4.4 *Contrast-enhanced microCT of intact mouse glenohumeral joint (top row), intact supraspinatus tendon enthesis (middle row), and failed tendon enthesis (bottom row) at each abduction angle.* The supraspinatus tendon (top row, outlined in blue) was straight at low abduction angles (0° - 30°) and buckled at high abduction angles (90° - 120°); (G: glenoid, HH: humeral head). 74

4.5 *The tendon enthesis mechanical behavior varied dramatically with the direction of loading.* (A) Strength (failure force) vs. displacement behavior. The mean failure strength (force) and failure displacement are represented by dots and cross-heads represent standard deviations. There were significant differences in tendon enthesis (B) strength, (C) stiffness, (D) toughness when tested quasistatically at varying angles *ex vivo*. The enthesis was weakest when samples were pulled at 120° of abduction and strongest when pulled at 30° ($p < 0.01$). The enthesis was stiffest when pulled at 60° ($p < 0.001$), and toughest when pulled at low angle of abductions (30° and 0°); (* $p < 0.05$, ** $p < 0.01$, *** $p < 0.001$, **** $p < 0.0001$, ANOVA followed by the Dunnett's multiple comparison test). 76

4.6	<i>The enthesis failed via bony avulsion in almost all samples and the size of fractured area was lowest at low angles of abduction. (A) Samples failed primarily via bony avulsion. However, at low angle of abductions (0°-30°), most samples failed at the grips. (B) The size of the fractured area decreased at low angles of abduction (p<0.01). (C) Fragment quantity distribution did not show a trend with loading angle. (D) There was a shift towards MF-B type failure when samples were pulled at 30° of abduction; (* p<0.05, ANOVA followed by the Dunnett’s multiple comparison test).</i>	77
4.7	<i>Positional-recruitment model simulation reproduced experimentally-observed enthesis mechanics as a function of abduction angle. (A) In silico strength vs. displacement plot. (B) Strength, stiffness, toughness results normalized against the case when fibers were pulled uniaxially without the geometric constraints.</i>	78
4.8	<i>The mechanism driving loading-angle dependent failure behavior of the tendon enthesis is position-dependent fiber recruitment. (A) Number of fibers engaged (recruited) with respect to displacement dependent on loading angle. (B) Normalized strengths, stiffness, and toughness responses for tendon enthesis simulated to be loaded in range of loading directions. Simulations were run with 20 fibers (N=20), round bone ridge (A₀ = B₀), fiber thickness of w=10 μm, fiber spacing s/w=1.5, and fiber failure stretch of λ_u = 1.2. Initial conditions were set as for energy storing tendons. Strength, stiffness, and toughness were normalized against idealized scenario where tightly packed fibers (s/w = 1) were pulled to failure uniaxially at 90°.</i>	79
4.9	<i>Fiber packing density influences joint position-dependent tendon enthesis mechanics. Effect of spacing between fibers (s/w) on enthesis mechanics. Simulations were run with 20 fibers (N=20), a circular bone ridge (A₀ = B₀), fiber thickness of w = 10 μm, and a variable spacing between fibers. Fiber failure stretch was set to λ_u = 1.2. Initial conditions were set as for energy storing tendons. Strength, stiffness, and toughness were normalized against idealized scenario where tightly packed fibers (s/w=1) were pulled to failure uniaxially at 90°.</i>	80
4.10	<i>Energy storing tendons prioritize toughness over strength, while positional tendons prioritize consistent stiffness. Loading angle dependent mechanical responses for energy storing and positional tendon enthesis. Simulations were run with 20 fibers (N = 20), a circular bone ridge (A₀ = B₀), fiber thickness of w = 10 μm, and fiber spacing s/w = 1.5. Fiber failure stretch was set to λ_u = 1.2. Initial conditions: constant gauge lengths were enforced for energy storing tendons and constant tendon enthesis fiber lengths were enforced for positional tendons. Strength, stiffness, and toughness were normalized against idealized scenario where tightly packed fibers (s/w = 1) were pulled to failure uniaxially at 90°.</i>	81

4.11	<i>The bony anatomy influences fiber recruitment patterns and resulting enthesis mechanics.</i> Anatomical bone ridge flattening on tendon enthesis mechanics. Simulations were run with 20 fibers ($N = 20$), fiber thickness of $w = 10 \mu\text{m}$, fiber spacing $s/w=1.5$, and a variable aspect ratio for the cylindrical bone ridge. Fiber failure stretch was set to $\lambda_u = 1.2$. Initial conditions were set as for energy storing tendons. Strength, stiffness, and toughness were normalized against idealized scenario where tightly packed fibers ($s/w = 1$) were pulled to failure uniaxially at 90°	82
5.1	<i>To assess compositional contributions to tendon enthesis strength and toughness, mineral or proteoglycans were chemically removed ex vivo.</i> Samples were immersed in decalcifying agent to completely remove mineral (left) or in chondroitinase ABC for 5 days to remove proteoglycans (right).	90
5.2	<i>Both protocols were effective in removing constituents of the tendon enthesis.</i> (A) Contrast enhanced microCT imaging showed that demineralization treatment completely removed the mineral from the tendon enthesis and the humeral head bone. Scale is $500 \mu\text{m}$. Yellow arrows indicate changes in the coefficient of attenuation due to the mineral loss in the sample. (B) Alcian blue staining of the tendon enthesis showed that chondroitinase ABC treatment removed proteoglycan components from the unmineralized portion of the enthesis (change in staining outlined by orange dashed ellipsoid). Scale is $100 \mu\text{m}$	94
5.3	<i>Tendon enthesis strength is dependent on mineral composition.</i> (A) Strength (failure force) vs. displacement behavior. The mean failure strength (force) and failure displacement are represented by dots and cross-heads represents standard deviations. (B) Removal of mineral led to a dramatic decrease in strength; removal of proteoglycan led to a relatively small decrease in strength. (C) Removal of mineral or proteoglycan led to significant decreases changes in stiffness. (D) Removal of mineral led to a significant decrease in toughness; removal of proteoglycan did not affect enthesis toughness. (* $p<0.05$, **** $p<0.0001$, ANOVA followed by the Dunnett's multiple comparison test)	95
5.4	<i>Loss of mineral or proteoglycan did not significantly alter the failure modes of the tendon enthesis.</i> (A) Post-failure contrast enhanced microCT scanning showed that most samples failed via bone avulsion, while a small number of samples depleted in proteoglycans failed at the edge of unmineralized fibrocartilage (pink arrow). Scale is $500 \mu\text{m}$. (B) Failure mode distributions. (C) There were no significant differences in failure (avulsed) area due to removal of proteoglycans. Note that the failure area for demineralized enthesis samples was not obtainable with current methodologies.	96

6.1	<i>To enable physiologically relevant control of compositional changes, we subjected tendon entheses to pathological loading conditions using in vivo murine rotator cuff tendinopathy models. 10-week-old mice were subjected to two degeneration models: underuse degeneration was induced via muscle paralysis by injecting botulinum toxin (BtxA) and overuse degeneration was achieved through downhill treadmill running for 4 weeks.</i>	103
6.2	<i>The back-of-the-envelope estimation for tendon enthesis failure behaviour models loading of tendon-to-bone attachment as a circular clamped plate loaded with uniform pressure. In this model, a is distance between clamps (i.e., trabecular spacing), p is the applied pressure (i.e., force), and t is plate thickness (i.e., cortical thickness).</i>	108
6.3	<i>Tendon entheses optimized strength, while compromising toughness under pathologic loading in vivo. (A) Strength (failure force) - displacement curves showed that healthy and overuse -degenerated attachments failed catastrophically, showing little post-yield behavior, while underuse-degenerated attachments failed at lower forces and showed distinct post-yield behavior. (B) The tendon cross-sectional area (TCSA) of the supraspinatus tendon was significantly decreased due to treadmill running ($p<0.001$). (C) Strength was decreased in the underuse-degenerated attachments ($p<0.01$) (D) Stiffness was increased in the overuse-degenerated attachments ($p<0.001$), while decreased for underuse-degenerated attachments ($p<0.05$). (E) Both overuse and underuse loading conditions reduced toughness, with significant decrease in overuse ($p<0.05$) and trend in underuse ($p=0.075$) compared with that of control.</i>	111
6.4	<i>Physiological in vivo degeneration models reduced the ability of the enthesis to protect against failure. (A) Contrast enhanced microCT imaging showed that pathological tendon-to-bone attachment exhibited exclusively avulsion-type failures, similar to that of control. Yellow arrow represent failure site. Scale is $500\ \mu\text{m}$. (B) Fracture area and (C) fracture quantity increased for underuse group compared with the control cage activity group ($p<0.01$). (D) Pathologic loading led to a shift in the fracture location: overuse led to more failures at the MF-B interface, while underuse led to more failures at the B-T interface.</i>	112
6.5	<i>Pathologic loading led to adaptations in bone architecture underlying the tendon enthesis. Bone morphometric analysis revealed that underuse led to loss of bone mineral density underlying the attachment (BMD and TMD, $p<0.0001$), reduced cortical and trabecular thickness ($p<0.0001$) and trabecular number ($p<0.001$). Overuse led to gain of bone volume in the humeral head (BV/TV, $p<0.05$), trabecular mineral density (BMD, $p<0.05$) and increase in trabecular thickness ($p<0.01$). Overuse also led to a decrease in mineralized fibrocartilage volume (MFC, $p<0.01$).</i>	113

- 6.6 *Mechanistic changes in failure modes were driven by local changes in trabecular microarchitecture underlying the enthesis. (A)* Individual trabecula segmentation (ITS) analysis showed that the ratio between trabecular plates and trabecular rods significantly decreased due to underuse compared to control (PR ratio, $p < 0.05$). Trabecular plate volume (pBV/TV) significantly decreased due to underuse ($p < 0.0001$) and significantly increased due to overuse ($p < 0.0001$) compared to control. There were no significant differences between groups in trabecular rod volume (rBV/TV). **(B)** Trabecular plate analysis showed that the number of trabecular plates (pTb.N) significantly decreased due to underuse ($p < 0.0001$), while trabecular plate thickness (pTb.Th) and surface area (pTb.S) significantly increased due to overuse ($p < 0.05$). **(C)** Trabecular rod analysis showed that there were no differences in rod number (rTb.N) thickness (rTb.Th). However, the length of trabecular rods (rTb.L) significantly increased due to underuse compared to that of control ($p < 0.05$) 114
- 6.7 *The orientation of load-bearing trabecular microarchitecture is actively remodeled to adapt to new loading directions. (Top)* Coarse and **(bottom)** fine orientation distribution of trabecular rods and plates from ITS analyses. Compared to cage active controls, trabecular plate loss were uniform along all directions for samples from underuse loading conditions. On the other hand, trabecular plate density increased in 60° - 30° and 30° - 0° directions compared to that of control for overuse loaded samples. While there were some trends, there were no significant differences in trabecular rod architecture between groups. The angle was taken with the axis normal to the supraspinatus tendon insertion surface, with respect to principle loading direction, or in this case defined by angle of abduction. (* $p < 0.05$, ** $p < 0.01$, **** $p < 0.0001$, 2-way ANOVA followed by Dunnet's multiple comparison test; for fine orientation analysis: green star represent significance between undersue and control, while red star represent significance between overuse and cotrol, "t" represents trends) 115
- 6.8 *Bony microarchitecture underlying the enthesis is optimized for tendon enthesis toughness: a small increase in strength leads to significant gain in energy absorption at the time of enthesis fracture.* The relationship between normalized fracture energy (Γ/Γ_o) and **(A)** trabecular spacing, Tb.Sp, (a/a_o) or **(B)** mineralized bony base thickness (t/t_o) was plotted against nomrralized strength (p/p_o). **(C)** Normalized fracture energy increased with increase in trabecular spacing. **(D)** The mineralized bony base thickness had an inverse relationship with stored fracture energy. Both (C) and (D) show that, with a relatively small increase in normalized strength (p/p_o), there is a significant gain in fracture energy absorbed (Γ/Γ_o) for each a/a_o and t/t_o 117

- 6.9 *Enthesis strength correlated with underlying bony architecture, while entheses toughness correlated with entheses geometry.* Pearson correlation results obtained from entheses mechanical behavior, entheses failure behavior, entheses characteristics, and bony architecture under the entheses. Green represents a positive correlation, while red represents an inverse correlation. Blue gradient shows p values. Entheses strength correlated strongly with BMD ($R=0.60$, $p<0.001$), cortical thickness ($R=0.69$, $p<0.001$), and trabecular plate thickness ($R=0.59$, $p<0.001$), but not with tendon cross-sectional area. Entheses toughness correlated strongly with tendon cross-sectional area ($R=0.44$, $p<0.05$), and trended with mineralized fibrocartilage volume ($R=0.29$, $p=0.11$). 118
- 6.10 *Modifications to in vivo loading lead to distinct microarchitectural adaptations that compromise tendon entheses toughness.* Pathological loading leads to distinct micrometer-scale transformation of the underlying trabecular network. Overuse prompts a change from rod-like trabeculae to plate-like trabeculae. On the other hand, underuse prompts a change from plate-like trabeculae to rod-like trabeculae. Furthermore, overuse loading leads to active reinforcement of bone whereas unloading leads to active removal of bone underneath the entheses. Thus, the architecture of the bony structure at the tendon entheses is oriented to support and share the load according to the muscle loading level and direction. These distinct microarchitectural adaptations lead to changes to tendon entheses mechanical and failure characteristics. In both under- and over-loading pathologic conditions, there is a loss of tendon entheses toughness. (Upward arrows represents an increase and downward arrow represents a decrease compared with healthy entheses. A horizontal line represents no difference compared with healthy entheses.) 128
- 7.1 *Defining PPTT dimensions from MRI scans.* A partial tear was defined 2-fold: (1) signal change on fluid-sensitive sequences with signal in the tendon that is iso-intense to joint fluid and (2) morphological defect with the evidence of disruption or discontinuity of the fibers on (A) sagittal or (B, C) axial MRI. Arrows and long dashed line indicate PPTT, and short dashed line indicates tendon cross section. (D: 1, 4) Length dimensions were measured with sagittal MRI scans that maximally showed each dimension. (E: 2, 3, 5, 6) The width and thickness dimensions were measured in the axial view (anterior to posterior). (F) The exact location of the partial tear was determined by dividing the axial view into 9 sections. MRI, magnetic resonance imaging; PPTT, partial patellar tendon tear. 136
- 7.2 *Patient distribution included in this study.* Out of 85 symptomatic patients, 56 had partial tears. Out of 56 patients with partial patellar tendon tears, 11 underwent repair surgery after failing a minimum 6 months of nonoperative treatments, while remaining opted for nonoperative (conservative) treatments. 138

- 7.3 *Patellar tendon is thicker in patients with PPTTs.* There was a significant difference in patellar tendon thickness between controls and patients with PPTTs ($P < .001$) and between symptomatic patients with no tears and patients with partial tears ($p < 0.001$). There was no difference in tendon thickness if there was no tear in patellar tendon. PPTT: partial patellar tendon tear. Values are presented as median, interquartile range, 95% CI, and outliers. 140
- 7.4 *PPTTs are located in the posterior and the posteromedial region of the proximal patellar tendon.* PPTTs were almost exclusively (100%) located in the proximal part of the patellar tendon, near the patellar attachment, as shown in **(A)** the 3-dimensionally (3D) reconstructed patellar tendon of the representative knee MRI. 91% of PPTTs involved the posterior and posteromedial regions of the proximal patellar tendon as shown in **(B)** the frequency heat map in the axial slice. MRI, magnetic resonance imaging; PPTT, partial patellar tendon tear. 141
- 7.5 *The severity of PPTTs directly correlates to patients' patellar tendon thickness.* The plot represents relationship between percentage tear thickness and tendon thickness. There was a significant correlation between patellar tendon thickness and percentage tear thickness ratio ($R = 0.815$; $p < .001$). All patients in our cohort who underwent repair surgery had partial tear $>50\%$. Dotted lines indicate 95% CI. Black oval denotes axial view (anterior to posterior) of patellar tendon. Grey oval denotes a PPTT within a patellar tendon. A, anterior; L, lateral; M, medial; P, posterior. 142
- 7.6 *Increase in thickness and percentage tear thickness has shown to influence treatment choices.* Patients undergoing surgery for PPTT had **(A)** median tear thickness of 10.32 mm ($p < 0.01$) and **(B)** greater than 50% tear thickness on axial imaging of the tendon ($p < 0.01$). 142
- 7.7 *The most sensitive predictor for detecting the presence of a partial tear is patellar tendon thickness. The normalized percentage tear thickness predicts the effectiveness of nonoperative therapy.* Sensitivity analysis for PPTT predictors show **(A)** patellar tendon thickness measurement was an excellent predictor of whether the tendon was normal or had PPTTs ($AUC = 0.885$; $p < .001$). **(B)** Patellar tendon thickness ($AUC = 0.833$; $p = .001$) and normalized percentage tear thickness ($AUC = 0.749$; $p = .006$) were better predictors for PPTT treatment than tear thickness ($AUC = 0.527$; $p = .76$). AUC, area under the curve; PPTT, partial patellar tendon tear. 143
- 7.8 *In the PG classification system patellar tendon thickness and tear thickness increase by grade.* Patellar tendon **(A)** tear thickness and **(B)** thickness increased with increasing grade (tear percentage). Values are presented as median, interquartile range, 95% CI, and outliers. 145

7.9 *The Popkin-Golman classification system.* Representative MRI of the patellar tendon with the proposed PPTT grading scheme. The middle column is a zoomed axial slice, with the patellar tendon outlined in white and the PPTT outlined in yellow. The final column shows the Blazina grading correlate, with possible treatment options currently available for each Popkin-Golman grade. AP, anteroposterior; MRI, magnetic resonance imaging; PPTT, partial patellar tendon tear. 146

7.10 *Image-based PG classification correlates with the gold standard Blazina classification system.* Relationship between Blazina classification and proposed image-based quantitative Popkin-Golman (PG) classification system for 20 patients selected for intra-class correlation coefficient analysis. N/A, not applicable. 147

7.11 *Combining the PG classification system and clinical measures will guide treatment decisions and result in more predictable outcomes.* Blazina and PG grading for 20 patients randomly selected for ICC analysis. The bottom two line represents whether each patient had reconstructive surgery and whether patient returned to previously level of activity (returned to sport) at the time of follow-up (+ :yes, and - :no). Orange outline represents patients who might have benefited from employing the PG grading scheme in addition to the gold-standard Blazina classification system. 147

7.12 *Histological sections of healthy proximal patellar tendon.* Collagen fascicles in the anterior side were loosely packed with substantial interfascicular connective tissue. In contrast, tendon fascicles in the posterior-medial side, where PPTTs commonly occur, were tightly packed. Vascularity, as evidenced by the presence of capillaries (green arrows), was prevalent on the anterior side and rarely found on the posterior side. PPTT, partial patellar tendon tear 149

8.1 *The fibrous and mineral architectures of the tendon enthesis provide multiscale toughening mechanisms for a resilient attachment between tendon and bone.* At the millimeter length scale (**A**) the fibrous architecture of the tendon enthesis allows for fiber recruitment and re-orientation to optimize toughness over strength across a range of loading directions. At the micrometer length scale (**B**) the enthesis actively adapts its mineral architecture to maintain its strength along the axis of loading. At the micrometer-to-nanometer length scale (**C**) a spatial gradient in mineral across the enthesis reduced stress concentrations [64]. At the nanometer length scale (**D**) collagen damage localization protects against damage prorogating to higher length scales. 160

A.1 (A) Schematic of NF- κ B signaling. NF- κ B signaling was modulated by targeting NF- κ B kinase subunit b (IKK β) which acts upstream of the NF- κ B complex, using IKK β small-molecule inhibitor (ACHP hydrochloride). (B) The overall study design included *in vitro* and *in vivo* methods. For *in vitro* study, rat tendon fibroblasts were treated with 1 ng interleukin-1 β (IL-1 β), 1 μ M IKK β Inhibitor, or both for 4h, 24h, 48h, and compared to vehicle-treated controls. For *in vivo* study, rats were either underwent bilateral supraspinatus tendon injury-and-repair surgery or left as normal healthy controls. Animals were either left untreated (CTRL group) or administered the IKK β inhibitor (ACHP group) orally once a day for 7 days after surgery. NF- κ B: nuclear factor κ B; CTRL: control; ACHP: ACHP hydrochloride. 193

A.2 *In vitro* IKK β inhibitor dose response curve for rat tail tendon fibroblasts (4 hours after treatment). 198

A.3 A small-molecule IKK β inhibitor reduced inflammatory cytokine (IL-6) production in response to IL-1 β . ND represents that IL-6 was not detected by a multiplex immunoassay. ND: no detection 198

A.4 Gene expression in the tendon relative to the housekeeping gene. A significant difference compared with normal is indicated by #, while a significant difference with comparing treatment to no treatment is represented by a bar (* p<0.05, ** p<0.01, **** p<0.0001; ANOVA followed by the Bonferroni post hoc test compared with normal and the effect of treatment; a significant difference compared with normal is indicated by an “#” within a bar; a significant effect of healing time is indicated by a “t” symbol by the post surgery label) 200

A.5 Treatment with IKK β inhibitor (ACHP) had significantly increased toughness of attachment site at 4 weeks and 8 weeks of healing compared with untreated control. Treatment with ACHP also led to trend in increasing failure load and strength at 4 weeks and 8 weeks of healing, but a significant decrease in stiffness at 4 weeks of healing. The ACHP treatment did not affect mechanical properties for uninjured supraspinatus tendon-to-bone attachments. (* p<0.05, ** p<0.01; dashed line represent trend; ANOVA followed by the Bonferroni post hoc test compared with normal:healthy and the effect of treatment; a significant difference compared with normal is indicated by an “#” within a bar; when comparing the effect of time; a significant effect of healing time is indicated by a “t” symbol by the post surgery label). 201

A.6 (A) Treatment with ACHP led to increases in TMD and trabecular number and decreases in BV/TV, cortical thickness, and trabecular thickness. (* p<0.05, ** p<0.01, *** p<0.001; ANOVA followed by the Bonferroni post hoc test compared with normal:healthy and the effect of treatment; a significant difference compared with normal is indicated by an “#” within a bar; a significant effect of healing time is indicated by a “t” symbol by the post surgery label). TMD: tissue mineral density; BV/TV: bone volume/tissue volume. (B) Microcomputed tomography (microCT) based two-dimensional mineral density maps for representative samples show increased mineral density in ACHP treated group. Orange arrows show the location of the attachment site and black arrows indicate bone tunnel below the epiphysis. 203

A.7 Pentachrome-stained tendon-to-bone repair site. ACHP treatment (IKK β inhibitor treatment) led to improved insertion organization and insertion continuity compared to control (yellow: new collagen; B: bone, T: tendon. Tendon-to-bone attachment is outlined with blue dotted line). 205

Acknowledgements

Finishing this dissertation was a challenge in the year of pandemic, quarantine, and social unrest, yet overall, it was an exciting journey. Like any other journey, it was only possible with the scientific and personal support of many advisors, family members, and friends.

First and foremost, I would like to thank my advisor Professor Steve Thomopoulos who has guided me from day one of my graduate degree (at the time it was at Washington University in St. Louis) to the completion of my dissertation today. Despite being cautioned by many that moving universities and setting up a new lab would be a risky and timely endeavor, I believe it was the best decision of my life. I learned a set of skills beyond techniques related to my work, including how to search, decide, and negotiate while purchasing large laboratory equipment, and setting up, revamping, and optimizing bread-and-butter experimental procedures in our laboratory. I cannot thank Steve enough for his patience, continued guidance, and his presentation of an exemplary model for how to conduct amazing science, which pushed me to become a better scientist every day. I am forever grateful to Steve for allowing me to embark on a rather unconventional study with a clinical collaborator, as well as providing me his full support when I landed an internship. Steve is also a mentor on a personal level. He is one of the few professionals I know who successfully balances being committed to his work while being fully engaged in family life, the trait I hope to emulate as I move forward in my career. Steve is someone that I have and will always look up to, and it is an honor to be one of his mentees.

I have been blessed to receive strong scientific and professional mentorship from many outstanding faculty members at Columbia University, Washington University in St. Louis, and many

other universities around the country and the world. I would like to express my gratitude to my dissertation committee members, Professor X. Edward Guo, Professor Clark Hung, Professor Gerard Ateshian, and Professor Guy Genin for kindly offering their expertise and their excellent advice throughout the dissertation process. I would especially like to thank Professor Guy Genin who has become an outstanding mentor and friend. His enthusiasm for science is thrilling and contagious. Guy's intuition and creative mindset taught me that any complex problem can be digested to something tangible. He has been an amazing source of motivation for my work, keeping me excited even at the time of setbacks. I could not have completed this dissertation without his guidance, support, and his impressive wit. Next, I would like to thank my clinical mentor Dr. Charles Popkin. His raw energy, friendliness, and passion for improving health care and sports medicine have kept me inspired and excited for our weekly 6:30 am meetings. I knew exactly who to call when I tore my ACL and that I was in the safe hands. I am grateful for your mentorship and now we have an injury-classification system named after us! I would also like to thank Professor Victor Birman for his guidance, mentorship, and kindness; from connecting with his friends when he found out that I would like to pursue an alternative career to checking in after I got my second dose of the COVID-19 vaccine. I would also like to thank Professor Matt Silva who kindly hosted me at the Washington University Musculoskeletal Research Center for 9 months at the beginning of my research career, so that my move to Columbia University would be smooth. I would like to extend my thanks to many of my collaborators, specifically members of Vienna University of Technology and Professor Phillipp Thurner for providing me amazing images and precious insights for my work.

My work would have not moved forward if it was not for the current and former members of the Thomopoulos Lab. I would like to thank the many talented and passionate people who I had the pleasure to work with and constantly learn from. I would like to especially thank John Boyle and Alix Deymier. They have been an amazing help and inspiration for everything and made my life both inside and outside lab enjoyable, especially during times of difficulty. Being sane, while moving to a new city and navigating the start of my PhD research career, would have not been

possible if it were not for you both. I would like to thank Adam Abraham, Lee Song, and Fei Fang for their perpetual source of knowledge, kindness, and willingness to guide me through my journey. I enjoyed and looked forward to every week for our discussions on experimental design, newly published papers, engineering, traveling, or food. Your work ethic and passion have been my inspiration and something I hope to follow in my career. I would like to thank Xiaoning Li and Dimitirious Skouteris. They have taken countless hours to help me with my *in vivo* surgical models. If it was not for their character, perseverance, and knowledge both inside and outside orthopedic surgery, this work would have not been possible. Our conversations during surgeries on philosophy, psychology, medicine, football (soccer), and Taylor Swift is something that I will cherish forever. I would also like to thank Iden Kurtaliaj, Brittany Marshall, and McKenzie Sup for their help with my experiments and making my everyday inspiring. They have been a constant source of energy in my final years of graduate school, coming up with new ideas and experiments. I have no doubt the future in the Thomopoulos Lab is in good hands with you. I honestly could not hope for a more interesting, intelligent, and kind group of people to call my colleagues and friends.

I would also like to thank the members of the Carroll Laboratories for Orthopedic surgeries. I especially would like to Catherine Konradt and Anca Meret for making me feel at home and helping me out tremendously both inside and outside of lab. I cannot thank you enough for helping me out with the logistics in making my internship possible.

Finally, I wish to dedicate my dissertation to my family and friends who made me the person I am today. I would like to begin this section by thanking the most important people in the world: my family. I am forever thankful for my father and my mother for giving me the opportunity to follow my passion. My parents' bravery many years ago to immigrate to a new country, their persistent drive to put maximum effort in all of my endeavors through any adversity, and their unconditional support and encouragement as I moved to the USA, 14,000 km away, have granted me immense freedom to pursue my dreams and excel while doing it. Despite being far away, they have grounded me through my highs and lows and encouraged me every step of my way. I would like to thank my brother, Jacob (Yasha), for always being there for me and feeling so close no

matter the time or place, despite being across the country. His support and humor kept my spirits up and reminded me that there is more to life than science. Next, I would like to thank my best friend and partner, Sabrina Fruci. My life, in a way, turned around after meeting you. You can put a smile to my face anytime, even if none of my experiments are working. You are my number one fan and it is much easier to stay focused, maintain perspective, and remain optimistic about the future when you have a phenomenal supporter. I would like to extend many thanks to my friends and their families for practically “adopting”. I am grateful for the Parkers and Hunts for providing me a family in the USA that I can rely on. Without your help I would have not survived college, yet alone graduate school in the USA. I am grateful for the Edge family in helping me jump start my life at the University of Minnesota. I am forever grateful that I have always been lucky to have a supportive family and friends and no millstone I have reached could have been reached without their words of encouragement.

Dedication

Mama, Papa, and Yasha.

Chapter 1: Introduction

1.1 Architected materials

1.1.1 Key motivation: Competing for performance requirements of modern materials

Demanding mechanical performance requirements for engineering applications have fueled the research and development of modern materials with a combination of properties, including strength, stiffness, and toughness. Some structural properties, such as strength and stiffness, can be easily tuned together. However, strength (i.e., stress required to break the material) and toughness (i.e., the energy absorbed prior to breaking the material), both vital properties for most applications, are generally mutually exclusive [1]. The material performance trade-offs between strength and toughness have hindered the creation of simple homogeneous materials that satisfy ever-increasing performance requirements. The motivation to push the boundaries of this performance trade-off has, instead, led to the development of hybrid materials. These materials combine stiff and compliant material components at appropriate concentrations and architectures to achieve unprecedented combinations of strength and toughness [2]. Inspired by natural materials that are known to break the typical trade-off between strength and toughness [3, 4, 5, 6], this architected approach is rapidly expanding in engineering applications requiring both strength and toughness [7, 8, 9].

1.1.2 Architected materials: General characteristics

Architectural features at the micro- and meso-scales can lead to unique behavior at the full-length scale of the material. Architected materials exploit characteristics at this length scale through control of the microstructure (e.g., size, topology, and arrangement) to achieve optimized performance [2]. The key distinctions between architected materials and other homogeneous or hybrid materials are their characteristic length scales and periodic structural features.

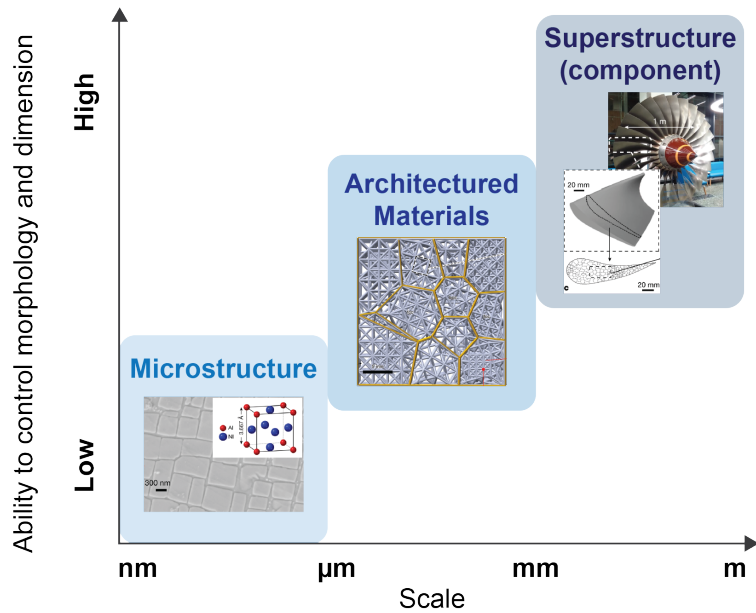


Figure 1.1: Architectural features at the micro- and meso-scales can lead to unique behavior at the full length scale of the material. Architected materials lie in the intermediate length scale between the microstructure and the superstructure. This allows architected materials to obtain high morphological control over the material microstructure and achieve optimal mechanical performance that meets a specific function (i.e., the engineering end-application). Here, the application of lightweight and damage-tolerant architected materials used for creating a fan in an airplane engine is shown. The images are adapted, with permission, from Pham *et. al.* [9].

When considering different levels of structural elements with respect to their characteristic length scales (**Figure 1.1**), architected materials occupy the intermediate lengths scale (10 μm to 100 mm) between the microstructure and the superstructure (i.e., component) [2, 10]. The mechanical behavior of materials designed at the scale of the microstructure (nanometers to 100 μm) is driven by the chemical composition, molecular structure, and granular structure (e.g., the grain structure of a metal) to achieve a desired material property, but this approach does not necessarily achieve all of the desired mechanical functions. Furthermore, there are significant challenges working at this scale with regard to the accuracy and fidelity of obtaining consistent dimensional control over the material. Many manipulation techniques at the sub-nanometer scales involve significant variations and defects/impurities associated with stochastic processes, including crystallization, polymerizations, and thermodynamic fluctuations, which require trial-and-error and make overall progress inefficient [11]. On the other end of the characteristic length scales of **Figure**

1.1 lies the design of engineering components (e.g., a fan of an airplane engine). At this length scale (millimeters to meters), many fabrication techniques are available to allow for high control over morphology and dimensional fidelity. While a component is designed with its engineering end-function in mind, the limited choices of material composition and geometry that conform and fulfill the function have led to significant performance trade-offs [1, 11]. Architected materials essentially mitigate the downsides of designing materials at the microstructure and superstructure length scales because they lie within the characteristic length scale that bridges microstructures and components. Novel top-down and bottom-up engineering fabrication techniques, such as self-assembly [12, 13] and 3D printing [14, 15, 16], allow for precise control over morphology and composition for designing materials at the intermediate length scales while meeting specific functional requirements. The use of topologically interlocked materials (TIMs) as structural panels is a prime example of applying architected materials in engineering. TIMs are fabricated via 3D printing, where an array of identically shaped base materials are interlocked from their shape and arrangement at the scale of 20-100 mm. The architecture of TIMs provides tunable stiffness, strength, and damage tolerance, despite being built entirely from brittle materials [17, 18].

The second key feature of architected materials lies in their structural periodicity. The architecture (e.g., geometry, thickness, morphology, and arrangement) of the building-blocks defines the mechanical performance at the macro-scale. This allows architected materials to sometimes achieve unprecedented mechanical responses, such as negative Poisson's ratios [19]. Assembling structural elements from the hierarchy (i.e., replacing micro-structures with sub-microstructures that span multiple length scales) [20] and/or implementing functional gradients (i.e., site-specific properties distributed within micro-structures) [6, 21] allows engineered architected materials to overcome typical performance trade-offs (**Figure 1.2**) [7].

1.1.3 Architected materials in nature

Natural (i.e., biological) materials are based on a limited number of building blocks: proteins (e.g., collagen, silk, keratin), polysaccharides (e.g., glycosaminoglycans, chitin, cellulose), and

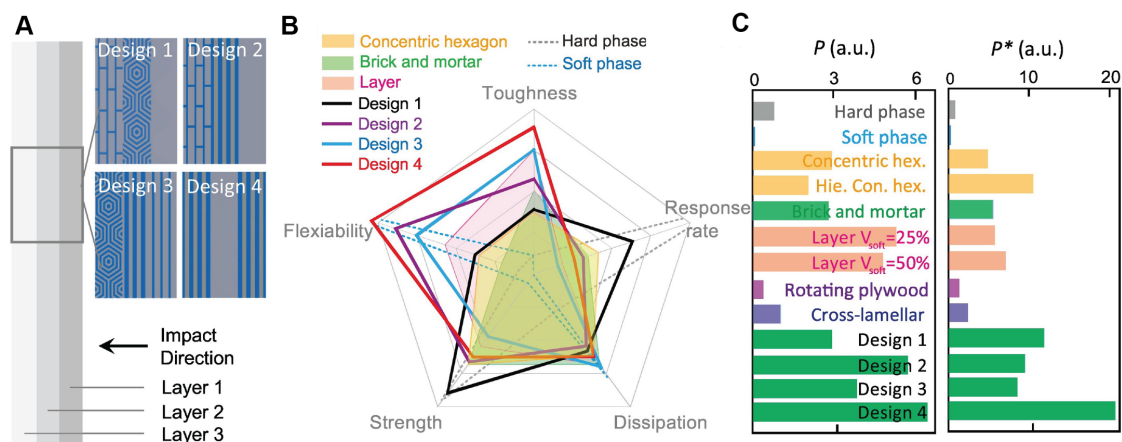


Figure 1.2: Bio-inspired engineered architected materials break typical performance trade-offs. (A) Hybrid designs of 3D printed engineered architected materials containing hierarchies and functional gradients. (B) Visualizing performance of engineered architected materials using a radar plot. (C) The overall performance comparisons between different designs of architected materials. Adapted, with permission, from Jia *et al.* [7] under the terms of the Creative Commons Attribution-NonCommercial-No Derivatives License.

minerals (e.g., hydroxyapatite, calcium phosphate, calcium carbonate). These natural building blocks by themselves have considerably poorer mechanical performance compared with those of many engineered materials [8]. However, by combining these elements in precise ways with architectural complexity, biologic materials achieve a remarkable set of mechanical properties that fit a diverse range of functions [2, 6], e.g., strength and toughness in bone [3] and strength and extensibility in silk spider webs [22]. Hence, natural materials has become a rich source of inspiration for the design of architectural materials [23, 24, 25]. Mimicking the layered structures seen in sea sponges [26], alternative distributions of coarse and fine grain layers at the micrometer scale led to strong and ductile architected metals [27]. Inspired by staggered “brick and mortar” architecture in nacre, staggering ceramic plates in microscale led to tough macrostructure that can be applied as armor [24, 25]. The composition and micro-architecture of two highly ordered natural architected materials, bone and tendon, are discussed below.

Bone: Assembled primarily from two major components, collagen type I and hydroxyapatite mineral crystals, bone achieves both strength and toughness beyond its individual constituents (or homogenous mixtures) by applying hierarchical gradients within its architecture (**Figure 1.3**) [3,

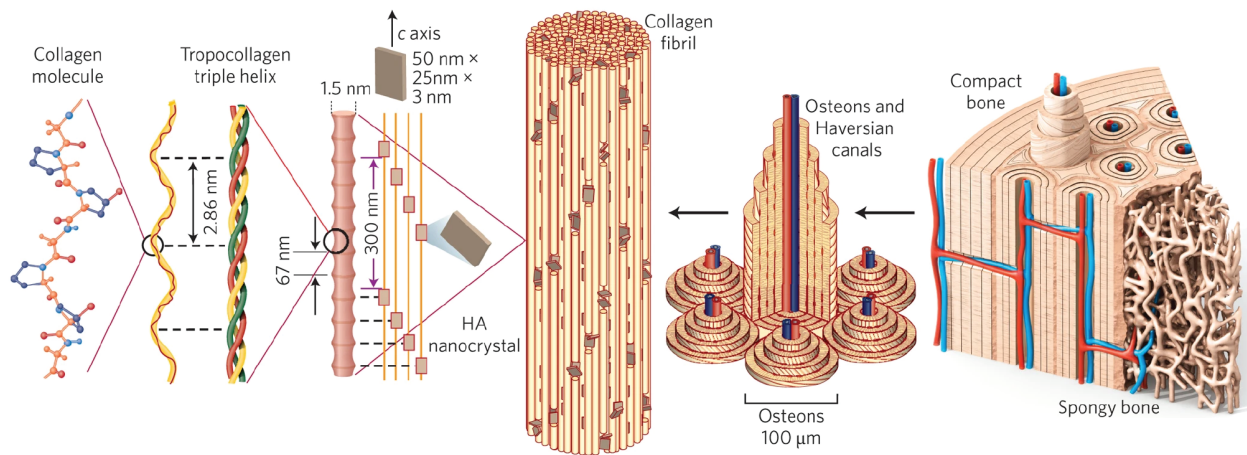


Figure 1.3: Bone derives its toughening mechanisms through a hierarchical architecture. Bone is primarily composed of collagen type I and hydroxyapatite mineral crystals that arrange into an intricate hierarchical structure. The origins of strength and toughness of bone result from a number of mechanisms that operate throughout its hierarchical architecture. Adapted, with permission, from Wegst *et. al.* [3].

5]. At the nano-scale, collagen type I molecules (300 nm in length, 1.5 nm in diameter) pack together to form a tropocollagen triple helix, which combine to form microfibrils, which further interdigitate to form fibrils (50-200 nm in diameter) [28]. Plate-shaped hydroxyapatite mineral nanocrystals accumulate on this collagen-based template in gap channels, in the intrafibrillar spaces, and on fibril surfaces [28, 29, 30]. Several mineralized collagen fibrils are then packed into fibers. The bone fibers arrange geometrically to form lamellar structured osteons. At the macro-scale, osteons and harversian canals make up cortical (i.e, compact) bone that surrounds the foam-like trabecular (i.e., spongy) bone. While the main stiffening elements in bone are the mineral platelets, bone derives its resistance to fracture through toughening mechanisms that are present through its architectural hierarchy [3]. At the sub-micrometer length scale, molecular uncoiling of collagen fibers [4], sacrificial bonds between the mineralized collagen fibrils [31], and microcracking [32] contribute to significant energy absorption and resistance to failure. At the micrometer scale, collagen-fiber bridging [3], uncracked-ligament bridging at the boundary of osteons [33], and crack deflection transverse to osteon orientations [34] are toughening mechanisms that serve to shield the crack tip once the crack begins to grow. Inspired by toughness amplifications seen in bone architecture, 3D printed engineered architected materials were able to reproduce the

fracture and toughening mechanisms of bone by mimicking cylindrical networks of osteons [35].

Tendon: Similar to the structure of bone, tendons have hierarchical architecture (**Figure 1.4**) [36, 37]. The building block of tendons is the collagen type I molecule. At the nano-meter length scale, tropocollagen molecules self-assemble into fibrils (50-200 nm in diameter). Molecules are arranged in a quarter-stagger pattern, which is responsible for the 67 nm d-banding observed by electron microscopy [38]. Chemical cross-linking by lysyl oxidase [39, 40] and non-enzymatic glycation also happen at this length scale [41]. While its mechanical contribution are still debated, small leucine rich decorin proteoglycans also interact with collagen fibril at this level [42, 43, 44]. At the next length scale, collagen fibrils assemble to form fibers (3-20 μm in diameter). In tendons of large animals and humans, fibers combine to form fascicles (with diameters on the order of micrometers), and form a characteristic “crimp” pattern which can be seen histologically [45, 46]. Finally, fascicles are bundled together through a fascicular membrane to form tendon (with a diameter on the order of millimeters or centimeters). Recent work in animals suggest that the physical size and the number of hierarchical levels of tendon depends on the anatomic location and species [37]. Several fiber-based tissue engineered solutions were recently developed mimicking the hierarchical architecture of tendons. [22, 47, 48].

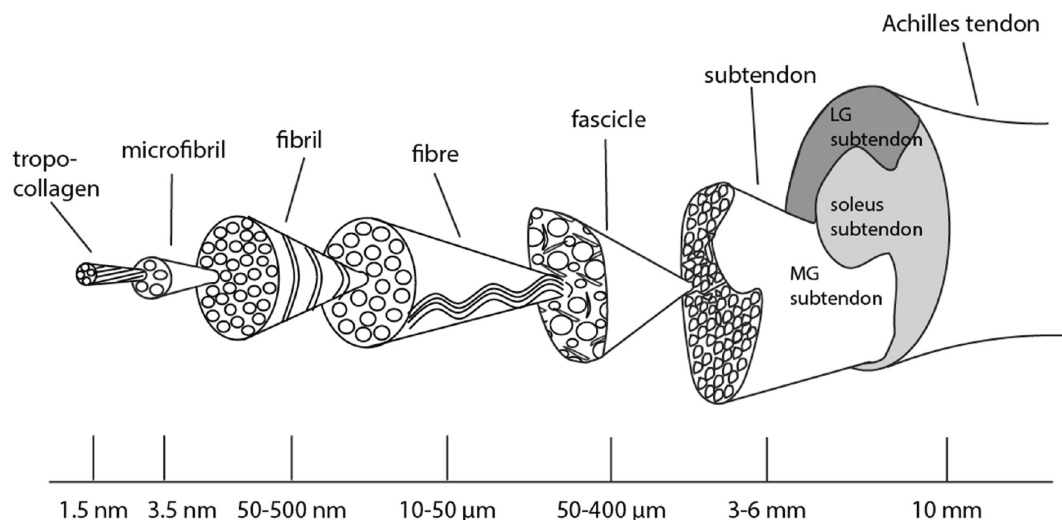


Figure 1.4: *Hierarchical architecture of tendon.* Here, the nomenclature for the human Achilles tendon hierarchy is shown. MG refers to medial gastrocnemius and LG refers to lateral gastrocnemius sub-tendons. Adapted, with permission, from Handsfield *et. al.* [37].

1.2 The Dilemma: Attaching two architected materials

Engineered architected materials offer tailored mechanical properties that overcome the typical performance trade-offs inherent in monolithic materials. However, the use of this new class of materials is limited by a lack of understanding on how to attach them. Typical features of architected materials (e.g., microtruss composites) lead to local elevations in stress that can reduce strength and toughness when they are connected to other materials [4]. This issue has impeded the application of architected materials in engineering practice. This ever-present problem in connecting dissimilar materials exists due to a mismatch between material properties that causes significant stress singularities (i.e., stress concentrations) at their interfaces [49, 50]. These singularities can induce material failure at significantly smaller loads than those at which the individual materials fail [51]. Since the early description of this phenomena by Williams in the 1950s [49], an array of engineering solutions, including adhesively bonded attachments and bolted connections, were developed to increase attachment toughness. Nevertheless, these solutions are inadequate in meeting ever-increasing requirements of structural performance in modern engineering. For example, adhesively bonded attachments provide mechanical damage tolerance against cyclical loading and obtain additional energy dissipation via shear-lag behavior [52]. However, adhesives are also known for their high residual stresses and do not tolerate multi-modal, multi-directional loading because they are sensitive to peeling and transverse shear stresses that lead to debonding [53]. Where should we look for solutions to these problems? The answer lies in attachment systems found in nature: at the tendon-to-bone attachment, i.e., the enthesis, two vastly different architected materials connect with impressive strength and toughness.

1.3 The Solution: The mechanics of the healthy tendon enthesis

1.3.1 The tendon enthesis as a guide to designing bi-material attachments

The stability and mobility of a joint is achieved through effective transfer of muscle load through two structurally and mechanically dissimilar architected materials: tendon (compliant ‘soft’ tis-

sue) to bone (stiff and brittle ‘hard’ tissue). Considering their bulk mechanical responses, these two architected materials have polarizing properties; Poisson ratios under stretching in the principle loading direction differ by an order of magnitude ($\nu_{tendon} \sim 3$ and $\nu_{bone} \sim 0.3$), while the elastic moduli in the principle loading direction differ by as much as 100-fold ($E_{tendon} \sim 0.4\text{GPa}$ and $E_{bone} \sim 20\text{GPa}$) [54, 55]. Such soft-hard interfaces with large mismatches in mechanical properties usually present a significant engineering challenge, even under simple uniaxial tension, because these attachments are expected to fail due to Bogy- or Williams-type stress singularities arising at their interface [49, 50]. Nevertheless, nature has developed an effective biologic solution to connect two highly architected materials at the tendon-to-bone attachment site, known as the tendon enthesis. The healthy tendon enthesis has a hierarchical architecture that can bear multi-modal and multi-directional loads by dissipating stress away from the attachment site (**Figure 1.5**).

1.3.2 Multi-scale mechanisms reduce stress-concentrations at the tendon enthesis

The tendon enthesis is a complex composite biomaterial with gradations in cell phenotypes, matrix composition, tissue organization, and mechanical properties. At the macroscale, the tendon enthesis appears as a graded tissue with four visually distinct regions: (1) tendon, (2) unmineralized fibrocartilage, (3) mineralized fibrocartilage, and (4) bone. Region (1), tendon, consists of highly aligned type I collagen, with small amounts of proteoglycan, decorin, and primarily fibroblast-like cells (tenocytes) [58, 59]. Region (2), unmineralized fibrocartilage, is mainly composed of a mixture of type II and type III collagen (**Figure 1.6**) in addition to the proteoglycan aggrecan [60, 61]. Type I, IX, and X collagens are also present in limited quantities [62]. Fibrocartilaginous cells with rounder cell morphologies primarily reside in this region. Region (3), mineralized fibrocartilage, is characterized by an onset of mineralization to region (2) [56, 63]. Region (4), bone, consists of mineralized type I collagen with the distinct architecture discussed in the prior section (**section 1.1.3**). While this traditional macroscopic view of the tendon enthesis with four distinct regions would imply an increased risk of failure at each of the interfaces within the tendon enthesis due to elevation in stress concentrations, recent refined characterization techniques and modeling

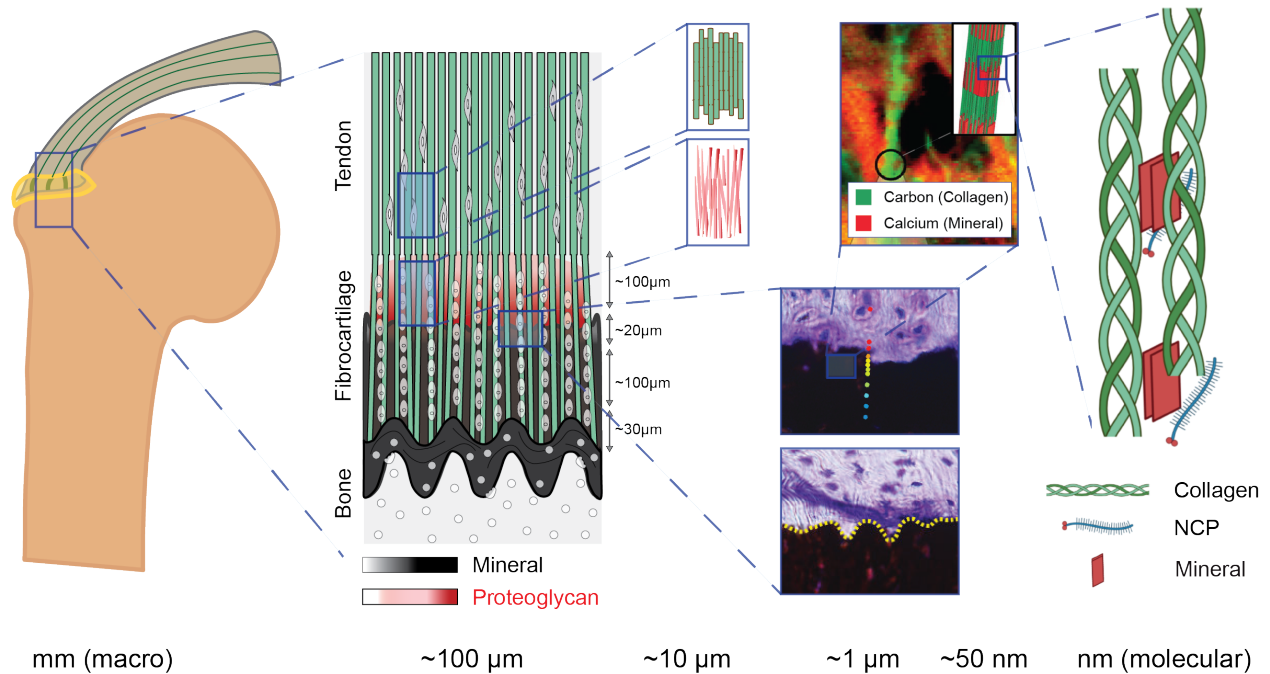


Figure 1.5: The healthy tendon enthesis presents multiscale solutions to the problem of attaching two dissimilar materials under physiologic loading conditions. At the millimeter scale, allometric scaling of the attachment footprint area and the splaying shape of the attachment site were shown to effectively reduce stress concentrations. At the micrometer scale, strong attachment at the tendon enthesis arises from a zone of compliant transitional tissue that mitigates stress concentrations through functional gradation in fiber orientation, biomolecular composition, and mineral concentrations. Furthermore, the interdigitations at mineralized and unmineralized tissues leads to a balance between attachment strength and toughness. At the nanometer scale, the particular arrangement of mineral crystal relative to the collagen fibril dictate the stiffening of the matrix. It is also suggested that, at this scale, non-collagenous proteins (NCPs) interact with the tendon enthesis fibers and mineral crystals to aid effective load transfer. Adapted under the terms of the Creative Commons Attribution-NonCommercial-No Derivatives License from Schwartz *et al.* [56]. Adapted, with permission, from Hu *et al.* [57] and Alexander *et al.* [30].

work showed that the tendon enthesis is rather a continuous, functionally graded tissue (i.e., with a gradual variation in composition, architecture, and mechanical proprieties over a defined volume that combines to provide distinctive properties) [6, 61]. The functional grading, typically incorporated in engineering materials at the microscale, occurs at the tendon enthesis over a range of length scales to attenuate stress concentrations and provide smooth transfer of load between the two dissimilar materials (**Figure 1.5**).

Millimeter length scale: The tendon enthesis attaches to bone with a splayed geometry over

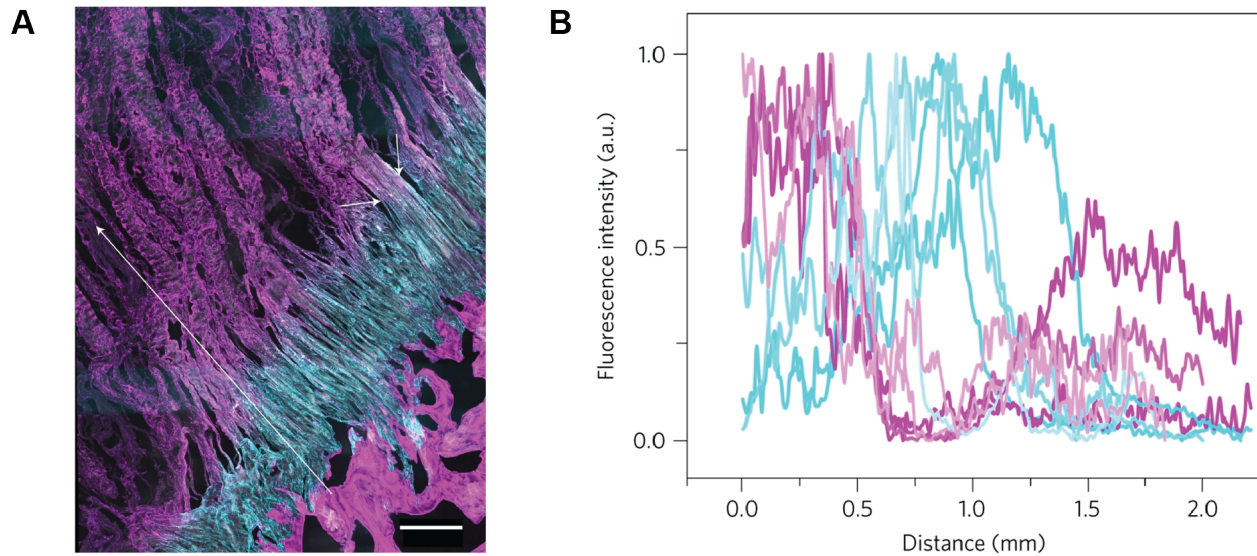


Figure 1.6: Tendon enthesis collagen composition changes from type I to type II before attaching to bone. (A) Confocal image of representative the porcine Achilles tendon enthesis, immunostained for collagen type I (magenta) and type II (cyan). Scale is $300\mu\text{m}$. (B) Fluorescence intensities plotted over the tendon enthesis (0.0 - bone and 2.0 - tendon). Adapted, with permission, from Rossetti *et al.* [61].

a large surface area. For instance, the attachment footprint area is as much as 3 times larger than that of the minimal tendon cross-sectional area in mice [64]. Allometry studies confirmed that this millimeter length scale stress alleviation mechanism is conserved across species [65]. The attachment footprint area increases isometrically with muscle size (i.e., physiologic cross-sectional area of muscle), implying that interfacial stresses are maintained across species. Modeling work further confirms this concept by showing that the stress concentration factor (i.e., a metric for stress singularities) remains constant with respect to animal body mass (**Figure 1.7**) [66]. The geometrical shape, shallow attachment angle, and the outward splay of tendon enthesis fibers also contribute to shield the tendon enthesis from stress concentrations at the macro-scale [54].

Micrometer length scale: The tendon enthesis presents as a continuous, functionally graded tissue with spatial gradations in collagen organization, proteoglycan composition, and mineral composition. Indeed, this functionally graded architecture allows the tendon enthesis to effectively transfer load across its bi-material attachment site through: (1) a compliant zone that minimizes

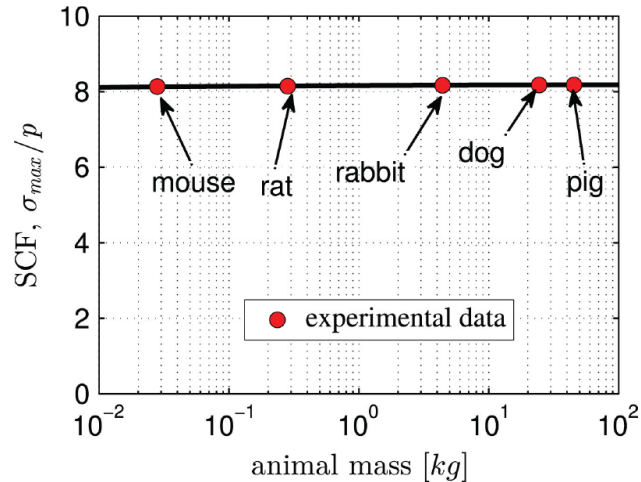


Figure 1.7: The tendon enthesis attachment area increases isometrically with muscle size, maintaining constant interfacial stress concentrations across animal species. Modeling results revealed that the stress concentration factor (SCF) does not vary across animals whose mass varies as much as three orders of magnitude. Adapted, with permission, from Saadat *et al.* [66].

stress concentrations, (2) fiber orientation distributions that introduce heterogeneity and randomness, (3) interdigitations that increase toughness, and (4) mineral gradations that increase stiffness without increasing localized stress.

- (1) **The compliant region:** Experimental and numerical analyses indicated that the functionally graded architecture at the tendon enthesis results in unique macro- and micro-scale mechanical behaviors due to the presence of a “compliant region” that exhibits higher deformation than either the soft tissue (i.e., tendon) or hard tissue (i.e., bone) [54, 60, 67]. This region of high local deformation, where the tissue near the insertion has a lower stiffness than the tendon mid-substance, was initially observed in the rat supraspinatus tendon enthesis [60]. Over the years, this high-compliance region has been experimentally shown across species, including in human supraspinatus tendon entheses, and other musculoskeletal soft-hard tissue interfaces, such as the patellar tendons, anterior cruciate ligament, and meniscus [68, 69, 70, 71]. While these studies have extrapolated deformation behaviors from macro-scale (tissue scale) mechanical testing and local image correlation, a recent experimental study on micro-mechanical properties of the tendon enthesis confirmed the existence of the micro-meter scale compliant region near the mineralized gradient of the tendon enthesis (**Figure**

1.8A) [72]. The presence of this compliant region is seemingly illogical from an engineering perspective: engineering practice would follow the intuitive approach of linearly interpolating mechanical properties (e.g., stiffness) between the two dissimilar tissues. However, a numerical model of the tendon enthesis, optimizing for minimizing stress concentrations, surprisingly showed that the biomimetic model (i.e., a model with compliant region at the tendon enthesis) produces the best case for reducing stress concentrations at the interface (**Figure 1.8B**)[67].

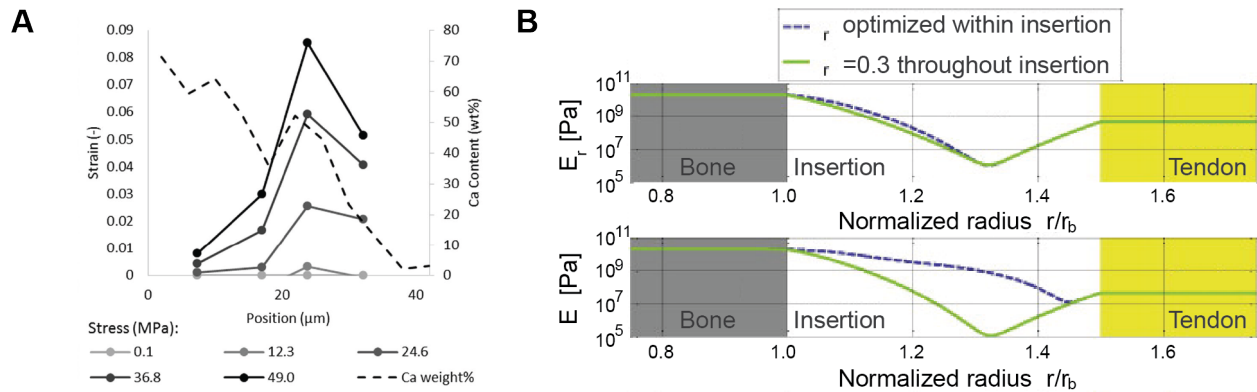


Figure 1.8: The tendon enthesis contains a high compliance region near the mineralized gradient that is optimized to reduce stress concentrations at the attachment. **(A)** Micro-mechanical testing of the mouse tendon enthesis confirmed the existence of a compliant region near the mineralization gradient within the tendon enthesis. **(B)** Numerical modelling showed that the biomimetic gradation in material properties containing a region that is more compliant than both tendon and bone, is optimized to reduce stress concentrations at the attachment. Adapted, with permission, from Deymier *et al.* [64] and Liu *et al.* [67].

- (2) **Fiber orientation:** Spatial variations in collagen fiber alignment are key micro-architectural features of the healthy tendon enthesis that reduce stress concentrations at the bi-material attachment. Quantitative assessments of collagen fiber organization using polarized light microscopy on rat supraspinatus tendons showed well-aligned collagen at the proximal end of the tendon enthesis (i.e., near the tendon mid-substance) that became increasingly disordered at the fibrocartilaginous portion of the enthesis as it attached to the bone [60, 73]. The peak angular deviations (i.e., higher randomness in the fiber alignment) were reported in the region just proximal to the mineral tidemark, approximately in the same location

where micro-mechanical testing shows the presence of the compliant region. The human supraspinatus tendon enthesis also showed highly inhomogeneous fiber organization at the insertion site [70]. *Ex vivo* cadaver mechanical testing with concurrent imaging showed that fiber distributions became more aligned under uniaxial loadings, with regional differences in the alignment significantly contributing to the local tissue mechanical properties [70]. Numerical models, both mathematical and using finite elements, showed that the increase in randomness to collagen fiber alignment contributes to a reduction in stiffness and stress concentrations at the tendon enthesis [54, 74, 73]. Recent experimental findings also suggest that the behavior of the tendon enthesis more closely resembles that of a networked solid [55], where only a fraction of fibers carry load depending on the loading direction [75, 76]. These findings suggest that deviations in fiber organization may endow toughness to the tendon enthesis.

- (3) **Interdigitation:** Another example of structural randomness that allows effective load transfer at the tendon enthesis is seen at the wavy, irregular interface between the unmineralized and mineralized fibrocartilage in the enthesis (**Figure 1.5**) [57]. Similar interfacial interdigitations are present throughout nature at mineralized interfaces in nacre [2], crayfish [5], and bone [4]. At the tendon enthesis, these interdigitations are rough, randomized, and they separate two structurally dissimilar materials, rather than two relatively stiff materials as observed within the nacre or bone. A first-order numerical model showed that increasing the roughness and stochasticity of the interdigitations at the bi-material interface improved overall toughness while sacrificing strength [57]. However, the interdigitation characteristics of the tendon enthesis showed a large gain in toughness for a relatively small loss in strength, demonstrating an optimized balance between the two mechanical parameters. Allometry also showed that tendon enthesis interdigitation roughness does not vary with muscle load (i.e., across species) [65], suggesting that this feature plays an important role in dissipating stresses at the micro-scale.

(4) **Mineral gradient:** In addition to organic compositional gradients, the tendon enthesis contains smooth gradations in mineral composition at the micrometer scale (**Figure 1.5**). Imaging the mouse supraspinatus tendon enthesis stained with von Kossa (which stains for mineral deposits) under an optical microscope showed an abrupt transition between unmineralized and mineralized fibrocartilage with a mineral “tidemark” [57]. However, quantitative Raman spectroscopy analysis showed a smooth gradient across the tidemark over a scale of $25 \mu\text{m}$. Similar functionally graded mineralized structures are commonly seen in other biological systems [6], including exoskeletons of arthropods [77], byssal threads of mussels [78], beak tips of squids [79], mouthparts of crayfish [80], and other soft-hard interfaces in mammals [81, 82, 83]. In the mouse tendon enthesis, this microscale mineral gradient develops postnatally, around 1 week after birth, and remains constant over the course of development, even though the animal size increases by as much as 10-fold [56]. Allometry revealed that the mineral gradient is constant, in the range of $20\text{-}60 \mu\text{m}$, across species [65]. Numerical models show that functional gradation in mineral content across the tendon enthesis width contributes to stiffening of the enthesis fibers only after mineral concentrations beyond the “percolation threshold” are achieved [54]. After this threshold, mineral crystals connect from one end of the fiber to the other, forming a continuous mineral network that carries most of the load instead of the collagen fibers. Hence, the modeling results demonstrate that a smooth microscale gradation in mineral content plays a critical role in increasing the tendon enthesis stiffness to mediate load-transfer at the micro-scale, thereby minimizing the formation of stress concentrations.

Nanometer length scale: Similar to what has been described in bone (**section 1.1.3**), the tendon enthesis nano-scale bioapatite (i.e., mineral) crystal platelets accumulate in the intrafibrillar spaces (i.e., within the gap zones of the collagen fibrils) and/or in the extrafibrillar space (i.e., on collagen fibril surfaces) [30]. Within the mineral gradient of the tendon enthesis, there is a gradation in mineral crystal organization relative to the enthesis fibers. In the regions of low mineralization, mineral crystals are located in the extrafibrillar space, while in the region of high min-

eralization, these crystals are located in both intra- and extra-fibrillar spaces [64, 84]. Interestingly, *in vivo* unloading of the tendon enthesis leads to changes in the size, composition, crystallinity, and arrangement of the mineral crystals at the tendon enthesis. For example, unloading decreased mineral crystal size, mineral carbonate content, and increased misalignment of mineral crystals relative to the primary loading axis of the tendon enthesis leading to an overall decrease in tendon enthesis stiffness [64]. Numerical modeling showed the importance of mineralization sequence, mineral crystal orientation, as well as mobility of mineral crystals in shifting load-sharing mechanisms between collagen and mineral at the tendon enthesis [64, 85, 86]. While not examined at the tendon enthesis, non-collagenous proteins such as osteopontin and proteoglycan molecules are predicted to increase the degree of plasticity and load-transfer at the tendon enthesis, similar to what is seen in cartilage and bone [31, 87, 88].

1.3.3 Gap in knowledge: Limited understanding of strength and toughness mechanisms

The healthy tendon enthesis presents with a number of multi-scale mechanisms, described above (**section 1.3.2**), to effectively transfer load across two architected materials. However, these mechanisms were only evaluated under physiologic loading conditions (i.e., sub-damage loading regimes) and mechanical behavior of the tendon enthesis in the inelastic (“post yield”) and failure regimes were not established. As will be discussed in the next section (**section 1.4**), the seemingly robust attachment does fail due to degeneration and/or injury, and healing of injured entheses does not recreate any of the aspects described above that endow the healthy tendon enthesis with its mechanical behavior.

1.4 The clinical significance: Injured enthesis does not regenerate toughening mechanisms, resulting in failure of repairs

1.4.1 Prevalence of tendon and tendon enthesis injuries

Musculoskeletal injuries, typically presenting as pain, limited mobility, dexterity, and overall level of joint function, are becoming a greater burden to society every year. In the United States,

approximately two-thirds of adults are affected by musculoskeletal conditions [89]. Over 100 million injuries are reported per year costing over \$980 billion annually, with associated direct and indirect costs [90]. The prevalence of musculoskeletal injuries is twice as high amongst the elderly population (i.e., individuals over 75 years old) compared to that of active younger population (i.e., age 25-44 years old) [91]. Changes to work environment, shifts in lifestyles, and an increase in the geriatric population, has results in as much as an 85% increase in the number of consultations for musculoskeletal injuries compared to 10 years ago, far surpassing cases for circulatory and respiratory diseases [92]. Of those consultations, approximately 35% involve full thickness tears or sub-failure tissue damage to seemingly intact soft connective tissues at or near the tendon enthesis [89]. These injuries are particularly painful and debilitating, leading to lost days from work, occupational challenges, and recreational limitations [93, 94]. In addition, injuries can instigate other health concerns, including obesity and depression, ultimately decreasing one's quality of life [95]. A large market size and a steady growth in consultations have fueled multi-billion-dollar industry for treating orthopedic soft tissue injuries. Nevertheless, the innovations in this field have largely focused on rehabilitation and surgical strategies, with only limited success.

1.4.2 Characteristics of tendon enthesis injury and repair

Soft tissue injuries at or near tendon enthesis occur in various locations throughout the body, such as at the supraspinatus tendon of rotator cuff, the Achilles tendon of the ankle, and the patellar tendon of the knee. These injuries are primarily classified into two categories: acute or chronic [36, 96]. Acute injuries happen suddenly on otherwise healthy tissues and are usually associated with a traumatic event, e.g., during sports (e.g., due to sudden change of body direction, hyper extension of the joint, collision) or accidents (e.g., due to laceration). Chronic tears are characterized by degenerative changes to the entheses, often due to overuse and repeated sub-failure injuries. The majority of entheses injuries result from chronic degeneration, and are most frequently presented in the clinic as joint pain, tenderness, and reduced range of motion or strength [97]. In addition to a physical examination, imaging modalities such as ultrasound and magnetic resonance imaging

are typically used to further classify tendon and the tendon enthesis injuries according to size (e.g., full thickness tear or partial thickness tear) and failure type (e.g., tendon mid-substance ruptures, enthesis ruptures, or bony avulsion). Regardless of the categorization (**Figure 1.9**), most tendon and tendon enthesis injuries do not heal on their own and require surgical reattachment of torn tendon(s) to their bony insertion(s) [98, 99]. While the classifications are useful to guide surgical repair techniques and rehabilitation options, most repairs only show moderate success rates, and re-injury is commonplace [100]. The state of several clinically significant tendon and tendon entheses injuries are discussed below.

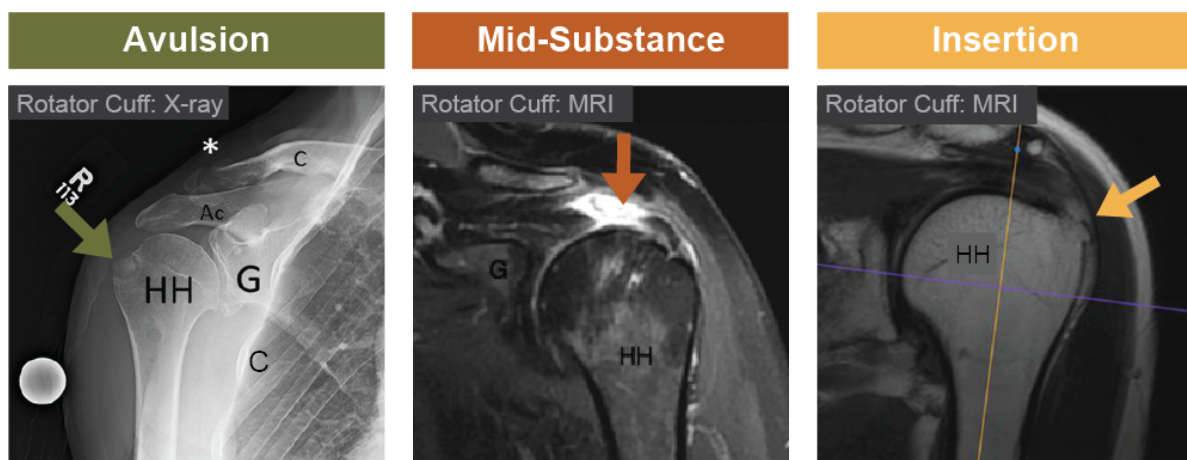


Figure 1.9: *Tendon entheses often fail due to injury or degeneration.* Clinically, bone avulsion fractures or tendon mid-substance ruptures are commonly seen in high-impact injuries and in pediatric patients, while insertion failures are prominent for the degenerated rotator cuff in adult patients. Arrows indicate failure locations. HH - humeral head; G - glenoid; Ac - acromion; C - clavicle. Adapted, with permission, from Jeong *et al.* [101], Godin *et al.* [102], and Ghazanfari *et al.* [103].

Rotator cuff: In the upper extremity, rotator cuff injuries, and particularly injuries to the supraspinatus tendon enthesis, are among the most common musculoskeletal disorders and estimated to affect more than 17 million individuals in the United States [104]. The incidence of rotator cuff tears is high, with approximately 50% of the population over the age of 65 having a rotator cuff tear [105]. Rotator cuff tears are classified as acute injuries (e.g., sports injuries due to aggressive overhead motions, typically seen in baseball pitchers, swimmers, golfers, and tennis players) and chronic injuries (e.g., injuries following years of tissue degeneration). Both types of

injuries commonly occur at or near the supraspinatus tendon enthesis (i.e., insertion rupture) [101, 106]. Chronic rotator cuff tears are significantly more prevalent in the elderly population. These injuries typically present with significantly altered tendon enthesis architecture (including fatty accumulation in the associated muscle), which negatively impacting the mechanical properties and healing capacity of the tissue [107, 108]. Rotator cuff tears do not heal on their own and require surgical reattachment, leading to more than 450,000 rotator cuff surgical repairs performed annually in the United States [109, 110]. Although cost-effectiveness analysis estimates dramatic net societal cost savings with successful surgical repairs on full thickness rotator cuff tears for patients under 61 years old, only moderate improvements in quality-adjusted life years (QALYs) outcomes is seen due to poor surgical outcomes [94]. For example, in one study, the average healing rate after rotator cuff repair at 12 months was 56% [111], with recurrent tears occurring in 20% for young, healthy athletes and increasing to as high as 94% of cases for elderly patients with massive tears [100].

Achilles tendon: Achilles tendon ruptures are the most common tendon tears in the lower extremity, with an incidence rate of 31 per 100 000 per year, frequently affecting the young to middle aged active populations (age 25-44 years old) [112]. A recent meta-analysis showed a bimodal age distribution for Achilles tendon ruptures: the first peak occurring in patients aged 25 to 40 years with tears associated with high-energy sports injuries (e.g., forced planter flexion of the foot while playing tennis, basketball, soccer, or badminton), while the second peak occurring for patients over 60 years with tears associated with low-energy activities (i.e., spontaneous rupture) primarily due to tissue degeneration [113]. Achilles tendon ruptures commonly occur in the tendon mid-substance, 2-6 cm proximal to the tendon enthesis [114]. While infrequent, Achilles tendon injuries may also present as insertion ruptures (i.e., tendon tears at the Achilles tendon enthesis) or calcaneal bony avulsions [115]. Given that injuries to the Achilles tendon are significantly debilitating, surgical repairs have been historically recommended over conservative management. However, a recent meta-analysis showed that operative treatments of Achilles tendon ruptures only moderately reduce the risk of re-rupture rates compared to non-operative treatments [116].

Patellar tendon: Patellar tendinopathy, an overuse injury to the patellar tendon, frequently affects athletes involved in jumping sports, such as basketball. The tendinopathy, typically referred to as jumper's knee, may progress to partial patellar tendon tears and ultimately lead to full thickness patellar tendon rupture [117]. In the United States, patellar tendon ruptures occur in approximately 0.5% of the population each year, commonly affecting elite and recreational male athletes [118]. While pathophysiology is still under debate, patellar tendon ruptures are typically attributed to tensile overload on the extensor mechanisms of a weakened tendon [119]. These injuries are reported to occur when the quadriceps muscle suddenly contracts with the knee in a flexed position, such as when athlete is landing from a jump, or suddenly stopping to change directions when running [120]. Patellar tendon ruptures are most commonly located at the proximal insertion to the inferior pole of patellar bone, with or without a bony piece from the inferior pole of the patella (i.e., either insertion rupture or bony avulsion failure) [121]. While relatively rare, patellar tendon mid-substance ruptures and bony avulsions of the patellar tendon from the tibial tubercle are also reported [118]. Similar to that of rotator cuff ruptures, patellar tendon ruptures do not heal on their own and require surgical reconstruction. While success rates for patellar tendon repairs are relatively high in terms of QALYs and return to play outcomes, low rates of return to pre-injury level of play are reported in elite athletes [122]. In a National Football League (NFL) study, 5 out of 19 NFL players (26%) with full thickness tears failed to return to play after the repair [117], while in a National Basketball Association (NBA) study, 3 out of 10 NBA players (30%) with full thickness patellar tendon tear were forced to retire after the repair, and others with repair have reported decreases in total minutes played after repair [123].

1.4.3 Compromised enthesis architecture is not regenerated during healing after surgical and natural repair

The mechanical challenge in attaching two architected materials is apparent in the outcomes after surgical repair of tendon to bone: moderately high failure rates are seen after surgical re-attachment of compliant tendons to rigid bones, and typically occur within three months after re-

pair [124]. In addition, repair tissues tend to have toughness that is so vastly inferior to the healthy entheses that decreased functional outcomes (i.e., reduced QALYs, return to play outcomes, or retirement from sport) and re-injury are commonplace. Many factors have been associated with inadequate clinical outcomes following surgical or natural repair, including patient age, gender, size of injury, chronicity of injury, extent of muscle atrophy, bone quality, diabetes, and smoking [107, 125]. Recent clinical and animal studies reveal that at the root of these failures is a poor healing response that does not regenerate the tendon enthesis architecture [97, 126, 60]. Many studies have shown that high levels of inflammation after injury-and-repair leads to fibrovascular scar rather than aligned collagen (**Figure 1.10**) [127, 128, 129, 130]. Significant bone loss near the tendon enthesis is also observed for both acute and chronic *in vivo* rat rotator cuff injury-and-repair models [131, 132, 133], mirroring the osteopenia correlated with the severity and chronicity of rotator cuff re-tears seen in clinical settings [134]. Hence, compromised architecture due to injury and inadequate healing lead to poor mechanical responses and deleterious clinical outcomes. Therefore, there is a pressing need to identify, reconstitute, and/or replace the mechanisms underlying toughness of the healthy enthesis following surgical repair.

1.5 The final piece of the puzzle: understanding toughening mechanisms

Application of functionally architected materials is hindered by the challenge of connecting them together. Historically, natural materials provided a rich source of inspiration for the design of architected engineering materials. Understanding the mechanisms of load transfer at the tendon enthesis, nature's solution for attaching two architected materials, would be valuable for informing both biological and engineered attachment of dissimilar materials. While prior works on the healthy tendon enthesis (**section 1.3.2**) have focused on understanding the sources of stiffness and strength (i.e., the onset of injury), the sources of toughness (i.e., the energy absorption that protects against failure following the onset of injury) are largely unknown. Indeed, a better understating of the architectural features that determine enthesis toughness can guide engineering and medical solutions for bimaterial attachment.

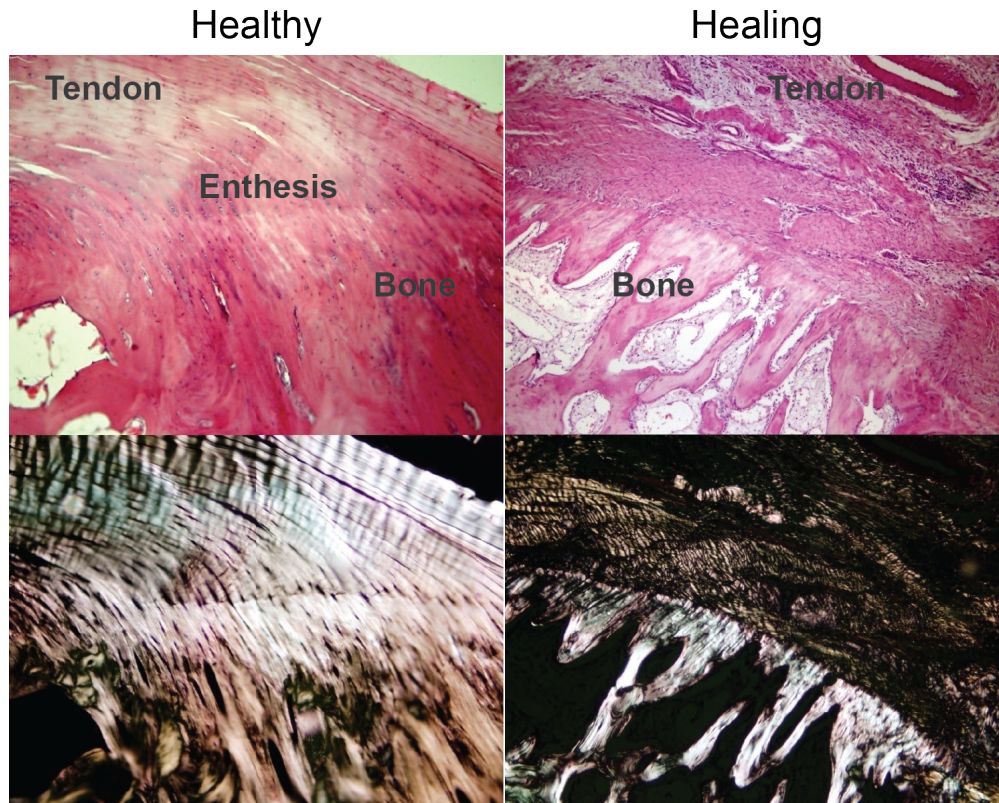


Figure 1.10: *Tendon enthesis architecture is not regenerated after healing.* Histological sections stained with heamatoxylin and eosin of intact and healing canine flexor digitorum profundus tendon viewed under **(top)** bright-field and **(bottom)** polarized light. Highly aligned collagen architecture is evident in healthy, while disorganized scar tissue is apparent in healing tendon enthesis after injury-and-repair. Adapted, with permission, from Silva *et al.* [127].

Experimental and modeling approaches for identifying the features of the tendon entheses that endow them with toughness are not yet available, and animal models of toughness have not yet been established. Specifically, developing a mouse model of enthesis failure would be useful for studying the fundamental mechanisms that relate tendon enthesis architecture with its toughness, including *in vivo* responses to maintain this toughness. Hence, the overall goal of this dissertation is to establish the architectural contributions to tendon enthesis toughness by determining the multiscale failure mechanisms in healthy and pathologic mouse tendon entheses. The central hypothesis of this thesis is that multi-length scale energy absorption is the fundamental toughening mechanism by which dissimilar tissue attachments resist injury-level loads.

1.6 Scope and procedure of the dissertation

This thesis describes toughening mechanisms for the attachment of architected materials by investigating architectural and compositional contributions to enthesis toughness in healthy and pathological mice. In **Chapter 2**, a novel view of the fibrous architecture of the tendon enthesis is uncovered via the development of a high-resolution contrast-enhanced micro computed tomography (microCT) visualization technique. Using this imaging technique in conjunction with a protocol of interrupted mechanical testing and fluorescent microscopy, **Chapter 3** identifies how the fibrous networks of the healthy tendon enthesis accumulates damage through monotonic (acute) and cyclical (degenerative) loading. In **Chapter 4** and **Chapter 5**, the primary toughening mechanisms of the tendon enthesis are demonstrated to be derived from joint position (i.e., diverging collagen organization and fiber recruitment due to loading angle) and composition (i.e., mineral and proteoglycan content), respectively. In **Chapter 6**, mice are subjected to pathologic *in vivo* loading to induce changes in enthesis mineralization and architecture leading to changes in toughness. **Chapter 7** describes a clinical example that applies these concepts to patient care: tracking changes to tendon enthesis architecture is an accurate predictor of clinical outcomes. Demonstrating an example of tendon-to-bone healing, **Appendix A** uncovers the therapeutic opportunity for pharmacological inhibition of $\text{IKK}\beta$ to enhance tendon-to-bone healing after rotator cuff repair in a rat model.

1.6.1 Specific Aims

Aim 1: Identify the toughening mechanisms of the healthy murine tendon enthesis subjected to multi-modal and multi-directional loading *ex vivo*.

Hypothesis A — Architectural mechanisms: The distinct fibrous architecture of the tendon enthesis will allow the interface to absorb enough energy that failure will occur in the adjacent tendon or bone.

Approach: To characterize the healthy tendon enthesis architecture, a novel contrast-enhanced microCT-based imaging technique will be developed to simultaneously observe mineralized and unmineralized portions of the tendon enthesis at sub-micrometer resolution. To understand the mechanical failure mechanisms of the tendon enthesis, mouse tendon enthesis samples will be tested in tension at quasi-static rates. Mechanical properties, failure modes, failure surfaces, and tendon/bone morphology will be analyzed via nano- though milli-scale characterization techniques, including electron microscopy, contrast-enhanced microCT, conventional microCT, histology, and visual inspection (**Chapter 2**).

Hypothesis B — Failure mechanisms (multi-modal loading): The nature of mechanical loading will contribute to differences in tendon enthesis failure behavior, with distinct molecular-level injury localization and propagation mechanisms depending on the mode of loading. Molecular-level damage will initiate either at the unmineralized fibrocartilage and propagate to failure in bone or will initiate and accumulate at the unmineralized fibrocartilage and propagate to failure at the insertion.

Approach: Failure mechanisms of mouse entheses will be characterized by investigating whole tissue (macroscale) failure mode and molecular level (nanoscale) collagen damage localization and propagation. Loading modes will include monotonic and cyclical loading conditions. Mechanical testing of tendon enthesis specimens will be interrupted at prescribed loading levels (i.e., toe, linear, yield, and failure regions for monotonic loading; low and high load amplitude for cyclical loading) and imaged with microCT (for macroscopic- and fiber network-level damage) and fluorescence imaging of collagen damage (i.e., molecular-level damage). Failure modes, failure surfaces, fiber organization and tendon/bone

morphology will be analyzed at these loading levels (**Chapter 3**).

Hypothesis C — Structural mechanisms (multi-directional loading): Tendon enthesis architecture is designed to optimize toughness of the attachment for a wide range of loading positions. Increasing loading angle will decrease the strength and toughness of the tendon enthesis.

Approach: Mouse tendon enthesis samples will be subjected to *ex vivo* mechanical testing oriented and loaded at varying loading angles. Intact and failed tendon enthesis samples will undergo contrast-enhanced microCT imaging to determine the tendon enthesis architecture, failure modes, and failure surfaces across a range of loading directions. Based on imaging characteristics, a numerical model will be developed to further elucidate putative fibrous toughening mechanisms observed at the tendon enthesis (**Chapter 4**).

Hypothesis D — Compositional mechanisms: Removal of proteoglycan will reduce tendon enthesis toughness while removal of mineral will reduce both tendon enthesis strength and toughness.

Approach: The compositional contributions on enthesis toughness will be evaluated by chemically removing the constituents (i.e, mineral or proteoglycan) and examining enthesis mechanical behavior (**Chapter 5**).

Aim 2: Identify loading-induced adaptations to toughening mechanisms in murine tendon entheses *in vivo*.

Hypothesis A: Underuse degeneration will reduce mineralization at the tendon enthesis, contributing to decreases in strength and toughness.

Hypothesis B: Overuse degeneration will increase mineralization at the tendon enthesis, contributing to increases in stiffness, strength, and a decrease in toughness.

Approach: Physiologically relevant adaptations to the tendon enthesis architecture will be induced by subjecting mice to *in vivo* either increased or decreased loading. Increased (overuse) loading will be applied using treadmill running and decreased loading will be applied using botulinum toxin A-induced paralysis. As in Aim 1, structural and compositional characterization will be performed from nano- through milli-scales to define the mechanisms driving mechanical behavior (**Chapter 6**).

Clinical Example: Determine the location, point of initiation, and size of partial patellar tendon tears and predict the failure risk in patients with patellar tendinopathy.

Hypothesis A: Patellar tendon tears originate near the bony attachment at the inferior pole (proximal part) of the patellar and can be visualized via MRI due to changes to its architecture.

Hypothesis B: Patellar tendon tear size inversely correlates with surgical outcomes and return to sport/activity measures.

Approach: Retrospectively identify pathological architectural adaptations to the patellar tendon and its enthesis using magnetic resonance imaging and correlate these characteristics with clinical outcomes measures, such as the requirement for surgical reconstruction and/or return-to-sports outcomes (**Chapter 7**).

Chapter 2: Attachment at the enthesis relies on a fibrous architected material system

Portions of this chapter are currently under review: Golman M, Abraham AC, Kurtaliaj I, Marshall BP, Hu YJ, Schwartz AG, Guo XE, Birman V, Thurner PJ, Genin GM, Thomopoulos S. Toughening mechanisms for the attachment of architected materials: The mechanics of the tendon enthesis.

2.1 Introduction

The enthesis presents a tough attachment between tendon and bone, two architected tissues with vastly different mechanical properties. As discussed in the previous chapter (**section 1.3.2**), this transitional tissue has previously been shown to mitigate stress concentrations through functional gradations of composition and structure, including: allometric scaling to normalize stress according to muscle size [65, 66], interdigitation to increase toughness [57], a compliant zone to minimize stress concentrations [67, 74, 54], fiber orientation distributions that introduce heterogeneity [60, 73], and mineral gradations to increase stiffness without increasing localized stress [74, 56]. Consistent across all prior descriptions of tendon-bone attachment is the implication that the enthesis is architected to favor toughness (i.e., the energy absorption that protects against failure following the onset of injury) over strength (i.e., the onset of injury), allowing for effective load transfer without failure. Nevertheless, these prior studies have mainly characterized mechanisms of load transfer under sub-damage loading conditions, and mechanical behavior of the tendon enthesis in the inelastic (“post yield”) and failure regimes are not established. Understanding and predicting the failure behaviors of the tendon enthesis may facilitate development of biomimetic repair strategies that reconstitute natural toughening mechanisms at the tendon enthesis.

To investigate how the architecture of the enthesis gives rise to its toughness, a high-resolution imaging technique was developed to simultaneously image the mineralized and unmineralized fibrous network of tendon-bone attachment at the sub-micrometer level using microcomputed tomography (microCT). To understand the mechanical failure mechanisms of the tendon enthesis, mouse tendon enthesis samples were tested in tension at a quasi-static rate (i.e., at a rate sufficiently slow that inertial forces can be neglected). We hypothesized that, under quasi-static loading conditions, the enthesis would fail at the interface between mineralized and unmineralized fibrocartilage, where the material mismatch would lead to stress concentrations.

2.2 Methods

2.2.1 Sample Preparation and Study Workflow

All animal procedures were approved by the Columbia University Institutional Animal Care and Use Committee. Supraspinatus tendon-to-bone attachment units (humerus-tendon-muscle) were harvested from adult (>12 weeks) male C57BL6/J mice (n=37). After dissection, samples were fresh-frozen in PBS and stored at -20°C . The experimental workflow was dependent on two categories: (1) unloaded/intact sample characterization; and (2) loaded sample characterization.

For unloaded-sample characterization, defrosted samples were subjected to initial experimental protocol described in the sections below, or in the next chapters, and imaged via contrast enhanced microCT or via light microscopy, as the imaging techniques were terminal. For characterizing samples undergoing loading, defrosted samples were first scanned by conventional microCT before being subjected to experimental protocol and mechanical testing. After mechanical testing, samples were secured at terminal displacements and either submerged in a 5% mercury chloride (HgCl_2 , Sigma-Aldrich) or fixed with 4% paraformaldehyde (Sigma-Aldrich) to analyze for macroscopic and fiber network level damage.

2.2.2 Contrast enhanced and conventional micro computed tomography (microCT) imaging

Simultaneous visualization of soft and hard tissues of tendon enthesis samples was achieved by staining samples with 5% mercury chloride solution prior to scanning with microCT. A 5% mercury chloride solution was prepared fresh for each experimental day by dissolving mercury (II) chloride (HgCl_2 , Sigma-Aldrich) in distilled and de-ionized water (MilliQ water, MilliporeSigma) at room temperature until the saturation was achieved. Tendon enthesis samples, either intact or post-mechanical testing, were submerged in this solution for 24 hours and washed three times in distilled and de-ionized water for 10 minutes each before they were imaged with microCT (Skyscan 1272, Bruker).

The same preparations and scan settings were used when visualizing enthesis samples with both conventional and contrast enhanced microCT. To prepare for scanning, the distal end of supraspinatus-humerus unit were embedding in 2% agarose (Sigma-Aldrich) and mounted in the scanning chamber, so that tendon enthesis specimens were hung loosely and in line with the scanning axis. Scans were performed with 60kVp, 166uA, and Al 0.5mm filters with isometric resolution of $2.5 \mu\text{m}$. To visualize enthesis insertions and failure surfaces, high resolution images were obtained at $0.75 \mu\text{m}$ resolution. The acquired microCT data were reconstructed with the software (nRecon, Bruker) provided with the CT scanner using alignment optimization and beam-hardening correction. The reconstructed image data was visualized with built-in program (DataViewer and CTvox, Bruker).

2.2.3 Tendon cross-sectional area, mineralized fibrocartilage area, footprint area, insertion area, and failure area determination

Conventional and contrast enhanced microCT scans of murine tendon enthesis samples were analyzed to determine minimal tendon cross-sectional area, mineralized fibrocartilage (MFC) area, enthesis footprint area, insertion area, and failure area. The minimum tendon cross-sectional area and mineralized fibrocartilage area for each sample were determined from conventional microCT scans that were performed on samples prior to mechanical testing (or prior to staining with HgCl_2)

and analyzed via built-in image processing algorithms (CTAn, Bruker). Minimum cross-sectional tendon area was determined by thresholding the transverse slices through the tendon, calculating the area encompassing the tendon, and selecting the smallest area of a tendon that is within 500 μm from the tendon insertion site.

Apparent footprint area, insertion area, and failure area were estimated using HgCl_2 stained contrast enhanced microCT images of enthesis samples, as the imaging technique allows for differential absorbance coefficients between each tissue selected. Since the regions of interest were along the curved volume (i.e., humeral head), a custom semi-automated MATLAB (Matlab2019a, MathWorks) routine was developed to calculate the overlapping polyhedron surface meshes from two arbitrary volumes (e.g., humeral head and tendon enthesis) from the same imaging data set. The first region represents the surface of the bone: either the surface of the humeral head (for calculating footprint area or insertion area), or the surface of avulsed pieces (for calculating failure area). This region was obtained by thresholding and semi-automatically contouring via shrink-wrapping algorithm built-in to the manufacturers' imaging processing software (CTAn, Bruker). The second region for calculating *footprint area* or *insertion area* represents volume of the tendon enthesis that intersects with the surface of the humeral head along the edge of the tendon attachment. The second region for calculating the *failure area* represents a volume that contains only the fractured surface of the avulsed piece. The edges of the second region for in both cases were determined visually by manually contouring appropriately slices for each region of interest. The output volume sets were triangularly meshed to determine the surface area between the overlapping volumes.

2.2.4 Scanning Electron Microscopy (SEM)

Failed tendon enthesis samples (n=10) were dried at 37 °C, fixed on SEM aluminum pin mounts using carbon tape and silver paint and carbon-coated (30 nm). Prepared samples were imaged by scanning electron microscope (FEGSEM, Quanta 250F, FEI Company, Hillsboro, OR, USA) in backscattered electron mode using a concentric backscattered detector and acceleration voltages of 5-15 KV at a working at different magnifications from 250x to 20,000x. SEM was carried out

using facilities at the University Service Centre for Transmission Electron Microscopy, TU Wien, Austria.

2.2.5 Histological Analysis

Some intact and failed samples (n=5 each) were fixed in 4% paraformaldehyde for 48h, decalcified in formic acid (StatLab, Immunocal) for 5 days, dehydrated in graded ethanol, and embedded in paraffin. 5 μ m sections were obtained and stained with toluidine blue to highlight the enthesis fibrocartilage, pentachrome and picrosirius red to visualize collagen. Picrosirius red-stained sections were imaged using a polarized light microscope, while other stains were imaged via bright field microscopy with 10 \times and 40 \times objectives.

2.2.6 Mechanical Testing

Samples were mechanically tested in a saline bath at 25°C to prevent thermal collagen denaturation on a table-top tensile tester (Electroforce 3230, TA Instruments) fitted with 10 lb. load cell (TA instruments). Before testing, the supraspinatus muscle was carefully removed from supraspinatus-humerus unit. Samples were placed into custom 3D-printed fixtures [135]. The tendon were secured between two layers of thin paper (Kimwipe) with a drop of cyanoacrylate adhesive (Loctite, Ultra Gel Control) before mounting onto custom grips. Samples were secured in fixtures and tested in an orientation corresponding to 90° shoulder abduction. Mechanical testing protocol consisted of: (1) pre-loading to 0.05 N; (2) pre-conditioning by applying 5 cycles of sinusoidal wave consisting of 5% strain and 0.2%/s; (3) resting for 300 seconds; and (4) quasi-statically and uniaxially strained in tension at 0.2 %/s to failure.

Enthesis structural properties, such as failure load (referred as strength in text), stiffness, and work to failure (area under the curve through failure load, referred as toughness in text) were determined from load-deformation curves. Stiffness was calculated by a custom algorithm in MATLAB that identifies the best fitting line within a sufficient bin width (i.e., remove data below 10% of max load and above 95% of max failure force) by implementing the random sample correlation

(RANSAC) [52].

2.2.7 Statistical Analysis

To compare tendon cross-sectional area, footprint area, and insertion area repeated measure ANOVAa followed by the Tukey's multiple comparison tests were performed. All statistical analyses were performed using Prism 9 (GraphPad). All data shown as mean \pm standard deviation, with $p < 0.05$ considered statistically significant. Sample size, n , represents biological replicates.

2.3 Results

2.3.1 The tendon enthesis exhibits fibrous architected material system

Contrast enhancement with mercury (II) chloride staining allowed simultaneous, sub-micrometer imaging of unmineralized and mineralized tissue in the mouse supraspinatus tendon enthesis using high-resolution microCT scanning. This technique did not require destructive sample preparation steps and prevented potential distortions to the sample, as it would be the case for serial sectioning [136]. The new imaging methodology uncovered the fibrous nature of tendon enthesis architecture, as it allowed to visualize the enthesis fibrous network at sub-micrometer resolution in three dimensions under physiological orientations (**Figure 2.1A**).

Imaging of intact specimens revealed that, hidden within the well-known larger attachment apparent footprint area (**Figure 2.1B**, within blue dotted line), exists a smaller, much denser "primary" insertion site where tendon fibers directly insert into the bone surface (**Figure 2.1B**, within green dotted line). Tendon enthesis collagen fibers were continuous throughout the majority of attachment unit (from muscle to bone), but branched into smaller diameter fibers as they inserted into bone on one end, or muscle at the other. The existence of primary insertion site was further confirmed via histological analysis. Representative images of pentachrome-stained coronal section of the tendon enthesis (**Figure 2.1C**) showed the dense primary tendon (bulk tendon), stained in red (i.e., representing maturity of dense collagen), is surrounded by peritenon tissue stained in yellow.

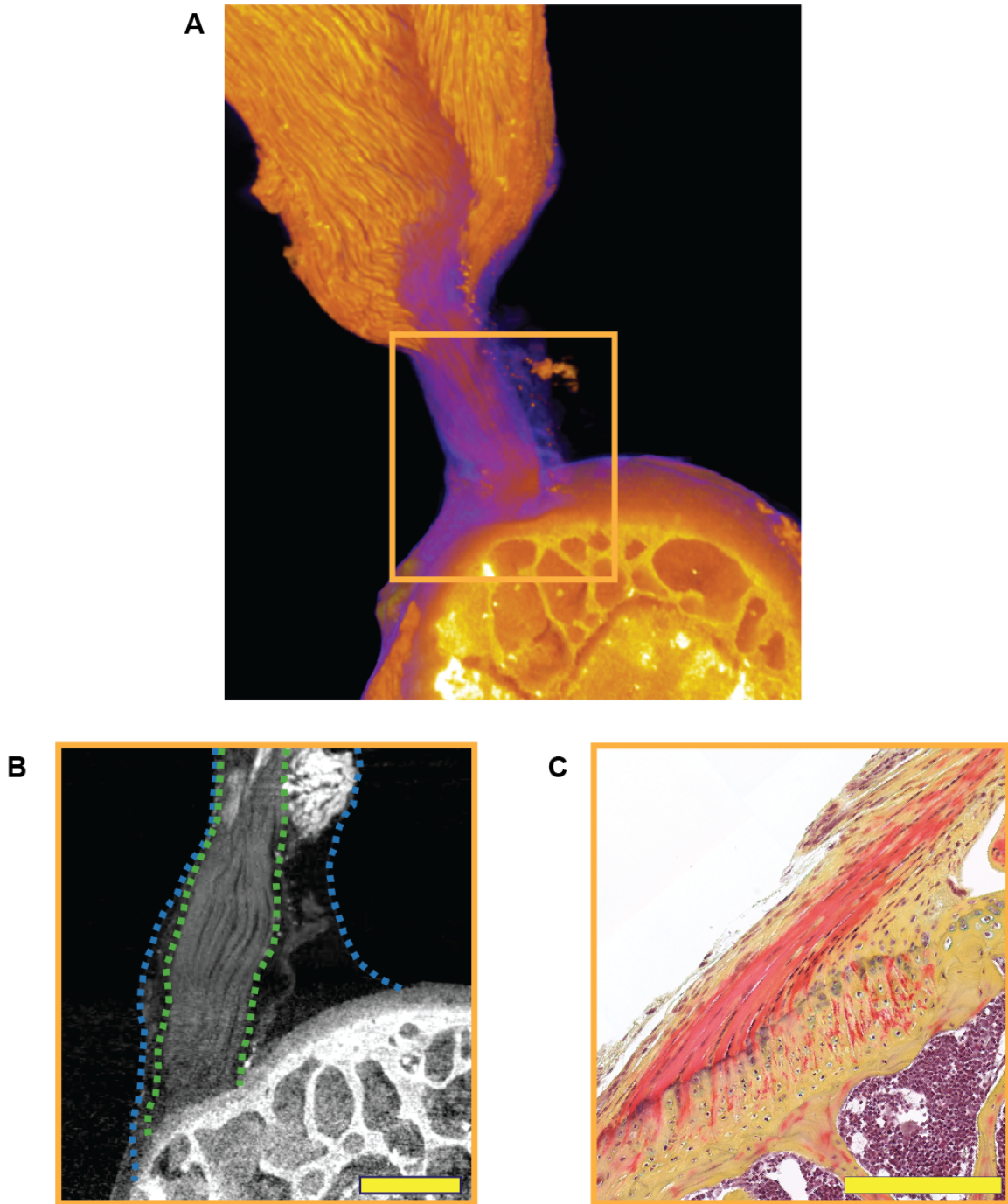


Figure 2.1: Mercury (II) chloride-stained contrast enhanced high-resolution microCT imaging revealed that, hidden within the well-known larger apparent attachment footprint area, is a smaller, much denser primary insertion site where tendon fibers insert directly into the bone. (A), Three-dimensional volume rendering of representative intact enthesis. (B), Magnified cross sectional view of yellow box in (A); within blue dotted lines outline apparent enthesis and within green dotted lines outline dense primary insertion. (scale: 200 μm). (C), Representative image of pentachrome-stained coronal section of the tendon enthesis, where red stain shows mature collagen fibers, yellow stain shows mineralized tissue and connective tissue. (scale: 200 μm)

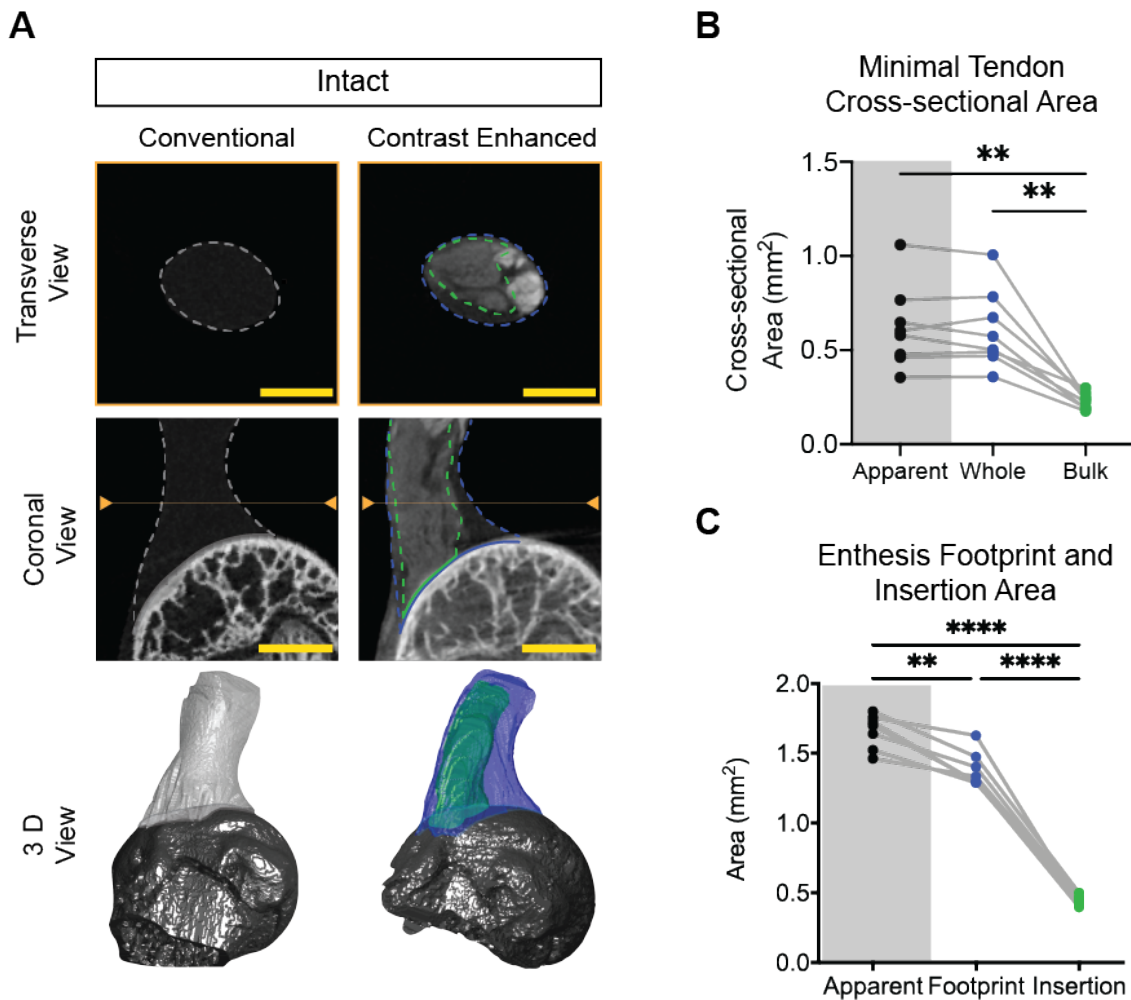


Figure 2.2: The newly visualized fibrous primary insertion site was only 32% of the overall footprint area and slightly larger than that of tendon bulk cross-sectional area. **(A)** Intact images of tendon enthesis obtained by conventional and contrast enhanced high resolution micro computed tomography (microCT) technique. The location of images shown in the transverse view are represented as a line within orange arrow heads in the coronal view imaging. The 3D view was generated using MATLAB from volume contouring and rendering. 2D image scaling is $800\ \mu\text{m}$ for all images. 3D representations are not to scale. **(B)** Minimal tendon cross-sectional area and **(C)** entheses apparent footprint, true footprint, and insertion area obtained from microCT images of tendon enthesis. Gray shaded measurement was obtained using conventional microCT technique, while all other measurements were obtained using contrast enhanced microCT technique. (** $p < 0.01$, *** $p < 0.001$, repeated measures ANOVA followed by the Tukey's multiple comparison test)

Three-dimensional reconstruction and visualization of the enthesis using high-resolution microCT presented the opportunity to perform quantitative analysis on tendon enthesis architecture (**Figure 2.2A**). At the site of minimal tendon cross-sectional area, approximately 500 μm above the insertion site, the cross-sectional area of whole tendon was $0.61 \pm 0.21 \text{ mm}^2$, while newly visualized “primary” tendon’s (bulk tendon) cross-sectional area was $0.22 \pm 0.04 \text{ mm}^2$, approximately 38% of that of the whole tendon (**Figure 2.2B**). The primary tendon insertion site area ($0.45 \pm 0.03 \text{ mm}^2$) consisted of only 32% of the broader footprint area ($1.39 \pm 0.13 \text{ mm}^2$) (**Figure 2.2C**), and slightly larger than that of “primary” tendon’s (bulk tendon) cross-sectional area. When novel contrast enhancement was tested for shrinkage or damage of enthesis samples, the repeated-measures ANOVA showed that the values obtained for whole tendon cross-sectional area matched the measurements obtained prior to submerging to the mercury (II) chloride solution.

2.3.2 The tendon enthesis fails via bony avulsion at its primary insertion site

When tendon enthesis samples were pulled uniaxially, quasi-statically to failure, the enthesis tissue showed a nonlinear loading response (**Figure 2.3A**). The force displacement curves showed that, under this loading regime, the tendon attachment failed catastrophically, with little to no yielding. Visual inspection of enthesis samples before and after mechanical testing revealed that the core of the tendon (bulk tendon) appears to separate from the peritenon tissue (tendon sheath) as enthesis sample fails. Surprisingly, the peritenon tissue surrounding the primary insertion site still attached at the time of failure (**Figure 2.3B**, clear tissue indicated by blue arrow). While not immediately apparent from visual inspection, microCT imaging from before and after testing revealed that all samples exhibited a failure crater at the attachment site where the mineralized tissue was fractured (i.e., bone avulsion failure) (**Figure 2.3C**, orange dotted ellipse).

Further histological analysis confirmed that the underlying bone remained largely intact post-failure (**Figure 2.4**). Toluidine blue staining of intact and failed tendon enthesis (**Figure 2.4, top**) showed that avulsed fragment contained both mineralized fibrocartilage and the underlying trabecular bone. This region was characterized by interdigitations where the trabecular bone integrates

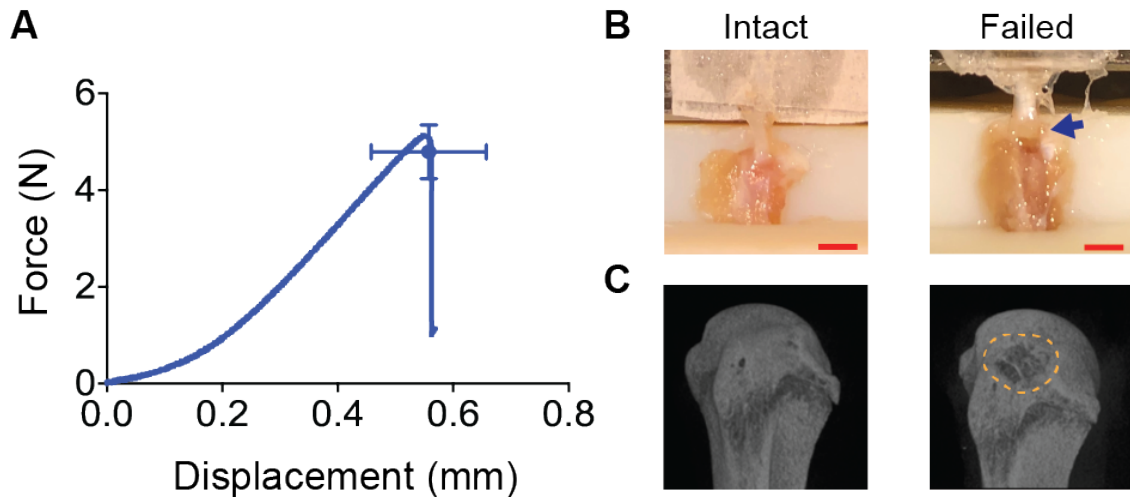


Figure 2.3: *Tendon enthesis samples failed catastrophically, creating failure craters at the attachment site.* (A) Tendon enthesis force-displacement curve indicates a nonlinear loading response of the tissue when enthesis samples were pulled uniaxially, quasi-statically to failure. Enthesis samples fail catastrophically upon reaching maximum loading. Mean failure load and failure displacement is represented by a blue dot, crossheads represent errors. (B) Representative murine tendon enthesis sample pictures before and after mechanical testing (scale: 2 mm). While majority of the primary insertion was avulsed, peritenon tissue surrounding the primary insertion site was still attached post failure (blue arrow). (C) MicroCT imaging from before and after testing revealed that all samples exhibited failure craters at the attachment site (outlined in orange dotted line).

into fibrocartilage. Polarized light microscopy images colored to indicate the collagen fiber direction (**Figure 2.4, bottom**) showed that mineralized fibrocartilage is highly aligned relative to the underlying trabecular bone. At the interfaces where the mineralized fibrocartilage meets the bone, the fibers are not continuous and often change direction dramatically. Nevertheless, failures did not occur exclusively at this interface, as apparent from **Figure 2.4, (bottom right)**.

Contrast enhanced CT imaging of tendon enthesis samples recovered post-testing at its failure displacements confirmed previous findings from visual inspections, conventional microCT imaging, and histological analysis, in addition to providing some additional insights in uncovering failure mechanism of tendon entheses. All tendon enthesis samples failed with a mineralized “bone plug” avulsed from the primary insertion site (**Figure 2.5**). Failure area consisted of $22.4\% \pm 6.2\%$ ($0.29 \pm 0.09 \text{ mm}^2$) of the apparent insertion site and $64.4\% \pm 14.2\%$ bulk tendon insertion site, showing that the majority of the primary insertion was avulsed, while some tendon enthesis

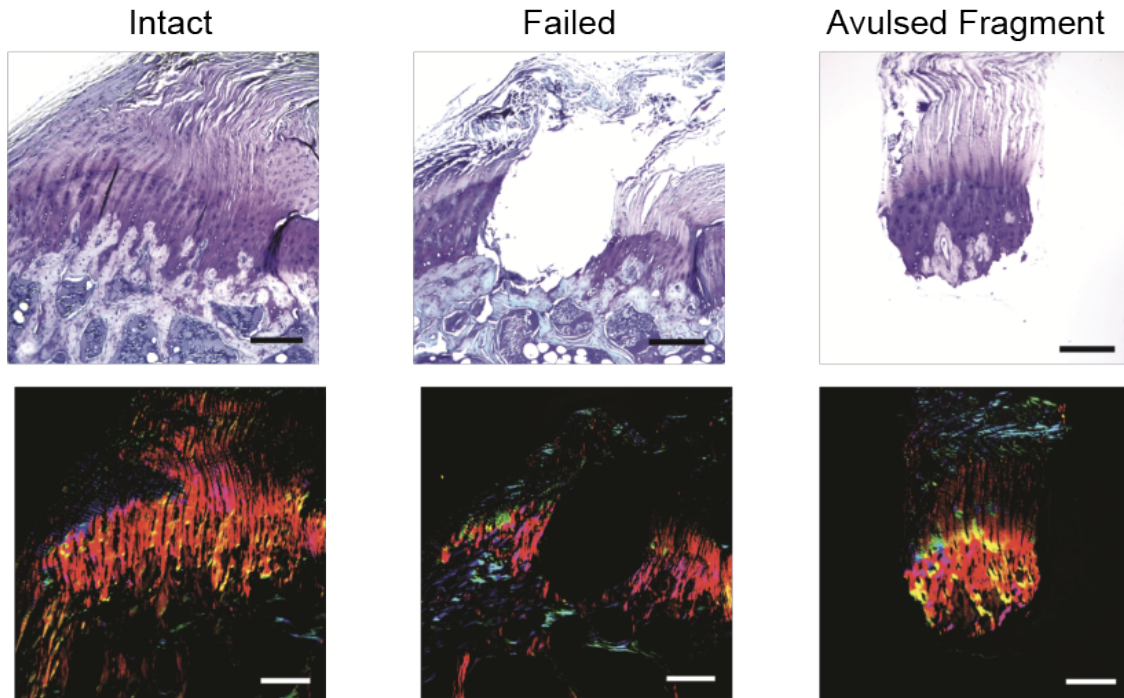


Figure 2.4: Histology of intact and failed entheses show that the avulsed fragment contained mineralized fibrocartilage and bone tissue. **(Top)**, Toluidine blue staining of intact and failed tendon enthesis highlights the enthesis fibrocartilage. The avulsed fragment contains interdigitations where the trabecular bone integrates into fibrocartilage. **(Bottom)**, Polarized light images corresponding to above images, with a color map overlay indicating the local collagen fiber alignment. Scale is 200 μm .

fibers were still attached (**Table 2.1**). As indicated by visual inspections, all the peritenon tissue surrounding the primary insertion site was still attached to the bone at the time of failure. 3D reconstruction of avulsed fragment revealed that the bone plug likely consist of mineralized fibrocartilage from the tendon enthesis and in some cases part of humeral head trabeculae (**Figure 2.5**, red arrow). Coronal image stacks of failed enthesis showed crack propagation around the avulsion site (**Figure 2.6B**, red arrows). This crack propagation was also confirmed by scanning electron microscopy imaging of failure site (**Figure 2.7**).

Further analysis of avulsed fragment using images from both conventional and contrast enhanced microCT revealed that healthy tendon entheses exhibit two failure types (**Figure 2.8**). Failure occurred either at the interface between mineralized fibrocartilage and bone (MF-B fail-

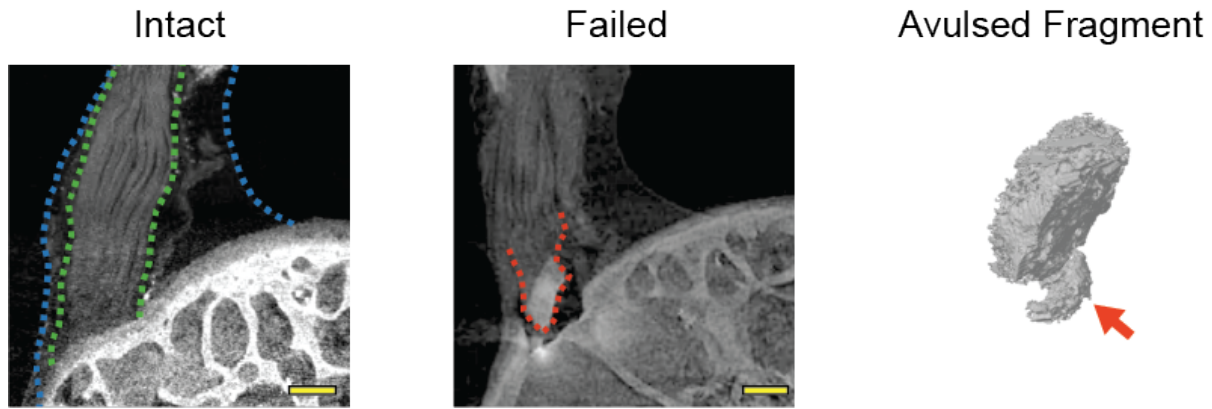


Figure 2.5: Contrast enhanced microCT imaging of failed enthesis revealed that the majority of the primary insertion was avulsed, while some tendon enthesis fibers were still attached at the time of failure. Intact dense primary insertion fibers are outlined in green. Avulsed bony fragment at primary insertion site, outlined with a red dotted line. Scale is 200 μm . Three-dimensional representation of avulsed fragment showing portions of trabeculae at the failure site (red arrow).

Table 2.1: Enthesis Footprint, Insertion, and Failure Area

	Area \pm Std. Deviation (mm^2)	P-value vs. Insertion Area
Apparent	1.66 ± 0.12	$p < 0.0001$
Footprint	1.39 ± 0.13	$p < 0.0001$
Insertion	0.45 ± 0.03	-
Failure	0.29 ± 0.09	$p < 0.05$

ure type), or within trabecular bone (B-T failure type). For MF-B failure type, failure surface corresponds to the interface between the layer of mineralized fibrocartilage and the underlying trabecular bone, as the failure creator did not extend all the way through the fibrocartilage to expose the marrow cavity. On the other hand, for B-T failure type, failure surface was within trabeculae, and marrow cavity was exposed at the failure creator. For healthy enthesis samples, the failure type distribution was exactly 50% each, (n=5: MF-B failure type, n=5: B-T failure type), with no significant differences in failure load, stiffness, or toughness for each failure type.

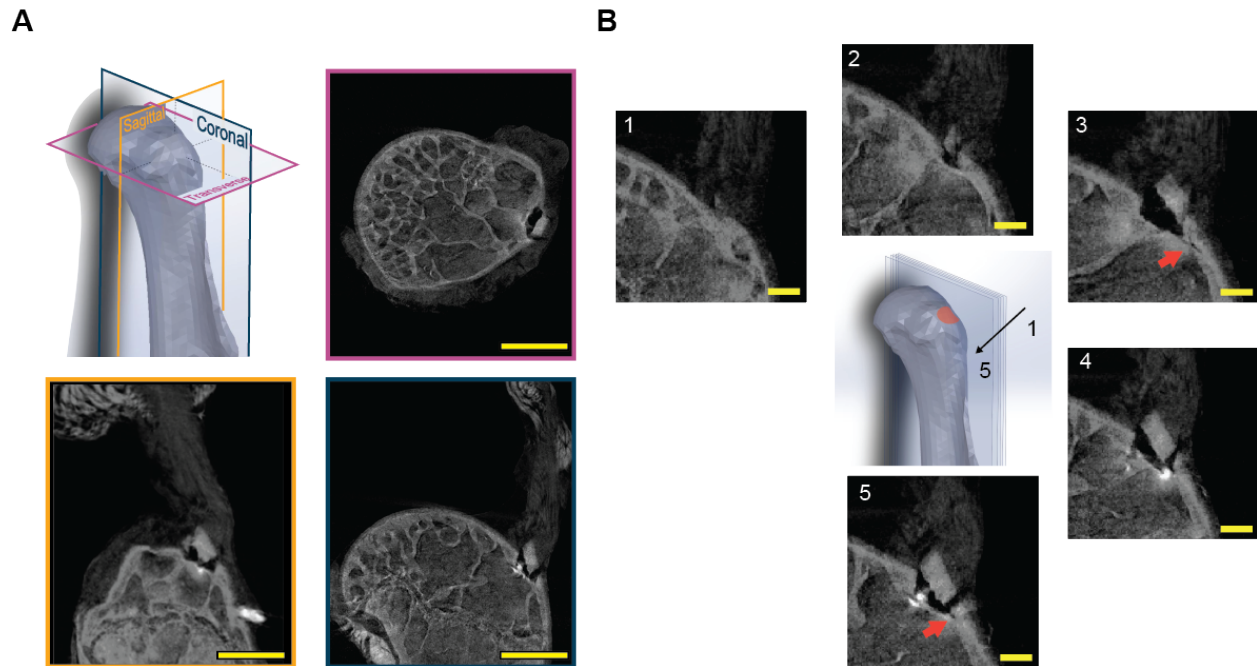


Figure 2.6: Contrast enhanced microCT images of the failure site suggest crack propagation around the avulsion site. (A) Bone avulsion site visualized via contrast enhance microCT in coronal, sagittal, and transverse view. Scale is $500\ \mu\text{m}$. (B) Coronal slices from the edge of the failure site to the center of avulsed fragment. Scale is $100\ \mu\text{m}$.

2.4 Discussion

Tough attachment of dissimilar materials is a challenge throughout engineering. As discussed in **Chapter 1**, an elegant architected solution for this problem can be found at the tendon enthesis. Prior investigations have focused on identifying multi-scale mechanisms that effectively alleviates stress concentrations at the attachment site (**section 1.3.2**). However, there is a need to identify mechanisms of how the tendon enthesis architecture relates to toughness because surgical repair does not restore the toughness of the natural tissue when the tendon enthesis fails due to injury or degeneration (**section 1.4**). As a first step towards understanding putative mechanisms of enthesis toughening, this chapter focused on developing high-resolution imaging technique that visualizes the tendon enthesis architecture and establishing a mice model of the tendon enthesis failure that characterizes mechanical behavior of attachments at pre-yield, post-yield, and failure loading regimes. The simultaneous sub-micrometer scanning resolution of both unmineralized and

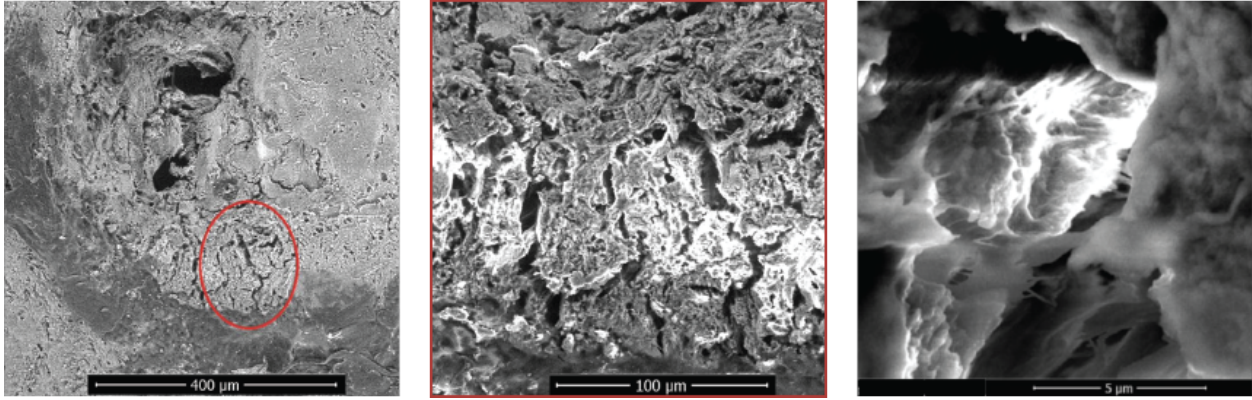


Figure 2.7: Scanning electron microscopy of the failure site shows crack propagation around the avulsion site. Crack propagation around the avulsion site is outlined in red circle, with zoomed in images following the crack propagation site. Images were obtained in BSE mode.

mineralized portions of the tendon enthesis revealed the continuous, fibrous architecture of the tendon enthesis. Failure analysis of the mouse tendon entheses showed that the primary insertion site resists failure loads by alleviating stress concentrations at the tough mineralized fibrocartilage and instead fails at the more brittle (and more easily regenerated) bone [137].

High-resolution microCT imaging revealed a fibrous primary insertion site within the mouse supraspinatus tendon enthesis. The fibrous architecture was evident throughout the entire attachment unit (bone-tendon-muscle), with continuous enthesis fibers from one end (bone) to the another end (muscle). The imaging also revealed that enthesis fibers unravel into thinner fibers and directly attach at a dense primary insertion site on the bone end or at the muscle end. The fibrous nature of the enthesis has been recently reported [61, 38, 138, 139]. Rosetti et al. reported that porcine Achilles tendon-bone enthesis fibers continue from tendon towards bone, with significant changes in fiber diameters as interface fibers attach to bone, with interface fiber diameters decreasing by as much as 10 times compared to that of bulk tendon fibers [61]. Sartori et al. performed 3D fiber tracking analyses on images obtained from phase-contrast microCT of mouse Achilles tendon insertions [139]. They found that the number of tendon enthesis fibers were constant along the entire attachment unit. Limited branching of enthesis fibers was observed, with only a small number of branching clusters and a low level of divergence along the tendon. Sartori et al. also showed that the fiber cross-sectional area decreased near the insertion with the bone, primarily due

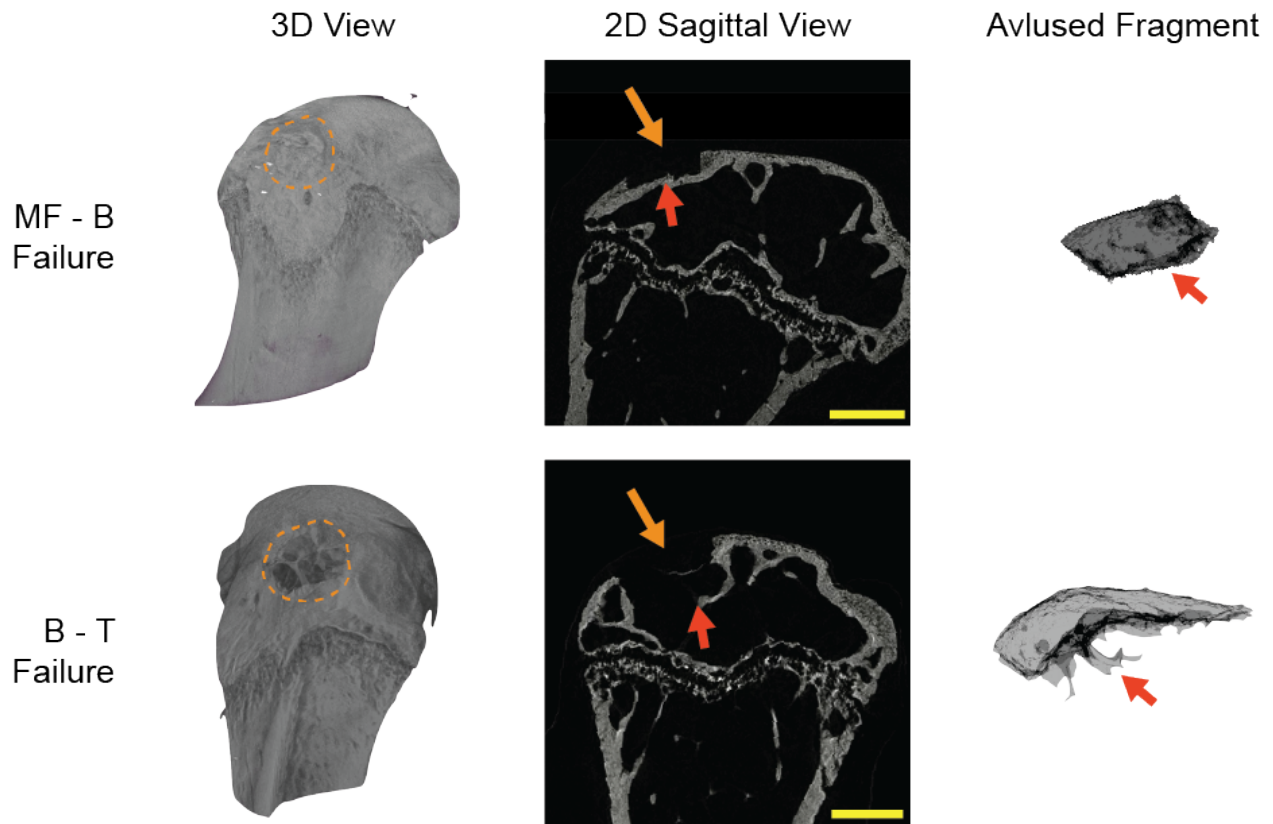


Figure 2.8: Tendon entheses failed either at the interface between mineralized fibrocartilage and bone (*MF-B failure type*), or in the underlying trabecular bone (*B-T failure type*). Conventional microCT imaging of post-failure humeral head samples (3D rendering and 2D sagittal view) and 3D visualization of avulsed fragment. Orange outline and orange arrows represent site of entheses attachments (humeral head post failure crater). Red arrows represent fracture (failure) surfaces. Scale is 500 μm .

to a decrease in fiber sizes (not a decrease in in fiber numbers) [139], corroborating the findings from the current study.

Quantitative analysis of high-resolution 3D volumes of tendon enthesis architecture demonstrated features of the enthesis that had previously been misunderstood. The newly visualized fibrous primary insertion site was only 32% of the overall footprint area and slightly larger than that of the tendon bulk cross-sectional area. These results revealed that the newly identified primary insertion site splayed out its fibers over the attachment area to theoretically decrease edge stress singularities that should exist at the corners of interface between two dissimilar materials [74, 49, 50], yet the area of attachment is significantly smaller than what has been conventionally

established [65, 64]. Prior modeling efforts revealed that the tendon enthesis forms a broadened insertional microarchitecture to optimize reduction of stress concentrations by increasing the area over which forces are transduced [66, 74]. Furthermore, numerical simulation studies also predicted that the outward splay of the tendon shields the tendon enthesis from stress concentrations at the edges of the attachment by allowing forces to be transduced at shallower angles [74]. Albeit small, fibrillar angular deviations at the insertion site reported in prior studies also allow for enthesis fibers to respond to multi-modal and multi-directional loadings [61], while reducing the stress concentrations. The dense fibrous insertion site visualized in this study points towards a new view that the tendon enthesis is architected to behave like a fibrous network [55]. Contrary to what earlier tendon enthesis models have predicted, where the enthesis was modeled to behave as an affinely deforming connective tissue, the fibrous architecture shown here allows the tendon enthesis to behave as a networked solid, in which a fraction of the fibers accept and shed load in particular direction, depending on the direction of loading [75, 76]. This concept will be further explored in **Chapter 4**.

To test the hypothesis that the primary insertion site was responsible for load transfer, tendon enthesis specimens were stretched to failure quasi-statically. Although failure was expected at the mineralized interface within fibrocartilage, where the stress concentrations were predicted to occur [66, 67], the enthesis failed with a mineralized “bone plug” avulsed from its primary, fibrous insertion site, suggesting mechanisms to alleviate stress concentrations. Contrast-enhanced microCT imaging revealed that the majority of the primary insertion was avulsed, but with peritenon tissue surrounding the primary insertion site still attached. This suggests that the core-sheath (bulk tendon-peritendon) structure of the tendon plays an important role in the failure behavior of the enthesis, and that the core dominates the mechanical strength of the tissue. A single rapid drop in force at the time of failure indicates that bone avulsion occurred rapidly as a single catastrophic event, and that the failure crater did not widen substantially after the peak load was reached. Close examination of post-testing samples revealed that failure occurred either at the interface between mineralized fibrocartilage and bone (MF-B failure type) or within trabecular bone (B-T failure

type), and in all cases with crack propagation around the avulsion site. With no significant differences in mechanical properties between two failure types, the concept of disarray (randomness) within the enthesis tissue, initially proposed by Genin and Thomopoulos as a key microarchitectural feature of effective load transfer between two dissimilar tissues [55], was further expanded. Similar to features previously identified in mineral deposition [54], mineral crystal orientations [64], and tide-mark interdigitation [57], the high-resolution imaging revealed that the random, fibrous nature of the tendon enthesis endowed toughness to protect the attachment from injury. Indeed, this study shows that for the quasi-static loading regime, the fibrous primary enthesis was tougher than cortical bone, with the more compliant fibrocartilage storing enough energy to fracture and avulse the bone. Questions remain on whether failure mechanisms of mouse entheses also depend on the loading regime and/or extracellular matrix composition, or due to tissue pathologies. These concepts will be further explored in **Chapter 3**, **Chapter 5**, and **Chapter 6** respectively.

Findings from this study show that the large outer, non-fibrous, portion of the tendon enthesis may not have a distinct mechanical role for the attachment. Nevertheless, the purpose of this tissue at the insertion remains elusive. The uniaxial, quasi-static loading at an orientation corresponding to 90° abduction showed that this tissue is non-load bearing at this particular loading regime. However, it is possible that this tissue exists to ease gliding of primary insertion fibers (lubricating layer for multi-modal loading), or to reduce axial stress at the attachment by converting shear to normal forces. Apart from its possible role in enthesis mechanics, the large non-fibrous portion of tendon enthesis may possess a crucial biological function, such as in repair and regeneration. The peritenon tissue surrounding the adult tendon has been implicated in adult tendon healing [97]. Howell et al., showed the significant infiltration of α SMA expressing cells from peritenon region after mice Achilles injury [140]. Although it has not been previously considered to be a site of resident immune cell surveillance, Sherlock. et al. have identified enthesis-resident T lymphocytes ($CD3^+CD4^-CD8^-IL-23R^+ROR-\gamma t^+$ T-cells) that are primed for inflammation [141]. A recent study that recapitulated human rotator cuff tendinopathy *in vivo* using persistent activation of IKK β activation in tendon stromal cells (IKK β CA^{Scx} mice) showed significant increases in

inflammatory cells (CD68⁺ macrophages) within peritendon tissue at the enthesis of IKK β CA^{Scx} mice [129], exactly at the non-fibrous portion of the tendon enthesis insertion site identified in the current study. It is possible that the newly identified large, non-fibrous area serves as a reservoir for the cells that monitor and recognize biomechanical and cellular stresses to maintain tissue homeostasis and, if necessary, trigger tendon enthesis repair and regeneration pathways.

Compared to recently published soft tissue visualization techniques [61, 138, 139], the novel methodology of the current study did not require chemical fixation, cell-maceration, demineralization, or extensive dehydration (e.g., critical-point drying). Mouse tendon enthesis samples were submerged in a mercury (II) chloride solution overnight and then imaged using microCT with conventional scan setting (60kVp, 166uA, and Al 0.25mm filter); hence, preserving near physiologic shape and orientations of the fibrous architecture when the tendon enthesis was scanned. With this technique, X-ray absorption for each micro-structure within the whole attachment unit were distinct and sufficiently high enough to segment from each other allowing visualization of collagen fibers from tendon (unmineralized) to bone (mineralized). One of the key limitations of HgCl₂ based contrast enhancement was the variability in the penetrability of HgCl₂ between samples to samples. While the same concentration (saturation concentration) of HgCl₂ was used for staining, there were some variability in quality of final X-ray images. Even with rigorous washing of samples after staining, in some cases, there were significant precipitation along the surfaces of samples, while in some other cases, there were precipitation pockets within samples that caused high attenuation peaks within images. It is possible that these artifacts were caused by limited diffusion or caused by the high concentration of the HgCl₂ solution. The penetrability of HgCl₂ is reported to be low and, hence, this contrast enhancement method maybe only be used for very small samples (a few cm³) [142]. Future studies are required to optimize HgCl₂ penetration to limit variability in visualization outcomes.

The volume data was used to establish key tendon enthesis areas according to their fibrous structure and compare them to gold-standard measurements that are obtained from using conventional microCT imaging (i.e, apparent tendon cross-sectional area and apparent footprint area).

While staining with other contrast agents, such as PTA, is known to cause up to 25% volume shrinkage in tendon (28) and demineralization or dehydration each lead to about 20% volume shrinkage [143], staining with mercury (II) chloride solution did not cause significant shrinkage or damages. Repeated-measures ANOVA showed that whole tendon cross-sectional area matched measurements obtained prior to submerging in mercury (II) chloride solution. While repeated-measures ANOVA showed significant difference between apparent (conventional) and whole (contrast enhanced) footprint areas, this was attributed to the resolution of imaging. The contrast enhancement clearly distinguished edges of the supraspinatus enthesis from other tendons inserting into humeral head, while it was not possible to do this using images obtained from conventional microCT (which required relying on humeral head bony features), likely leading to overestimating the apparent footprint area. Future comparisons with other imaging modalities, such as high-frequency ultrasound, high-resolution MRI, phase-contrast microCT, and other contrast enhanced microCT techniques, may provide additional references for further quantification of the tendon enthesis architecture.

The failure mode described in this study was not obvious from visual inspection during testing. This has important implications for commonly used surface strain tracking methods and typical visual determination of failure modes [144]. The bulk tendon was covered by a non load-bearing peritendon tissue that did not deform along with the underlying tendon enthesis. Hence, staining the enthesis samples with ver Hoeff's stain to create a speckle pattern to optically track tissue strains is futile for measuring local strain patterns, as the speckles only cover the non-load bearing peritendon tissue. The other limitation of the study is that the novel contrast enhancement technique required non-reversible chemical binding. Hence, while contrast enhancement allowed for visualization of fibers post-failure, the method was terminal and not useful for continuously tracking the enthesis fiber deformations under loading. To establish micromechanical properties of the tendon enthesis architecture, future studies may require samples to be loaded while simultaneously acquiring high-resolution ultrasound or high-resolution confocal images to measure local strain fields.

2.5 Conclusion

This chapter described a new view of the tendon enthesis dominated by a fibrous primary insertion site. This provides guidance for how dissimilar materials can be effectively attached. Mechanical testing of mouse tendon entheses showed a remarkable ability for the enthesis to store energy and provide resilience against attachment failure, instead fracturing the highly mineralized (and easily regenerated) bone. Such a distribution of functions between the enthesis and the bone (i.e., the enthesis being responsible for energy dissipation and the bone being the limiting factor for strength) may be beneficial for attaching engineering materials. The fibrous networked structure reported may allow the tendon enthesis to respond differently with changes in loading type and/or changes in loading angles; these ideas will be explored in upcoming chapters.

Chapter 3: Multiscale toughening mechanisms enable the tendon entheses to exhibit distinct failure modes under varying loading conditions

Portions of this chapter are currently under review: Golman M, Abraham AC, Kurtaliaj I, Marshall BP, Hu YJ, Schwartz AG, Guo XE, Birman V, Thurner PJ, Genin GM, Thomopoulos S. Toughening mechanisms for the attachment of architected materials: The mechanics of the tendon enthesis.

3.1 Introduction

Natural and engineering architected materials are designed to fulfil specific functions [2], and the tendon enthesis is no exception. The healthy tendon enthesis resists static and dynamic loading conditions under daily activities and shows a remarkable ability to withstand loads equivalent to as much as 12.5 times body weight [145]. It is hypothesized that the hierarchical architecture described in **Chapter 1 (section 1.3.2)** and the novel view of fibrous architecture uncovered in **Chapter 2** leads to a resilient attachment across a broad range of physiologic loading. Nevertheless, as is the case for engineered materials, accumulation of sub-failure damage or high impact loading events can lead to tendon enthesis failure. Clinically, tendon entheses failures can present as bony avulsion fractures, insertion site failures (i.e., fibrocartilage failures), or tendon mid-substance ruptures (**section 1.4**). For example, avulsions are commonly seen in high-impact injuries in pediatric patients [146, 147], whereas tendon ruptures are prominent in degenerated rotator cuffs of older patients [107, 106]. Once tissue damage has propagated to the macroscopic level, even with surgical intervention, physiologic healing processes do not restore a functional attachment unit. Although a large body of work has established the sources of strength (i.e., the onset of injury) for the tendon enthesis, the sources of toughness (i.e., the energy absorption that protects against failure follow-

ing the onset of injury) are largely unknown. Furthermore, the root and evolution of mechanical damage across the tendon enthesis' architecture that results in seemingly intact tissue to fail is not known. Defining the failure characteristics of the tendon enthesis, including multi-length scale damage localization and propagation under differential loading regimes, may facilitate improved design of surgical and tissue engineered solutions for tendon-to-bone repair.

This chapter will describe tendon enthesis toughening mechanisms using the laboratory model of enthesis failure established in the previous chapter (**Chapter 1**). Failure mechanisms of mouse entheses were characterized by investigating whole tissue level (macroscale) failure modes and molecular level (nanoscale) collagen damage localization and propagation under different loading conditions. Using contrast enhanced microCT imaging in conjunction with a protocol of interrupted mechanical testing and fluorescent microscopy, this chapter will reveal the first quantification on how fibrous networks degrade through monotonic (acute) and cyclical (degenerative) loading. Guided by clinical observations, it is hypothesized that the nature of mechanical loading will contribute to differences in tendon enthesis failure behavior with distinct molecular level injury localization and propagation mechanisms.

3.2 Methods

3.2.1 Sample Preparation and Study Workflow

All animal procedures were approved by the Columbia University Institutional Animal Care and Use Committee. Supraspinatus tendon enthesis sample (humerus - supraspinatus tendon - supraspinatus muscle) were harvested from adult (>12 weeks) male C57BL6/J mice (n = 62). After dissection, samples were fresh-frozen in PBS and stored at -20°C . The experimental workflow was dependent on two categories: (1) unloaded/intact sample characterization and (2) loaded sample characterization. Both unloaded/intact samples and loaded samples were imaged via contrast enhanced microCT or light microscopy, as the imaging techniques were terminal. For characterizing samples undergoing loading, defrosted samples were first scanned by conventional microCT before subjecting them to mechanical testing. After mechanical testing, samples were secured at

terminal displacements and either submerged in 5% mercury chloride (HgCl_2 , Sigma-Aldrich) or fixed with 4% paraformaldehyde (Sigma-Aldrich) to analyze for damage at the macroscopic (fiber network) level or at the molecular collagen level.

3.2.2 Mechanical testing

All samples were mechanically tested in a saline bath at 25°C (to prevent thermal collagen denaturation) on a table-top tensile tester (Electroforce 3230, TA Instruments) fitted with 10 lb. load cell (TA instruments). Before testing, the supraspinatus muscle was carefully removed from the supraspinatus tendon-humerus unit. Samples were placed into custom 3D-printed fixtures [135] and supraspinatus tendons were secured between two layers of thin paper (Kimwipe) with a drop of cyanoacrylate adhesive (Loctite, Ultra Gel Control) before mounting onto custom grips.

For all mechanical testing protocols, samples were first pre-loaded to 0.05 N, pre-conditioned by applying 5 cycles of sinusoidal wave consisting of 5% strain and 0.2%/s, and rested for 300 seconds. The unloaded control group consisted of samples that were prepared and mounted in the mechanical tester, but not loaded ($n=5$).

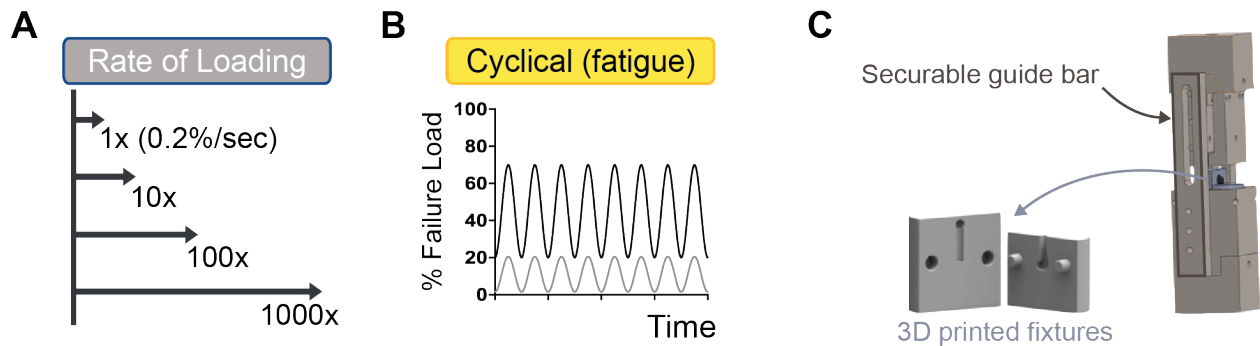


Figure 3.1: *Experimental set up.* To examine effect of loading on failure mode, samples were loaded (A) across a range of loading rates to simulate acute injuries or (B) loaded cyclically to simulate degenerative loading. (C) 3D printed securable guide bars and 3D printed fixtures were used for interrupted testing. The gripping system allowed for enthesis samples to be secured and recovered post-testing at their loading levels or failure displacements.

Quasi-static and monotonic uniaxial loading: post pre-loading, pre-conditioning, and rest, samples were strained in tension at 0.2%/s to failure (for all loading conditions unless specified

otherwise below). The healthy failed control samples (CTRL) were healthy adult enthesis samples strained in tension at 0.2%/s to failure in an orientation corresponding to 90° shoulder abduction. For interrupted testing, samples were strained in tension at 0.2%/s to 1 N, 2 N, 3 N (n=3 per rate). To examine the role of strain rate in enthesis failure, samples were tested under three additional strain rates (2%/sec, 20%/sec, 200%/sec, n=10 per rate) until failure (**Figure 3.3A**).

Fatigue (cyclical) loading: after pre-loading and preconditioning, samples were either subjected to 2 Hz sinusoidal loading from 0.1-1 N (1%-20% of failure force, n=4) or 1-3 N (20%-70% of failure force, n=5). To investigate molecular level damage localization in the entheses, additional samples were loaded to 10,000 cycles (n=3), 40,000 cycles (n=3), and to failure (> 50,000 cycles, n=5) using the second protocol (**Figure 3.3B**).

A novel slidable, securable guide bar was used for all mechanical testing protocols (**Figure 3.3C**). This 3D printed guide bar and 3D printed fixture allowed mechanical tests to be interrupted and, if necessary, fixed at prescribed loading/displacement levels. The gripping system also allowed specimens to be recovered post-testing at their loading levels or failure displacements.

Enthesis structural properties, such as failure load (referred to as strength in the text), stiffness, and work to failure (area under the curve through failure load, referred to as toughness in the text) were determined from load-deformation curves. Stiffness was calculated by a MATLAB custom algorithm that identified the best fitting line within a sufficient bin width (i.e., remove data below 10% of max load and above 95% of max load) by implementing the random sample correlation (RANSAC) technique [52].

3.2.3 Contrast enhanced and conventional micro computed tomography (microCT) imaging

Simultaneous visualization of soft and hard tissues of tendon enthesis samples was achieved by staining samples with 5% mercury chloride solution prior to scanning with microCT. A 5% mercury chloride solution was prepared fresh for each experiment day by dissolving Mercury (II) chloride (HgCl₂, Sigma-Aldrich) in distilled and de-ionized water (MilliQ water, MilliporeSigma) at room temperature until the saturation was achieved. Tendon enthesis samples, either intact or

post-mechanical testing, were submerged in this solution for 24 hours and washed three times in distilled and de-ionized water for 10 minutes each before they were imaged with microCT (Skyscan 1272, Bruker).

The same preparations and scan settings were used when visualizing enthesis samples with both conventional and contrast enhanced microCT. To prepare for scanning, distal end of supraspinatus-humerus unit were embedding in 2% agarose (Sigma-Aldrich) and mounted in the scanning chamber, so that tendon enthesis specimens were hung loosely and in line with the scanning axis. Scans were performed with 60kVp, 166uA, and Al 0.5mm filters with isometric resolution of 5 μm . The acquired microCT data were reconstructed with the software (nRecon, Bruker) provided with the CT scanner using alignment optimization and beam-hardening correction. The reconstructed image data was visualized with built-in program (DataViewer and CTvox, Bruker).

3.2.4 Collagen damage visualization

Unloaded and loaded tendon enthesis samples allocated for analyzing molecular-level collagen damage were stained with F-CHP (3 Helix) [148] and visualized via fluorescence microscopy. Post mechanical testing, samples were first secured and fixed at their appropriate displacements with 4% paraformaldehyde (PFA, Fisher Sci) overnight. Tendon enthesis samples were washed 3 times in PBS for 10 min each at room temperature. After washing, each tendon enthesis sample was placed in a tube containing 450 μl of PBS solution. F-CHP staining protocol was adapted from what have described previously in staining rat tendon fascicles [148]. CF-CHP stock solution (150 μM) was heated at 80°C for 10min to thermally dissociate trimeric CHP to a monomeric state and quenched in ice bath for approximately 20 seconds to prevent artificial thermal damage to samples. 50 μl of monomeric CF-CHP were then added to a tube containing tendon enthesis sample, resulting in a final F-CHP concentration of 15 μM . Samples were incubated overnight at 4°C and washed in PBS 3 times for 30 min in a room temperature to remove any unbound F-CHP molecules. Stained samples were mounted on a glass slide and imaged and captured using an automated ZEISS Microscope (10x objective, excitation at 488nm channel). Images were captured

by CCD camera using the built-in image acquisition and stitching features and analyzed with ZEN lite software (ZEISS).

3.2.5 Statistical Analysis

Tendon enthesis characteristics, biomechanics results, failure properties, and bone morphometry results were compared between treatment groups using ANOVA and specific differences from control conditions were determined using Dunnett's multiple comparisons test. $p < 0.05$ was considered significant. All statistical analyses were performed using Prism 9 (GraphPad). All data are shown as mean \pm standard deviation.

3.3 Results

3.3.1 Macroscale: tendon enthesis mechanical failure depends on its loading history

Three distinct failure modes were observed, depending on the loading regime: bone avulsion, tendon mid-substance failure, and fibrocartilage insertion failures (**Figure 3.2**). Under monotonic loading with increases in loading rate, most samples had avulsion failures, while at higher rates some samples failed at the mid-substance. In contrast to monotonic loading, all samples cyclically loaded at high, 20%-70% failure force, failed in the unmineralized fibrocartilage portion of the attachment, which we termed here as "insertion failure". Samples cyclically loaded at low, 1%-20% failure force, did not fail, even after 100,000 cycles.

Effect of strain rate on enthesis mechanical behavior is shown in **Figure 3.3**. Tendon enthesis stiffness responses were strain-rate insensitive. However, strength (failure load) and toughness (work to failure, calculated as the area under the force-displacement curve) increased at higher strain rates as much as 1.4-fold ($p < 0.0001$) and 1.6-fold ($p < 0.01$), respectively, compared to those of control test cases ($n=10-12$ /case).

Analyzing contrast enhanced images of monotonically failed tendon enthesis samples at their failure displacements provided significant insights on the effect of strain rate on enthesis failure mode (**Figure 3.4A**). Avulsed (failed/fractured) area increased with loading rate and clustered in

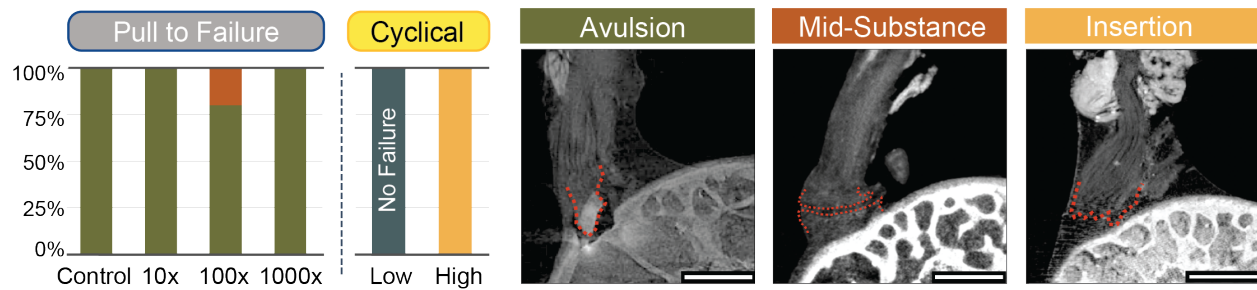


Figure 3.2: There were three distinct failure modes, depending on the loading regime: bone avulsion, tendon mid-substance failure, and fibrocartilage interface. Under monotonic loading, most samples failed by bony avulsion. Under “high” cyclical loading (20%-70% failure force), all samples failed at the insertion. Under “low” cyclical loading (1%-20% failure force) samples did not fail, even after 100,000 cycles. Scale is 500 μ m

two segments at high loading rates (**Figure 3.4B**, $p < 0.05$). Closer examination of the avulsed pieces revealed that the number of avulsed fragments increased with loading rate (**Figure 3.4C**). Failure interface (MF-B vs. B-T) did not significantly change with the an increase in loading rate, and trended towards failures at the B-T interface at higher loads (**Figure 3.4D**).

3.3.2 Nanoscale: the tendon enthesis toughening mechanism to resist cyclical loading

Whole sample fluorescence images of tendon entheses showed that F-CHP fluorescence intensity, indicative of collagen molecule damage accumulation, increased with applied load or number of cycles (**Figure 3.5**). Under monotonic loading, there was little to no fluorescent signal in the low force group (1-2N). The fluorescent signal accrued near the insertion site when loads exceeded 3 N. For cyclically loaded samples, the fluorescent signal was initially concentrated in a few fibers near the tendon mid-substance (10,000 and 40,000 cycles) and ultimately propagated down the entire tendon in concentrated bands.

3.4 Discussion

Depending on the loading regime, mouse supraspinatus entheses exhibited three distinct failure modes: bone avulsion, tendon mid-substance failure, and tendon-bone fibrocartilage interface failure. Monotonic loading led primarily to avulsion failures, regardless of loading rate, and in

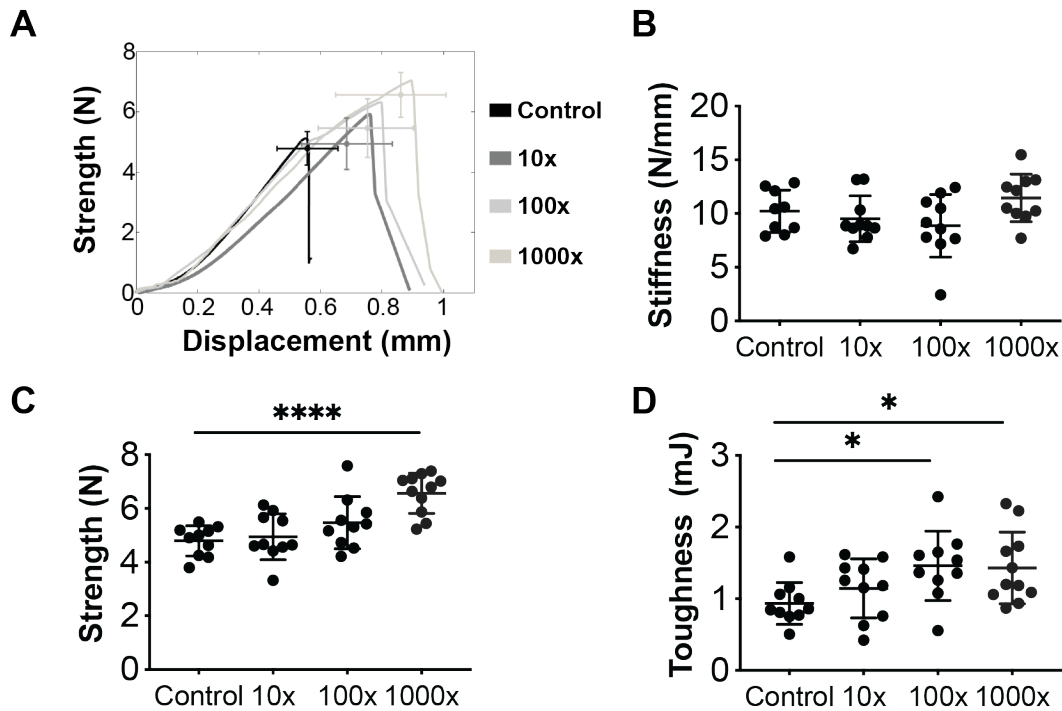


Figure 3.3: Mechanical responses of tendon enthesis were largely strain-rate insensitive, with increases in strength and toughness when loaded at higher strain rates. (A) Representative strength (force)-displacement curves for monotonic loadings. (B) Stiffness was not affected by increase in strain rates. However, (C) enthesis strength (i.e., failure load) and (D) enthesis toughness (i.e., energy absorption) increased with the loading rate.

small number of cases to tendon mid-substance failures. Cyclical loading led to tendon-bone interface failures. These results supported the hypothesis that failure mode is dependent on the loading regime. To identify potential nanoscale mechanisms that could explain this behavior, molecular damage under the various loading regimes were quantified using fluorescein-labeled collagen hybridizing peptide (F-CHP). These experiments revealed key aspects of energy absorption by the tendon enthesis: when the attachment was pulled monotonically to failure, the energy stored in the enthesis was sufficient to fracture and avulse the mineralized tissue; however, when the attachment was pulled cyclically, energy was dissipated in the enthesis and damage accumulated in the tendon followed by tendon rupture.

The enthesis is durable against the complex and repeated loadings of daily activities [149], but clinical observations show that failure mechanisms change with loading regime and age [150]. For example, most rotator cuff injuries seen in the elderly population exhibit tears near the insertion site

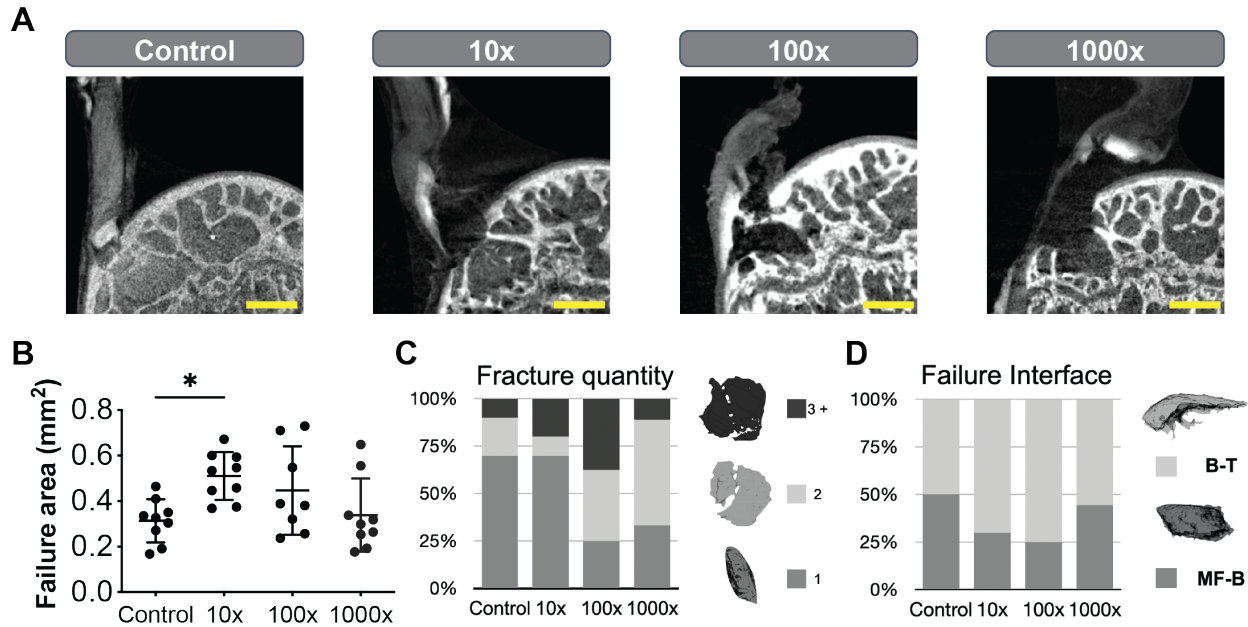


Figure 3.4: The enthesis stored enough energy, even at high loading rates, to shift the fracture away from the attachment and towards the bone. **(A)** Representative contrast enhanced images of failed samples after increases in loading rate. Scale is 250 μ m. **(B)** Avulsed (failed/fractured) area increased with loading rate, with bimodal distribution at high loading rates (10x and 100x). **(C)** The number of avulsed (fractured) pieces increased with an increase in loading rate. **(D)** The failure interface (MF-B vs. B-T) did not significantly change with an increase in loading rate, although trending towards B-T failure type with an increase in loading rate.

of the tendon onto the greater tuberosity of the humerus; tears typically occur after years of tendon degeneration [107, 101]. Case studies also report that some rotator cuff injuries present as bony avulsions, where the avulsed bone remains attached to the tendon fibers [146, 147], similar to the avulsion failures seen in the current *ex vivo* study under monotonic loading. While it has been reported in a handful of cases in adults, the majority of avulsion failures occur in individuals younger than 25 years old [146, 147]. Given the fact that bony avulsions have been reported to occur after acute injuries and not due to chronic degradation, Bhatia et al. suggest that bony avulsion-type failures occur for individuals that exhibit healthy tendon-to-bone attachments and not directly affected by the age of individuals [151]. Interestingly, high impact injuries in the Achilles tendons, the anterior cruciate ligament, and the patellar tendon (see **Chapter 7**) typically manifest in tendon mid-substance ruptures in adults [152, 118, 153, 115], while failures can present as bony avulsions in young athletes (i.e., Segond fractures and Sinding-Larsen syndrome [121, 154]). It is possible

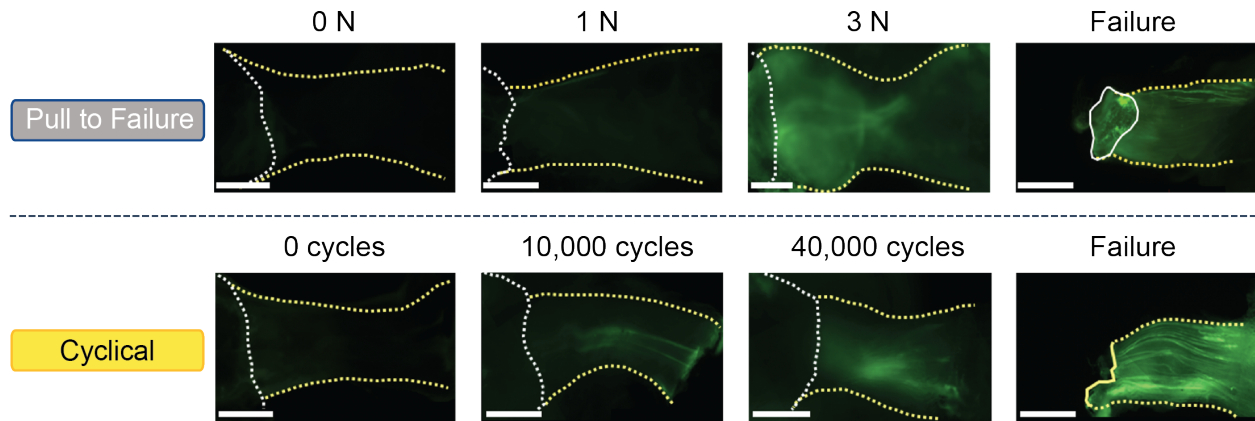


Figure 3.5: *F-CHP fluorescence intensity, indicative of collagen molecule damage accumulation, increased with the level of applied load and with the number of cycles. Representative whole-sample images of mouse entheses that were subjected to quasi-static (top), or cyclic loading (bottom). For quasi-statically loaded samples (top), there was little to no fluorescent signal in the low force group (1N-2N), followed by increased staining near the attachment site at higher loads (3N and failure). For cyclically loaded samples (bottom), F-CHP staining was initially concentrated in a few fibers near the tendon mid-substance (10K-40K cycles) and ultimately propagated down the entire tendon in concentrated bands. Dotted lines represent outline of bone (white) and tendon (yellow). Solid line represents failure surface. Scale is 500 μ m.*

that, in addition to its loading history and the health of enthesis tissue, the mineral architecture underneath the enthesis plays a key role in dictating the failure type. For humans, epiphyseal closure (i.e., a metric of skeletal maturity) begins in childhood and is typically complete by 25 years of age [155]. In addition, clinical findings show that loss of mineralized tissue at the attachment site correlates with higher rates of re-tearing following surgical repair [132]. While mice used in this study were healthy adults (>12 weeks old) with no known genetic disposition to musculoskeletal injuries, these mice were not fully skeletally mature. The predominance of avulsion failures during *ex vivo* testing may be the consequence of mineral composition and bony architecture of murine tendon enthesis. This concept on whether changes in tendon enthesis composition and architecture affect tendon enthesis failure mode will be explored in **Chapter 5**. Nevertheless, *ex vivo* loading regimes in the current chapter were able to recapitulate the failure mechanisms observed clinically, showing that tendon enthesis failure behavior was driven by its mechanical loading history.

Tendon enthesis stiffness responses were relatively strain-rate insensitive, consistent with previous studies in tendons [156, 157]. Interestingly, strength and toughness increased at higher strain

rates by as much as 1.6-fold. This demonstrates that there is some effect of loading rate on tendon enthesis strength and toughness. These results are consistent with the strain rate–dependent ultimate tensile strength (UTS) previously reported for ligaments and tendon fascicles [158, 159, 160]. Contrary to the hypothesis, there was a relatively consistent failure mode (i.e., bony avulsion failure) across the strain rates investigated, with failure occurring in the tendon mid-substance only occasionally at the highest strain rates. Several previous studies have demonstrated that the loading rate affects the failure mode [160, 161, 162, 163]. These studies were done on larger animal models, such as primates, lapines, and canine knees, which have higher enthesis tissue density, collagen fiber density, higher bone mineral density, and denser trabecular architecture compared to small animal models such as the mice used in this study. Furthermore, Woo et al., reported that changes in failure mode with strain rate also correlated with changes in loading position (i.e., loading directions) [160, 164]. The results in the current study, consistent with previous results, suggest that the strain rate may not be the key factor in predicting failure mode (bony avulsion failures or tendon mid-substance failures). The effect on loading direction on tendon enthesis failure behavior will be explored in **Chapter 4**.

The strain-rate dependent increases in tendon enthesis toughness did not result in significant changes to its failure mode: almost all of the tendon enthesis samples failed via bony avulsion, irrespective of loading rate. To understand energy absorption under acute loading, avulsed bony pieces were characterized using methodologies developed in the previous chapter (**Chapter 2**). Avulsed (failed) area increased with loading rate and clustered in two segments at high loading rates. In some cases, the failure area was even larger than that of the primary insertion site (see **Chapter 2** for comparison). The reasoning behind the bimodal failure area distribution at high strain-rates was uncovered by looking at the number of avulsed fragments. The number of fragments (avulsed pieces per sample) increased with loading rate. This failure pattern might be easily understood with the analogy of breaking a wooden stick in half. When the stick is bent slowly, it breaks into two clean pieces. However, when the stick is bent very quickly, the stick failure pattern becomes unpredictable. In addition to creating two pieces, there is enough energy stored

and dissipated during fracture to generate many small fragments. Indeed, the results for the effect of monotonic increases in loading rate showed that the healthy enthesis loaded at high loading rate stored and dissipate enough energy to either propagate its crack to a larger-than-primary insertion area bony avulsed piece, or to form many smaller bony fragments. This failure pattern is consistent with previous observations on rate-sensitivity of bone fractures [165, 166].

In contrast to acute loading, all samples cyclically loaded to 20%-70% strength failed at the insertion. This failure mode was reminiscent of degenerative rotator cuff tears seen in elderly patients [107]. Samples cyclically loaded at lower, physiologically relevant loads (1%-20% of strength), did not fail, even after 100,000 cycles, indicating that these loading levels were under the enthesis fatigue limit. The concept of fatigue limit and a probable physiological loading range for tendons have been recently reported in several studies [158, 167, 168]. Ros et al. used *in situ* rat tail tendon (RTT) fatigue loading model with pre- and post- fatigue second harmonic generation (SHG) imaging and transmission electron microscope (TEM) to show that RTTs undergoing low cycle (1.0%, 500 cycles) loadings presented with highly aligned collagen with no evidence of kinking, fibrillar deformation, or damage, compared to that of the high cycle group (2.5%, 300 cycles fatigue), which exhibited severe and larger areas of fibril deformation and kinking [167]. In the *in vivo* rat patellar tendon subrupture fatigue damage accumulation model, no difference in apoptotic activity (a metric for cellular damage) occurred in low cycle groups, while greater apoptotic activity was seen in high cycle groups [168]. In the mouse Achilles tendon, toe-region and elastic-region strain loading are nondamaging, since these groups did not differ from control for any mechanical parameter [46]. Our results showed that at high cyclically loaded samples, tendon entheses failed at the interface between mineralized and unmineralized fibrocartilage, exactly where the material mismatch would lead to stress concentrations [54, 72]. Results thus suggested that the mechanisms protecting the fibrocartilaginous enthesis might be gradually attenuated under sufficiently severe cyclical loading.

The contrasting behaviors after monotonic and cyclical loading imply that there are distinct mechanisms driving their failures. Specifically, does localization and propagation of molecular

(nanoscale) damage leading to ultimate failure (macroscale) under monotonic vs. cyclic loading? To answer this question, CHP was used to track molecular level sub-failure damage to collagen that occurs in *ex vivo* loading in both loading conditions. Similar to what has been reported in RTT fascicles, molecular-level collagen damage occurred at sub-failure levels of strain, increased with applied load or number of cycles, and correlated with changes in tissue mechanics [148, 158]. The whole sample fluorescence imaging showed distinct mechanisms for each loading conditions. Under acute loading, fluorescent signal accrued near the primary insertion site when loads exceeded 70% of strength. Under cyclic loading, signal was concentrated in a few fibers near the tendon mid-substance, then propagated down the entire tendon. Distinct staining on some fibers suggests that sub-sets of the enthesis fibers were overloaded, while some were underloaded, further supporting the concept that the tendon enthesis behaves as a fibrous network. Indeed, studying propagation of mechanical damage of collagen revealed key aspects in energy absorption by the tendon enthesis: in addition to absorbing energy, the structural and composition adaptations within the compliant zone of partially mineralized tissue may serve to reduce or attenuate tendon energy storage following cyclical loading. When the attachment was pulled to failure, energy stored in the tendon near the enthesis was sufficient to fracture and avulse the mineralized tissue; however, under cyclical loading, the fibrocartilaginous insertion attenuated stress concentrations and shifted the failure site to the tendon (**Figure 3.6**). Thus, the enthesis contains fiber-level toughening mechanisms to resist monotonic loading and an underlying nanoscale mechanism to resist cyclical loading.

Tendon enthesis cells are known to be mechanosensitive, with the ability to alter the extracellular matrix in response to the local loading environment. The major limitation of the current *ex vivo* loading conditions is that it does not fully recapitulate how the accumulation of sub-failure damage or high impact loading events can lead to attachment failure, as the cells within enthesis were nonviable and were not capable of orchestrating biologic responses to mechanical damage. Nevertheless, the current study showed distinct molecular damage localization and propagation at the enthesis depending on the loading regime. Interestingly, studies with the rat patellar tendon *in vivo* fatigue model showed biologic responses in the exact region current *ex vivo* experimental results

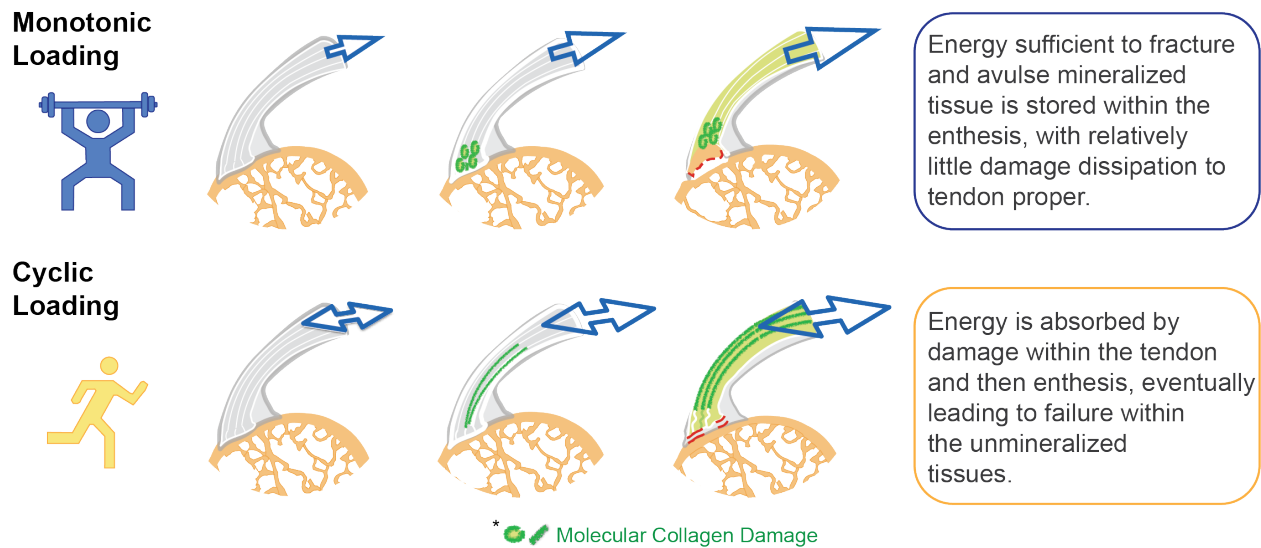


Figure 3.6: *Multiscale toughening mechanisms enable the entheses to exhibit distinct failure modes under varying loading conditions.* This chapter revealed key aspects of energy absorption by the fibrous nature of tendon enthesis: when the attachment was pulled monotonically to failure, the energy stored in the enthesis was sufficient to fracture and avulse the mineralized tissue; however, when the attachment was pulled cyclically, energy was dissipated in the enthesis and damage accumulated in the tendon followed by tendon rupture. Hence, the enthesis contains fiber-level toughening mechanisms to resist monotonic loading and an underlying nanoscale mechanism to resist cyclical loading.

show [168, 169]. One day post-fatigue loading, at the insertion, there were no significant changes in the extracellular matrix (ECM) protein staining and mild increases in aggrecan content, suggesting attenuation of degeneration at the insertion. In contrast, the tendon mid-substance showed degeneration of ECM, coupled with unaltered pro-collagen I and increase in aggrecan, a proteoglycan that is atypical in that region if the tissue was healthy. Furthermore, this study also showed that 7 days post-fatigue loading, the insertion region had significant ECM damage, while the mid-substance region had increased ECM remodeling [169]. It is no surprise that mechanically induced nano-scale damage caused a cascade of cellular responses that ultimately altered macro-scale local tissue structures. While it remains unclear what cell types monitor and recognize molecular damage, several *in vitro* studies have suggested that direct cellular detection of denatured collagen may play a role in initiating the biological remodeling response [170, 171]. It is possible that portions of denatured collagen bind to pattern recognition receptors (PRRs) of the immune cells, as recent

in vitro study showed that macrophage-like cells migrate towards mechanically overloaded collagen fibrils exhibiting kinked disruption (i.e., molecular and fibular damage) and promote collagen proteolysis [171]. The importance of the current study is in understanding the dependence of special localization and propagation of molecular-level damage in the tendon enthesis with the type of damage-inducing loading. While *in vivo* characterization of enthesis toughening mechanisms due to *in vivo* pathological loadings will be explored in **Chapter 6**, future investigations using *ex vivo* organ culture models or genetic mouse models with predisposition to chronic rotator cuff injuries should be conducted to further parse the effect of location-dependent and load-dependent cellular remodeling due to molecular damage.

Engineered architected materials are designed to fulfil specific functions, including having specific deformation and failure mechanisms to achieve specific mechanical behaviors. Damage and failure mechanisms can vary significantly due to material composition and loading conditions (i.e., monotonic loading or cyclical loading)[7]. The architecture of the tendon enthesis is also designed with loading in mind; this chapter demonstrated that the nature of the loading dictated the initiation and propagation of damage through the attachment. Under monotonic loading, energy storage in the compliant region of the fibrous attachment was protective, precluding fracture of the intricately architected transitional tissue and instead leading to bony fracture. This finding further reinforced the importance of the “compliant” band (introduced in **Chapter 1**) in connecting two highly dissimilar materials. Indeed, the conceptual applications of massive energy absorbing compliant materials has been seen in the commercial 3M Command™ strips, where pulling on compliant polymer allows it to displace and store enough energy to overcome adhesive shear stresses to remove wall-hung pictures. This counter-intuitive principle of adding compliant materials in attaching two dissimilar materials has recently has been implemented in both bottom-up and top-down fabrication processes of architecture materials intended for monotonic loading [2, 4]. The next frontier in connecting two architected materials will be harnessing the nano-scale energy absorption mechanisms of the tendon enthesis that resists fatigue loading, as described in the current chapter, for engineering attachments that are indented for cyclical loading.

3.5 Conclusion

Understanding the the evolution of sub-failure damage through ultimate tissue failure is critical for understanding injury and repair of the tendon enthesis. Mouse supraspinatus entheses had three distinct failure modes that were dependent on the loading regime. Studying localization and propagation of molecular collagen damage with changes in loading regime revealed that, in monotonic loading to failure, energy sufficient to avulse bone was stored in the enthesis with relatively little energy dissipation, while in cyclical loading, energy was absorbed by damage within the tendon and enthesis, eventually leading to failure within the unmineralized tissues. This chapter revealed insights into the ways that the tendon enthesis resists failure arising from physiologically relevant loads: the enthesis contains fiber-level toughening mechanisms to resist monotonic loading and an underlying nanoscale mechanism to resist cyclical loading. The identified sources of strength and toughness in the enthesis can enable improved design of surgical and tissue engineered solutions for tendon-to-bone repair.

Chapter 4: Differential recruitment of collagen fibers and the shape of the bony attachment endows toughness to the tendon enthesis across loading directions

Portions of this chapter are currently under review: (1) Golman M, Abraham AC, Kurtaliaj I, Marshall BP, Hu YJ, Schwartz AG, Guo XE, Birman V, Thurner PJ, Genin GM, Thomopoulos S. Toughening mechanisms for the attachment of architected materials: The mechanics of the tendon enthesis; and, (2) Golman M, Birman V, Genin GM, Thomopoulos S. Enthesis strength, toughness, and stiffness: an image-based model comparing positional and energy storing tendons with varying bony attachment geometries.

4.1 Introduction

Joint stability and mobility require transfer of muscle forces across the tendon enthesis. **Chapter 2** uncovered the fibrous character to the tendon enthesis, where the tendon enthesis fibers were continuous from one end (muscle) to the other (bone), with little to no branching. Other groups have also recently confirmed the fibrous nature of the enthesis using serial block face-scanning electron microscopy and phase-contrast micro computed tomography (microCT) [38, 138, 139]. The high resolution contrast enhanced images of the tendon enthesis architecture from **Chapter 2** show that tendon enthesis fibers splay and unravel as they anchor to bone, confirming prior findings [61, 73]. This fibrous architecture suggests that the enthesis behaves as a networked solid, where groups of fibers are recruited to bear load [75, 76], enabling the interface to withstand multi-modal and multi-directional loading. Indeed, **Chapter 3** revealed that the fibrous tendon enthesis contains fiber-level toughening mechanisms to resist monotonic loading and an underlying nanoscale mechanism to resist cyclical loading. However, the toughening mechanisms that enables the ten-

don enthesis to resist failures across a range of loading directions are not known.

The fibrous architecture of a tendon and its bony attachment varies according to the functional requirement of the particular joint. In positional tendons, such as the supraspinatus of the shoulder and the flexor tendons of the hand, stability must be maintained with loads across a large range of loading angles to move joints with precision [172, 173]. In energy-storing tendons, such as the Achilles tendon and the patellar tendon, elasticity is paramount to enable efficient locomotion by tissue stretching and recoiling to store and release energy, respectively, during movement [174, 175]. Furthermore, the excursion and deformation of positional tendons differs significantly from those of energy storing tendons, and range of motion (ROM) varies greatly from joint to joint. For example, the supraspinatus tendon in the shoulder ranges from 0° to 120° , the Achilles tendon in the ankle ranges from -40° to 20° , and the patellar tendon in the knee ranges from 0° to 140° (**Figure 4.1**) [176]. As we will show, both types of tendons from various joints insert into bone via a fibrous enthesis, with fibrous tissue abutting a bony ridge prior to insertion into bone. The conservation of this motif across positional and energy-storing tendons is surprising given the different loadings and the critical role of the attachment in resisting debilitating injury [106, 177].

The shoulder joint, for example, is capable of a remarkably large range of motion, resulting in high mechanical demand and widely varying static and dynamic forces on the rotator cuff tendon enthesis. Previous studies using both cadaveric [178, 179, 180] and animal shoulders [181] demonstrate position-dependent mechanical properties for the supraspinatus tendon. *Ex vivo* experiments showed the alignment of collagen fibers at the supraspinatus tendon enthesis reduce stress concentrations for 90° of shoulder abduction [73]. However, this alignment changes dramatically over the course of shoulder motion, with significant consequences for the strength of the attachment [178, 181]. A role of collagen fiber recruitment and buckling has been recognized since the 1930s [182], and a range of continuum models using statistical distributions of collagen fibers and their crimping exist to accurately predict the associated non-linear behavior of uniaxially loaded tendons [183, 184, 185, 186]. However, being constitutive models, these prior approaches don't capture failure behavior nor do they describe interactions between fibers and the bony anatomy of the en-

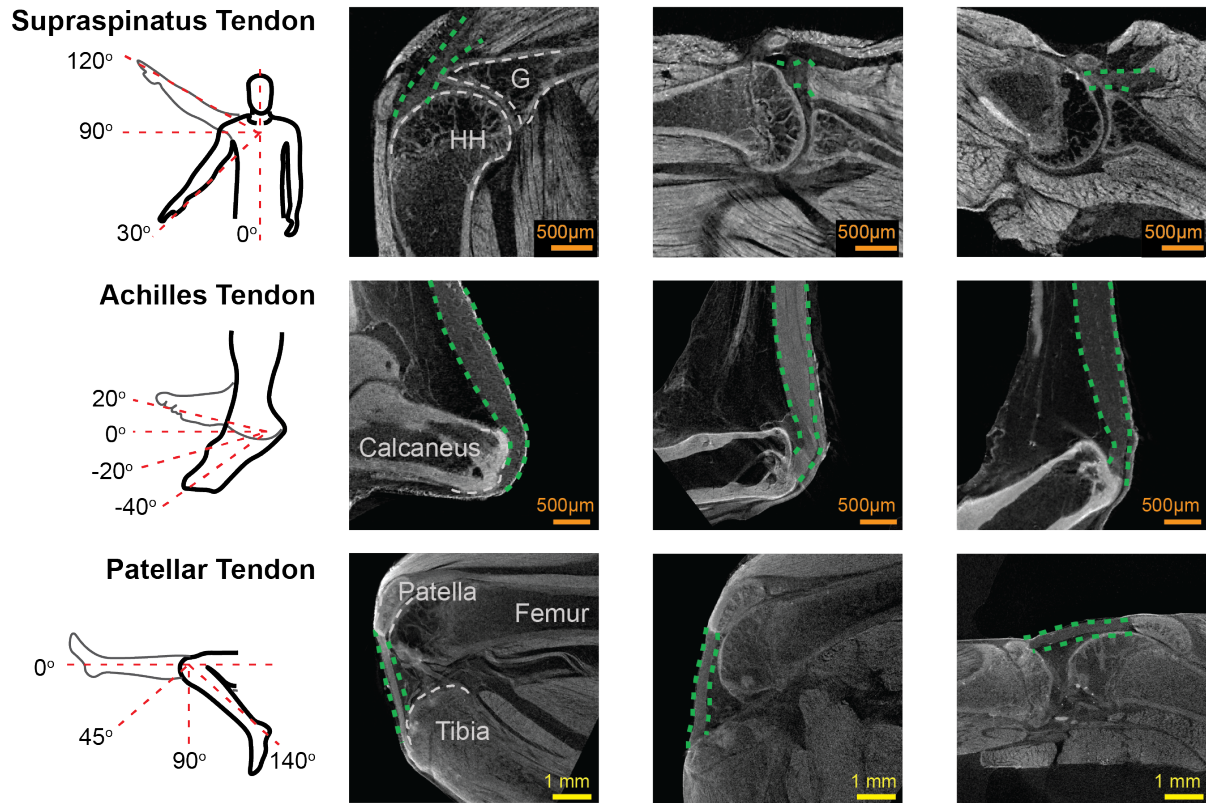


Figure 4.1: Range of motion (ROM) for supraspinatus, Achilles, and patellar tendon with corresponding contrast enhanced images of murine rotator cuff (supraspinatus tendon), ankle (Achilles tendon), and knee (patellar tendon) joints at flexion, straight, and extension. Green dashed lines outline tendons at each position. HH-humeral head; G-glenoid.

thesis. Rather than treating the enthesis as a material that must avoid continuum singularities, as other work has done [54, 67, 74], a better understanding of fibrous toughening may be achieved by characterizing fibrous structure interacting with a bony ridge.

In the current chapter, we seek to understand how the simple motif of a fibrous insertion and a tailored bone ridge could endow different entheses with resilience across the range of insertion sites and loading directions. This knowledge will provide insights into techniques for surgical repair of tendon-to-bone attachments and more broadly define mechanisms for the attachment of highly dissimilar materials. Therefore, this chapter will cover the roles of architectural and positional factors on enthesis toughness. The first part of the chapter will establish dependence of loading directions on mechanical behavior of the tendon enthesis by performing tensile tests on mouse supraspinatus tendon enthesis samples in a range of loading directions. The second part of

the chapter will describe a *positional-recruitment model* that explains the experimentally observed macroscale mechanical behavior of the tendon enthesis, with a focus on the trade-off between toughness and strength. Given the fibrous nature of the tendon enthesis, the overall hypothesis for this chapter is that the tendon enthesis' architecture is designed to optimize toughness of the attachment for a wide range of loading positions. It is hypothesized that increasing loading angle will decrease the strength and toughness of the tendon enthesis in *ex vivo* experiments. Numerical modeling is expected to predict loading direction-dependent fiber recruitment and crimping resulting the in experimentally observed failure patterns. Furthermore, it is hypothesized that energy storing tendons prioritize toughness over strength relative to positional tendons regardless of loading direction, and that the bony anatomy of each enthesis dictates its toughness profile with changing loading direction.

4.2 Methods

4.2.1 *Ex vivo*

4.2.1.1 Sample preparation and study workflow

All animal procedures were approved by the Columbia University Institutional Animal Care and Use Committee. Supraspinatus, patellar, and Achilles tendon-to-bone attachment units were harvested from healthy adult (>12 weeks) C57BL6/J mice were harvested from adult (>12 weeks) male C57BL6/J mice (n = 102). After dissection, samples were fresh-frozen in PBS and stored at -20°C . The experimental workflow was dependent on two categories: (1) unloaded/intact sample characterization and (2) loaded sample characterization. For unloaded-sample characterization, defrosted samples were secured at the appropriate loading direction and imaged via contrast enhanced microCT. For characterizing samples undergoing loading, defrosted samples were first scanned by conventional microCT before being subjected to mechanical testing. After mechanical testing, samples were secured at terminal displacements and submerged in a 5% mercury chloride (HgCl_2 , Sigma-Aldrich) in preparation for contrast-enhanced micro computed tomography (microCT).

4.2.1.2 Mechanical testing

All samples were mechanically tested in a saline bath at 25°C to prevent thermal collagen denaturation on a table-top tensile tester (Electroforce 3230, TA Instruments) fitted with a 10 lb load cell (TA instruments). Before testing, the supraspinatus muscle was carefully removed from supraspinatus-humerus unit. Samples were placed into custom 3D-printed fixtures [135] that secured samples in an orientation corresponding to various angles of abductions (0°, 30°, 60°, 90°, and 120°; n=10-12 per angle). Supraspinatus tendons were secured between two layers of thin paper (Kimwipe) with a drop of cyanoacrylate adhesive (Loctite, Ultra Gel Control) before mounting onto custom grips. For all mechanical testing protocols, samples were first pre-loaded to 0.05 N, pre-conditioned by applying 5 cycles of sinusoidal wave consisting of 5% strain and 0.2%/s, and rested for 300 seconds. Enthesis structural properties, such as failure load (referred to as strength in text), stiffness, and work to failure (area under the curve through failure load, referred to as toughness in text) were determined from load-deformation curves. Stiffness was calculated by a MATLAB (Matlab2019a, MathWorks) custom algorithm that identifies the best fitting line within a sufficient bin width (i.e., remove data below 10% of max load and above 95% of max load) by implementing the random sample correlation (RANSAC) technique [52].

4.2.1.3 Imaging

Simultaneous visualization of soft and hard tissues of tendon enthesis samples were achieved by staining samples with 5% mercury chloride solution prior to scanning with microCT. A 5% mercury chloride solution was prepared fresh for each experiment day by dissolving Mercury (II) chloride (HgCl₂, Sigma-Aldrich) in distilled and de-ionized water (MilliQ water, MilliporeSigma) at room temperature until the saturation was achieved. Tendon enthesis samples, either intact or post-mechanical testing, were submerged in this solution for 24 hours and washed three times in distilled and de-ionized water for 10 minutes each before they were imaged with microCT (Skyscan 1272, Bruker). All scans were performed with with 60kVp, 166uA, and Al 0.5mm filters. Intact whole-joints pictures were obtained by scanning glenohumeral, ankle, and knee

joints at flexion, straight, and extension (n=3-4 per position). The supraspinatus tendon enthesis samples were additionally scanned as whole joint (i.e., glenohumeral joint) and as fully dissected (i.e., containing only supraspinatus tendon to humeral head bone attachment unit) at 0°, 30°, 60°, 90°, and 120° abduction angles (n=5-6 per angle). Whole joint contrast enhanced microCT images were obtained at 5 μm resolution. Intact tendon enthesis samples were scanned at 1 μm resolution, while post-failure samples were scanned at 2.5 μm resolution. The acquired microCT data were reconstructed with the software (nRecon, Bruker) provided with the CT scanner using alignment optimization and beam-hardening correction. The reconstructed image data was visualized with built-in program (DataViewer and CTvox, Bruker).

4.2.1.4 Failure mode and failure area characterization

Failure mode characterization, such as failure interface and failed fragment quantity, was determined from manual inspection of post-failure contrast enhanced images, following the criterion described in **Chapter 2**. The failure area was determined using a custom semi-automated MATLAB (Matlab2019a, MathWorks) routine that calculates the overlapping polyhedron surface meshes from two arbitrary volumes (e.g., avulsed fragment and edges of avulsed pieces) from the same imaging dataset.

4.2.2 *In silico*

4.2.2.1 Positional-recruitment model

This mathematical model was developed based on our imaging of fibrous architecture and bony anatomy at the enthesis. The two-dimensional model considered N linear elastic collagen fibers of thickness w , with the n^{th} fiber spaced a distance A^n from an elliptical bone ridge with semi-major and semi-minor axis lengths A_0 and B_0 , respectively (**Figure 4.2**), and the centerline of the first fiber situated a distance of $w/2$ from the edge of the bone ridge. To model the observation that, in both mice and human enthesis samples [139, 178, 182], the reference lengths of the outer fibers exceed those of the inner fibers, the fibers were modeled as having increasing initial unstretched

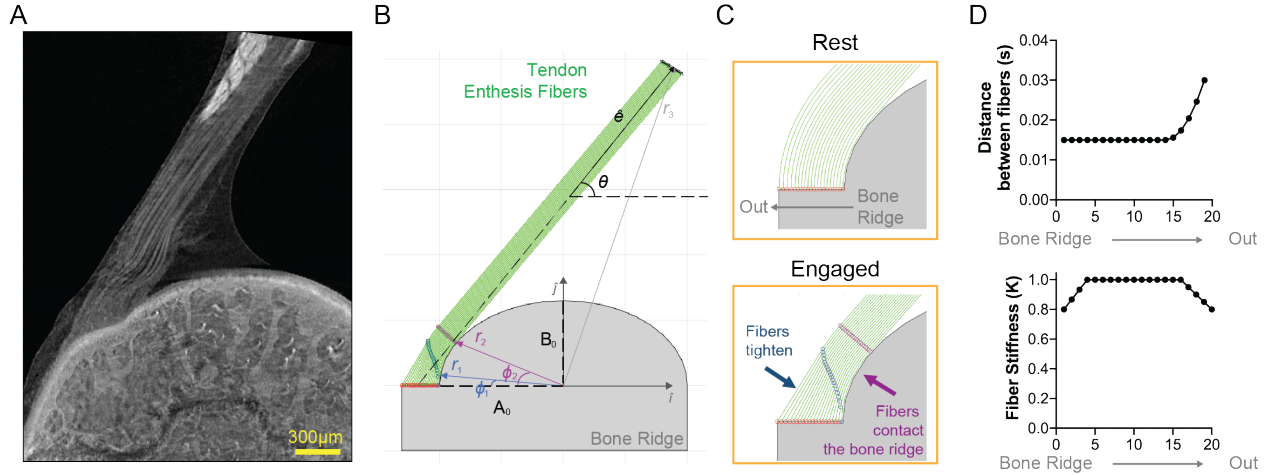


Figure 4.2: *Positional-recruitment model.* (A) Coronal section of high resolution contrast-enhanced microCT image of a murine supraspinatus tendon attached to the humeral head. (B) Tendon enthesis fibers are shown in green, the bone is shown in gray, and the black arrow represents the direction of loading. (C) At rest, the length of the outer fibers is larger than the length of the inner fibers. When a fiber is engaged and oriented so that it contacts the bone ridge, it tightens until it reaches the tangent to the humeral head curvature (blue arrow) and the tangent point to the tendon fiber (purple arrow). (D) To approximate the distribution of fibers at the enthesis, with middle fibers being more numerous and storing more energy, fiber density was varied across the attachment. Specifically, (D, top) the distance between fibers was increased at the outer edges and (D, bottom) fiber stiffness K was increased for middle fibers.

length as distance from the bony ridge increased. Specifically, bony insertions of the fibers were spaced over a flat region of bone abutting the bone ridge, so that the fiber insertion position for the n^{th} enthesis fiber from the bone ridge was $\vec{r}_0^1 = -A_1 \hat{i}$, where the \hat{i} unit vector parallels the flat region of bone and $A_1 = A_0 + w/2$. Fiber insertion point for each enthesis fibers increases with the distance from the bone ridge of fiber n , $A_0^n = A_0 + 0.5t + (n - 1)s$, where s is the average spacing between fibers identified from the images. Tendon enthesis insertion imaging from current work and the literature [139] show that show that fiber density changes at the insertion footprint. Enthsis footprint is rather oblong, with fibers further from the curve of the bone typically having much longer initial lengths. To comply with this, s was set constant for the majority of fibers, and for the outer 20% of fibers s was geometrically increased until spacing between the last two fibers ($A^{(N-1)}$ and A^N) reached $2s$ (Figure 4.2 D, top).

During loading, fibers engage and contact their neighbors or the bone ridge at a point

$$\vec{r}_1^n = -A^n \cos \phi_1^n \hat{i} + B^n \sin \phi_1^n \hat{j} \quad (4.1)$$

where the long axis and short axis of the centerline of the wrapped fiber (when the curvature takes an effect) is $A^n = A_0 + (n - 0.5)w$ and $B^n = B_0 + (n - 0.5)w$. The contact angle is $\cos \phi_1^n = A^n / A_0^n$.

To model both muscle loading and the boundary conditions of experimental data, the distal ends of the fibers, $\vec{r}_3^n(0^+)$, were restrained throughout loading of the tendon to maintain their initial positions relative to one another, so that for tendon loading parallel to a unit vector \hat{e} , the line connecting to the fiber ends (the line connecting the center of the insertion, $\langle \vec{r}_0^n \rangle = \frac{1}{2}(\vec{r}_0^N + \vec{r}_0^0)$, and the center of the distal ends of the fibers, $\langle \vec{r}_3^n(0^+) \rangle$) remained perpendicular to \hat{j} . This line was rotated to a defined loading angle, θ , as depicted in **Figure 4.2 B**.

The grip was displaced along the direction of $\langle \vec{r}_3^n(0^+) \rangle - \langle \vec{r}_3^n \rangle$ so that

$$\vec{r}_3^n(t) = \delta t \hat{e}_g + \vec{r}_3^n(0^+), \quad (4.2)$$

where $\hat{e}_g = (\langle \vec{r}_3^n(0^+) \rangle - \langle \vec{r}_0^n \rangle) / (\|\langle \vec{r}_3^n(0^+) \rangle - \langle \vec{r}_0^n \rangle\|)$, δ is the displacement rate, and t is time.

Each fiber remained slack until it contacted either the bone ridge or the engaged fibers positioned between it and the bone ridge (**Figure 4.2 C**). The range of angles over which such contact was maintained could be calculated from straightforward trigonometry. To derive the contact angle, $\cos \phi_2^n$, we first assume the initial rest state (**Figure 4.3**), where the grip is placed so that all the fibers are not in tension when the enthesis fibers are pulled horizontally ($\theta=0$ and fibers aligned with the \hat{i} direction):

$$\vec{r}_3^n(0^-) = x_3^0 \hat{i} + B^n \hat{j}; \quad \vec{r}_2^n(0^-) = B^n \hat{j}. \quad (4.3)$$

where x_3^0 (gauge length) is set for each experiment. Hence, the initial length for n^{th} fiber can

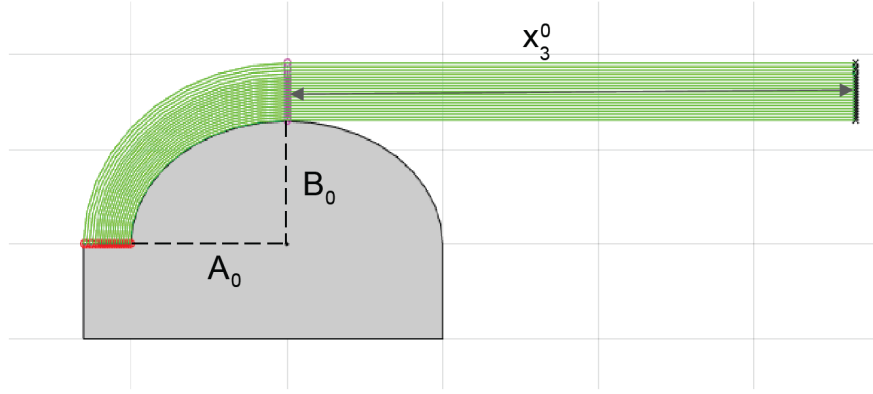


Figure 4.3: *Initial rest state.* At rest length, the outer fibers are larger than the inner fibers. The grip (black points) is placed so that the innermost fiber is not in tension when tendon is oriented horizontally ($\theta = 0$ and fibers aligned with the \hat{i} direction). x_3^0 is the gauge length and was defined as constant for all fibers of energy storing tendons.

be expressed as

$$L_0^n(t) = \text{Arc}_{L_0^n} \Big|_0^{\frac{\pi}{2}} + \|\vec{r}_3^n(0^-) - \vec{r}_2^n(0^-)\|. \quad (4.4)$$

The $\text{Arc}_{L_0^n}^n$ is the arc length of an ellipse from 0 to $\pi/2$ with the long axis A^n and short axis B^n , computed using the Ramanujan formula, where the perimeter of the complete ellipse was approximated as $L_{\text{ellipse}} = \pi (3(A + B) - \sqrt{(3A + B)(A + 3B)})$.

The grip was then rotated by an angle θ about the center of the insertion site to represent positional change, so that

$$\vec{r}_3^n(0^+) = Q^n(\theta)(\vec{r}_3^n(0^-) - \langle \vec{r}_0^n \rangle) \quad (4.5)$$

where the insertion is centered at the average position $\langle \vec{r}_0^n \rangle = \frac{1}{2}(\vec{r}_0^{N} + \vec{r}_0^0)$ and the elliptical rotation matrix is

$$Q^n(\theta) = \begin{bmatrix} \cos \theta & -\frac{A^n}{B^n} \sin \theta \\ \sin \theta & \cos \theta \end{bmatrix} \quad (4.6)$$

As the grip rotated and stretched in a direction \hat{e} , the angle at which contact is lost was determined by the innermost fiber, that was assumed to always stay in tension. As described above, the contact was lost at the point, $\vec{r}_2^n(t)$ at which the unit vector between $\vec{r}_2^n(t)$ and the connection point

on the grip for the strand, $\vec{r}_3^n(t)$, is tangent to the ellipsoid formed by the midline of fiber, n . The slope, m , of the tangent at the point $\vec{r}_2^n(t) = A^n \cos \phi_2^n(t) \hat{i} + B^n \sin \phi_2^n(t) \hat{j}$ is expressed as

$$m = \frac{dy}{dx}(A^n \cos \phi_2^n(t), B^n \sin \phi_2^n(t)) = -\frac{B^n \cos \phi_2^n(t)}{A^n \sin \phi_2^n(t)} \quad (4.7)$$

Additionally, this slope, m , was also defined by two points $\vec{r}_3^n(t) = r_{3x}^n(t) \hat{i} + r_{3y}^n(t) \hat{j}$ and $\vec{r}_2^n(t) = A^n \cos \phi_2^n(t) \hat{i} + B^n \sin \phi_2^n(t) \hat{j}$. Hence,

$$m = \frac{r_{3y}^n(t) - B^n \sin \phi_2^n(t)}{r_{3x}^n(t) - A^n \cos \phi_2^n(t)} = -\frac{B^n \cos \phi_2^n(t)}{A^n \sin \phi_2^n(t)} \quad (4.8)$$

Using trigonometric properties, the above relationship was expressed in terms of $\cos \phi_2^n$:

$$\alpha \sqrt{1 - (\cos \phi_2^n)^2} - \beta (\cos \phi_2^n) - \gamma = 0 \quad (4.9)$$

where $\alpha = A^n r_{3y}^n(t)$, $\beta = B^n r_{3x}^n(t)$, and $\gamma = A^n B^n$. Solving the above equation for $\cos \phi_2^n$, we have

$$\cos \phi_2^n = \frac{\sqrt{\alpha^4 - \alpha^2 \beta^2 - \alpha^2 \gamma^2} - \beta \gamma}{\alpha^2 + \beta^2}. \quad (4.10)$$

Using this we can determine the maximum length of a fiber when it is engaged and contacts the bone ridge:

$$L_{en}^n(t) = \|\vec{r}_1^n - \vec{r}_0^n\| + \text{Arc}_{L_{en}}^n \Big|_{\phi_1^n}^{\phi_2^n(t)} + \|\vec{r}_3^n(t) - \vec{r}_2^n(t)\|. \quad (4.11)$$

The $\text{Arc}_{L_0}^n$ is the arc length of an ellipse from ϕ_1^n to ϕ_2^n with the long axis A^n and short axis B^n computed via the Ramanujan formula.

If a fiber is engaged, but does not contact the bone ridge, the maximum length of a fiber is

$$L_{en}^n(t) = \|\vec{r}_3^n(t) - \vec{r}_0^n(t)\|. \quad (4.12)$$

This occurs when $\phi_2^n(t) < \phi_1^n$ and

$$\frac{\vec{r}_3^n(t) - \vec{r}_0^n}{\|\vec{r}_3^n(t) - \vec{r}_0^n\|} \cdot \hat{j} \equiv \hat{e}_{03}(t) \cdot \hat{j} < \frac{\vec{r}_1^n(t) - \vec{r}_0^n}{\|\vec{r}_1^n(t) - \vec{r}_0^n\|} \cdot \hat{j} \equiv \hat{e}_{10}(t) \cdot \hat{j}. \quad (4.13)$$

Modelling positional and energy storing tendons: The tendon gauge length was defined as a distance between the tangent points of the fibers to an elliptical bone ridge, $\vec{r}_2^n(0^+)$, and the distal ends of the fibers at the grips, $\vec{r}_3^n(0^+)$. The tendon enthesis fiber length was defined as the full length of the fiber, which includes gauge lengths and the arc lengths of the fiber to the tangent point to an elliptical bone ridge, $Arc_{Len}^n \Big|_{\phi_1^n}^{\phi_2^n(t)}$. A constant gauge length was enforced for energy storing tendons, with $L = 2500 \mu\text{m}$, and a constant tendon enthesis fiber length $L = 2500 \mu\text{m}$ was enforced for positional tendons. This represented distinct muscle properties and their functional length range relative to their tendon lengths [187]. For positional tendons, we assumed constant tendon fiber lengths across a wide range of loading angles because extrinsic muscles of positional tendons are short-fibered and represent only a fraction of their functional length range compared to the tendon length [188]. For energy-storing tendons, we assumed constant gauge lengths of tendons (i.e., constant functional length) to represent consistent active muscle force generation over the range of loading angles.

Fiber kinematics: The response of the enthesis to stretching was then predicted by treating the fibers as linear elastic and tracking loading direction-dependent fiber recruitment, with each fiber resisting enthesis displacement with a force $F^n(t)$:

$$F^n(t) = \begin{cases} 0, & \lambda^n(t) \leq \lambda_m \\ K(\lambda^n(t) - 1), & \lambda_m \leq \lambda^n(t) < \lambda_u \\ 0, & \lambda^n(t) > \lambda_u \end{cases} \quad (4.14)$$

where the threshold stretch ratio for fiber recruitment was set to $\lambda_m = 1$, the failure stretch ratio was set to $\lambda_u = 1.2$, K^n is a linear spring constant that was adjusted in proportion to out-of-plane tendon thickness to account for the 3D shape of tendon (**Figure 4.2 D, bottom**), and the stretch

ratio in each fiber was uniform:

$$\lambda^n(t) = \begin{cases} 1, & L_{en}^n(t) \leq L^n(0) \\ \frac{L_{en}^n(t)}{L^n(0)}, & L_{en}^n(t) > L^n(0). \end{cases} \quad (4.15)$$

in which $L^n(t)$ is the current length of fiber n , and $L^n(0)$ is its undeformed reference length. As described in the appendix, steric, frictionless interactions between neighboring fibers and the bone ridge were tracked carefully and had strong on enthesis response.

4.2.2.2 Numerical experiments

Quantitative anatomical parameters of the tendon enthesis were determined from mercury (II) chloride contrast enhanced images of murine supraspinatus tendon insertions obtained via high-resolution microCT imaging (n=6 biological replicates, **Table 4.1**).

Table 4.1: Supraspinatus tendon enthesis 2D measurements and selected model parameters

	Measurements (mean \pm SD)	Model parameters
Number of Fibers (N)	18.67 \pm 4.3	20
Fiber thickness (w)	8.8 \pm 3.0 μm	10 μm ($t = 0.01$)
Distance between fibers (s)	13.4 \pm 4.8 μm	15 μm ($s = 0.015$)
Long Axis Length (A)	1192 \pm 52.4 μm	1000 μm ($A = 1$)
Short Axis Length (B)	997 \pm 157.2 μm	1000 μm ($B = 1$)

To model energy storing tendons, gauge lengths for all pull directions simulated were kept constant, making initial length of each enthesis fiber change with pull directions simulated. To model positional tendons, initial lengths of each enthesis fiber were kept constant for all pull directions simulated. To note, all simulations were conducted using initial conditions of energy storing tendons, unless specified otherwise. To evaluate the effect of fiber density, the fiber spacing was varied over the range $1 \leq s/w \leq 3$, with all other parameters constant. To evaluate the effect of bone ridge morphology, the aspect ratio of the bone ridge was varied over the range $0.2 \leq A_0/B_0 \leq 1$, with all other parameters constant.

4.2.3 Statistical Analysis

Tendon enthesis characteristics, biomechanics results, and failure properties results were compared between treatment groups using ANOVA and specific differences from control conditions were determined using Dunnett's multiple comparisons test. $P < 0.05$ was considered significant. All statistical analyses were performed using Prism 9 (GraphPad). All data shown as mean \pm standard deviation.

4.3 Results

4.3.1 *Ex vivo*

4.3.1.1 Orientation and engagement of tendon enthesis fibers depends on joint position

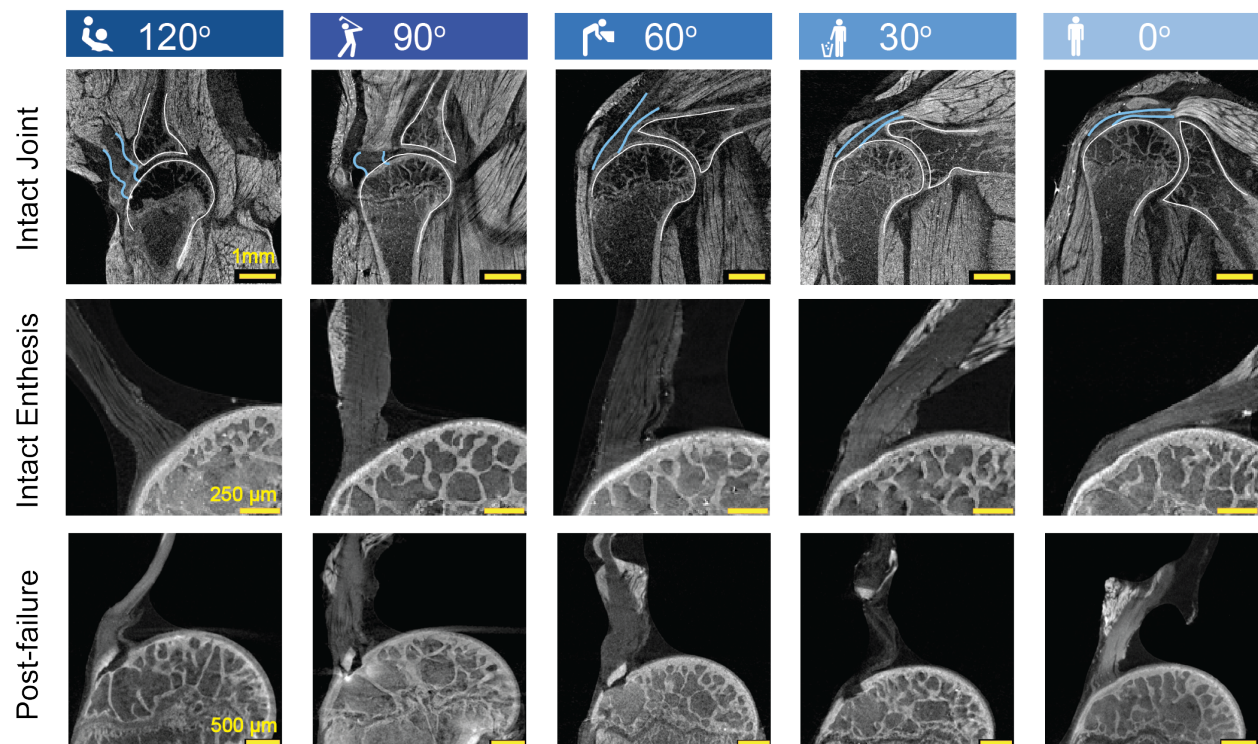


Figure 4.4: Contrast-enhanced microCT of intact mouse glenohumeral joint (top row), intact supraspinatus tendon enthesis (middle row), and failed tendon enthesis (bottom row) at each abduction angle. The supraspinatus tendon (top row, outlined in blue) was straight at low abduction angles (0°-30°) and buckled at high abduction angles (90°-120°); (G: glenoid, HH: humeral head).

Contrast enhanced images of rotator cuff, ankle, and knee joints at flexion, straight, and extension positions showed that the bone ridge anatomy where tendon attaches to bone significantly affected the orientation and engagement of tendon enthesis fibers (**Figure 4.1**). For example, enthesis fibers of the Achilles tendon in flexion were buckled and compressed against the *tuber calcanei* bone ridge. In contrast, joints in extension showed minimal contact of tendon enthesis fibers with their associated bone ridges.

To further characterize tendon enthesis architecture across a range of arm positions, collagen fiber architecture of both intact and mechanically failed mice supraspinatus tendon entheses were visualized at the macro-scale (joint-level) and the sub-micro meter scale (fiber-level) (**Figure 4.4**). Imaging tendon enthesis architecture of mouse glenohumeral joints at 5 μm resolution revealed that the collagen fibers of the supraspinatus tendon enthesis were engaged at low abduction angles (0° and 30°) and buckled at high abduction angles (90° and 120°) (**Figure 4.4, top**). Imaging at 0.75 μm resolution further showed that outer (i.e., bursal) fibers were longer than inner (i.e., articular) fibers (**Figure 4.4, middle**). Furthermore, images at this fiber-level scale confirmed that tendon enthesis fiber orientation and recruitment depend on arm position, with buckled fibers observed for outer fibers in certain positions (90° and 120°) and full recruitment of fibers observed when tendon enthesis is positioned at low abduction angles.

4.3.1.2 Tendon enthesis failure behavior depended strongly on the angle of abduction

Tendon enthesis failure behavior depended strongly on the angle of abduction (**Figure 4.5**). The enthesis was weakest when samples were pulled at 120° of abduction and strongest when pulled at 30° ($p < 0.01$). The enthesis was stiffest when pulled at 60° ($p < 0.001$) and most compliant at 0° ($p < 0.01$). The enthesis toughness increased with decrease in abduction angle. The mice supraspinatus tendon enthesis was toughest at 30° ($p < 0.001$).

The enthesis failed via bony avulsion in almost all samples (**Figure 4.4, bottom; Figure 4.6 A**). When loaded at low angles of abduction (0° and 30°), an increasing number of samples failed at the grips. When loaded at an orientation of 0° abduction, samples primarily failed at the grips (9/10),

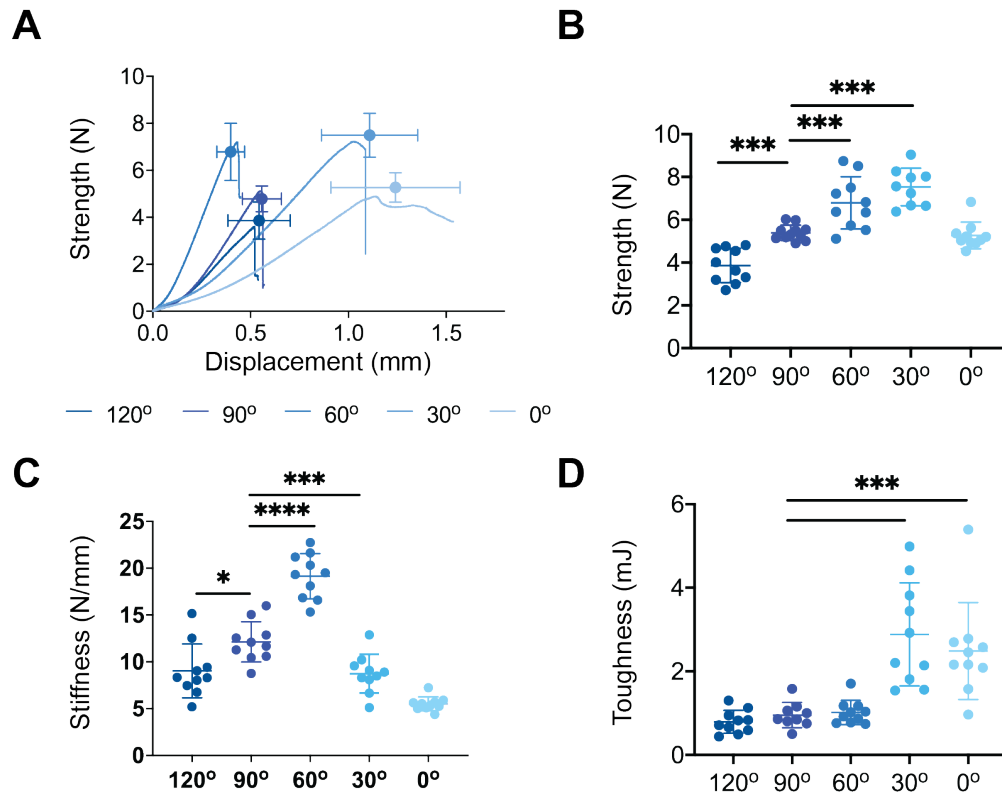


Figure 4.5: The tendon enthesis mechanical behavior varied dramatically with the direction of loading. (A) Strength (failure force) vs. displacement behavior. The mean failure strength (force) and failure displacement are represented by dots and cross-heads represent standard deviations. There were significant differences in tendon enthesis (B) strength, (C) stiffness, (D) toughness when tested quasistatically at varying angles *ex vivo*. The enthesis was weakest when samples were pulled at 120° of abduction and strongest when pulled at 30° ($p < 0.01$). The enthesis was stiffest when pulled at 60° ($p < 0.001$), and toughest when pulled at low angle of abductions (30° and 0°); (* $p < 0.05$, ** $p < 0.01$, *** $p < 0.001$, **** $p < 0.0001$, ANOVA followed by the Dunnett's multiple comparison test).

with only one sample failing at the insertion. To note, grip failure is attributed to an experimental limitation: decreased abduction angles resulted in increased sample gripping lengths (to maintain constant gauge length for testing). This resulted in less tendon secured with cyanoacrylate adhesive at the grips, which in turn led to failures at the grips.

The size of the fractured area was lowest at low angles of abduction ($p < 0.01$) (Figure 4.6 B). The fragment quantity distribution did not show a trend with loading angle (Figure 4.6 C). However, there was a shift towards MF-B failure type as angle of abduction decreased, as 90% of samples loaded at 30° of abduction failed at MF-B interface. (Figure 4.6 D).

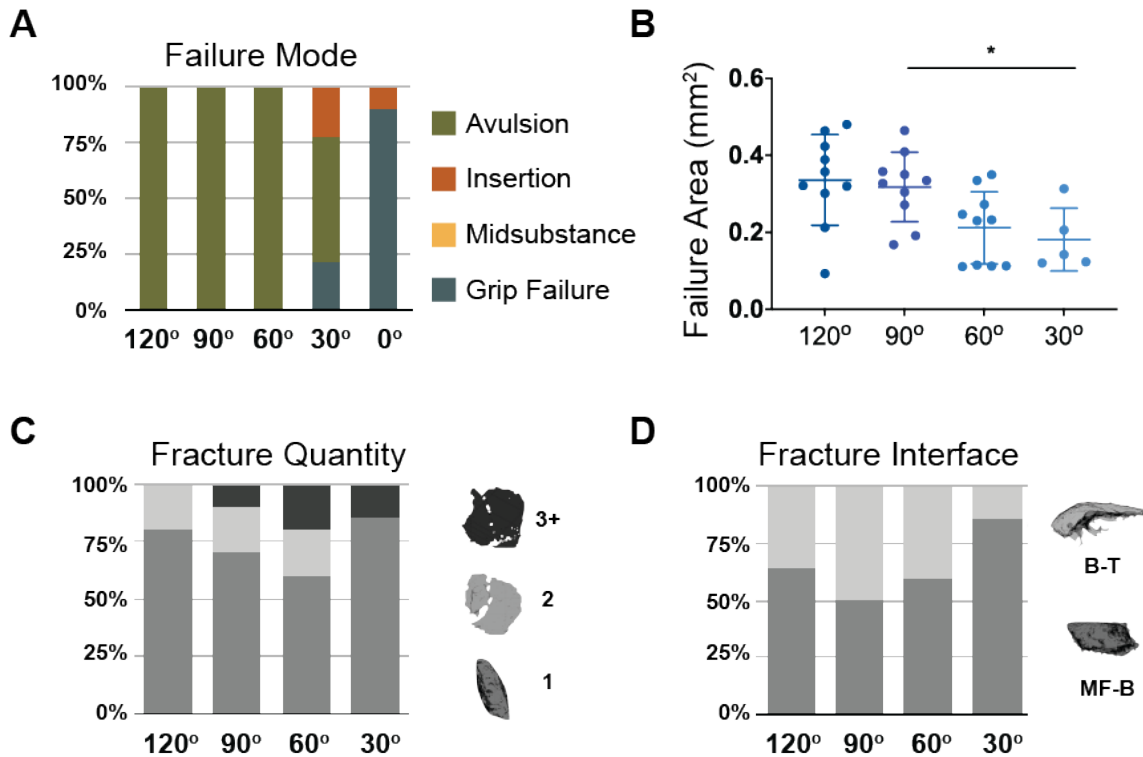


Figure 4.6: The enthesis failed via bony avulsion in almost all samples and the size of fractured area was lowest at low angles of abduction. (A) Samples failed primarily via bony avulsion. However, at low angle of abductions (0°-30°), most samples failed at the grips. (B) The size of the fractured area decreased at low angles of abduction ($p < 0.01$). (C) Fragment quantity distribution did not show a trend with loading angle. (D) There was a shift towards MF-B type failure when samples were pulled at 30° of abduction; (* $p < 0.05$, ANOVA followed by the Dunnett's multiple comparison test).

4.3.2 *In silico*

4.3.2.1 *Positional-recruitment model* simulation successfully reproduced experimentally observed enthesis mechanics as a function of abduction angle

The position-dependent fiber kinematic model was run with parameters described in **Table 4.1** and load-displacement curves were generated for abduction angles ranging from 0-120°. The model successfully reproduced the fiber recruitment trends and variations in mechanical behavior shown in the *ex vivo* experimental data (**Figure 4.7 A**). The simulation showed that normalized force was weakest at 120° of abduction and largest at 60° of abduction. Stiffness was weakest at

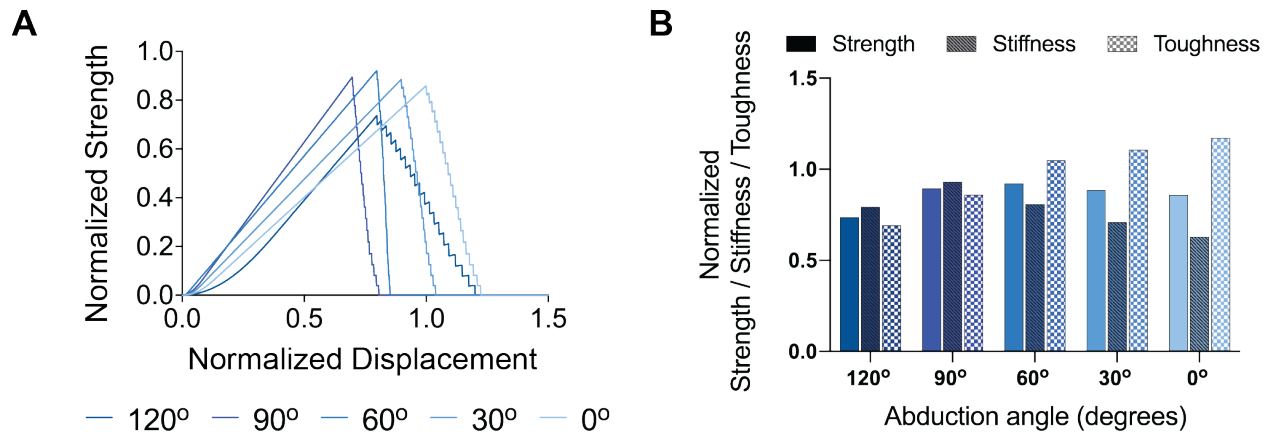


Figure 4.7: Positional-recruitment model simulation reproduced experimentally-observed entheses mechanics as a function of abduction angle. **(A)** In silico strength vs. displacement plot. **(B)** Strength, stiffness, toughness results normalized against the case when fibers were pulled uniaxially without the geometric constraints.

0° of abduction, and largest at 90° of abduction. Toughness increased gradually with decreasing angles of abduction (**Figure 4.7 B**).

4.3.2.2 The balance between tendon enthesis strength, toughness, and stiffness varies across loading directions

Positional fiber recruitment simulations revealed distinct mechanical responses across a range of physiologically relevant loading directions. The relationship between fiber engagement and displacement was plotted (**Figure 4.8 A**), where each point represents the percentage of fibers engaged at a given displacement. A relatively small amount of displacement was necessary to engage (recruit) all of the fibers ($N=20/20$) when the tendon was pulled at 90°. In contrast, the percentage of fibers engaged at each displacement decreased with decreasing loading angles, which contributed the increase in the displacement needed to engage all fibers at low loading angles. For example, relative to 90°, a 6-fold increase in displacement was necessary to engage all fibers when loaded at 30° and a 13-fold increase in displacement was necessary to engage all fibers when loaded at -30°. Furthermore, a 20-fold increase in displacement was necessary to engage all fibers when loaded at 120°. Simulations showed that tendon enthesis strength and stiffness decrease with decreasing loading angles (from 90° to -30°) whereas toughness increased with decreasing loading

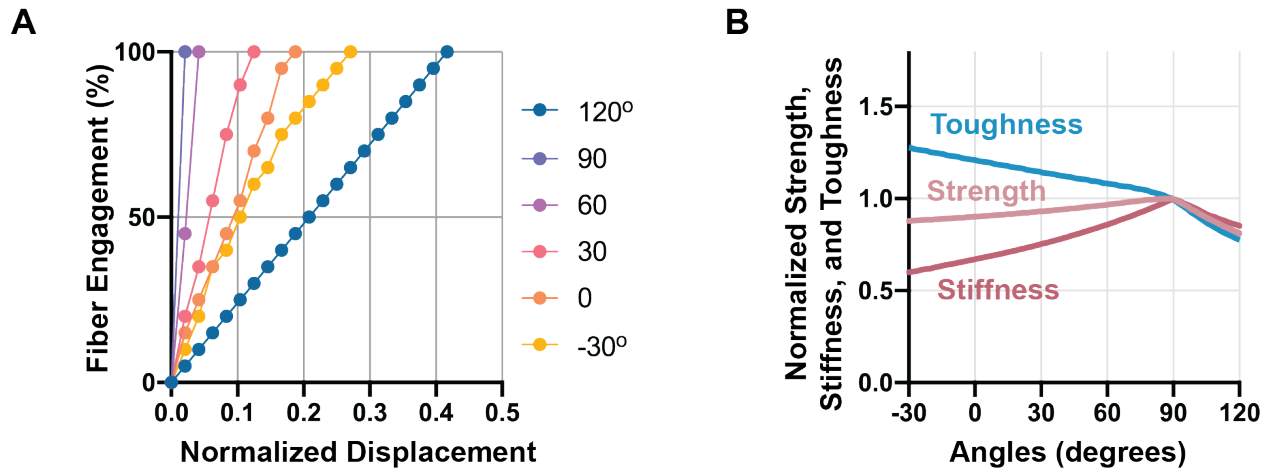


Figure 4.8: The mechanism driving loading-angle dependent failure behavior of the tendon enthesis is position-dependent fiber recruitment. **(A)** Number of fibers engaged (recruited) with respect to displacement dependent on loading angle. **(B)** Normalized strengths, stiffness, and toughness responses for tendon enthesis simulated to be loaded in range of loading directions. Simulations were run with 20 fibers ($N=20$), round bone ridge ($A_0 = B_0$), fiber thickness of $w=10 \mu\text{m}$, fiber spacing $s/w=1.5$, and fiber failure stretch of $\lambda_u = 1.2$. Initial conditions were set as for energy storing tendons. Strength, stiffness, and toughness were normalized against idealized scenario where tightly packed fibers ($s/w = 1$) were pulled to failure uniaxially at 90° .

angles (**Figure 4.8 B**). Strength, stiffness, and toughness decreased dramatically beyond a loading angle of 90° .

4.3.2.3 Fiber packing density influences joint position-dependent tendon enthesis mechanics

To examine the effect of fiber density on tendon enthesis mechanics, fiber packing was varied in the model by adjusting the ratio between fiber spacing, s , and fiber thickness, w . Strength and stiffness were normalized to the idealized scenario where tightly packed fibers ($s/w=1$) were loaded at 90° (**Figure 4.9**). Simulations revealed that the spacing between fibers affected the normalized strength, stiffness, and toughness, and that the effect depended on joint position. Irrespective of the degree of fiber packing, normalized strength and toughness were the lowest for the case when the tendon enthesis was loaded at 120° . When fibers were tightly packed ($s/w=1$), the strength was independent of loading angle. Increased fiber spacing resulted in a monotonic decrease in strength for all angles simulated. Increased fiber spacing also resulted in a decreased stiffness for each loading direction simulated; however, stiffness was largely dictated by the loading angle, highest at 90°

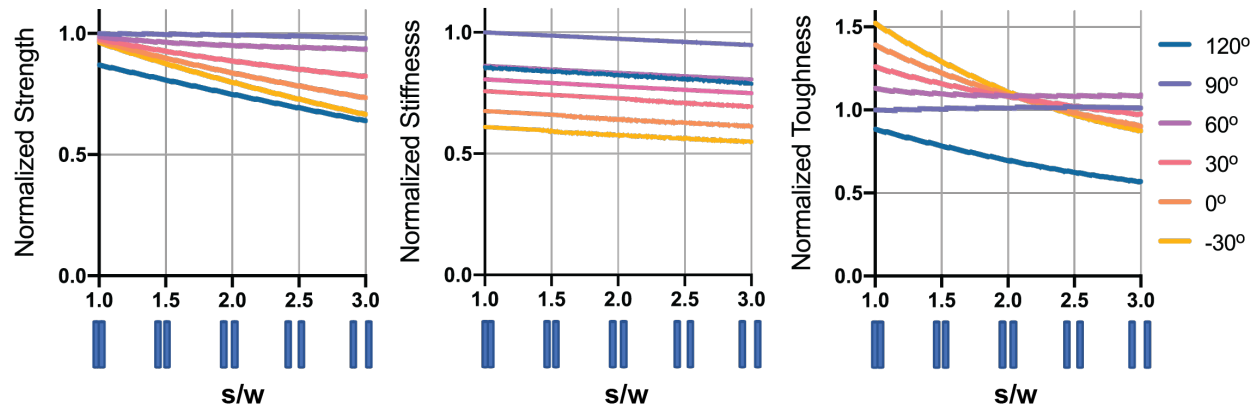


Figure 4.9: Fiber packing density influences joint position-dependent tendon enthesis mechanics. Effect of spacing between fibers (s/w) on enthesis mechanics. Simulations were run with 20 fibers ($N=20$), a circular bone ridge ($A_0 = B_0$), fiber thickness of $w = 10 \mu\text{m}$, and a variable spacing between fibers. Fiber failure stretch was set to $\lambda_u = 1.2$. Initial conditions were set as for energy storing tendons. Strength, stiffness, and toughness were normalized against idealized scenario where tightly packed fibers ($s/w=1$) were pulled to failure uniaxially at 90° .

and lowest at -30° . Stiffness was similar for the 60° and 120° cases. Toughness depended strongly on position and fiber packing, decreasing with increased fiber spacing for low loading angles (-30° to 30°) and at 120° . In contrast, toughness increased slightly with increased fiber spacing for the 60° and 90° loading cases, with both cases showing toughness gains (i.e., normalized toughness > 1) for all fiber spacing simulated. Toughness gains were most apparent when tendon entheses were loaded at low angles at high fiber packing densities. At loading angles of -30° through 60° , toughness was equivalent for $s/w = 2$, revealing a packing density that optimizes toughness across a wide range of joint positions.

4.3.2.4 Energy storing tendons prioritize toughness over strength, while positional tendons prioritize consistent stiffness

Simulations of energy storing and positional tendons were performed. Fiber lengths increased with distance from the bone ridge and loaded fibers were recruited sequentially according to the loading direction. In all simulations, the innermost fibers engaged and failed first, regardless of loading angle. Results revealed clear joint position-dependent differences between positional tendons and energy storing tendons (Figure 4.10). The strength of energy storing tendons peaked

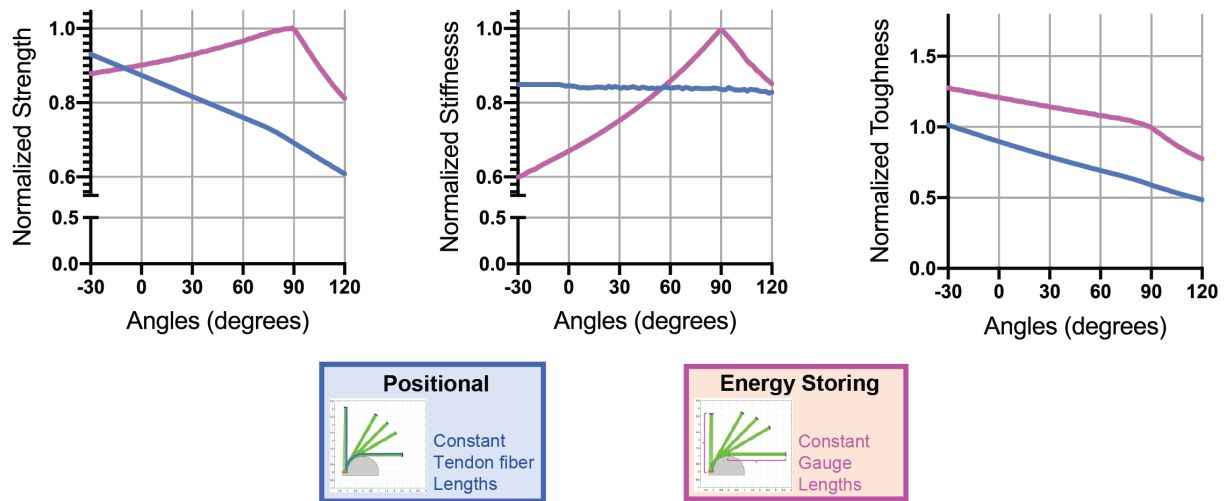


Figure 4.10: Energy storing tendons prioritize toughness over strength, while positional tendons prioritize consistent stiffness. Loading angle dependent mechanical responses for energy storing and positional tendon entheses. Simulations were run with 20 fibers ($N = 20$), a circular bone ridge ($A_0 = B_0$), fiber thickness of $w = 10 \mu\text{m}$, and fiber spacing $s/w = 1.5$. Fiber failure stretch was set to $\lambda_u = 1.2$. Initial conditions: constant gauge lengths were enforced for energy storing tendons and constant tendon enthesis fiber lengths were enforced for positional tendons. Strength, stiffness, and toughness were normalized against idealized scenario where tightly packed fibers ($s/w = 1$) were pulled to failure uniaxially at 90° .

when the tendon enthesis was pulled at 90° , decreased rapidly at higher loading angles, and decreased gradually at lower loading angles. In contrast, the strength of positional tendons was highest at -30° and decreased gradually with increasing loading angles. The stiffness profile for energy storing tendons followed their strength profile. In contrast, the stiffness of positional tendons was relatively constant for all loading angles. When examining toughness across all loading angles, energy storing tendons absorbed more energy before failure than positional tendons, with gradual decrease in toughness with increasing loading angle.

4.3.2.5 The bony anatomy onto which the tendon attaches influences fiber recruitment patterns and resulting enthesis mechanics

The effect of bone ridge anatomy on the position-dependent mechanics of the tendon enthesis was evaluated using energy storing tendon models. The simulations revealed that strength and

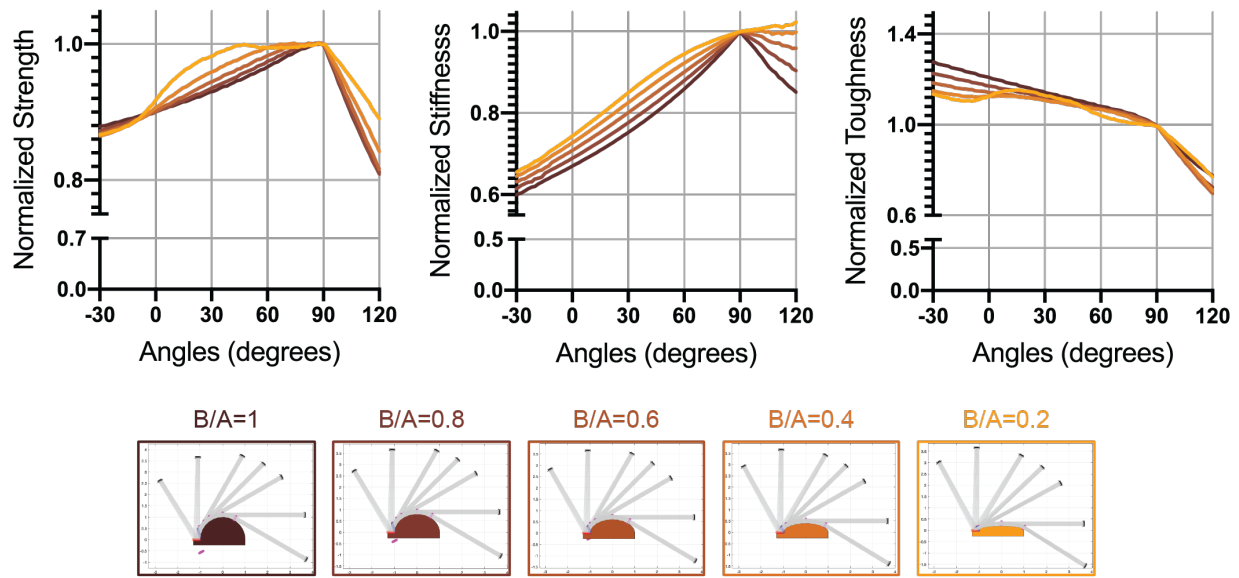


Figure 4.11: *The bony anatomy influences fiber recruitment patterns and resulting enthesis mechanics.* Anatomical bone ridge flattening on tendon enthesis mechanics. Simulations were run with 20 fibers ($N = 20$), fiber thickness of $w = 10 \mu\text{m}$, fiber spacing $s/w=1.5$, and a variable aspect ratio for the cylindrical bone ridge. Fiber failure stretch was set to $\lambda_u = 1.2$. Initial conditions were set as for energy storing tendons. Strength, stiffness, and toughness were normalized against idealized scenario where tightly packed fibers ($s/w = 1$) were pulled to failure uniaxially at 90° .

stiffness increased with bone ridge flattening (lower B_0/A_0 , **Figure 4.1**). Notably, with increased bone ridge flattening, the range of loading angles over which high strength was maintained increased. For example, for a circular bone ridge ($B_0/A_0 = 1$), a 2% decrease in strength occurred over 15° range of loading (90° to 75°), while for a flat bone ridge ($B_0/A_0 = 0.2$), a 2% decrease in strength occurred over a 60° range of loading (90° to 30°). Stiffness was primarily determined by bone ridge anatomy and was higher for a flat bone ridge ($B_0/A_0 = 0.2$) than for a circular bone ridge ($B_0/A_0 = 1$). Relatively modest changes in toughness were observed, with toughness highest for a circular bone ridge at all loading angles, and toughness gains (i.e., normalized toughness > 1) evident for all bone ridge geometries for loading angles below 90° .

4.4 Discussion

Although all joint motion requires transfer of muscle load across the tendon enthesis to the skeleton, the functional requirements for this vary according to the particular joints. Tendons have been categorized as either positional or energy storing [172, 173, 174, 175]: the rotator cuff tendons of the shoulder must accommodate a relatively large range, the flexor tendons of the hand must enable precise positional control, and the Achilles tendon of the ankle must store energy for locomotion. Based on observations on the fibrous character of the enthesis from **Chapter 2**, it was hypothesized that the nanoscale toughening mechanisms described in **Chapter 3** are supplemented by macroscale toughening mechanisms that depended on the fibers and their recruitment. To investigate how the tendon enthesis achieves function across a wide range of loading directions, the current chapter presented a series of *ex vivo* experiments and a position-dependent fiber recruitment model that described tendon enthesis mechanics for positional and energy storing tendons and for varying bone attachment geometry. We observed experimentally that tendon enthesis mechanical behavior varied dramatically with loading angle. The simulations revealed toughening mechanisms across a range of joint orientations and a balance between strength and toughness that depended on the particular functional requirements of the joint.

The high-resolution contrast enhanced images of murine supraspinatus tendon entheses obtained in the current study showed continuous tendon fibers from the bony insertion site to the myotendinous junction, similar to recently published studies in rat and porcine Achilles tendons [61, 138, 139]. Consistent with these previous qualitative descriptions of the human supraspinatus tendon [182], the joint-level and fiber-level contrast enhanced images of tendon enthesis architecture obtained in this chapter further confirmed the fibrous nature of the tendon enthesis: tendon enthesis fiber orientations were clearly dependent on loading position and proximity to the bone ridge attachment. Contrast enhanced imaging revealed three features of the fibrous tendon attachment: (1) the inner (articular side) fibers were shorter than the outer fibers, (2) a subset of tendon fibers were buckled at high angles of abduction, and (3) with loading, fibers engaged, re-oriented,

and, came into contact with their neighboring fibers or the humeral head. To determine how this position-dependent fiber recruitment dictates enthesis mechanics, the first portion of this chapter described mechanical and failure behavior of mouse tendon enthesis loaded across a range of shoulder positions. Tendon entheses tested in tension at varying abduction angles (0° , 30° , 60° , 90° , and 120°) showed distinctive tendon enthesis failure behavior that depended strongly on the angle of abduction, and hence the recruitment of collagen fibers. This behavior is consistent with reported local strains fields at the tendon insertion site tested at two different angles [61], as well as study conducted on rat supraspinatus tendon enthesis [181]. The position-dependent mechanical behavior, observed *ex vivo*, suggest that the distinct fiber architecture of the tendon enthesis is reoriented, recruited, and subsequently ruptured to balance strength and toughness across a wide range of motion.

To understand how fiber recruitment could explain the experimentally-observed mechanical effects of loading angle, a position-dependent fiber kinematic model was developed. The model incorporated the new observations of tendon enthesis fiber architecture. Simulations successfully described the experimental observations; normalized strength and stiffness decreased with decreasing loading angle (corresponding to the shoulder abduction angle), while toughness increased with decreasing loading angle. The mechanism driving this behavior was fiber recruitment, which varied with the direction of loading, and the interactions of fibers with the bone ridge. For example, as the loading angle increased, fiber recruitment for energy storing tendons occurred at lower displacements and full engagement was achieved relatively rapidly. The resulting load-displacement curves replicated previous reports [181] of a shorter toe-region and higher stiffness for increasing loading angle.

The tradeoff between strength and toughness is a well-known design dilemma in material design, with increases in toughness typically coming at the cost of decreased strength and stiffness [1, 4]. Results suggested that the tendon enthesis optimizes toughness, with gains in toughness achieved through comparably small losses in strength. Imaging and simulations showed that different portions of the fibrous architecture of the tendon enthesis engaged depending upon loading

angle, and that the differential engagement enabled toughness across a wide range of motion. The trade-off was particularly apparent at lower loading angles, where, for instance, muscle loads are highest at the rotator cuff [189]. These observations are complementary to the balance between strength and toughness previously described for other structural features of tendon enthesis, including mineralization patterns that achieve toughness at the expense of strength [54, 67, 74] and microscale interdigitation that toughens the attachment [57].

The model simulations shed light on differences between relatively injury-prone, energy storing tendons, and relatively stiff and strong positional tendons [190, 191, 44]. While others have understood these differences in the context of fiber structure, cross-linking, and biomolecular composition [192, 193, 44], we modeled them in terms of fiber recruitment and interactions with bony anatomy. Viewing the simulations in this light revealed that, while energy-storing tendons have entheses that appear optimized for toughness, positional tendons appear optimized to maintain stiffness across a range of loading directions. This suggests that positional tendons may function to move joints with precision, with a constant stiffness allowing for better muscle control of fine motions across a wide range of joint angles.

Ex vivo and *in silico* results also suggested three ways in which bony anatomy and fiber architecture at the tendon enthesis explain function and injury. First, simulations suggested insights into why thresholds for injury differ across loading angles and joints. Partial tears in rotator cuff and patellar tendons are more commonly observed on the articular side of the tendon, proximal to the bone ridge [101, 194]. Consistent with this, and consistent with strains fields reported at the loaded tendon enthesis [178], our simulations predicted that the innermost (articular) fibers were the first to engage and the first to fail at every loading angle simulated. Second, results were consistent with experimental observations of differences in full thickness tendon tears across tendons. Typical acute rotator cuff tears occur at high abduction angles (110°) [195]. Typical Achilles tendon ruptures occur with sudden plantar flexion of the foot (-30°) [99]. Typical patellar tendon ruptures occur with the extensor mechanism with the knee flexed (corresponding to 30° in **Figure 4.1**) [118]. These joint positions coincide with the lowest respective strengths in the simulations

(**Figure 4.1**). Third, the model revealed the importance of the bony ridge at the enthesis in enthesis mechanics. Flattening of this ridge (reduction of B_0/A_0), as seen at the patellar tendon insertion of the knee, contributed to the maintenance of strength over 43% of the range of motion, which may assist the patellar tendon in high stress activities such as running, jumping, and kicking over a significant range of orientations [118, 194]. This feature can be seen in energy storing tendons across other species, such as the insertion of the supracoracoideus tendon into the dorsocaudal surface of the humerus, just distal to the tuberculum dorsale [196], at the wings of birds, which may achieve the effect of bone ridge flattening to optimize strength over powered wing flapping [197].

Engineering architected materials are designed and optimized to achieve specific combination of properties and functions. The networked behavior of the tendon enthesis seen in both *ex vivo* and *in silico* experiments show clear advantage in making the interface fibrous: depending on loading direction, fibers re-orient, accept, share load, and as a result, sequentially fail. This behavior not only provides additional toughness to the enthesis, but also allows for the body to physiologically regenerate damaged fibers. A similar concept has now been applied in designing topologically interlocked material (TIM) panels, where failure in TIM architecture panels is designed to involve one or contiguous panels, allowing the rest of the panels to remain intact and functional, and giving the opportunity for the damaged block to be replaced at a later time [2, 17, 198]. While adaptations to enthesis architecture occur due to aberrant loadings, as will be discussed in (**Chapter 6**), the findings from the current chapter reveal fundamental design characteristics that may facilitate design and development of engineered architected attachments that can bear multi-directional loads.

A limitation of the positional-recruitment model is its two-dimensional implementation. The analysis of contrast-enhanced imaging and subsequent parameter value determinations were within what has previously reported in the literature [61, 138, 139]. However, three dimensional (3D) modeling based on 3D fiber tracking that accurately captures fiber density, fiber counts, fiber branching, and fiber curvature along the length of tendon enthesis may add additional insights into position-dependent fiber recruitment kinematics. A further limitation is that fibers were linear-

elastic and did not interact with each other in shear. Although adding complexity to the model, e.g, non-linear behavior, post-yield resistance, and cross-linking of adjacent collagen fibers, would more accurately represent the tendon enthesis, the effects revealed in the current simplified model allow for straightforward first-order understanding of fiber recruitment effects at the tendon enthesis. The simulation results revealed a clear role of bony anatomy and fiber recruitment in tendon enthesis toughening and explained how fundamental features of positional and energy storing tendons are driven by these factors. The next chapter (**Chapter 5**) will investigate the nature of biomolecular composition on tendon enthesis mechanics.

4.5 Conclusion

Results from this chapter reveal that tendon enthesis toughness across a range of joint motion arise from fiber reorientation, recruitment, and rupture, and are mediated by interactions between fibers at the enthesis and the bony ridge abutting it. *Ex vivo* experiments using mouse tendon entheses, loaded in a range of directions, showed a clear dependence of enthesis mechanical and failure responses on joint position. A mathematical model of enthesis toughness predicted that fibrous architecture and bony geometry combine to enable energy storing tendons to prioritize toughness over strength, and positional tendons to prioritize consistent stiffness across all loading directions. The results from this chapter revealed key toughening mechanisms that protect the tendon-bone interface from injury and identified several design parameters for improved attachment of architecture materials.

Chapter 5: Mineral content is crucial for tendon enthesis strength

Portions of this chapter are currently under review: Golman M, Abraham AC, Kurtaliaj I, Marshall BP, Hu YJ, Schwartz AG, Guo XE, Birman V, Thurner PJ, Genin GM, Thomopoulos S. Toughening mechanisms for the attachment of architected materials: The mechanics of the tendon enthesis.

5.1 Introduction

Advances in engineering materials have relied on optimizing a wide array of compositions, molecular structures, and granular structures to achieve particular functions. Natural tissues, on the other hand, must achieve mechanical function using a limited number of building blocks, typically relying on fibrillar proteins (e.g., collagen), minerals (e.g., hydroxyapatite), and sugars (e.g., proteoglycans). Using these biomaterial building blocks, natural organisms create architected composite materials that achieve remarkable mechanical performance, often outside of the bounds of the composite rule of mixtures [3, 8, 5]. For example, in bone, hydroxyapatite mineral crystal platelets (referred to hereafter as "mineral") accumulate in collagen fibril gap channels, intrafibrillar spaces, and fibril surfaces to provide strength and stiffness [58, 29]. In articular cartilage, the role of proteoglycans in providing compressive properties is well-established [199, 200]. Negatively charged proteoglycans embedded in a fibrillar collagen extracellular matrix provide viscoelasticity and resilience to compressive loads through electrostatic and non-electrostatic forces [201, 202, 203].

Tendon entheses are complex composite biomaterials with gradients in mineral and proteoglycan composition, previously described in **Chapter 1**. Mechanical models have described the role of the spatial gradient in mineral for mitigating stress concentrations at the tendon-bone interface

and for stiffening the tissue after a percolation threshold is reached [67, 54, 85]. The nanoscale mineralization pockets [85, 86, 30] observed from the TEM imaging of the insertion site, as well as microscale mechanical testing of laser-dissected tendon entheses [72], supported these ideas. In terms of proteoglycan composition in the tendon enthesis, quantitative proteome analysis showed enrichment of the relatively large chondroitin sulfate proteoglycan in the interface region compared to the tendon mid-substance [61]. Roles for proteoglycans and glycosaminoglycans (GAGs) in articular cartilage and tendon have been shown using knockout animal models and enzymatic degradation [42, 204, 205, 206], however, the role of proteoglycans in enthesis mechanical behavior remains unclear. Understanding how the distinct enthesis biomolecular composition introduced in **Chapter 1** allows the attachment to absorb and dissipate mechanical energy and thereby avoid catastrophic failure would be beneficial for designing engineering and medical solutions for biamaterial attachments.

This chapter assesses the compositional contributions on enthesis toughness by chemically removing the constituents of enthesis (i.e, mineral or proteoglycan) and examine its failure behavior. Given the fact that proteoglycans are common in tissues under compressions (e.g., cartilage) and minerals are associated with increased stiffness, it is hypothesized that removal of proteoglycan will reduce tendon enthesis toughness, while removal of mineral will reduce tendon enthesis strength.

5.2 Methods

5.2.1 Sample Preparation and Study Workflow

All procedures were performed in this chapter were approved by the Institutional Animal Care and Use Committee (Columbia University). Supraspinatus tendon-to-bone attachment units (humerus-supraspinatus tendon-supraspinatus muscle) were harvested from a total of 34 male adult C57BL6/J mice (n=10-12/group; 12> weeks). After dissection, samples were fresh-frozen in PBS and stored at -20°C .

To determine the roles of mineral and proteoglycan composition on enthesis mechanics, these

components were chemically removed *ex vivo* prior to characterization (n=3-5/group) or mechanical testing (n=10-12/group). Characterization consisted of chemical treatment to remove mineral or proteoglycan followed by contrast enhanced microCT imaging (Skyscan 1272, Bruker) or light microscopy (ZEISS Microscope). For mechanical characterization, samples were chemically treated to remove mineral or proteoglycan, scanned using conventional microCT, and then mechanically tested. After mechanical testing, samples were secured at terminal displacements and submerged in a 5% mercury chloride (HgCl₂, Sigma-Aldrich) for 24 hours and scanned again with microCT.

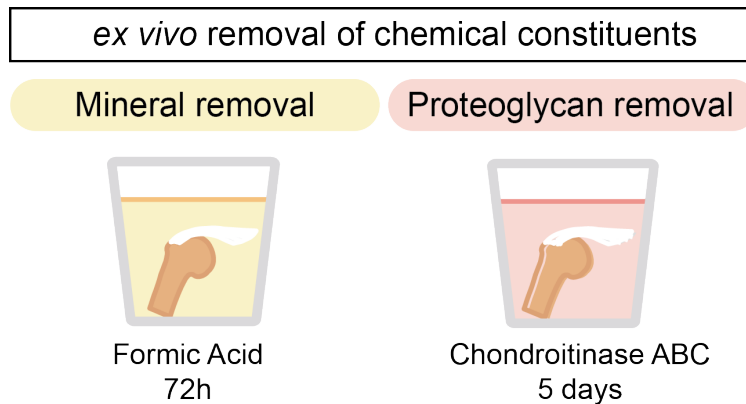


Figure 5.1: To assess compositional contributions to tendon enthesis strength and toughness, mineral or proteoglycans were chemically removed *ex vivo*. Samples were immersed in decalcifying agent to completely remove mineral (left) or in chondroitinase ABC for 5 days to remove proteoglycans (right).

5.2.2 *Ex vivo* removal of chemical constituents of the tendon enthesis

Mineral was chemically removed from the tendon enthesis by incubating in 5mL formic acid (Immunocal, StatLab) for 72 hours (**Figure 6.1, left**). Samples were washed in 1xPBS solution 3 times for 30 minutes before subjecting them to microCT imaging to confirm that all the mineral was removed.

Proteoglycans were removed from the tendon enthesis samples by chemically digesting glycosaminoglycans (GAGs) using chondroitinase ABC (ChABC). This treatment protocol (**Figure 6.1, right**) has been shown to degrade GAG chains in tendon [42]. After conducting a series of concentration- and time-dependent tests, we determined that 0.5 U/mL was an optimum concen-

tration for ChABC for digesting GAGs from the tendon enthesis samples. In this protocol, whole samples (humerus-supraspinatus tendon-supraspinatus muscle units) were incubated for 5 days in 2mL of 0.5 U/mL chABC buffered solution (the buffer solution consisted of 50 mM Tris, 60 mM sodium acetate, 0.02% bovine serum albumin). After 5 days, digested samples were washed in 1xPBS solution 3 times for 30 minutes before subjecting them to microCT imaging and quasi-static mechanical testing. To evaluate the efficiency of ChABC treatment, we performed histological analysis on a subset of samples. These samples (n=2) were fixed in 4% paraformaldehyde for 24 hours, decalcified in formic acid (StatLab, Immunocal), dehydrated in 70% ethanol, and embedded in paraffin. 5 μ m thickness paraffin sections were stained with Alcian blue using manufacturers protocol (Alcian Blue Stain Kit, Abcam) and imaged via bright field microscopy with 10 \times and 40 \times objectives (automated ZEISS Microscope, analyzed with ZEN lite software, ZEISS).

5.2.3 Contrast Enhanced and Conventional Micro-computed tomography (microCT) Imaging

The same preparations and scan settings were used to visualize enthesis samples with both conventional and contrast enhanced microCT. To prepare for scanning, the distal end of the supraspinatus-humerus unit was embedding in 2% agarose (Sigma-Aldrich) and mounted in the scanning chamber of the microCT machine (Skyscan 1272, Bruker), so that tendon enthesis specimens were hung loosely and in line with the scanning axis. Scans were performed with 60kVp, 166uA, and Al 0.5mm filters with isometric resolution of 5.0 μ m for pre-mechanical testing scan, and 2.5 μ m for post-mechanical testing scans. The acquired microCT data were reconstructed with the software (nRecon, Bruker) using alignment optimization and beam-hardening correction. The reconstructed image data was visualized with the native scanner software (DataViewer and CTvox, Bruker).

Contrast enhancement was achieved by staining samples with 5% mercury chloride solution prior to scanning with microCT. A 5% mercury chloride solution was prepared fresh for each experiment by dissolving Mercury (II) chloride (HgCl₂, Sigma-Aldrich) in distilled and de-ionized water (MilliQ water, MilliporeSigma) at room temperature until the saturation was achieved. Tendon enthesis samples, either intact or post-mechanical testing, were submerged in this solution for

24 hours and washed three times in distilled and de-ionized water for 10 minutes each before they were imaged with microCTs. Failure properties were characterized using methodologies initially described in **Chapter 2**.

5.2.4 Mechanical Testing

After conventional microCT scanning, the dissected samples (i.e., humerus and supraspinatus tendon) were mechanically tested by performing quasi-static uniaxial tension tests to failure using a table-top tensile material testing frame (Electroforce 3230, TA Instruments) fitted with a 10 lb. load cell (TA instruments). All samples were mechanically tested in a saline bath at 25°C to prevent thermal collagen denaturation. Tendon enthesis samples were prepared by removing the supraspinatus muscle from its tendon. Samples were placed into custom 3D-printed fixtures [135] and supraspinatus tendon were secured between two layers of thin paper (Kimwipe) with a drop of cyanoacrylate adhesive (Loctite, Ultra Gel Control) before mounting onto custom grips. Samples were secured in fixtures and tested in an orientation corresponding to 90° shoulder abduction. Samples were preconditioned by applying 0.05 N initial load (i.e., pre-load), then sinusoidally loaded from 0.2% strain to 5% strain for 5 cycles at 0.2%/s, rested for 300 seconds. Samples were then loaded at 0.2% strain/s to failure. Enthesis structural properties, such as failure load (referred to as strength in text), stiffness, and work to failure (area under the curve through failure load, referred to as toughness in text) were determined from load-deformation curves. Stiffness was calculated using a MATLAB (Matlab2019a, MathWorks) custom algorithm that identifies the best fitting line within a sufficient bin width (i.e., remove data below 10% of max load and above 95% of max load) by implementing the random sample correlation (RANSAC) technique [52].

5.2.5 Statistical Analysis

Tendon enthesis microCT and biomechanical results were compared between treatment groups using ANOVAs and specific differences from control conditions were determined using Dunnett's multiple comparisons test. $P < 0.05$ was considered significant. All statistical analyses were per-

formed using Prism 9 (GraphPad). All data shown as mean \pm standard deviation.

5.3 Results

5.3.1 Removal of Extracellular Matrix Components

Contrast enhanced microCT imaging showed that the demineralization treatment completely removed the mineral from the tendon enthesis and the humeral head bone, as the attenuation coefficient for mineralized and unmineralized collagen matched (**Figure 5.2A**). Histological sections of tendon enthesis samples subjected to chondroitinase ABC treatment stained with Alcian blue showed less proteoglycan content than that of control samples. Specifically, chondroitinase ABC treatment removed proteoglycan components from the unmineralized portion of the enthesis (changes in staining outlined by orange dashed ellipsoid, **Figure 5.2B**), although only slightly reducing proteoglycan content in the mineralized fibrocartilage. Based on the qualitative assessment of contrast enhanced microCT imaging and histology, collagen density and collagen organization remained unchanged for samples after treatments.

The quasi-static mechanical testing results of tendon enthesis samples after removal of biochemical constituents are shown in **Figure 5.3**. Complete removal of mineral decreased strength and stiffness ($p < 0.0001$), but also decreased toughness ($p < 0.0001$). Removal of proteoglycan contributed to slight decreases in the tendon enthesis failure load and stiffness ($p < 0.05$), yet did not change toughness. Of note, strength (failure force) vs. displacement behavior of ChABC treated sample showed decreases in toe-region strains (i.e., samples reach linear region earlier than that of control samples) and a notch in load-displacement curve at around 2.5N.

Removal of mineral or proteoglycan did not significantly alter failure modes under monotonic loading (**Figure 5.4A,B**). Tendon enthesis samples failed primarily via bone avulsion, with 20% (2/10 samples) of samples in the proteoglycan depletion group failing at the edge of unmineralized fibrocartilage (i.e., at the insertion). There were no significant differences in failure (avulsed) area due to removal of proteoglycans (**Figure 5.4C**). It is important to note that current methodologies of determining enthesis failure area require large difference in X-ray attenuation between min-

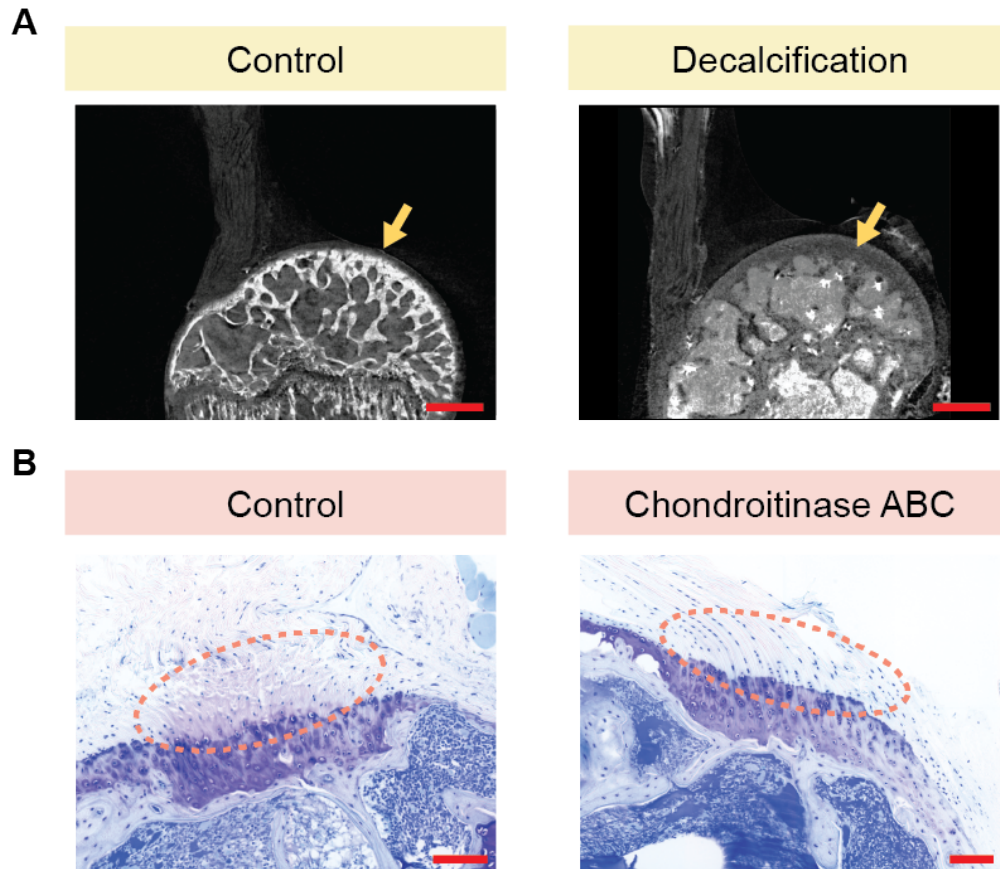


Figure 5.2: Both protocols were effective in removing constituents of the tendon enthesis. **(A)** Contrast enhanced microCT imaging showed that demineralization treatment completely removed the mineral from the tendon enthesis and the humeral head bone. Scale is 500 μm . Yellow arrows indicate changes in the coefficient of attenuation due to the mineral loss in the sample. **(B)** Alcian blue staining of the tendon enthesis showed that chondroitinase ABC treatment removed proteoglycan components from the unmineralized portion of the enthesis (change in staining outlined by orange dashed ellipsoid). Scale is 100 μm .

eralized tissue (i.e., bone plug) and unmineralized tissue (i.e., tendon enthesis fibers and avulsion crater). With the demineralization of the tendon enthesis, contrast enhanced imaging of failed sample did not produce high contrasted image between bone plug and that of tendon enthesis fibers, preventing the accurate determination of failure area (**Figure 5.2A**). While it was possible to determine that demineralized samples failed via avulsion by noting the presence of bone marrow cavity at the failure site (**Figure 5.4A**), it was not possible to determine their failure areas.

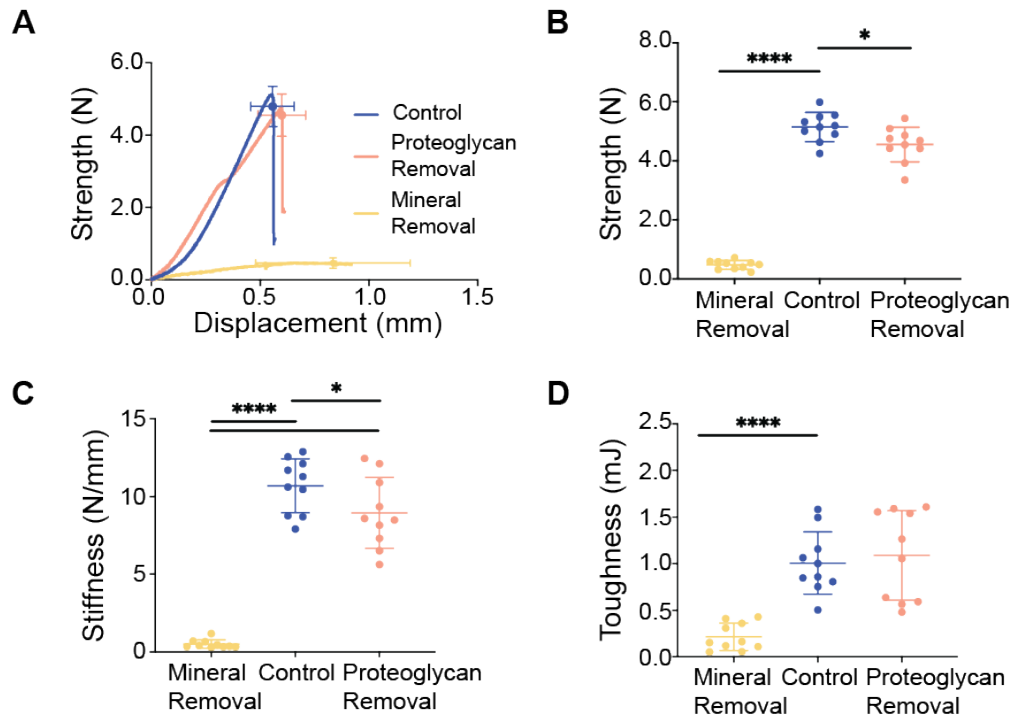


Figure 5.3: Tendon enthesis strength is dependent on mineral composition. (A) Strength (failure force) vs. displacement behavior. The mean failure strength (force) and failure displacement are represented by dots and cross-heads represents standard deviations. (B) Removal of mineral led to a dramatic decrease in strength; removal of proteoglycan led to a relatively small decrease in strength. (C) Removal of mineral or proteoglycan led to significant decreases changes in stiffness. (D) Removal of mineral led to a significant decrease in toughness; removal of proteoglycan did not affect enthesis toughness. (* $p < 0.05$, **** $p < 0.0001$, ANOVA followed by the Dunnett's multiple comparison test)

5.4 Discussion

The functionally graded composition of the tendon enthesis, initially introduced in **Chapter 1**, suggests an intricate balance in stiffening and toughening constituents to allow for load transfer between tendon and bone. Indeed, thinning of collagen fibers at the enthesis, as shown in **Chapter 2**, and loading-dependent energy absorption at the enthesis, as shown in (**Chapter 3**), imply critical roles for the main components of the enthesis, mineral and proteoglycan. The current chapter examined the biomechanical effects of chemically removing each of these constituents on the tendon enthesis. The results showed that tendon enthesis composition, particularly the mineral content, drives enthesis strength and stiffness, yet does not significantly affect its failure mode.

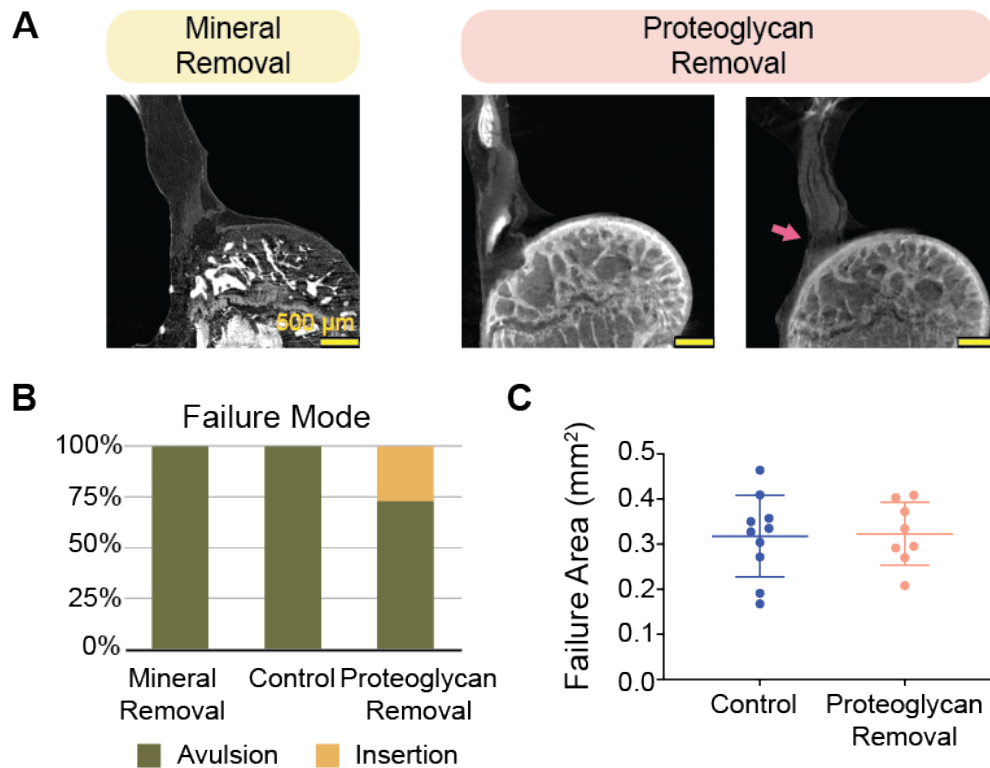


Figure 5.4: Loss of mineral or proteoglycan did not significantly alter the failure modes of the tendon enthesis. (A) Post-failure contrast enhanced microCT scanning showed that most samples failed via bone avulsion, while a small number of samples depleted in proteoglycans failed at the edge of unmineralized fibrocartilage (pink arrow). Scale is 500 μm . (B) Failure mode distributions. (C) There were no significant differences in failure (avulsed) area due to removal of proteoglycans. Note that the failure area for demineralized enthesis samples was not obtainable with current methodologies.

Submerging tendon enthesis samples in formic acid for 3 days successfully removed all the mineral content from tendon enthesis and its bony base (i.e., humeral head), while preserving overall fibrous morphology and organization at the enthesis. As hypothesized, removal of mineral decreased strength, stiffness, and toughness of tendon enthesis significantly. The force deformation curve shows distinct post-yield behavior, as if the fibers were peeling from each other. The post-failure contrast enhanced imaging revealed that enthesis without mineral still failed at the interface between mineralized fibrocartilage and bone (MF-B), and not at the site where thinning of the fibers is observed and predicted to have high stress concentrations [74, 67]. The failure mode and failure site observed may be due to the sharp change in collagen fiber alignment between the mineralized fibrocartilage and underlying bone, as seen from polarized microscopy images in

Chapter 2 (Figure 2.4, bottom). Fibrochondrocytes within the enthesis mineralized fibrocartilage deposit mineral parallel to the direction of tendon enthesis fibrils, resulting in a matrix consisting of highly aligned collagen fibrils parallel to the direction of muscle force along the tendon [56, 84, 73]. On the other hand, osteoblasts in the bone tissue deposit mineral in the direction of loading and perpendicular to the direction of its collagen fibrils [58]. This results in a cortical shell with collagen fibrils deposited parallel to the surface, almost perpendicular to insertion interface and, hence, perpendicular to the primary collagen fiber orientation characterized at the tendon enthesis. It is possible that this severe mismatch in collagen fiber alignment causes stress concentrations. The results from de-mineralization experiments support the notion that the fibrous tendon enthesis has the potential to store significant amounts of energy, and that a spatial gradient in the mineral stiffens and strengthens the interface after reaching a percolation threshold [54, 85, 86].

Enzymatic treatment with ChABC for 5 days depleted a large portion of glycosaminoglycans (GAGs) from the tendon enthesis. Qualitative histological evaluations revealed that efficient proteoglycan degradation was achieved at the non-mineralized portion of the enthesis, while GAGs still remained at the mineralized portion of the enthesis. Contrary to the hypothesis, removal of proteoglycans did not change toughness, although decreases in strength and stiffness were observed. Previous studies looking at the mechanical effect of GAGs on connective tissues have not shown consistent results. Proteoglycan-depleted human medial collateral ligaments (MCLs) [204, 207], supraspinatus tendons [42], and rat tail tendons [208, 209] did not exhibit altered mechanical responses (i.e., strengths and stiffness) when pulled in tension. Other studies using mouse Achilles tendons showed unchanged stiffness after proteoglycan depletion, yet with inferior collagen fiber realignment during loading [87, 210]. While enthesis fiber reorganization during loading was not evaluated in this chapter, the mechanism described above may also be present at the mice tendon enthesis evaluated here, as strength-deformation curves showed decreased toe-region strains. The mechanical responses of proteoglycan-depleted tendon entheses in this chapter, however, are in agreement with prior findings at the scale of collagen fibrils [211]. Andriotis and colleagues showed nano-scale stiffening of collagen fibers and reduced strength in

response proteoglycan depletion induced osmotic pressure, with higher pressure reducing the distance between tropocollagen molecules and resulting in an increase of the potential well depth and a decrease in the equilibrium intermolecular distance, ultimately requiring higher forces to separate the molecules upon tensile loading [211]. It is possible that proteoglycans at the tendon enthesis form proteoglycan-collagen networks capable of absorbing deformation energy [212, 213], or the sheer size of proteoglycan molecules may allow tendon entheses to absorb energy by resisting fiber reorientations during loading [87]. Nevertheless, with no significant differences observed in its failure mode (apart from 2 samples that failed at the insertion), the bio-compositional effect of proteoglycans on tendon enthesis load transfer and injury preventative mechanisms remain elusive.

It is well-known that the biomolecular composition of natural materials, including bone, tendon, and enthesis, adapt in response to their physiologic loads [214, 215, 64]. A major limitation in the demineralization experiments described this chapter is that the tendon enthesis was chemically altered in a non-physiologic, aggressive way. To address this limitation, physiologically relevant adaptations to the tendon enthesis architecture and biomolecular composition will be discussed in next chapter (**Chapter 1**). A second limitation of the experimental techniques employed in this chapter is that depletion of proteoglycan under the protocol used here resulted only in removal of proteoglycan from the unmineralized portion of the enthesis. Therefore, any possible proteoglycan-mineral interactions are yet to be elucidated. A third limitation is that the depletion protocols were not rigorously controlled. Mineral was either entirely removed or left in place. Proteoglycans were either completely digested in one portion of the enthesis or left completely intact in the adjacent portion of the enthesis. Ideally, controllable and sequential digestions of biomolecular components would be implemented to further evaluate the structure-function relationships between each component and enthesis mechanics. A final limitation lies in the choice of the mechanical test used in the current study. It is possible that proteoglycans do not play a significant role for toughness under tensile loading. Indeed, it has been shown that proteoglycan content plays a role in connective soft-tissues viscoelastic behavior (9, 30). Additional mechanical testing protocols, such as cyclical loading, stress-relaxation, or creep, may provide further insights

into how the biomolecular compositional features of the tendon enthesis give rise to its toughness.

5.5 Conclusion

Chemical digestion of mineral and proteoglycans from tendon entheses demonstrated that tendon enthesis mineral content drives its strength, stiffness, and toughness. The role of proteoglycan content on tendon enthesis mechanics, on the other hand, remains unclear, as the only partial digestion was achieved at the enthesis, and loss of proteoglycan did not lead to decrease in toughness.

Chapter 6: The tendon enthesis actively adapts its architecture *in vivo* in response to loading by controlling its mineral composition and microarchitecture

Portions of this chapter are currently under review: Golman M, Abraham AC, Kurtaliaj I, Marshall BP, Hu YJ, Schwartz AG, Guo XE, Birman V, Thurner PJ, Genin GM, Thomopoulos S. Toughening mechanisms for the attachment of architected materials: The mechanics of the tendon enthesis.

6.1 Introduction

It is well known that musculoskeletal tissues are highly responsive to *in vivo* loading, maintaining a homeostasis of tissue architecture and composition to support physiologic loads. Despite progress in understanding how the tendon enthesis achieves a strong attachment under sub-damage loading regimes, it remains unclear how toughness arises and is adapted with loading to prevent interfacial failure. **Chapter 3** uncovered that load-dependent energy absorption at the tendon enthesis was due to its fiber-level and molecular-level toughening mechanisms. **Chapter 4** revealed that the fibrous architecture of the enthesis is designed to maximize toughness in a direction-dependent manner, with enthesis fibers reorientation, recruitment, and subsequently rupture across a wide range of motion. **Chapter 5** confirmed that the nano-scale mineral composition of the tendon enthesis dictates its strength. Indeed, the experiments and models described in the previous chapters demonstrated how the tendon enthesis achieves a remarkable balance between toughness and strength through its fibrous architecture and biomolecular composition to resist injurious loads. Nonetheless, even if no apparent macroscale damage is detected, aberrant *in vivo* joint loadings, sub-failure injury, or degeneration of joint tissues (muscles, tendons, the enthesis, and bone) cause

compositional and architectural changes that lead to adverse mechanical behavior of the attachment unit. Investigating how aberrant joint loadings affect these architectural and compositional features of the tendon enthesis may provide guidelines to predict the risk and extent of failure at the enthesis, and further facilitate rehabilitation strategies and improved design of surgical and tissue engineered solutions for tendon-to-bone repair.

The remodeling of tissue composition and architecture in response to loading was described for trabecular bone by Julius Wolff in 1892 and has been exhaustively studied for that tissue [214, 216, 215]. Loss of mechanical load due to disuse, paralysis, or microgravity results in rapid resorption and loss of bone mass, leading to decreased bone mechanical properties and functional deficits [217, 218, 219, 220]. Similarly, overloading can lead to trabecular and bone damage and adaptations that result in decreased bone mechanical properties and increased risk of fracture [221, 222, 223]. *In vivo* non-invasive axial loading of mouse long bones showed that, depending on loading parameters (e.g. peak force, strain, or frequency) the biologic response can be either anabolic (i.e., formation of lamellar bone) or injurious (i.e., formation of woven bone or resulting in stress fractures) [216, 224, 225, 226, 227]. A growing literature also shows that unloading and overloading can significantly affect tendons [228, 229]. Some studies reported that unloading decreases collagen production leading to decreased tendon stiffness and changes in viscoelastic responses [230, 231], whereas others reported the opposite effects [232, 233]. Tendon overloading can lead to altered matrix organization, collagen fiber morphology, cell shape, and increased inflammation [234, 235, 236, 237].

The sensitivity of the enthesis to its mechanical environment is consistent with the responses reported for bone and tendon. Previous work established that muscle loading is necessary for the fetal and postnatal development of a functional tendon enthesis [84, 238]. Moreover, unloading for extended periods of time was detrimental to healing of tendon to bone at the rotator cuff enthesis [239, 240]. More recently, it was shown that that the adult tendon enthesis is sensitive to its loading environment, with dramatic changes in structure, composition, and mechanics of the enthesis after paralysis [64]. However, there remains a gap in knowledge on how enthesis composition

and architecture are modulated to maintain toughness at the enthesis under varied *in vivo* loading environments.

In this chapter, we examine the tendon enthesis mechanoresponsiveness to pathologic levels of over- and under-loading *in vivo* by varying the loading environment of mouse shoulders via botulinum toxin A-induced underuse/paralysis or treadmill-induced overuse. It is hypothesized that the enthesis is sensitive to its *in vivo* loading environment and will adapt its architecture and composition to maintain toughness.

6.2 Methods

6.2.1 Sample preparation and study workflow

All procedures were performed in this chapter were approved by the Institutional Animal Care and Use Committee (Columbia University). Supraspinatus tendon-to-bone attachment units (humerus-supraspinatus tendon-supraspinatus muscle) were harvested from a total of 34 male adult C57BL6/J mice (n=10-12/group; 12 > weeks). Two groups of mice were first subjected to *in vivo* degeneration models (**Figure 6.1**). After the completion of the *in vivo* protocol, tendon entheses were dissected, fresh-frozen in PBS, and stored at -20°C . At the time of testing, *in vivo* degenerated entheses were first scanned by conventional microCT and then mechanically tested. After mechanical testing, samples were secured at terminal displacements and submerged in a 5% mercury chloride (HgCl_2 , Sigma-Aldrich) for 24 hours and scanned again with microCT.

6.2.2 *In vivo* degeneration models

10-week old C57BL6/J mice (n=10/group, Jackson Laboratories) were subjected to two *in vivo* loading models, where the supraspinatus muscle activity was modulated to modify supraspinatus tendon enthesis loading environment (**Figure 6.1**). (1) Underuse-degeneration (underuse) was induced via muscle paralysis by bilaterally injecting 0.2 U (0.1U/10 μl per 100 g of body weight) of botulinum toxin (BtxA, Allergan) into the supraspinatus muscle, resulting in temporary muscle paralysis [64]. After injections, mice were allowed to free cage activity for 4 weeks. (2) Overuse-

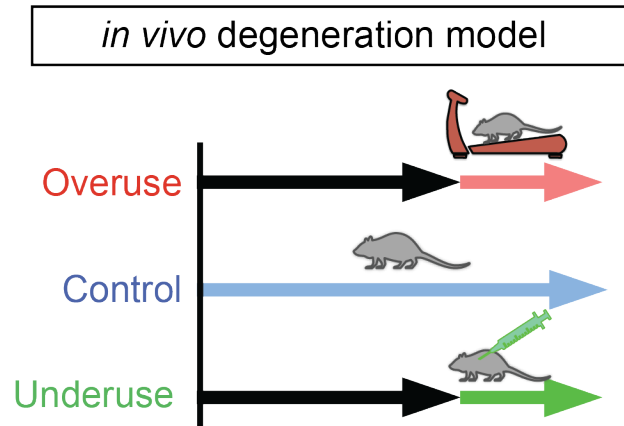


Figure 6.1: To enable physiologically relevant control of compositional changes, we subjected tendon entheses to pathological loading conditions using *in vivo* murine rotator cuff tendinopathy models. 10-week-old mice were subjected to two degeneration models: underuse degeneration was induced via muscle paralysis by injecting botulinum toxin (BtxA) and overuse degeneration was achieved through downhill treadmill running for 4 weeks.

degeneration (overuse) was achieved using downhill treadmill running (overuse) with an initial rate of 17 cm/s for 10 minutes followed by 25 cm/s for 40 min each day at a decline of 15 degrees, 5 days a week, for 4 weeks [129]. To acclimate the mice to treadmill exercises, 1 week prior to the overuse protocol, mice underwent training: exercising for each day for 10 minutes at 17 cm/s for 5 days followed by 2 days of rest. For both *in vivo* models, after 4 weeks since the protocol initiation, mice were euthanized and their supraspinatus tendon entheses were harvested, soaked in PBS, and stored at -20°C. All procedures were performed bilaterally, and results were compared to age-matched cage activity control animals.

6.2.3 Contrast enhanced and conventional micro-computed tomography (microCT) imaging

The same preparations and scan settings were used to visualize entheses samples with both conventional and contrast enhanced microCT. To prepare for scanning, distal end of supraspinatus-humerus unit were embedding in 2% agarose (Sigma-Aldrich) and mounted in the scanning chamber of the microCT machine (Skyscan 1272, Bruker), so that tendon entheses specimens were hung loosely and in line with the scanning axis. Scans were performed with 60kVp, 166uA, and Al 0.5mm filters with isometric resolution of 5.0 μm for pre-mechanical testing scan, and 2.5 μm for

post-mechanical testing scans. The acquired microCT data were reconstructed with the software (nRecon, Bruker) using alignment optimization and beam-hardening correction. The reconstructed image data was visualized with built-in program (DataViewer and CTvox, Bruker).

The contrast enhancement was achieved by staining samples with 5% mercury chloride solution prior to scanning with microCT. A 5% mercury chloride solution was prepared fresh for each experiment day by dissolving Mercury (II) chloride (HgCl_2 , Sigma-Aldrich) in distilled and de-ionized water (MilliQ water, MilliporeSigma) at room temperature until the saturation was achieved. Tendon enthesis samples, either intact or post-mechanical testing, were submerged in this solution for 24 hours and washed three times in distilled and de-ionized water for 10 minutes each before they were imaged with microCTxs.

6.2.4 Bone morphometry and individual trabecula segmentation (ITS) analysis

Bone morphometry, and mineral density of the humeral head, as well as parameters obtained from Individual Trabecula Segmentation (ITS) analysis were determined using pre-mechanical testing micrCT scans of tendon enthesis. Reconstructed images were first contoured by an experienced user to only include humeral head proximal to the growth plate as the region of interest (ROI). The ROI were then evaluated using a segmentation algorithm that separates cortical and trabecular bone (CTAn, Bruker). Parameters examined included: cortical tissue mineral density (Cortical TMD), cortical thickness (Cr.Th), trabecular bone mineral density (Trabecular BMD), trabecular bone volume fraction (BV/TV), trabecular thickness (Tb.Th), trabecular spacing (Tb.Sp), and trabecular number (Tb.N).

Segmented trabecular images were subjected to subsequent micro-architectural ITS analysis, where trabecular microstructures were decomposed to individual rod-and-plate based trabecular parameters [241]. In short, the thresholded trabecular bone images were reduced to topology-preserved structural skeletons using digital topological analysis-based skeletonization technique. Each skeletal voxel was then recovered to original topology using an iterative reconstruction method, while classifying whether the resulting trabecular structure belong to either a trabecu-

lar plate (surface) or a trabecular rod (curve) using digital topological classification methodology. Trabecular network and morphology parameters, such as plate-to-rod ratio (PR ratio), rod and plate bone volume fraction (rBV/TV and pBV/TV), number density (rTb.N and pTb.N), thickness (rTb.Th and pTb.Th), average plate trabecular surface (pTb.S), and rod trabecular length (rTb.L) were then evaluated from resultant three-dimensional rod-and-plate classified trabecular morphology (see **Table 6.1**). The angular orientational analysis was also performed by evaluating each rod-and-plate angle with respect to perpendicular to the loading axis corresponding to 90 degrees abduction (i.e., relative to the dominant fiber insertion direction in the supraspinatus tendon). The average angular distribution for each sample was normalized by the total trabecular volume within each sample's humeral head.

6.2.5 Determining tendon cross-sectional area (TCSA), mineralized fibrocartilage (MFC) area, and failure area

The minimum tendon cross-sectional area (TCSA) and mineralized fibrocartilage (MFC) area for each sample was determined from conventional microCT scans that were performed on samples prior to mechanical testing and analyzed via built-in image processing algorithms (CTAn, Bruker). The minimum TCSA was determined by thresholding the transverse slices through the tendon, calculating the area encompassing the tendon, and selecting the smallest area of a tendon that is within 500 μm from the tendon insertion site. For some scans, re-alignment was necessary, which was performed in three-dimensions by rotating the tendon primary fiber direction along a reference vertical axis using data visualization software (DataViewer, Bruker). MFC volume was determined by contouring, thresholding, and integrating all the areas of MFC from sagittal slices of humeral head. Since the absorption coefficients of the MFC was in between that of tendon and bone, and did not change significantly between samples, a single range of threshold values was selected to identify and estimate volume of the MFC.

Failure area was determined using HgCl_2 stained contrast enhanced microCT images of failed tendon enthesis samples. A custom semi-automated MATLAB (Matlab2019a, MathWorks) rou-

Table 6.1: Definition of ITS-Based Microarchitectural Parameters

Abbreviation	Full Name	Definition	Unit
PR ratio	Plate-to-rod ratio	The total volume of trabecular plates divided by the total volume of trabecular rods	-
pBV/TV	Plate bone volume fraction	The total volume of trabecular plates divided by the bulk volume	-
rBV/TV	Rod bone volume fraction	The total volume of trabecular rods divided by the bulk volume	-
pTb.N	Trabecular plate number density	The cubic root of the total number of trabecular plates divided by the bulk volume	$1/\mu\text{m}$
rTb.N	Trabecular rod number density	The cubic root of the total number of trabecular rods divided by the bulk volume	$1/\mu\text{m}$
pTb.Th	Mean trabecular plate thickness	The average thickness of trabecular plates	μm
rTb.Th	Mean trabecular rod thickness	The average thickness of trabecular rods	μm
pTb.S	Trabecular plate surface area	The average surface area of trabecular plates	mm^2
rTb.L	Trabecular rod length	The average length of trabecular rods	μm

tine that calculates the overlapping polyhedron surface meshes from two arbitrary volumes was used in quantifying failure area as the regions of interest were along the curved volume (i.e., bony avulsed piece(s)). For this analysis, the first region corresponded to bony avulsed fragment(s), which was obtained by thresholding and semi-automatically contouring via shrink-wrapping algorithm built-in to the manufacturers' imaging processing software (CTan, Bruker). The second region represented a volume that contained only the fractured surface of the avulsed piece, which was determined visually and manually contoured for appropriate slices for each region of interest. The output volume sets were triangularly meshed to determine the surface area between the overlapping volumes.

6.2.6 Mechanical testing

After conventional microCT scanning, the dissected samples (i.e., humerus and supraspinatus tendon) were mechanically tested by performing quasi-static uniaxial tension tests to failure using a table-top tensile tester (Electroforce 3230, TA Instruments) fitted with 10 lb. load cell (TA instruments). All samples were mechanically tested in a saline bath at 25°C to prevent thermal collagen denaturation. Tendon enthesis samples were prepared by removing the supraspinatus muscle from its tendon. Samples were placed into custom 3D-printed fixtures [135] and supraspinatus tendon were secured between two layers of thin paper (Kimwipe) with a drop of cyanoacrylate adhesive (Loctite, Ultra Gel Control) before mounting onto custom grips. Samples were secured in fixtures and tested in an orientation corresponding to 90° shoulder abduction. Samples were preconditioned by applying 0.05 N initial load (i.e., pre-load), then sinusoidally loaded from 0.2% strain to 5% strain for 5 cycles at 0.2%/s, rested for 300 seconds. Samples were then loaded at 0.2% strain/s to failure. Enthsis structural properties, such as failure load (referred to as strength in text), stiffness, and work to failure (area under the curve through failure load, referred to as toughness in text) were determined from load-deformation curves. Stiffness was calculated by a MATLAB (Matlab2019a, MathWorks) custom algorithm that identifies the best fitting line within a sufficient bin width (i.e., remove data below 10% of max load and above 95% of max load) by implementing the random sample correlation (RANSAC) technique [52].

6.2.7 Enthsis fracture model

To estimate the contribution of local bony architecture on the tendon enthesis failure behavior, we adapted previously published plate-in-bending model [64, 242], where loading at the tendon enthesis is modeled as a circular clamped plate loaded with uniform pressure (**Figure 6.2**). In this back-of-the-envelope model, the circular plate represents tendon enthesis and its mineralized base (i.e., mineralized fibrocartilage and cortical shell) that is clamped at the edges by load-bearing trabeculae (i.e., trabecular plates).

The mineralized bone plug is assumed to be thin relative to its radius, hence shear deformability

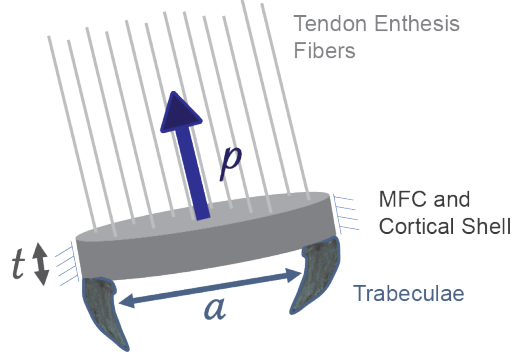


Figure 6.2: *The back-of-the-envelope estimation for tendon enthesis failure behaviour models loading of tendon-to-bone attachment as a circular clamped plate loaded with uniform pressure. In this model, a is distance between clamps (i.e., trabecular spacing), p is the applied pressure (i.e., force), and t is plate thickness (i.e., cortical thickness).*

is ignored. The maximum deflection of this plate-in-bending model can be expressed as

$$w_{max} = \frac{pa^4}{64D}, \quad (6.1)$$

where a is distance between clamps (i.e., trabecular spacing), p is the applied pressure (i.e., force), and D is the plate bending modulus that is proportional to elastic modulus, E , and plate thickness t (i.e., cortical thickness) to the 3rd power. In this model, we treat the tendon enthesis as being stretched to the point at which it will respond in a linear elastic fashion with no shear resistance, so that the stress drops with subsequent crack extension. The potential energy, PE , in the tendon enthesis associated with failure is

$$PE(a) = -\pi p \int_0^a w(r)r dr = -\frac{\pi a^6 p^2}{384D}. \quad (6.2)$$

Since avulsing over the area requires the energy, with the assumption that the process zone size is smaller compared with other dimensions, the internal energy is expressed as

$$U_{int}(a) = \pi a^2 \Gamma_{int}, \quad (6.3)$$

where Γ_{int} is the toughness of the interface that fractures. Failure mode characterization from

Chapter 2 showed healthy tendon enthesis fail at mineralized fibrocartilage and cortical shell interface (MF-B failure type) and at trabecular interface (B-T failure type) at relatively similar rate. By assuming that all the potential energy is converted to failing tendon enthesis, the fracture toughness of the tendon enthesis, Γ_{int} , will be expressed as

$$\Gamma_{int} = \frac{a^4 p^2}{384D}. \quad (6.4)$$

To investigate the contribution of trabecular spacing and mineralized base on enthesis strength and fracture toughness, we used above equation and conducted numerical experiment by varying each parameter by $\pm 50\%$.

6.2.8 Statistical analysis

Tendon enthesis characteristics, biomechanics results, failure properties, bone morphometry, and ITS analysis results were compared between treatment groups using ANOVAs and specific differences from control conditions were determined using Dunnett's multiple comparisons test. $P < 0.05$ was considered significant. Failure properties were correlated to bone morphometry outcomes using Pearson correlation. All statistical analyses were performed using Prism 9 (Graph-Pad). All data shown as mean \pm standard deviation and results from Pearson correlation were expressed using the color map.

6.3 Results

6.3.1 Mechanical and failure properties

Strength-displacement curves showed distinct mechanical responses for tendon enthesis samples under both degeneration conditions (**Figure 6.3**). Healthy and overuse-degenerated attachments failed catastrophically, showing little post-yield behavior, while underuse-degenerated attachments failed at lower forces and showed distinct post-yield behavior. Overuse decreased tendon cross-sectional area ($p < 0.01$), while underuse did not. Overuse degeneration did not change

the tendon enthesis strength, while increased enthesis stiffness ($p<0.01$) and decreased toughness ($p<0.05$). Underuse decreased strength ($p<0.01$), stiffness ($p<0.05$), and trended with decrease toughness ($p=0.075$) compared with that of control.

The failure properties of the tendon entheses subjected to pathologic loading are shown in **Figure 6.4**. The pathological tendon-to-bone attachment exhibited exclusively avulsion-type failures under monotonic uniaxial tensile testing. Failure area analysis showed that underuse loading led to 90% increase in avulsion area ($p<0.01$, **Figure 6.4B**). Pathological loading changed the tendon enthesis failure pattern. Avulsion fragment quantity increased in underuse degenerated samples, compared with that of overuse degenerated samples and that of control (**Figure 6.4C**). Furthermore, modified loading led to a shift in the fracture location: overuse led to more failures at the MF-B interface, while underuse led to more failures at the B-T interface (**Figure 6.4**).

6.3.2 Bone morphology and trabecular microarchitecture

Pathologic loading led to adaptations in fibrocartilage and bone architecture underlying the tendon enthesis (**Figure 6.5**). The mineralized fibrocartilage volume decreased significantly for overuse degenerated samples compared with that of control ($p<0.01$). Bone morphometric analysis of humeral head revealed that the overall ratio of bone volume to total volume (BV/TV) was significantly increased for overuse ($p<0.05$), while significantly decreased for underuse ($p<0.001$). Cortical bone was significantly affected by underuse. Cortical tissue mineral density (TMD, $p<0.0001$) and cortical thickness (Cr.Th, $p<0.0001$) was significantly lower for underuse samples compared with that of control. Both pathological loading conditions affected trabecular bone morphology. Trabecular bone mineral density (BMD) was significantly increased ($p<0.05$) for overuse, while significantly decreased ($p<0.0001$) for underuse compared with that of control. Trabecular thickness increased with overuse ($p<0.01$), while decreased with underuse ($p<0.01$). Trabecular number significantly decreased with underuse ($p<0.0001$). Trabecular spacing significantly increased with underuse ($p<0.001$).

Trabecular bone microarchitecture was successfully segmented into individual trabecular plates

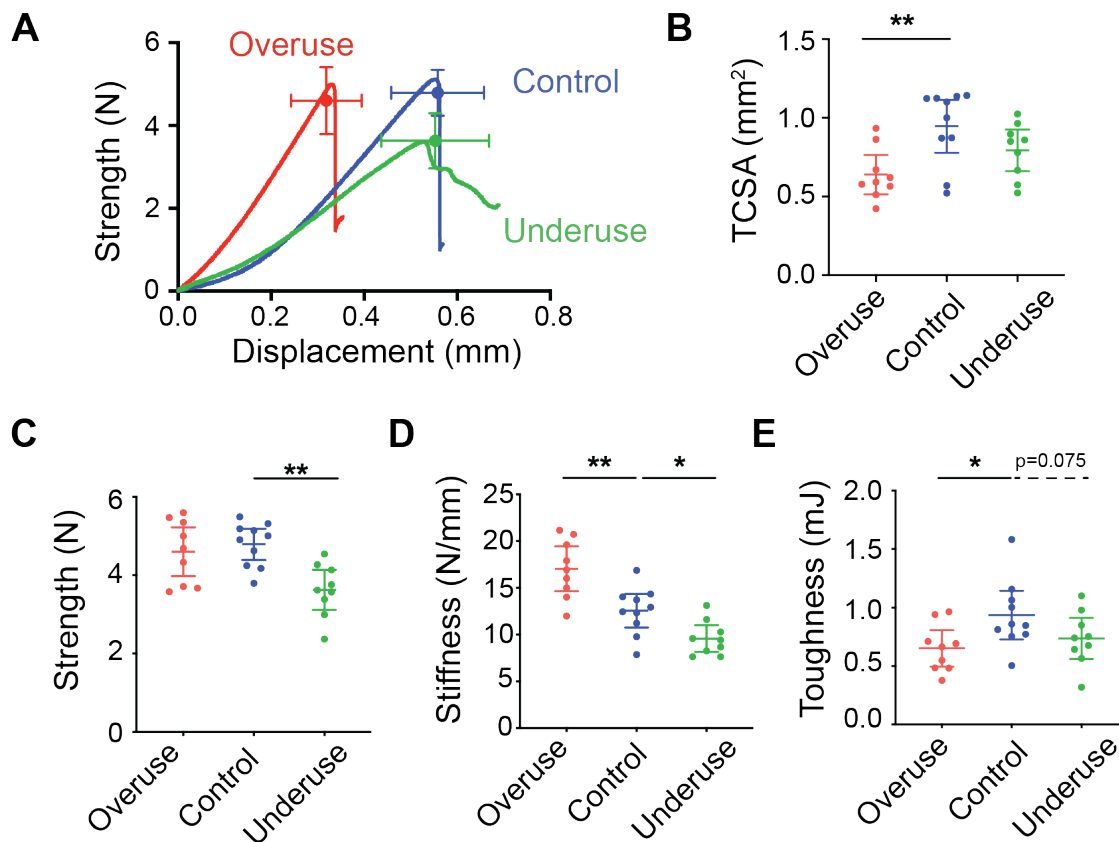


Figure 6.3: Tendon entheses optimized strength, while compromising toughness under pathologic loading *in vivo*. (A) Strength (failure force) - displacement curves showed that healthy and overuse -degenerated attachments failed catastrophically, showing little post-yield behavior, while underuse-degenerated attachments failed at lower forces and showed distinct post-yield behavior. (B) The tendon cross-sectional area (TCSA) of the supraspinatus tendon was significantly decreased due to treadmill running ($p < 0.001$). (C) Strength was decreased in the underuse-degenerated attachments ($p < 0.01$) (D) Stiffness was increased in the overuse-degenerated attachments ($p < 0.001$), while decreased for underuse-degenerated attachments ($p < 0.05$). (E) Both overuse and underuse loading conditions reduced toughness, with significant decrease in overuse ($p < 0.05$) and trend in underuse ($p = 0.075$) compared with that of control.

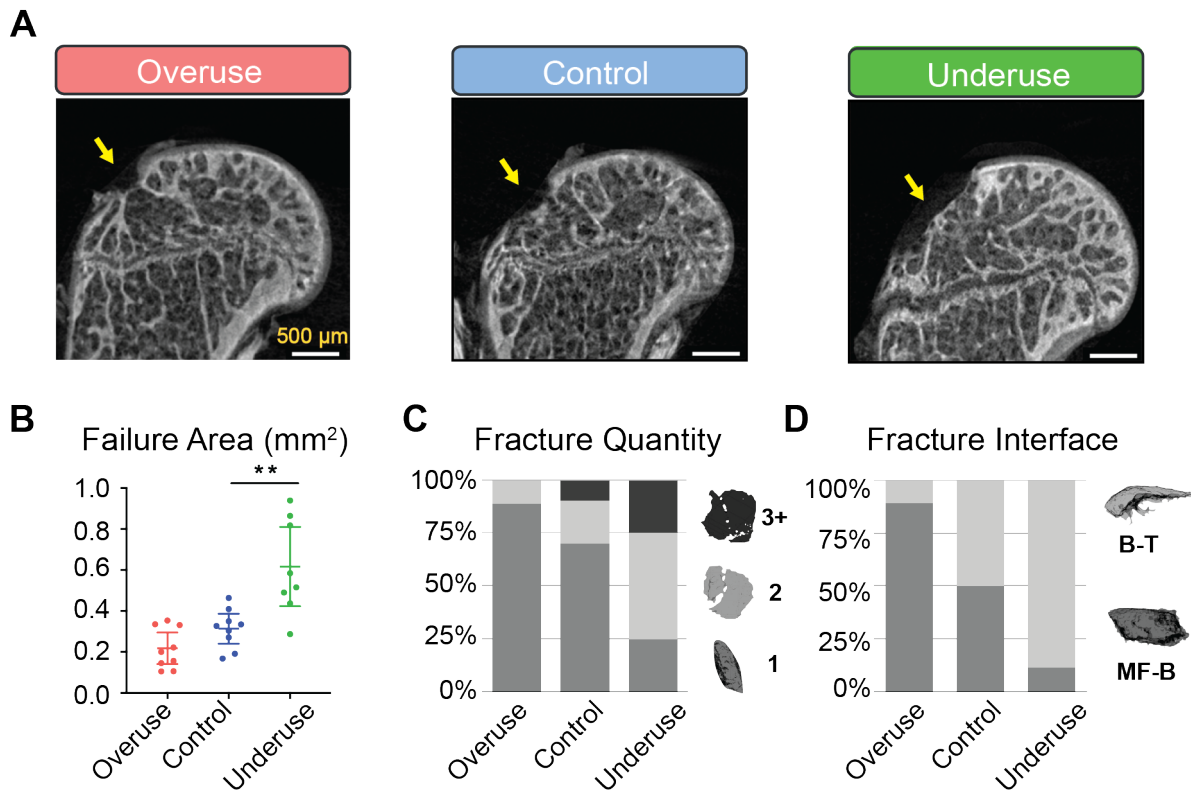


Figure 6.4: *Physiological in vivo degeneration models reduced the ability of the enthesis to protect against failure.* (A) Contrast enhanced microCT imaging showed that pathological tendon-to-bone attachment exhibited exclusively avulsion-type failures, similar to that of control. Yellow arrow represent failure site. Scale is 500 μm . (B) Fracture area and (C) fracture quantity increased for underuse group compared with the control cage activity group ($p < 0.01$). (D) Pathologic loading led to a shift in the fracture location: overuse led to more failures at the MF-B interface, while underuse led to more failures at the B-T interface.

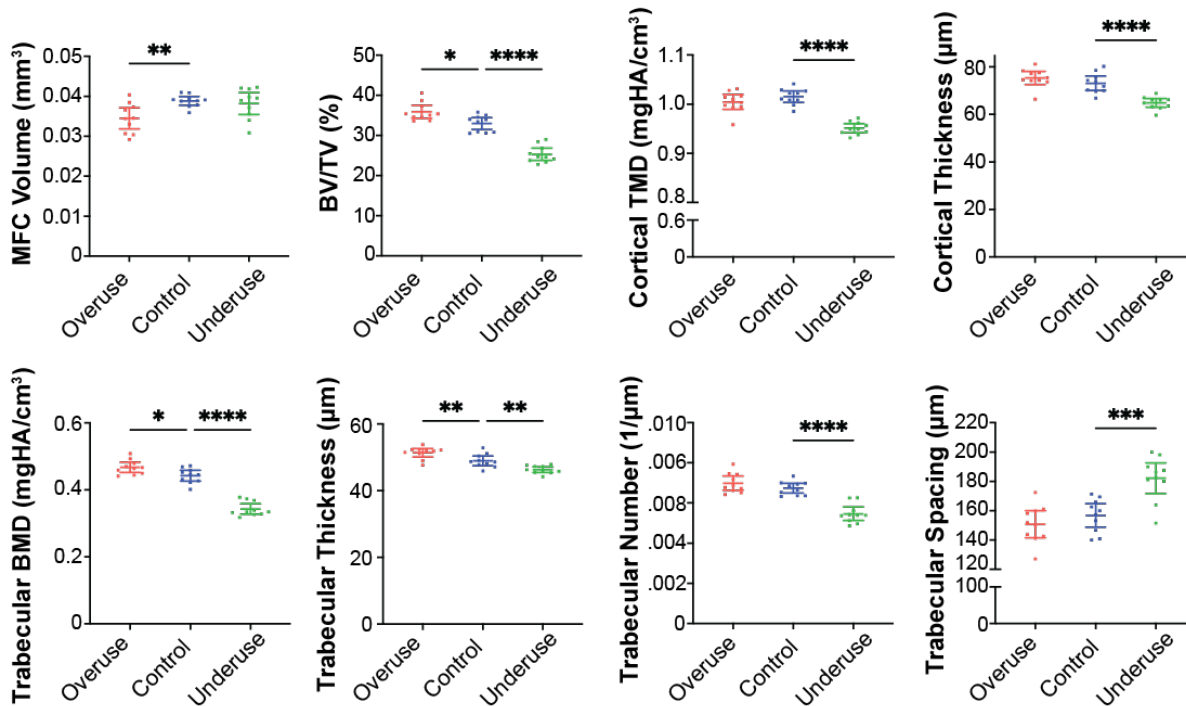


Figure 6.5: Pathologic loading led to adaptations in bone architecture underlying the tendon entheses. Bone morphometric analysis revealed that underuse led to loss of bone mineral density underlying the attachment (BMD and TMD, $p < 0.0001$), reduced cortical and trabecular thickness ($p < 0.0001$) and trabecular number ($p < 0.001$). Overuse led to gain of bone volume in the humeral head (BV/TV, $p < 0.05$), trabecular mineral density (BMD, $p < 0.05$) and increase in trabecular thickness ($p < 0.01$). Overuse also led to a decrease in mineralized fibrocartilage volume (MFC, $p < 0.01$).

and rods using individual trabecular segmentation (ITS) analysis. Results of ITS-based morphological analyses are shown in **Figure 6.6**. The plate-rod ratio was significantly lower for underuse samples compared with that of control. Trabecular plate bone volume fraction (pBV/TV) were 21.5% higher ($p < 0.0001$) for overuse, while 30.3% lower ($p < 0.0001$) for underuse compared to that of control. There were no significant differences in trabecular rod bone volume fraction (rBV/TV). Looking at trabecular plate morphology, trabecular plate number (pTb.N) was 16.1% lower ($p < 0.001$) for underuse compared to that of control. Overuse increased trabecular plate thickness (pTb.Th) as much as 29.6% compared with that of control ($p < 0.05$). Furthermore, overuse significantly increased plate surface area (pTb.S, $p < 0.01$). There were no significant changes for trabecular rod morphology, except for trabecular rod length, where overuse significantly increased rod lengths ($p < 0.05$) compared with that of control.

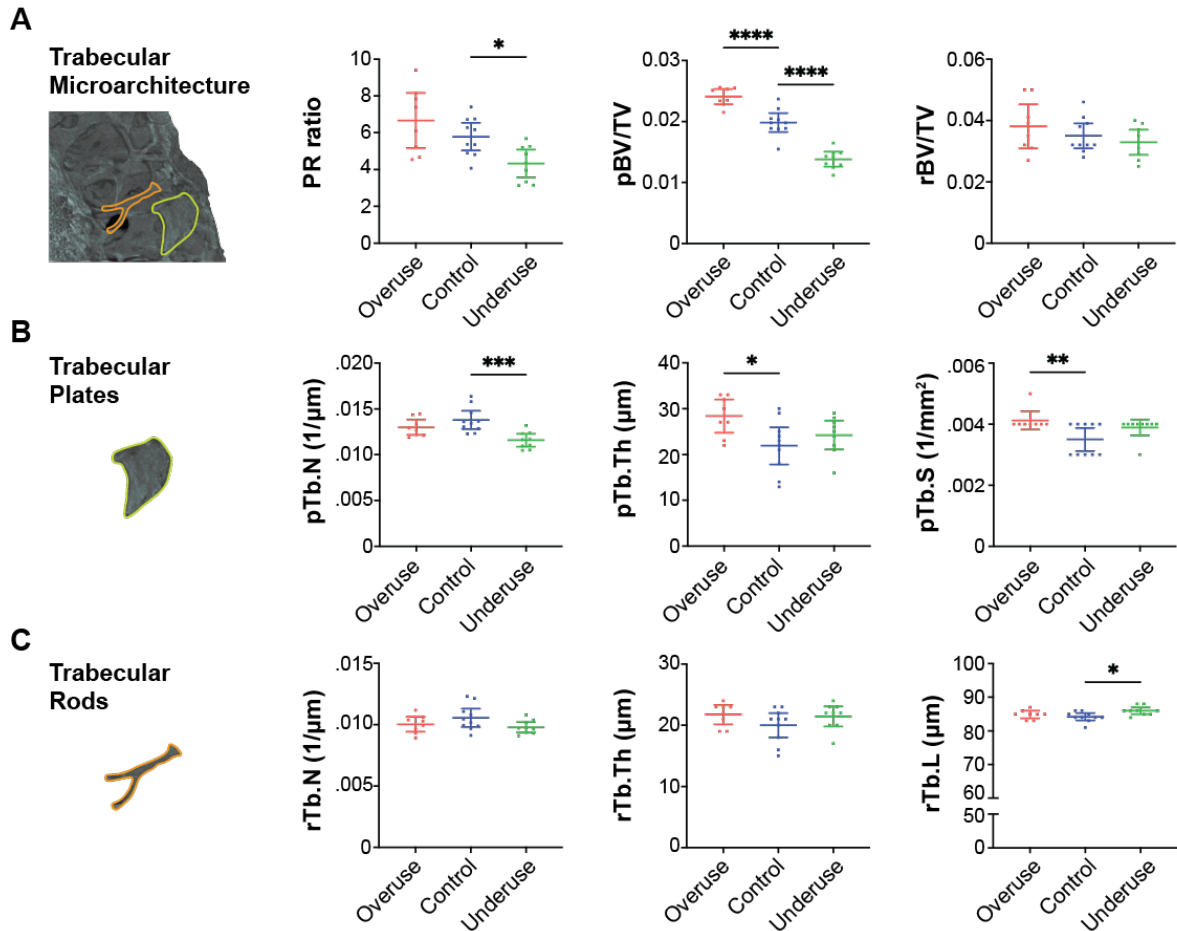


Figure 6.6: Mechanistic changes in failure modes were driven by local changes in trabecular microarchitecture underlying the enthesis. (A) Individual trabecula segmentation (ITS) analysis showed that the ratio between trabecular plates and trabecular rods significantly decreased due to underuse compared to control (PR ratio, $p < 0.05$). Trabecular plate volume (pBV/TV) significantly decreased due to underuse ($p < 0.0001$) and significantly increased due to overuse ($p < 0.0001$) compared to control. There were no significant differences between groups in trabecular rod volume (rBV/TV). (B) Trabecular plate analysis showed that the number of trabecular plates (pTb.N) significantly decreased due to underuse ($p < 0.0001$), while trabecular plate thickness (pTb.Th) and surface area (pTb.S) significantly increased due to overuse ($p < 0.05$). (C) Trabecular rod analysis showed that there were no differences in rod number (rTb.N) thickness (rTb.Th). However, the length of trabecular rods (rTb.L) significantly increased due to underuse compared to that of control ($p < 0.05$)

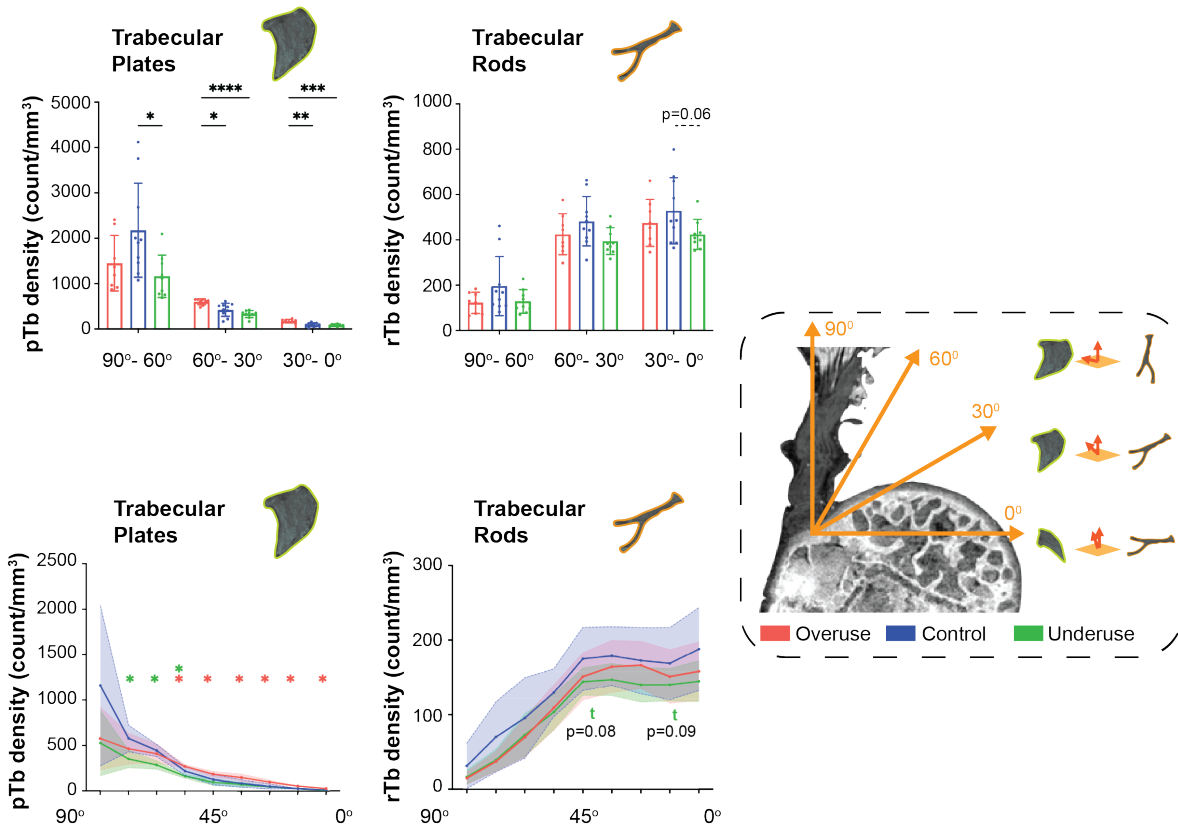


Figure 6.7: The orientation of load-bearing trabecular microarchitecture is actively remodeled to adapt to new loading directions. **(Top)** Coarse and **(bottom)** fine orientation distribution of trabecular rods and plates from ITS analyses. Compared to cage active controls, trabecular plate loss were uniform along all directions for samples from underuse loading conditions. On the other hand, trabecular plate density increased in 60°-30° and 30°-0° directions compared to that of control for overuse loaded samples. While there were some trends, there were no significant differences in trabecular rod architecture between groups. The angle was taken with the axis normal to the supraspinatus tendon insertion surface, with respect to principle loading direction, or in this case defined by angle of abduction. (* $p < 0.05$, ** $p < 0.01$, **** $p < 0.0001$, 2-way ANOVA followed by Dunnet's multiple comparison test; for fine orientation analysis: green star represent significance between undersue and control, while red star represent significance between overuse and cotrol, "t" represents trends)

Orientation analysis of trabecular rods-and-plates is shown in **Figure 6.7**. The trabecular network of healthy, cage-active control samples had the highest density of trabecular plates oriented at 90° - 60° relative to the dominant fiber direction in the supraspinatus tendon, and the lowest density of trabecular rods oriented in this range. Trabecular rods of healthy control samples were primarily aligned along the transverse direction (i.e., perpendicular axis to the dominant fiber direction). With overloading, trabecular plate density increased in 60° - 30° ($p < 0.05$) and 30° - 0° ($p < 0.01$) ranges, and there were no significant differences in changes in trabecular rod orientations compared with that of healthy control. With underuse, trabecular plate and rod loss occurred uniformly across all directions. Fine orientation analysis (**Figure 6.7**, bottom) showed that underuse significantly decreased the trabecular plate density in orientations corresponding to high angle of abductions (90° - 50°), while overuse significantly reinforced trabecular plates in orientations corresponding to mid-to-low angles of abductions (50° - 0°). Trabecular rods fine orientation profile revealed that both overuse and underuse followed the same profile up until 45° , where underuse showed even decreasing trends (**Figure 6.7**, bottom, denoted by "t" in green) from 45° - 0° .

6.3.3 Modeling enthesis fractures *in silico*

The back-of-the-envelope model of enthesis fracture predicted that the bony architecture underlying the enthesis is optimized to absorb energy before its failure. **Figure 6.8** shows that a 25% increase in normalized strength (p/p_o) contributed to as much as 60% increase in fracture energy (Γ/Γ_o) absorbed, while a 25% decrease in normalized strength led to approximately 40% decrease in fracture energy absorbed. The increase in load-bearing trabecular spacing (Tb.Sp), a/a_o , dramatically increased the fracture energy at the given failure strength. When considering the failure strength of the healthy enthesis ($p/p_o = 1$), a 20% increase in normalized Tb.Sp would lead to 107% increase in fracture energy absorbed, while a 20% decrease in Tb.Sp would be reduced by as much as 60% its absorbed fracture energy. The mineralized base thickness (t/t_o) showed the opposite trend to that of Tb.Sp in storing fracture energy. A 20% decrease in mineralized base thickness would result in 95% increase in fracture energy, while a 20% increase in thickness would decrease

energy absorption as much as 42%.

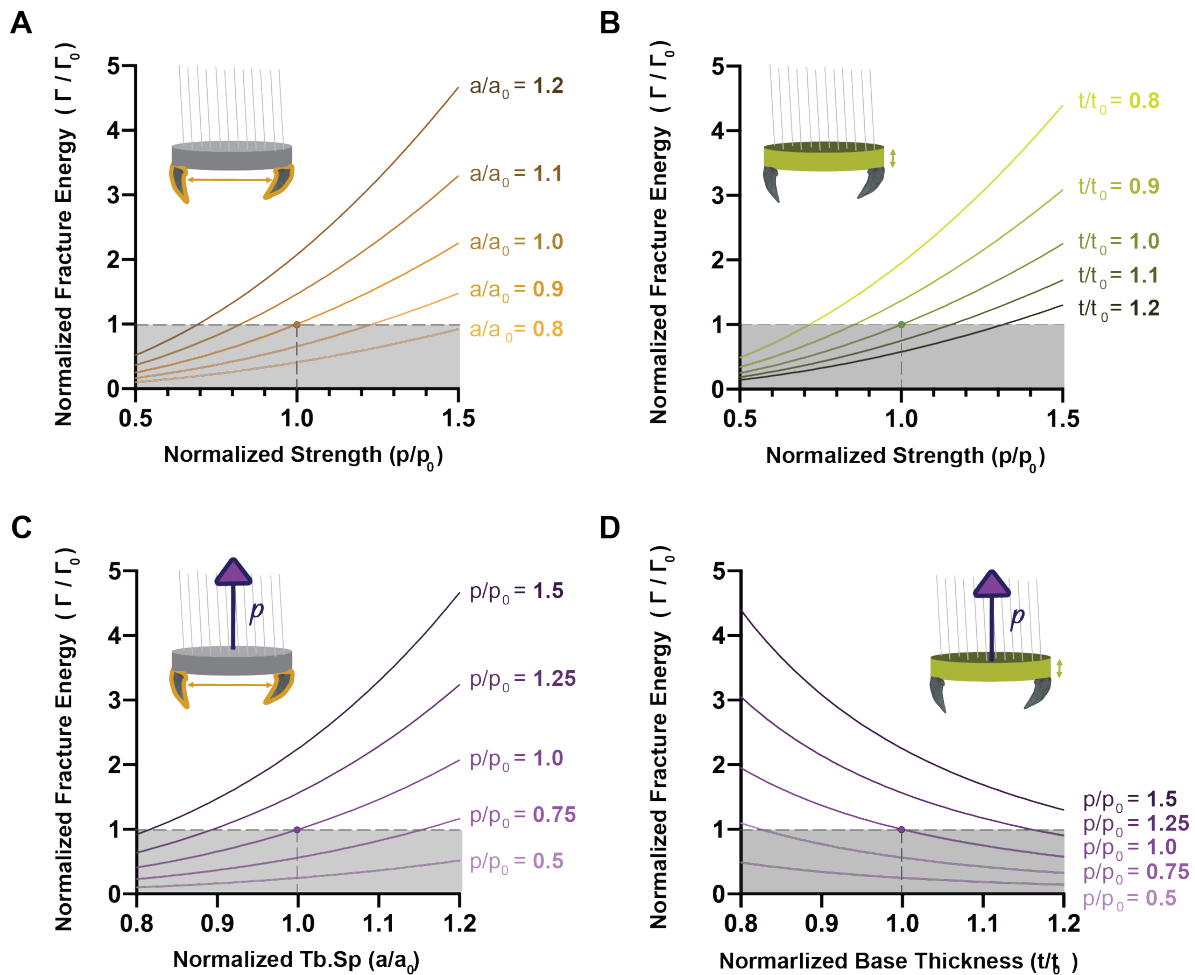


Figure 6.8: Bony microarchitecture underlying the enthesis is optimized for tendon enthesis toughness: a small increase in strength leads to significant gain in energy absorption at the time of enthesis fracture. The relationship between normalized fracture energy (Γ/Γ_o) and (A) trabecular spacing, Tb.Sp, (a/a_o) or (B) mineralized bony base thickness (t/t_o) was plotted against normalized strength (p/p_o). (C) Normalized fracture energy increased with increase in trabecular spacing. (D) The mineralized bony base thickness had an inverse relationship with stored fracture energy. Both (C) and (D) show that, with a relatively small increase in normalized strength (p/p_o), there is a significant gain in fracture energy absorbed (Γ/Γ_o) for each a/a_o and t/t_o .

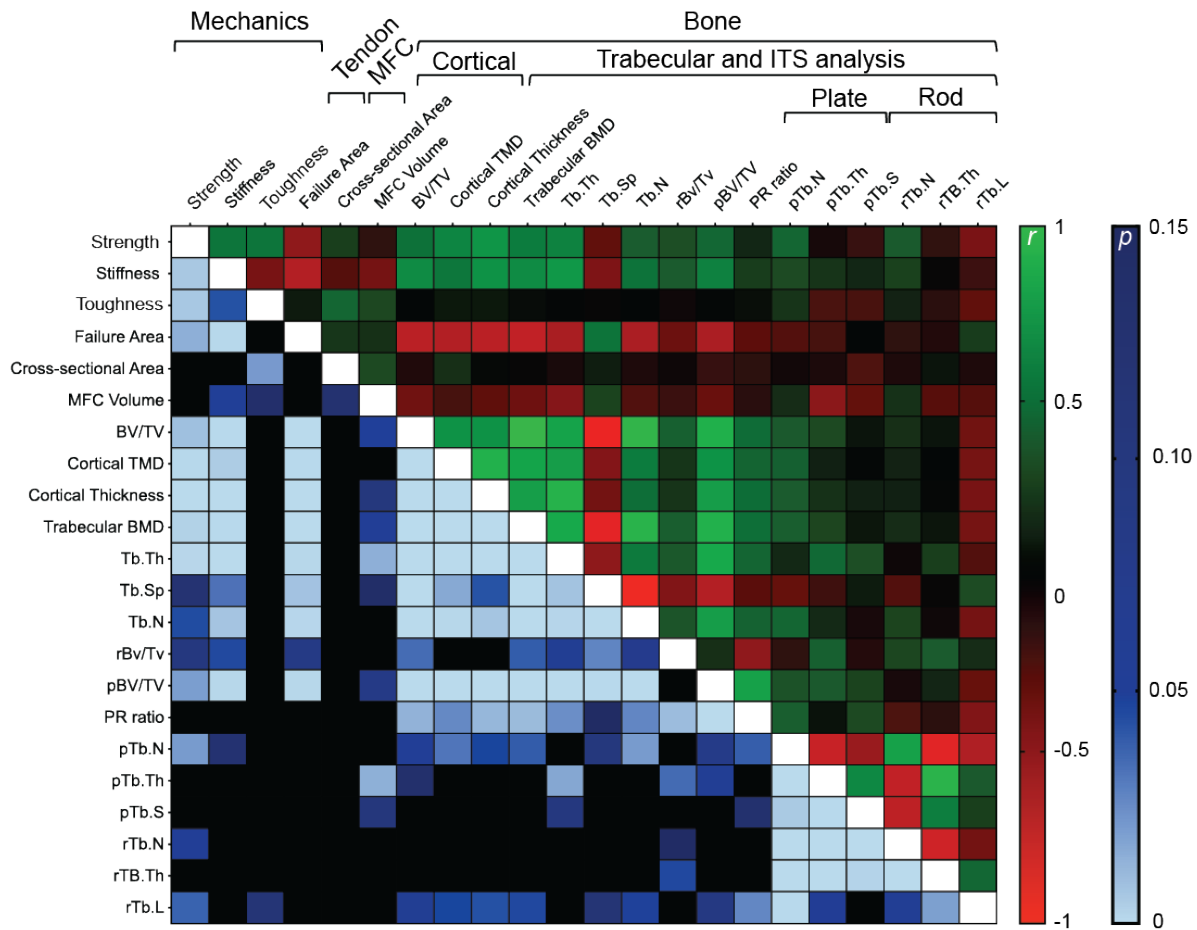


Figure 6.9: *Enthesis strength correlated with underlying bony architecture, while entheses toughness correlated with entheses geometry.* Pearson correlation results obtained from entheses mechanical behavior, entheses failure behavior, entheses characteristics, and bony architecture under the entheses. Green represents a positive correlation, while red represents an inverse correlation. Blue gradient shows p values. Enthesis strength correlated strongly with BMD ($R=0.60$, $p<0.001$), cortical thickness ($R=0.69$, $p<0.001$), and trabecular plate thickness ($R=0.59$, $p<0.001$), but not with tendon cross-sectional area. Enthesis toughness correlated strongly with tendon cross-sectional area ($R=0.44$, $p<0.05$), and trended with mineralized fibrocartilage volume ($R=0.29$, $p=0.11$).

6.3.4 Connecting enthesis morphology and trabecular microarchitecture to its mechanical and failure behavior

Results from Pearson correlations of enthesis mechanical behavior, enthesis failure behavior, enthesis characteristics, and bony architecture under the enthesis is shown in **Figure 6.9**. Enthsis strength correlated strongly with BMD ($R=0.60$, $p<0.001$), cortical thickness ($R=0.69$, $p<0.001$), and trabecular plate thickness ($R=0.59$, $p<0.001$), but not with tendon cross-sectional area. Enthsis toughness correlated strongly with tendon cross-sectional area ($R=0.43$, $p<0.05$), and trended with mineralized fibrocartilage volume ($R=0.30$, $p=0.11$).

6.4 Discussion

Developing and adult musculoskeletal systems are constantly subjected to mechanical forces and must therefore adapt their structure and composition to maintain their function. The findings from previous chapters demonstrated *ex vivo* how the tendon enthesis absorbs energy to prevent failure (**Chapter 2** and **Chapter 3**), how the fibrous architecture allows for a wide range of loading directions (**Chapter 4**), and how the mineral content dictates strength (**Chapter 5**). These features provide critical toughening mechanisms by which the *healthy* enthesis protects against injury-level loads. As described in **Chapter 1**, however, there is a significant lack of knowledge about how *in vivo* extrinsic (e.g., pathological loading) and intrinsic (e.g., changes in tissue architecture) factors compromise the enthesis and lead to rupture. Little is known about how pathological loading conditions affect the enthesis and its ability to transfer load between tendon and bone without failure. To understand how adaptations of the enthesis to loading lead to compromised strength and/or toughness, *in vivo* pathological loading conditions were examined in the current chapter. Modifications in the loading environment, overuse and underuse, achieved physiologically relevant changes to mineralization patterns at the enthesis and led to divergent changes in enthesis biomechanical and microarchitectural properties.

6.4.1 *In vivo* overuse and underuse lead to distinct changes to mechanical behavior

Both overuse and underuse reduced toughness, but via very different mechanisms. The loss in toughness in overuse entheses occurred due to a reduction in the failure displacement (i.e., up to 35% increase in stiffness) without a change in strength. In contrast, the loss in toughness in underuse entheses occurred due to a reduction in strength (up to 25% reduction in failure load) without affecting failure displacement (i.e., up to 24% decrease in stiffness). Counterintuitive to its mechanical responses, the minimal whole TCSA remained unchanged for underuse, while decreased as much as 33% for overuse.

The mechanical characteristics of underuse tendon entheses, which were subjected to muscle paralysis, are not surprising. Numerous reports, from both human [243, 244, 245] and animal *in vivo* joint inactivity models [232, 246, 247] show inferior mechanical properties (i.e., decreased strength, stiffness, and toughness). Human lower limb immobilization studies show decreases in stiffness, increases in the transition point (i.e., the displacement where loading responses transition from a nonlinear, low-stiffness phase to a high, constant-stiffness phase) for Achilles and patellar tendons, also without changes in TCSA [243, 248], mirroring responses seen in the mouse *in vivo* underuse tendon entheses reported here. One of the prevailing hypotheses that bridges joint unloading to tissue mechanics is that inactivity of the tendon enthesis removes mechanotransduction signals within the tissue leading to a catabolic state and inferior macro-scale mechanical properties. Several *in vivo* and *in vitro* unloading studies show downregulation of mRNAs related to tendon (e.g., *Tnmd*, *Scx*, and *Colla1*) and its cross-linking (e.g., *Lox*) [239, 249, 250, 251]. Nonetheless, the mechanisms by which relatively rapid changes in mechanical properties occur in the absence of overall changes to the size of the tendon enthesis remain elusive. It is possible that unloading affected bulk tendon morphometry, newly identified and characterized in **Chapter 2**, via reducing collagen fiber diameter or via reducing amounts of collagen cross-linking. The other possibility, discussed later in this chapter, is that the response to mechanical loading is largely dictated only by the mineralized portion of the enthesis.

Prior *in vivo* overuse models with downhill treadmill running in rats showed decreases in ten-

don enthesis strength and stiffness [235, 252, 253]. These changes were attributed to its reduced collagen content, fiber alignment, and phenotypic changes such as increase in lipid deposits, proteoglycan accumulation, and calcification [254, 255]. In contrast, the current mouse shoulder overuse model of four weeks of downhill treadmill running stiffened tendon enthesis, yet did not affect its strength and, surprisingly, reduced TCSA. The mechanical responses of the current overuse enthesis mouse model, thus, mirror those in humans and *in vivo* animal models of joint exercise, which stiffens tendons by as much as 65% [253, 256, 257, 258]. The decrease in minimal TCSA in overuse was the opposite of what was initially hypothesized. Human studies on tendon adaptation to either chronic overuse or exercise show an approximately 10% increase in TCSA in the Achilles and patellar tendons [228, 229] (see also results from **Chapter 7**). Several studies attribute this effect to loading-induced increases in collagen synthesis [259, 260], yet more recent studies indicate that tendon collagen fibrils are largely unaffected by overuse or exercise [261]. While animal studies on overloading-related changes in tendon fibril morphology show conflicting results, V-shaped adaptations to mouse tendon fiber diameter over time has been previously reported [262]. Michna et al reported that the mean fibril diameter, measured with electron microscopy, increased in the initial loading period (week 1-3), followed by a decrease (week 3-7), and a subsequent increase (week 10), when mice were subjected to over 2.5 months of treadmill running. Hence, it is possible that morphological changes to the tendon and the mechanical responses seen in overuse tendon entheses represent characteristics of early tendon enthesis pathology, preceding the degenerative changes in enthesis function and morphology seen in rat *in vivo* overuse models or those in human rotator cuff enthesis pathology.

6.4.2 *In vivo* overuse and underuse induced diverging failure behavior

Clinically, a weakened enthesis is often observed after high intensity overuse activities [263] and enthesis failures are prominent in degenerated rotator cuff tears of adult patients [105]. The *in vivo* degeneration models used in this chapter did not recapitulate clinically observable failure patterns at the rotator cuff. Regardless of treatment, tendon entheses subjected to pathologic loading

exhibited exclusively avulsion-type failures under monotonic uniaxial tensile testing. Nonetheless, load-displacement curves showed that there were distinct mechanical behaviors of attachments in the inelastic (“post yield”) and failure regimes depending on their *in vivo* loading history. Overused entheses failed catastrophically, with little to no post-yield behavior, while underused entheses failed with distinct post-yield behavior, with retention of some load even after peak load was reached. This contrast was also evident when examining the failure site. Overuse led to more failures at the MF-B interface, while underuse led to more failures at the B-T interface. Furthermore, overuse primarily failed with one bony avulsed fragment, while underuse showed multi-fragmentation of bony pieces, with some cases failing with larger failure areas than that of primary insertion site. The fibrous interface at the tendon enthesis was able to store enough energy to fracture and avulse bone, but at a limited scale under both pathologic settings *in vivo*. Visual inspection and post-failure high-resolution contrast enhanced imaging at the tendon enthesis did not reveal distinct pathology-induced changes to its fibrous network. Hence, the diverging mechanical and failure behavior seen with distinct aberrant loading suggests a mechanistic consequence of architectural adaptations to the mineralized base underneath the tendon enthesis.

6.4.3 Loading-induced architectural adaptations to the mineralized bony base underlying the enthesis dictate the extent of enthesis failure

It is well known that bone [214, 215], and more recently the entheses [64, 129], respond to loading by adapting their mineral content. For instance, unloading results in rapid resorption of bone tissue, which leads to decreased mechanical properties and an increase in fractures [227]. At the enthesis, joint unloading led to changes to mineral crystal size and alignment [64]. To investigate the architectural adaptations that drove the changes in the enthesis failure patterns we observed, changes in the bone underlying the tendon enthesis were characterized. Bone morphometry analysis showed that underuse led to loss of bone mineral and bony architecture underlying the attachment and overuse led to gain of mineral and bone volume of the humeral head. The results here corroborate clinical findings [100, 264, 265] as well as other *in vivo* studies [64, 131] that

show bony changes due to loading (e.g., bone loss due to unloading) concentrated primarily near the regions with altered loading (e.g., directly adjacent to unloaded tissue) leading to increased risk of fracture [266]. In the current study, underuse led to dramatic changes to local cortical and trabecular structure, with a 23% decrease in mineral density (BMD), 11% decrease in cortical thickness (Cr.Th), and as much as a 25% decrease in overall trabecular volume (BV/TV) and a 16% increase in trabecular spacing (Tb.Sp). Overuse showed statistically significant, yet modest, gains in supporting trabecular bone, with increases in up to 10% in overall trabecular volume (BV/TV) and a 5% gain in trabecular thickness (Tb.Th). Hence, modifications to the *in vivo* loading environment led to architectural and compositional adaptations to the bony base underneath the tendon enthesis, which contributed to tendon enthesis mechanical behavior, consistent with ideas initially introduced in **Chapter 3**.

The contribution of the local bony architecture to tendon enthesis failure behavior was next evaluated using an idealized fracture model. Here, the enthesis loading was modeled using a circular plate, that represented the enthesis and its mineralized base (i.e., mineralized fibrocartilage and cortical shell), clamped at the edges, representing load-bearing trabeculae, and loaded with uniform pressure (**Figure 6.2**). This model showed that, as the distance between load-bearing trabeculae increases, the resulting peak fracture energy increases to the 4th power (**Eq. 6.4**). Applying results from *in vivo* degeneration experiments to this model shows that adaptations to the bony architecture in overuse samples yields a 20% decrease in the fracture energy stored. In contrast, adaptations to the bony architecture in underuse samples results in an approximately 220% increase in the fracture energy stored in the circular plate, even when failing at 75% of normal (healthy) maximum failure force. Thus, the architectural changes in the entheses subjected to underuse contributed to an increase in the energy available to not only fracture the circumference of the avulsed bone, but also to generate many avulsion fragments in the process. These modeling results agree with experimental observations of failure properties, where overuse samples decreased in failure area by as much as 30% and primarily avulsed as single pieces, while underuse samples increased in failure area by as much as 90% and failed with many fragments. *In silico* numerical

simulations showed that even small adaptations to the enthesis bony base, such as 10% increases in trabecular spacing (or 10% decreases in cortical thickness), lead to an approximately 50% increase in fracture energy absorbed. Hence, the model uncovered that the bony architecture underlying the enthesis is designed with toughness in mind, mirroring the fibrous nature of the tendon enthesis that enables toughness across loading directions (described in **Chapter 4**).

6.4.4 Overuse and underuse led to diverging adaptations to local trabecular microarchitectural network underlying the tendon enthesis

Bone morphometry and the fracture mechanics analysis suggest the importance of local trabecular bony architecture in predicting the risk and extent of failure at the tendon enthesis. At the micro-scale, trabecular bone consists of an intricate network of rod-like and plate-like trabeculae, which undergo dynamic bone remodeling to maintain their microstructural integrity [241, 267]. Furthermore, these important microarchitectural features determine mechanical and failure properties of healthy and diseased trabecular bone [268], where trabecular plates dominate the overall mechanical properties of trabecular bone structure [241, 269]. Since the underlying bony trabecular network may be compromised in different ways depending on the type of altered loading, we next characterized the trabecular network of the *in vivo* degenerated tendon enthesis using ITS analysis.

ITS technology, typically implemented for three-dimensional human trabecular bone images, successfully segmented the murine trabecular network into rod-and-plate microarchitectures. The trabecular network of healthy cage activity control mice showed a higher ratio of loading-bearing trabecular plates to trabecular rods (PR-ratio) in the humeral head underlying the tendon enthesis. Furthermore, the highest density of trabecular plates was oriented at 90°-60° abduction of the tendon enthesis (i.e., dominant fiber direction), with few plates orientation at lower angles. The trabecular rod distribution had the opposite orientation profile compared with that of trabecular plates. Previous micro finite element analysis and *ex vivo* studies indicate that the majority of trabecular plates are orientated along the principal direction of loading, whereas trabecular rods mostly serve

as transverse connections between longitudinal plates [268]. Hence, the cross-scale load-transfer mechanism for tendon enthesis introduced in **Chapter 4** is present for the bony microarchitecture as well: loads from the tendon enthesis are transmitted via longitudinal plates (90° - 60° orientation) and dissipated away from the axial direction by transversely aligned trabecular rods.

Both degenerative loading environments at the tendon enthesis disrupted trabecular bone microarchitecture, but via different ways. Underuse decreased trabecular plate volume as much 30%, while keeping the trabecular rod volume constant. This decrease in plate volume was due to a decrease in the number of trabecular plates and not due to a decrease in trabecular plate thickness. The significant decrease in PR-ratio also suggests that trabecular microarchitecture changed from plate-like to rod-like for underuse degenerated samples, making the individual trabecular rods longer. Trabecular plate and rod loss occurred uniformly across all directions. Overuse, on the other hand, increased the volume of load-bearing trabecular plates as much as 20% of that of control mice by increasing trabecular plate thickness up to 30% and not changing the number of trabecular plates. Trabecular plate density increased in 60° - 0° orientations compared with control, with uniform loss of trabecular rod density across all loading directions.

Clinical studies using ITS technology show two types of changes to bony microarchitectures when comparing osteoporosis (OP) and osteoarthritis (OA). A change of trabecular bone microarchitecture from plate-like structure to rod-like structure, similar to what we observed due to underuse, occurs during OP and other metabolic bone diseases [270, 271]. In human OA, in contrast, ITS analysis detects a significant gain in plate bone volume beneath damaged cartilage, with trabecular plate and rod thickening and a decrease in trabecular rod numbers [20], similar to what we observed due to overuse. Orientation analysis of the trabecular network of human OA showed that trabecular rod loss was uniform along all directions, with the density of trabecular plates increasing significantly along the load-bearing direction beneath damaged cartilage. The increase in trabecular plate density in oblique (60° - 0°) directions (corresponding to mid-to-low angles of abductions) seen in overuse may be due to a compensatory mechanism to deal with the loss of trabecular rods in the oblique direction and to maintain effective load transfer, in addition to the

active reinforcement in the new “primary” loading direction with aberrant joint loading. Furthermore, the transformation of trabecular microarchitecture from rod-like to plate-like and thickening of trabecular plates due to overuse may be indicative of sclerotic changes in bone (comparable to the hardening of bone in OA, a hallmark of advanced OA). These changes possibly precede subsequent soft-tissue damage at the tendon enthesis, similar to how microstructural changes in the subchondral bone precede osteoarthritic in cartilage [272].

6.4.5 Enthesis strength correlated with underlying bony architecture, while enthesis toughness correlated with enthesis geometry

Previous studies using animal models have independently examined how altered loading patterns affect overall tissue mechanics. The current study showed distinct adaptations of the tendon enthesis micro- and macro-architecture due to loading. To understand which architectural features drove enthesis mechanical and failure behavior, Pearson correlation was used to relate tendon enthesis architecture to its mechanical function. Enthesis strength, stiffness, and failure properties correlated strongly with mineralized enthesis architecture (e.g., BMD, Cr.Th., and pTb.Th), and but not with the tendon portion of the enthesis. These results are consistent with clinical findings (41–43, 47). Patients with rotator cuff tears (i.e., with unloaded tendons entheses) exhibit reduced bone density at the supraspinatus tendon humeral head attachment site compared to their contralateral intact rotator cuffs [100, 264]. Galatz et al., also showed that the loss of mineralized tissue at the attachment site correlates with higher rates of re-tearing following surgical repair [100]. Regression analysis revealed that enthesis toughness only correlated with TCSA and MFC volume. However, a limitation of this analysis is that tendon enthesis collagen fiber dimensions, collagen content, unmineralized fibrocartilage area, and proteoglycan content were not included. Hence, the current regression analysis is incomplete. The addition of new these additional microstructural measures at the tendon and fibrocartilage portions of the entheses may provide further clues connecting enthesis mechanical properties with its underlying architecture. Based on the results of the current study, the next chapter (**Chapter 7**) presents a clinical example where axial patellar tendon

thickness ratio (i.e., normalized tendon dimension per patient) is used to define the relationship between partial patellar tendon tears (PPTTs) and injury progression.

6.4.6 Pathological loading conditions induce distinct microarchitectural adaptations that compromised tendon enthesis toughness

Based on findings from the current chapter and prior work, we postulate a potential model of dynamic architectural adaptations to tendon enthesis in response to pathological loading conditions (**Figure 6.10**). In the healthy enthesis, the fibrous architecture and bony micro-structure is optimally designed to balance strength and toughness and enable the tissue to absorb energy while resisting failure. However, under pathologic loading conditions, the enthesis adapts its architecture to accommodate the loading by actively remodeling the bony micro-architecture supporting the tendon enthesis.

When the tendon enthesis is underloaded due to paralysis or microgravity, there is a marked decrease in overall bone volume and bone density at the attachment site. Similar to what has been suggested for OP-induced hip fractures (59), millimeter-scale bone loss is due to micrometer-scale transformation of plate-like trabeculae, the primary mechanical loading carrier in the trabeculae network, to rod-like trabeculae. An overall reduction in the density of supporting trabecular plates in the primary loading directions may further contribute to nano-meter scale mineral crystal packing, such as increases in mineral crystal size and crystal orientations at the tendon enthesis (40). All these hierarchical changes due to unloading lead to overall inferior load-transfer and energy absorption at the tendon enthesis. This is confirmed by a marked increase in failure area or a change in failure mode that exposes bone marrow. Hence, these unloading-induced cross-scale microstructural changes disrupt the normal supporting bony architecture at the tendon enthesis, ultimately increasing the failure risk of the attachment.

When the tendon enthesis is overloaded due to strenuous activity, there is an increase in bone volume and mineral density, increasing strength while compromising toughness. The trabecular micro-architecture shows micrometer scale adaptations to the bony base reminiscent of the early

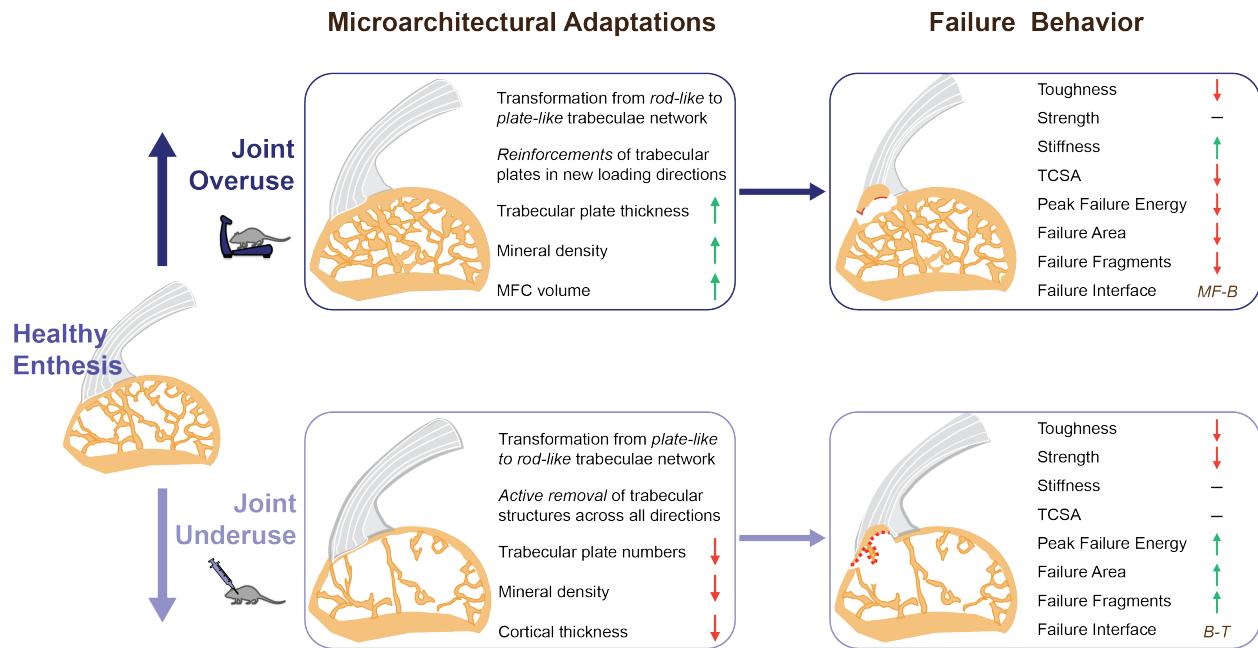


Figure 6.10: Modifications to *in vivo* loading lead to distinct microarchitectural adaptations that compromise tendon enthesis toughness. Pathological loading leads to distinct micrometer-scale transformation of the underlying trabecular network. Overuse prompts a change from rod-like trabeculae to plate-like trabeculae. On the other hand, underuse prompts a change from plate-like trabeculae to rod-like trabeculae. Furthermore, overuse loading leads to active reinforcement of bone whereas unloading leads to active removal of bone underneath the enthesis. Thus, the architecture of the bony structure at the tendon enthesis is oriented to support and share the load according to the muscle loading level and direction. These distinct microarchitectural adaptations lead to changes to tendon enthesis mechanical and failure characteristics. In both under- and over-loading pathologic conditions, there is a loss of tendon enthesis toughness. (Upward arrows represents an increase and downward arrow represents a decrease compared with healthy enthesis. A horizontal line represents no difference compared with healthy enthesis.)

stages of OA, as postulated by Chen et al. [20]. The increase in enthesis loading contributes to abnormal bone resorption, specifically attacking trabecular rods due to their thinner morphology and their higher surface-to-volume ratios. The changes in micro-architecture, consequently, result in increases in trabecular plate thickness and density at specific orientations to manage higher mechanical demand. These morphological changes disrupt the normal load-transfer and injury preventative mechanisms at the tendon enthesis. With the increase in loading, it is suspected that nano-scale mineral crystals at the enthesis become tightly packed can no longer absorb mechanical energy due to limited availability for crystal mobility [55]. An increase in the mineral stiffness will in turn increase the stiffness of the gradient region and that of the compliant zone, thereby reducing the tendon enthesis' ability to dissipate energy. The continuous unfavorable mechanical conditions, such as uneven loading of enthesis fibers and/or newly arising local stress concentrations, can have a devastating effect on the fibrous tendon enthesis, which has a very slow turnover rates [41]. The gradual structural and compositional alterations to the tendon enthesis eventually progress to tissue degeneration, as seen in enthesis pathologies such as rotator cuff disease.

While the current chapter describes dynamic architectural adaptations of the tendon enthesis in response to loading, there remains a critical gap in knowledge in understanding the biological mechanisms that control these responses. Studies on enthesal resident immune cells (e.g., enthesis resident T-cells and resident macrophages) show the potential of these cells to monitor damage and environmental stresses to prime neighboring stromal cells for tissue remodeling [97, 141]. Other studies have shown the importance of a unique population of Hh-responsive cells at the tendon enthesis in modulating the extent of mineralization of fibrocartilage at the tendon enthesis under the influence of loading or injury [63, 273, 274]. Further studies are required to define the roles of various molecular mechanisms that contribute to architectural adaptations during pathologic joint loading in order to reverse progression of chronic degeneration and prevent macroscopic tissue failure. Nevertheless, the observed adaptations of trabecular microarchitecture, which depended on aberrant loading, suggest that the quantitative evaluation of the internal structure of trabecular bone underlying the enthesis is a promising clinical tool for early diagnosis of enthesis disease and

progression of tissue degeneration and subsequent failure. Furthermore, the concepts discussed in this chapter may inspire and guide development of functionally graded architected materials in medicine.

6.5 Conclusion

Musculoskeletal tissues dynamically respond to their loading environment by actively adapting their composition and architecture. Using physiologically relevant *in vivo* loading, we showed that the tendon enthesis adapts its multi-scale architecture to optimize strength, while compromising toughness. The differential mechanical and failure behavior of compromised enthesis was dictated by changes to the underlying trabecular micro-architectural network. Overuse loading prompted active reinforcement and stiffening to maintain strength and compromise overall toughness, whereas underloading prompted active removal of the trabecular architecture underneath the enthesis to compromise both strength and toughness. Furthermore, the architecture of the bone at the enthesis re-oriented to support and share the load (or lack of load) into orientations of relatively low enthesis strength and toughness. The adaptations to tendon enthesis architecture reported here provide additional insights into guiding tissue-engineered solutions, as well as developing targeted treatments and therapy to improve mobility and function of bi-material attachments throughout the body.

Chapter 7: Clinical Example:

Rethinking Patellar Tendinopathy and Partial Patellar Tendon Tears

A Novel Classification System

Portions of this chapter were previously published in: Golman M, Wright ML, Wong TT, et al. Rethinking Patellar Tendinopathy and Partial Patellar Tendon Tears: A Novel Classification System. *The American Journal of Sports Medicine*. 2020;48(2):359-369.

7.1 Introduction

Over the previous chapters, we used murine models to identify several key features that endow toughness to the fibrous tendon enthesis. **Chapter 3** showcased how energy is absorbed across hierarchies of the tendon enthesis, with distinct molecular-level damage localization and propagation after acute (quasistatic) and fatigue (cyclical) loading. **Chapter 4** demonstrated that the fibrous network enhances energy absorption by recruiting and re-orienting distinct fiber networks to distribute failure processes depending on the loading direction. **Chapter 5** confirmed prior findings that mineral composition is crucial for the stiffening and strengthening the tendon enthesis [64]. In **Chapter 6**, we were able to manipulate the *in vivo* loading environment to show that the pathologic enthesis actively adapts its architecture to optimize strength, while compromising toughness. These mechanisms of toughening, demonstrated in mouse models, are fundamental for advancing design strategies for tough bimaterial attachments in medicine and engineering. However, understanding tendon and tendon enthesis architectural contributions to toughening can also be directly applied in clinical practice through diagnostic imaging of architectures through injury progression. The previous chapter (**Chapter 6**) showed that tissue mechanical properties correlated with tissue architecture and composition, revealing the potential for using changes in tendon

geometry as indicators of tissue health. Motivated by these basic science results, in this chapter we present a clinical example where a quantitative magnetic resonance imaging (MRI) approach was developed to identify and categorize patellar tendinopathy and partial patellar tendon tears, specifically correlating tear geometry with injury progression and prognosis.

Patellar tendinopathy, commonly known as jumpers' knee, is an overuse injury often found in athletes who are involved in repetitive or explosive activities with high peak strains in the patellar tendon, such as running, jumping, and kicking [120, 275, 276, 277]. The pathology underlying this condition is characterized by micro-injury to tendon fibers, local mucoid degeneration, necrosis, and loss of transitional fibrocartilaginous tissue that attaches tendon-to-bone, often without inflammation [278, 118]. The incidence of patellar tendinopathy is increasing throughout a wide age range in the athletic population and has been reported to be as high as 55% in elite men's basketball players [119, 228, 279]. Professional and recreational athletes with patellar tendinopathy continue to play with mild and moderate pain and aggravate their condition or cause PPTTs.

PPTTs are frustrating injuries for both athletes and treating physicians. For athletes, PPTTs can lead to prolonged recovery time, decreased performance, and increased time away from sport. In some cases, they can ultimately lead to the retirement of athletes from their sports [280]. For physicians, a variety of treatment options are available, yet the clinical outcomes can be relatively poor [278, 281, 282]. Of 20 athletes with patellar tendinopathy whom Kettunen et al [282] followed over 15 years, 53% were forced to retire from their sport owing to the condition, compared to 7% of control athletes retiring due to other forms of injury. Treatment typically begins nonoperatively with anti-inflammatory medications (i.e., NSAIDs), patellar tendon bracing, and physical therapy [281]. Further interventions can include extracorporeal shock wave therapy (ESWT) or platelet-rich plasma (PRP) injections, which have gained popularity more recently but have variable supporting literature [211]. Surgical debridement with or without tendon repair is typically attempted when nonoperative treatment fails [119, 281, 283, 284]. However, there is currently no classification system that connects the severity of patellar tendinopathy with guidelines for treatment.

Understanding the location and characteristics of partial patellar tendon tears (PPTTs) is fundamental to determining the prognosis of patellar tendinopathy, as well as the selection of the most effective therapy. However, few studies have investigated these characteristics and their relation to prognosis [285, 286, 276]. Diagnosis of patellar tendinosis is typically made with history and physical exam, with occasional confirmation of patellar tendinopathy using ultrasonography and/or magnetic resonance imaging (MRI). Current classifications of patellar tendinopathy, such as the Blazina classification and the Victorian Institute of Sport Assessment (VISA) score [287, 279] are based only on symptoms and do not necessarily provide objective treatment guidelines. Advances in ultrasound and MRI quality now allow for better visualization of the patellar tendon and its pathology and may add a more objective factor to the evaluation of athletes with patellar tendinopathy and/or partial tears. Recent studies have used these modalities to better understand and classify degenerative rotator cuff tears [107, 106], but to our knowledge, no study has investigated the relationship between PPTT geometry (i.e., tear size and location), clinical outcomes, and the related therapeutic choices for the patellar tendon. Therefore, the purpose of this chapter was to determine the imaging characteristics of partial patellar tendon tears and to correlate these characteristics with clinical outcomes. This study is a first step towards the creation of an imaging-based classification system to help guide clinicians when treating athletes with patellar tendinopathy and PPTTs.

7.2 Methods

7.2.1 Study Subjects

All athletes between the ages of 15 to 45 years who presented to our institution between April 2003 and April 2018 with signs and symptoms of patellar tendinopathy and underwent an MRI were considered for inclusion in this study. Patient data was retrospectively reviewed after the approval by the Columbia University Institutional Review Board. The inclusion criteria for this study was (1) presence or history of, and physical examination consistent with, recalcitrant patellar tendinopathy or suspicion of a PPTT; (2) inability to compete in the accustomed level of sports;

and (3) MRI confirmation of patellar tendinosis or partial patellar tendon tear, but not full thickness tear. Additional patients who underwent MRI of the knee for unrelated conditions were included in this study as healthy, athletic age-matched controls. An athlete was defined for this study as follows: training in a sport with the goal of improving one's performance, actively participating in sporting competitions, and being formally registered in a local, regional, or national sport organization [288]. MRI scans were evaluated by an attending orthopedic surgeon or a board-certified musculoskeletal radiologist for size of patellar tendon tear, thickness of tear, and location with respect to the entire patellar tendon. Presence and location of edema and tendinosis was also noted. Treatment modalities were evaluated, including operative and nonoperative treatments, dry needling, PRP injections. The success of treatment was judged by whether patients were able to return to their previous level of activity at the final follow up.

7.2.2 Determination of Partial Patellar Tendon Characteristics

All patients had knee MRI performed on a 1.5-T or 3-T scanner (GE Healthcare; Siemens Healthcare). All MRI scans were done according to the same standard knee MRI protocol [279] used at our institution (field of view in [cm], slice thickness in [mm], repetition time/echo time in [ms]). Sequence parameters for 1.5-T examinations were as follows: axial proton density fat saturation (16, 4, 1650/18), sagittal proton density (14, 3, 3000/34), sagittal proton density fat saturation (16, 3, 1867/17), coronal proton density (16, 3, 3000/minimum), and coronal proton density fat saturation (14, 3, 2070/minimum). Sequence parameters for 3-T examinations were as follows: axial proton density fat saturation (16, 4, 3000/30), sagittal proton density (14, 3, 3000/34), sagittal proton density fat saturation (16, 3, 3000/17), coronal proton density (16, 3, 3000/20), and coronal proton density fat saturation (14, 3, 4000/68). Matrix size ranged from 320-512 x 224-256 for all sequences. A partial tear was defined 2-fold: (1) signal change on fluid sensitive sequences with signal in the tendon that was isointense to joint fluid and (2) morphological defect with the evidence of disruption or discontinuity of the fibers on axial or sagittal images. Tendinosis was defined as signal seen on fluid sensitive sequences that was not isointense to fluid with intact mor-

phology, with no evidence of collagen or tendon disruption, unlike the partial tear. Images were reviewed on our institutional picture archiving and communication system (PACS). An electronic caliper tool in PACS was used to determine patellar tendon measurements. In this way, all measurements taken were automatically standardized regardless of scanner field strength (i.e., 1.5-T vs. 3-T). Six maximum tendon dimensions were measured using either sagittal or axial (anterior to posterior) views: (1) the length (proximal to distal) of the patellar tendon, (2) the width (medial to lateral) of the patellar tendon, (3) the thickness (anterior to posterior) of the patellar tendon on the first axial slice below the inferior patellar bone, (4) the length of the tear (5) the width of the tear, and (6) the thickness of the tear (**Figure 7.1**). The length dimensions (1 & 4), were measured using sagittal MRI scans that showed maximum dimension (**Figure 7.1, A and D**). The width and thickness dimensions (2 & 3 and 5 & 6) were measured in the axial view that maximally showed each dimension, which corresponded to one slice below the inferior pole of the patella (**Figure 7.1, B and E**). The partial tear location was determined by dividing the axial view (anterior to posterior, AP) into 9 sections: (anterior-medial, anterior, anterior lateral, medial, central, lateral, posterior-medial, posterior, and posterior-lateral) and selecting the region in which the partial tear was primarily located (**Figure 7.1, C and F**).

7.2.3 Statistical Methods

Normality testing for each variable measured (length, width, thickness, etc.) was performed using D'Agostino-Pearson normality testing. The only variable with a non-normal distribution was thickness. Hence, statistical comparisons for thickness were done using the non-parametric Mann-Whitney or Spearman rank correlation tests. Univariate and logistic regressions were performed to determine if there were correlations between tendon geometry and tear size. Tear geometry variables were compared to patient outcome measures (i.e. return to previous activity level, or surgical treatment) using T-tests or Mann-Whitney tests. Patients who underwent repair surgery were categorized into the "repair surgery" group, while those who underwent other conservative treatments (i.e., bracing, medications, therapy, dry needling, PRP injections, etc.) were categorized

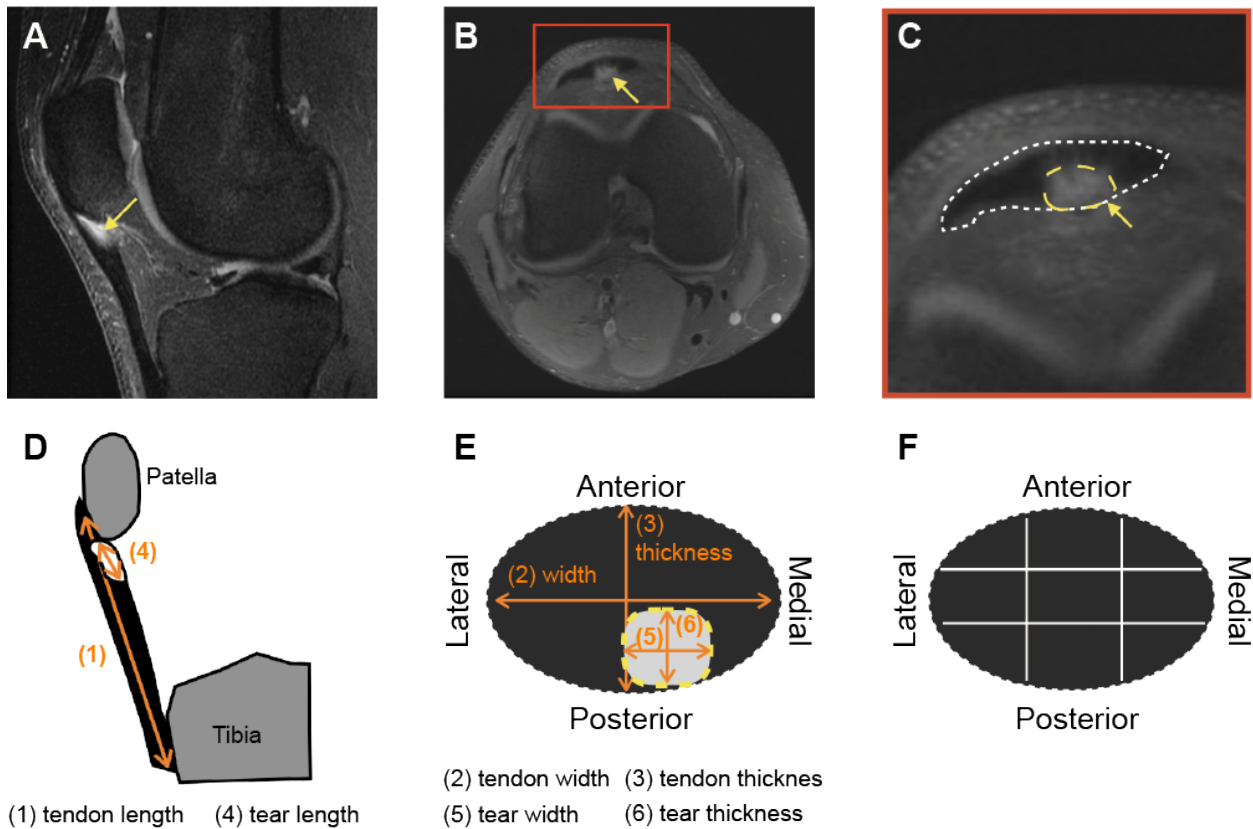


Figure 7.1: *Defining PPTT dimensions from MRI scans.* A partial tear was defined 2-fold: (1) signal change on fluid-sensitive sequences with signal in the tendon that is iso- intense to joint fluid and (2) morphological defect with the evidence of disruption or discontinuity of the fibers on (A) sagittal or (B, C) axial MRI. Arrows and long dashed line indicate PPTT, and short dashed line indicates tendon cross section. (D: 1, 4) Length dimensions were measured with sagittal MRI scans that maximally showed each dimension. (E: 2, 3, 5, 6) The width and thickness dimensions were measured in the axial view (anterior to posterior). (F) The exact location of the partial tear was determined by dividing the axial view into 9 sections. MRI, magnetic resonance imaging; PPTT, partial patellar tendon tear.

into the “nonoperative treatment” group. $P < 0.05$ was considered significant. Statistical analyses were performed using GraphPad Prism 7 (GraphPad Software).

To test the robustness of the classification system, intra- and inter-observer variability were assessed for patellar tendon and PPTT dimensions. Two board-certified attending orthopedic surgeons and two board-certified musculoskeletal radiologists independently measured these parameters for 20 pathological patellar tendons (5 patients randomly selected from proposed Popkin-Golman [PG] grades 1-4) in random order three times. Data sets were measured approximately a

week apart to mitigate analyzer recall bias. To assess intra-observer reliability, intraclass correlation coefficients (ICCs) for each measurement were calculated for each observer. For inter-observer reliability, ICCs were determined from mean measurements for each observer [289]. Furthermore, to test the viability of the new classification system, the results from the new classification approach were compared against the gold-standard Blazina classification. All ICC analysis was performed using IBM SPSS software (version 26.0.0.0; IBM Corp).

7.2.4 Histological Evaluation of Healthy Patellar Tendon

To identify the regional differences in Patellar tendons organization, patellar tendons from 3 fresh frozen cadavers (one male 64 years, and two females 69 years and 37 years), free of apparent disorders or patellar tendinopathy, were carefully dissected and fixed with 10% formalin solution for 72 hours. Samples were axially cut (to see the AP view) at proximal and distal parts of the patellar tendon. The specimens were dehydrated through graded ethanol, embedded in paraffin, and 5 micrometer thick sections were prepared. Sections were stained with either hematoxylin and eosin (H&E) and evaluated for tissue organization and presence of vasculature.

7.3 Results

7.3.1 Study Subjects and Presence of Partial Tears

Of the 171 athletes (range: 15-45 years; mean \pm SD, 23.5 \pm 8.1 years) included in the study, 85 patients (72 males, 13 females; mean age 24.9 \pm 8.1 years) had a clinical presentation concerning for patellar tendinopathy. A total of 86 controls patients had an intact and healthy patellar tendon (74 males, 12 females; mean 23.8 \pm 8.2 years). All participants with patellar tendinopathy or PPTT who were included in the study were athletes (i.e., active in sports in professional, semiprofessional, collegiate, or high school levels) before injury. Out of 85 symptomatic patients, 56 (65%) had PPTTs (**Figure 7.2**). The other 29 patients had clinical manifestations of recalcitrant patellar tendinopathy, with some patients having MRI confirmation of patellar tendinosis or edema but not partial- or full-thickness tears. All of these patients met inclusion criteria as described in

the Methods section and were included in the study.

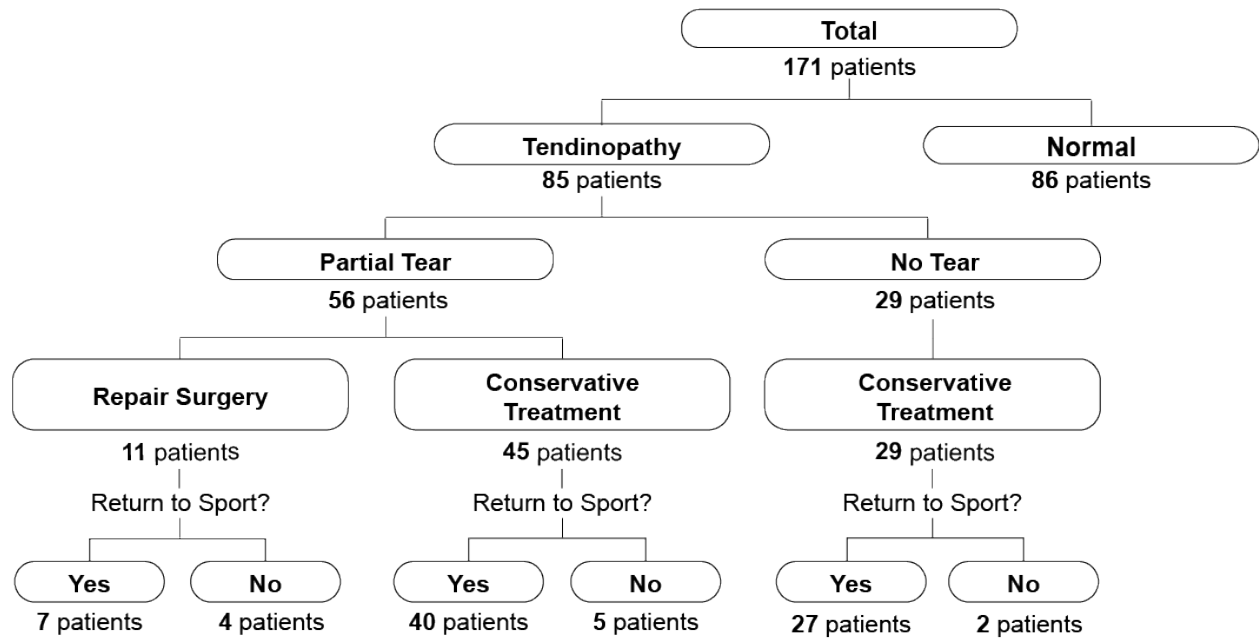


Figure 7.2: Patient distribution included in this study. Out of 85 symptomatic patients, 56 had partial tears. Out of 56 patients with partial patellar tendon tears, 11 underwent repair surgery after failing a minimum 6 months of nonoperative treatments, while remaining opted for nonoperative (conservative) treatments.

Of the 56 patients with PPTTs, 11 (20%) underwent surgical repair after failing nonoperative options for > 6 months. Surgical procedures included debridement alone (2 patients) and debridement with anchors (9 patients). The remaining patients chose nonoperative treatment. Of the 11 patients who underwent surgery, 4 (36%) were unable to return to their previous levels of activity at the time of final follow-up. Of the 45 patients who underwent nonoperative therapy, 5 (11%) were unable to return to their previous levels of activity. Among 29 symptomatic patients who did not have partial tears, 2 (7%) reported that they were unable to return to their previous levels of activity. Basketball, running (track and field), and soccer were the most common sports involved in the patient population (**Table 7.1**).

7.3.2 Patellar Tendon Size

Table 7.2 summarizes the patellar tendon dimensions analyzed in this study. When all patients (cases and controls) were included, patellar tendon dimensions were normally distributed for all

Table 7.1: Patient Sport/Activity Distributions

	Symptomatic Patients, n (%)
Basketball	24 (28.2)
Running	13 (15.3)
Soccer	11 (12.9)
Gym/Body Building	11 (12.9)
Baseball	8 (9.4)
Football	4 (4.7)
Volleyball	3 (3.5)
Others (cyclist, dancers, skiers, etc.)	3 (3.5)

dimensions except thickness. Mean patellar tendon width was 31.5 ± 3.7 mm (medial to lateral), mean length was 62.6 ± 9.6 mm (distal to proximal), and mean thickness was 7.9 ± 2.8 mm (anterior to posterior, axial view). When groups were separated into normal, pathologic without tear, and pathologic PPTT groups, there were significant differences in patellar tendon width and thickness, with the most distinct difference seen in patellar tendon thickness (**Figure 7.3**). On axial MRI views, there was a significant difference in patellar tendon thickness between normal and symptomatic patients ($p < 0.001$). Furthermore, patients with PPTTs had a mean tendon thickness of 10 mm, as compared with 6.1 mm for athletes with no PPTT ($p < 0.001$).

Table 7.2: Patellar Tendon Geometry

	Normal (mm)	Pathologic		Normal Distribution	P Value
		No Tear (mm)	PPTT (mm)		
Length	54.5 ± 6.2	60.3 ± 3.7	67.8 ± 3.7	Yes	.030
Widths	29.5 ± 2.7	30.4 ± 2.7	33.0 ± 3.8	Yes	0.025
Thickness	5.6 ± 1.0	6.1 ± 1.8	10.0 ± 2.2	No	<.001

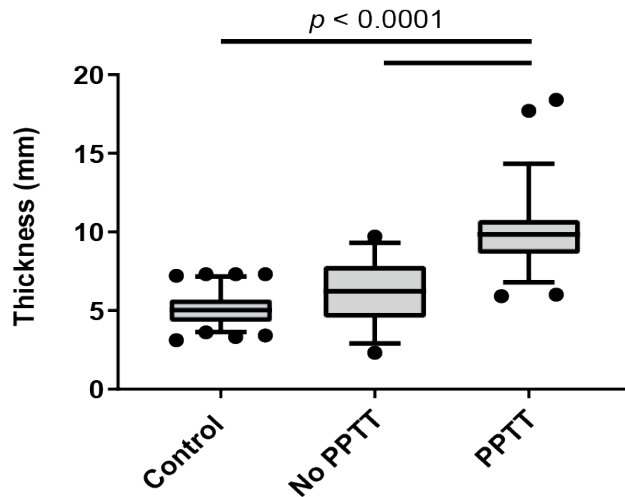


Figure 7.3: Patellar tendon is thicker in patients with PPTTs. There was a significant difference in patellar tendon thickness between controls and patients with PPTTs ($P < .001$) and between symptomatic patients with no tears and patients with partial tears ($p < 0.001$). There was no difference in tendon thickness if there was no tear in patellar tendon. PPTT: partial patellar tendon tear. Values are presented as median, interquartile range, 95% CI, and outliers.

7.3.3 PPTT Location and Size

Figure 7.4 shows the location frequency heat map for partial patellar tendon tears. The tears were almost exclusively located in the proximal portion of patella tendon: 51% of all partial tears were located in posterior aspect of the proximal patellar tendon and 40% of all tears were located in the posteromedial region of the proximal patellar tendon. The mean length of the tears was 9.1 ± 4.2 mm. The mean width was 6.2 ± 4.8 mm. The mean thickness of partial tears was 4.6 ± 2.2 mm. To control for variation in patient size, tear size was also calculated as a % ratio in each dimension (e.g., AP tear thickness relative to tendon thickness). This showed that, relative to the size of the entire tendon, patients' mean tears presented as follows: width $18.6\% \pm 12.7\%$ tear; length, $13.5\% \pm 5.7\%$; and thickness, $45.9\% \pm 17.7\%$ (**Table 7.3**).

7.3.4 Comparison of Partial Tear Size and Proposed Tear Size Classification System

There was a significant correlation between patellar tendon thickness and % tear thickness ratio ($R = 0.815$; $p < 0.001$) (**Figure 7.5**). However, there was only a moderate correlation for width of

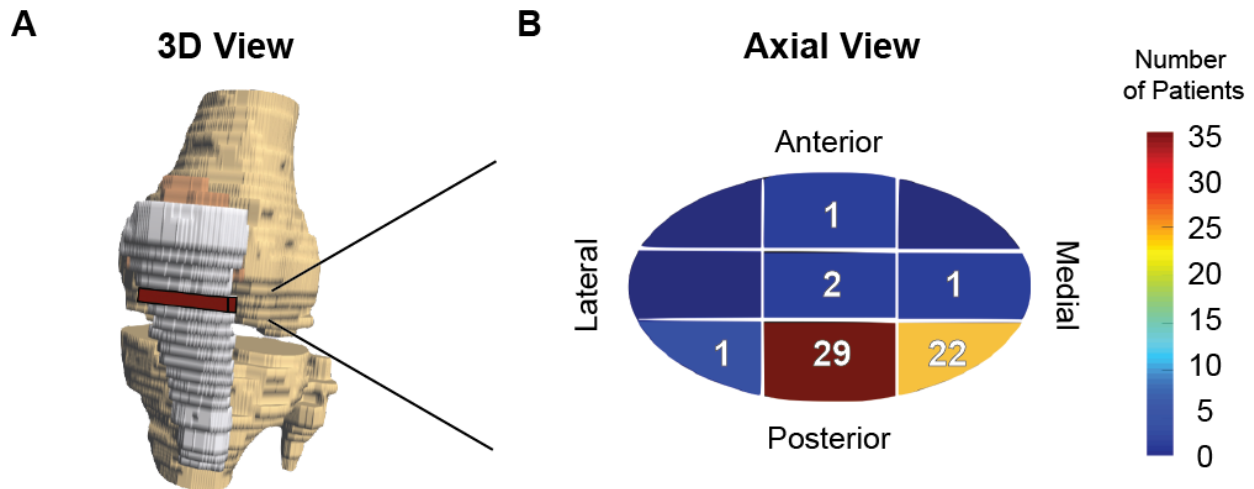


Figure 7.4: PPTTs are located in the posterior and the posteromedial region of the proximal patellar tendon. PPTTs were almost exclusively (100%) located in the proximal part of the patellar tendon, near the patellar attachment, as shown in (A) the 3-dimensionally (3D) reconstructed patellar tendon of the representative knee MRI. 91% of PPTTs involved the posterior and posteromedial regions of the proximal patellar tendon as shown in (B) the frequency heat map in the axial slice. MRI, magnetic resonance imaging; PPTT, partial patellar tendon tear.

Table 7.3: Partial Patellar Tendon Tear Geometry (N = 56 Patients)

Tear	Tear Size	
	Absolute Dimension (mm)	Normalized (%)
Length	9.1 ± 4.2	18.6 ± 12.7
Widths	6.2 ± 4.8	13.5 ± 5.7
Thickness	4.6 ± 2.2	45.9 ± 17.7

tendon and % tear width ($R=0.47, P=0.002$), and no significant correlation for length of tendon and percentage tear length ($R=0.26, P=0.54$). All patients who underwent repair surgery had tear sizes above 50% thickness (median 61.8%, $p < 0.01$) with median tear thickness of 10.32 mm ($p < 0.01$). There was no correlation between patellar tendon size, partial tear size, or % tear size and the ability of the subject to return to the previous activity level (**Figure 7.6**).

Logistic regression and sensitivity analyses showed that patellar tendon thickness measurement predicts whether the tendon is normal or symptomatic ($AUC=0.885, p < 0.001$) (**Figure 7.7A**). The analysis showed that patients with patellar tendon thickness > 7.46 mm were symp-

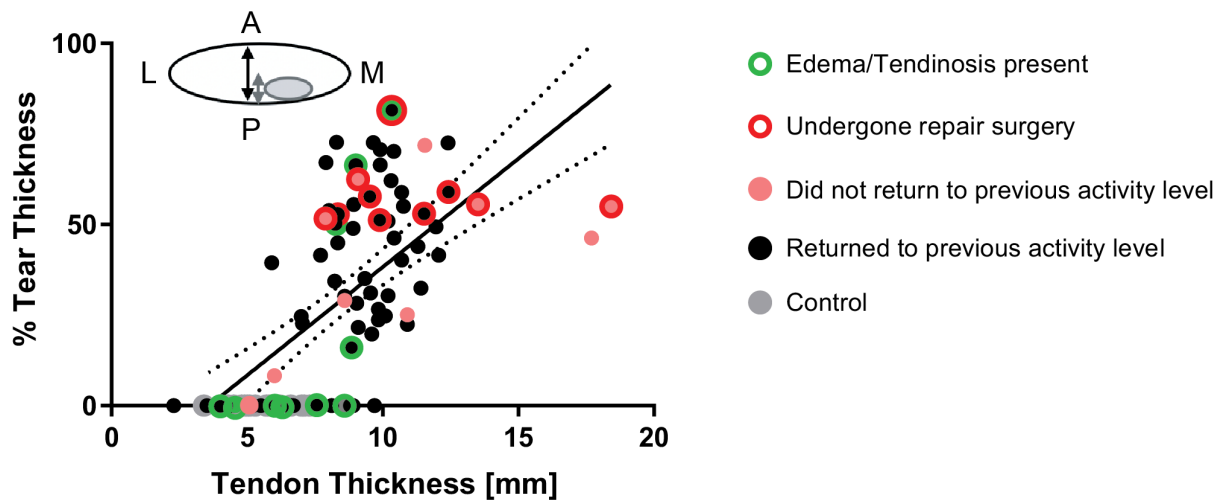


Figure 7.5: *The severity of PPTTs directly correlates to patients’ patellar tendon thickness.* The plot represents relationship between percentage tear thickness and tendon thickness. There was a significant correlation between patellar tendon thickness and percentage tear thickness ratio ($R = 0.815$; $p < .001$). All patients in our cohort who underwent repair surgery had partial tear $>50\%$. Dotted lines indicate 95% CI. Black oval denotes axial view (anterior to posterior) of patellar tendon. Grey oval denotes a PPTT within a patellar tendon. A, anterior; L, lateral; M, medial; P, posterior.

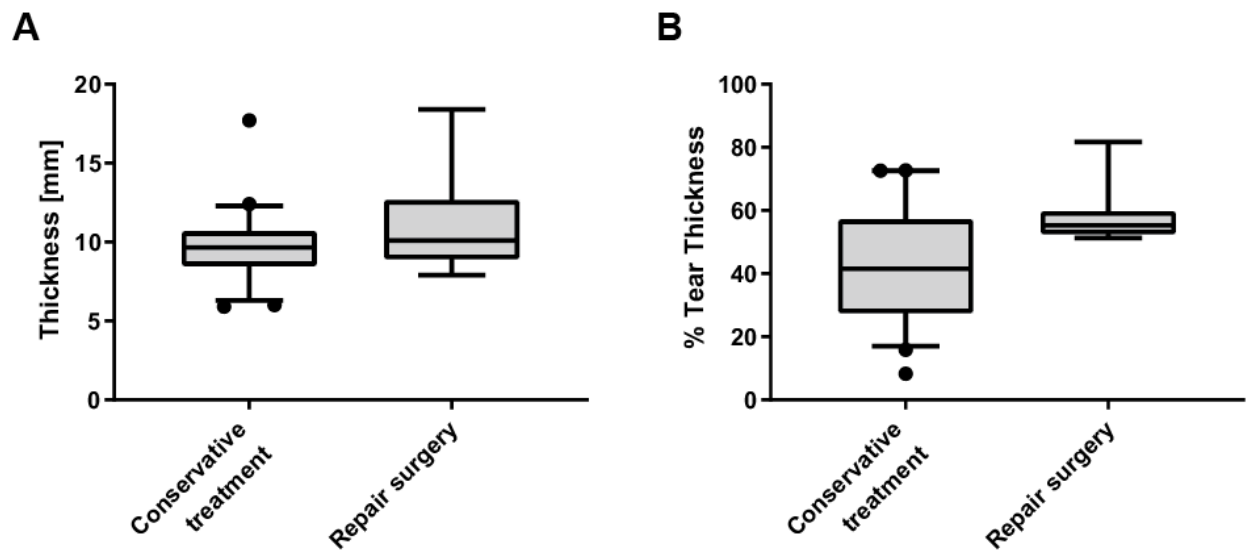


Figure 7.6: *Increase in thickness and percentage tear thickness has shown to influence treatment choices.* Patients undergoing surgery for PPTT had (A) median tear thickness of 10.32 mm ($p < 0.01$) and (B) greater than 50% tear thickness on axial imaging of the tendon ($p < 0.01$).

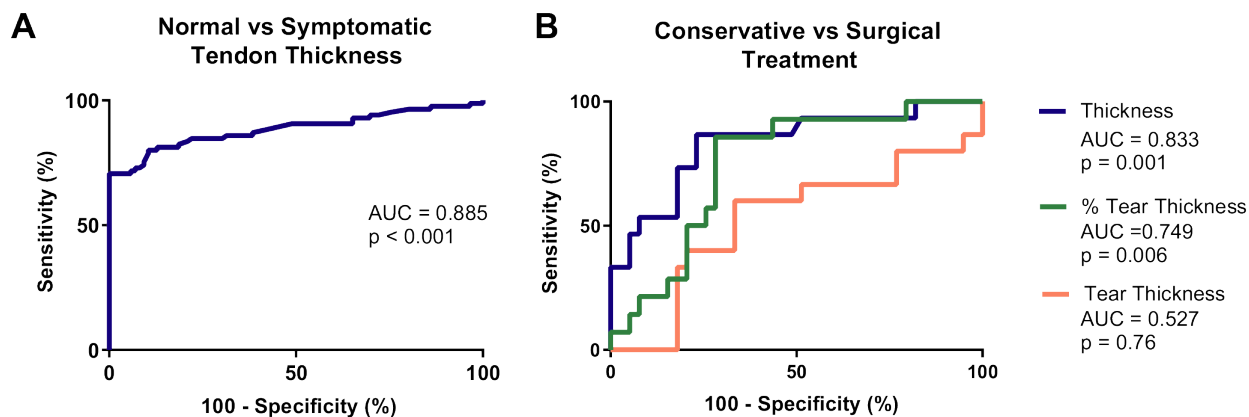


Figure 7.7: The most sensitive predictor for detecting the presence of a partial tear is patellar tendon thickness. The normalized percentage tear thickness predicts the effectiveness of non-operative therapy. Sensitivity analysis for PPTT predictors show (A) patellar tendon thickness measurement was an excellent predictor of whether the tendon was normal or had PPTTs (AUC = 0.885; $p < 0.001$). (B) Patellar tendon thickness (AUC = 0.833; $p = .001$) and normalized percentage tear thickness (AUC = 0.749; $p = .006$) were better predictors for PPTT treatment than tear thickness (AUC = 0.527; $p = .76$). AUC, area under the curve; PPTT, partial patellar tendon tear.

omatic (i.e., they had patellar tendinopathy with or without partial tear in the patellar tendon), with 100% specificity and 70.6% sensitivity. Furthermore, logistic regression analysis showed that tear thickness was not a good measure (AUC=0.527, $p=0.76$) to establish a treatment plan with high specificity (Figure 7.7B). However, tendon thickness (AUC=0.833, $p=0.001$) and % tear thickness (AUC=0.749, $p=0.006$) were more useful classifiers. Thickness of the patellar tendon > 11.45 mm predicted the need for surgical treatment in all patients, where the Youden's index (optimal threshold value) corresponded to tendon thickness > 8.8 mm (86.8% sensitivity and 76.9% specificity) Furthermore, PPTTs with tear thickness of 72.7% or more predicted surgical management in all patients, where Youden's index for surgical repair corresponded to a tear > 55.7% thickness (82.5% sensitivity and 75.8% specificity).

Based on the above results, an image-based PPTT classification, the Popkin-Golman (PG) classification system, is proposed. This system focuses on the normalized % tear thickness as a predictor of severity of pathology (Table 7.4). Similar to the established Cofield and Ellman rotator cuff classification system [290, 291, 292], we classified patellar tendinopathy as follows: Grade 1 – no tear, with tendinosis/edema present in the MRI scan (classic patellar tendinitis); Grade 2

– minor partial tears, with % tear thickness ratio < 25%; Grade 3 – moderate partial tears, with thickness tear % ratio between 25% and 50%; Grade 4 – severe partial tears, with tear % ratio is > 50%. The classification system found that patellar tendon thickness and tear thickness gradually increased as patients reached higher grades of disease (**Figure 7.8**). When the proposed PPTT classification system was used with the patients in the current study, 29 were classified as grade 1, 10 as grade 2, 21 as grade 3, and 25 as grade 4. A representative MRI scan for each grade is shown in **Figure 7.9**. The classification system demonstrates that patellar tendon thickness and tear thickness increase by grade, as predicted. All patients who underwent surgical repair were PG grade 4.

Table 7.4: Distribution of PPTTs According to Proposed Popkin-Golman MRI Grading

Grade	Criteria (% Tear Thickness)	Thickness (mm)		Patients (n)		
		Tendon	Tear	Overall	Surgery	Did Not Return to Sport
1	No tears	6.15 ± 1.86	0	29	0	2
2	< 25%	8.71 ± 1.65	1.8 ± 0.6	10	0	1
3	25% - 50%	10.03 ± 2.37	3.8 ± 1.4	21	0	3
4	>50%	10.27 ± 2.22	6.3 ± 1.5	25	11	5
Total				85	11	11

7.3.5 Robustness of the Proposed PPTT Classification System

The intraclass and interclass correlation coefficients (ICCs) for patellar tendon width, thickness, as well as partial tear width and thickness, are shown in **Table 7.5**. The intra-observer reliability for each observer was excellent (> 0.9). Furthermore, close agreement was found between observers for all parameters. Our image-based classification also correlated with the gold standard Blazina classification system (**Figure 7.10**). The number of patients with higher PG grading (i.e. PG grades 3 and 4) increased with the increase in Blazina grading for 20 patients randomly selected for ICC analysis. There were no patients who had Blazina grade 4 in our analyzed cohort. Out of

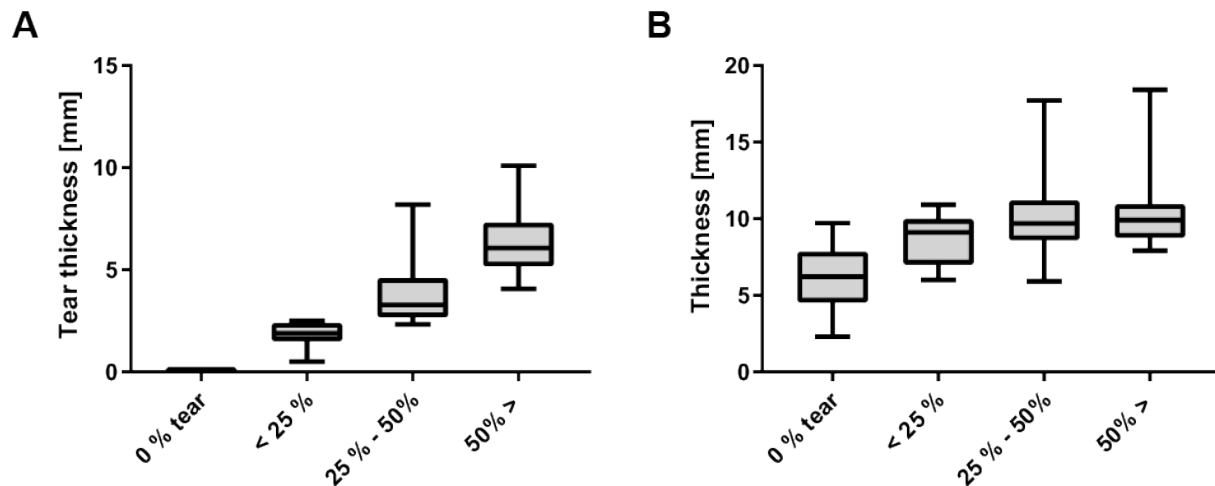


Figure 7.8: In the PG classification system patellar tendon thickness and tear thickness increase by grade. Patellar tendon (A) tear thickness and (B) thickness increased with increasing grade (tear percentage). Values are presented as median, interquartile range, 95% CI, and outliers.

9 patients with Blazina grade 3, 4 (44%) had PG grade 4. Of those patients, 2 had reconstructive surgery and a return to previous level of activity, while 1 did not return to sport after undergoing nonoperative treatment (Figure 7.11).

7.3.6 Histological Evaluation of Healthy Patellar Tendon

Collagen fiber density and vascularity varied along the patellar tendon cross section (Figure 7.12). There were no apparent organizational differences between the proximal and distal portions of the patellar tendon. However, there were apparent differences in patellar tendon collagen fascicle organization and density when comparing the anterior and posterior aspects of the patellar tendon. Collagen fascicles in the anterior tendon were loosely packed with substantial interfascicular connective tissue. In contrast, tendon fascicles in the posterior-medial side, where PPTTs commonly occur, were tightly packed. Vascularity, as evidenced by the presence of capillaries, was more prevalent on the anterior side of the tendon and rarely found in the posterior tendon.

Popkin-Golman Classification for PPTT

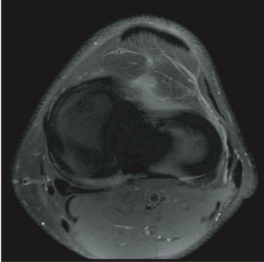
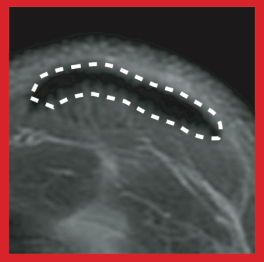
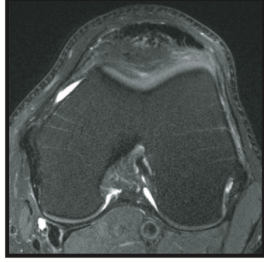
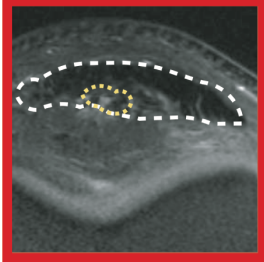
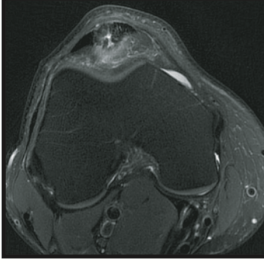
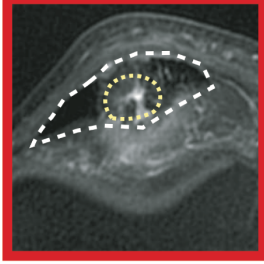
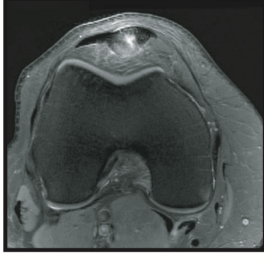
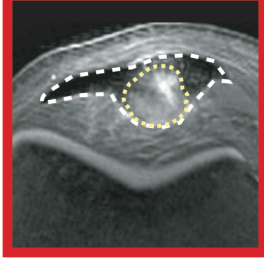
	Axial	Zoomed	Blazina correlate and treatment options
<p>Grade 1</p> <p>No Tear, Thickness on AP < 8 mm</p>			<p>Correlate:</p> <p>Blazina Grade 1 Tendinosis present, patellar tendon hypertrophy <8.8 mm</p> <p>Treatment options:</p> <p>Brace, physical therapy with eccentric strengthening, +/- NSAID</p>
<p>Grade 2</p> <p>Tear Thickness < 25 %</p>			<p>Correlate:</p> <p>Blazina Grade 1 - 2 PPTTs < 25 %</p> <p>Treatment options:</p> <p>Brace, physical therapy with eccentric strengthening, +/- NSAID, +/- PRP, +/- ESWT</p>
<p>Grade 3</p> <p>25% < Tear < 50 %</p>			<p>Correlate:</p> <p>Blazina Grade 2-3 PPTTs < 50%</p> <p>Treatment options:</p> <p>+/- dry needling, +/- PRP, +/- ESWT, brace, physical therapy with eccentric strengthening, +/- NSAID</p>
<p>Grade 4</p> <p>Tear Thickness > 50 %</p>			<p>Correlate:</p> <p>Blazina Grade 2 - 3 PPTTs > 50%, monitor for 6 mo</p> <p>Treatment options:</p> <p>+/- dry needling, +/- PRP, +/- ESWT, brace, physical therapy, +/- NSAID, possible surgical debridement and repair if not better after 6 mo.</p>

Figure 7.9: The Popkin-Golman classification system. Representative MRI of the patellar tendon with the proposed PPTT grading scheme. The middle column is a zoomed axial slice, with the patellar tendon outlined in white and the PPTT outlined in yellow. The final column shows the Blazina grading correlate, with possible treatment options currently available for each Popkin-Golman grade. AP, anteroposterior; MRI, magnetic resonance imaging; PPTT, partial patellar tendon tear.

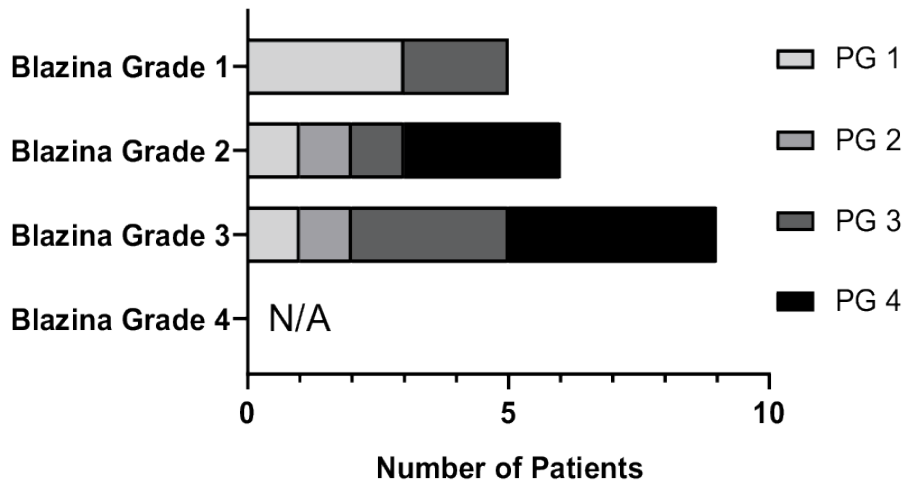


Figure 7.10: Image-based PG classification correlates with the gold standard Blazina classification system. Relationship between Blazina classification and proposed image-based quantitative Popkin-Golman (PG) classification system for 20 patients selected for intra-class correlation coefficient analysis. N/A, not applicable.

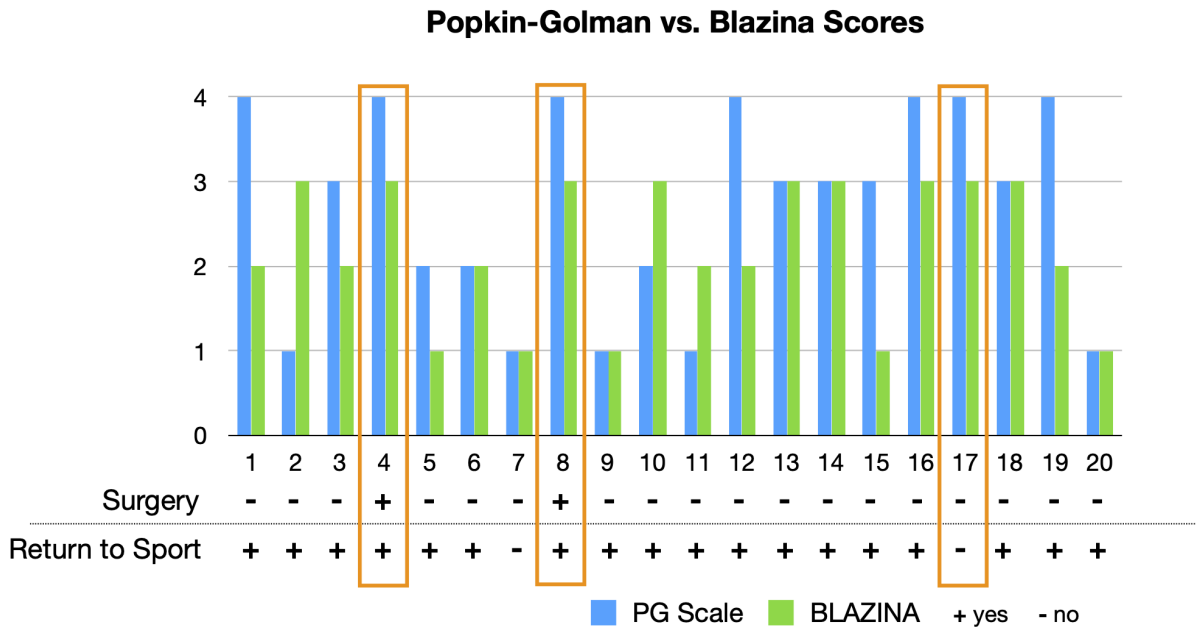


Figure 7.11: Combining the PG classification system and clinical measures will guide treatment decisions and result in more predictable outcomes. Blazina and PG grading for 20 patients randomly selected for ICC analysis. The bottom two line represents whether each patient had reconstructive surgery and whether patient returned to previously level of activity (returned to sport) at the time of follow-up (+ :yes, and - :no). Orange outline represents patients who might have benefited from employing the PG grading scheme in addition to the gold-standard Blazina classification system.

Table 7.5: Intra- and Inter- observer Reliability Analysis: Popkin-Golman (PG) MRI Grading

	Intra-rater Reliability		Inter-rater Reliability	
	ICC	95% CI	ICC	95% CI
PG Score	0.993	0.985 - 0.997	0.993	0.987 - 0.997
Blazina Score	1	1.000 - 1.00	-	-
PT				
Width	0.985	0.969 - 0.994	0.960	0.953 - 0.989
Thickness	0.992	0.983 - 0.997	0.972	0.941 - 0.988
Tear				
Width	0.995	0.989 - 0.998	0.931	0.844 - 0.972
Thickness	0.992	0.983 - 0.996	0.986	0.972 - 0.994
% Tear Thickness	0.989	0.976 - 0.995	0.977	0.954 - 0.990

7.4 Discussion

PPTTs are a clinically challenging problem, lacking a quantitative classification system to guide prognosis and treatment. The analysis from a previous chapter (**Chapter 6**) showed the possibility to correlate changes in tendon geometry with its diminished injury preventative mechanisms. Indeed, the current chapter successfully presents a clinical example where assessing geometric adaptations to the patellar tendon and its attachment via quantitative MRI-based analysis identified the different stages of tear progression. By statistically correlating injury progression and prognosis, an image-based partial patellar tendon tears classification system, was postulated. This classification system identifies high risk athletes likely to have a partial tear and can be used to guide treatment decisions for these patients.

To our knowledge, this is the first study to evaluate PPTT location and characteristics based on MRI and to correlate those characteristics with treatment choices. In the study, 91% of PPTTs were in the posterior and/or posteromedial region of the proximal tendon. Histological, biomechanical, and computational studies have examined the characteristics of the proximal tendon and demonstrated that fiber composition and stresses of the posterior tendon differ from those of the anterior tendon. Hamilton and Purdam [293], as well as Hansen et al [286], found that the posterior

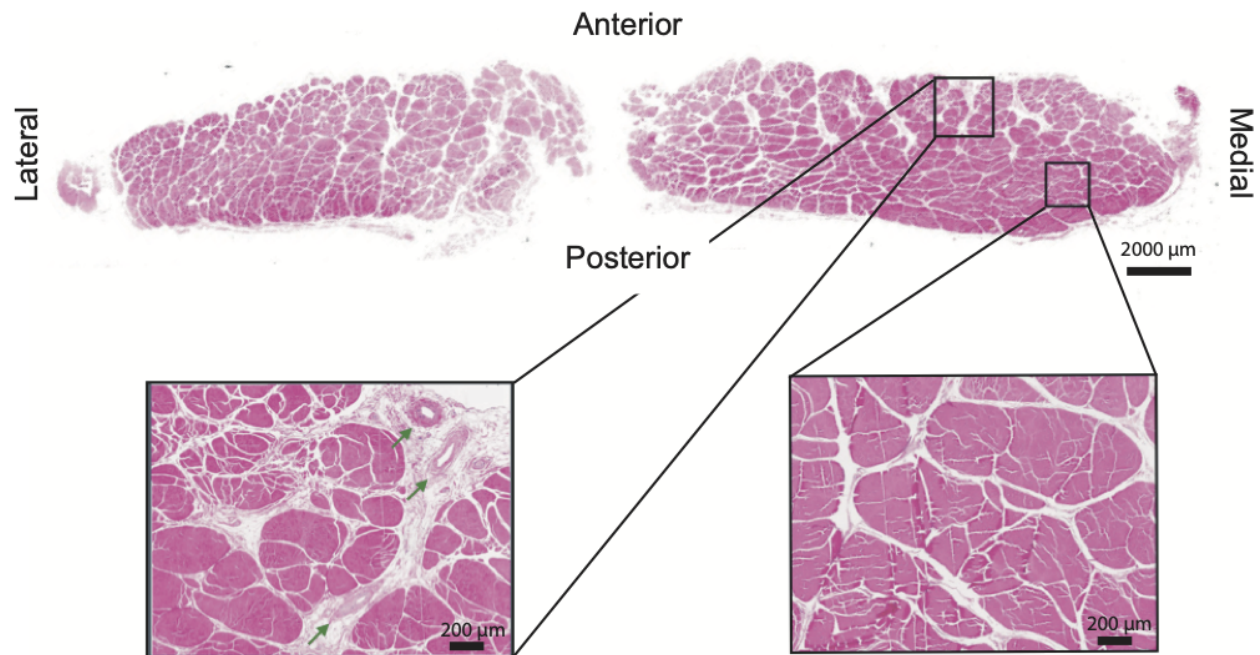


Figure 7.12: *Histological sections of healthy proximal patellar tendon.* Collagen fascicles in the anterior side were loosely packed with substantial interfascicular connective tissue. In contrast, tendon fascicles in the posterior-medial side, where PPTTs commonly occur, were tightly packed. Vascularity, as evidenced by the presence of capillaries (green arrows), was prevalent on the anterior side and rarely found on the posterior side. PPTT, partial patellar tendon tear

fibrils of the tendon were smaller in diameter, and shorter in length, and had a higher concentration of cross-linking as compared with anterior fibrils. Given the relative difference in the initial length of fibers, the shorter posterior fibers would experience greater strain for a given applied force, as depicted in the positional-recruitment model described in **Chapter 4**. Indeed, Basso et al [294] found that strain during knee flexion was highest in the posterior fibers and increased between 60° and 90° of flexion. A two-dimensional computational finite element analysis (FEA) model predicted that the mean localized strain increased significantly, almost doubling the applied strain, within the area of the proximal patellar tendon with the increase in the magnitude of applied patellar tendon strain. Furthermore, the maximum strain increased and moved posteriorly in the tendon as the knee flexion angle increased [119]. This was further corroborated clinically by a study that found that increased knee flexion during jump landings was associated with the development of patellar tendinopathy in male volleyball players [277, 295]. Thus, it is not surprising that posterior edema and tearing occur in athletes who are consistently landing with high forces and placing high

stresses on the posterior tendon.

Tendon cells are known to be mechanosensitive, with the ability to alter the extracellular matrix in response to the local loading environment [296, 297]. The morphological changes Hansen et al [286] reported in posterior fascicles of the patellar tendon (i.e., increase in cross-linking) might be a result of stress-induced local architectural adaptations to the extracellular matrix of the tendon. Furthermore, many studies show that the excessive and repetitive tensile overloading induces microscopic tissue damage within the tendon, which leads to tissue degeneration and ultimately tears [297, 298, 237, 299]. *In vivo* fatigue loading in an animal model showed increase formation of localized kinked fiber deformations, fiber delimitation, scar tissue formation, and increases in gene expression for various matrix metalloproteinases (MMPs) [298]. Biomechanical testing of cadaveric patellar tendons with loads up to 4250 N, reflecting the loading forces and knee joint flexion angles predicted to occur during jump landing, showed localized disruption in the tendon fascicle architecture in the posterior region of the patellar tendon [119], similar to where our study found PPTTs to occur. Indeed, the injury localization and propagation mechanisms of the patellar tendon under repetitive loading mirror the loading-dependent micro- and micro-scale toughening mechanisms described in **Chapter 3**. Taken together, under repetitive overloading, the proximal posterior and/or posteromedial region of the proximal tendon is at a greater risk for micro-level fibrillar damage to occur and further potentiate to macro-level injury (PPTTs).

The pathogenesis of PPTTs may be also influenced by the microvascular supply in the posterior/posterior medial side region of the tendon. Axial whole section histology revealed that vascularity is limited in that region of the patellar tendon, where PPTTs commonly occur. These findings are consistent with the work by Pang et al [300] in their cadaver study examining the arterial blood supply of the patellar tendon. The authors found the anterior patellar tendon to have a rich blood supply from 3 main vessels (inferolateral geniculate, anterior tibial recurrent, and inferomedial geniculate) with the posterior patellar tendon receiving blood supply from the smaller, retropatellar anastomotic arch in Hoffa fat pad. This is similar in concept to the watershed areas seen in the Achilles where tendon rupture occur [301, 302] and the hypovascular region in the supraspinatus

tendon where partial tears are located [107, 106].

While the current study did not follow the progression of imaging over time in patients with tendinopathy and partial tearing, the athletes did have a spectrum of severity on imaging that correlated with nonoperative treatment success. The spectrum of pathology included proximal thickening of the tendon, edema in the posterior aspect of the tendon, and partial tear of varying thickness on axial imaging. The thickness of the tendon was most predictive of the presence of partial tearing in the tendon, with thickness of 8.8 mm or greater on axial MRI being the most predictive. It is important to note that the majority of patients in this study were able to return to previous level of activity without surgical intervention. Participants with PPTTs that were classified as PG Grades 1-3 had an 87% return to activity (n=39/45) with nonoperative (i.e., conservative) measures including physical therapy, NSAIDS, dry needling, and PRP injections. However, a tear of > 55% of the total tendon thickness from anterior to posterior on the axial view was most predictive of failure of nonoperative treatment and eventual progression to surgery, as all patients in our study who underwent surgery had a tear > 50% tendon thickness. While nonoperative treatment is generally successful for patellar tendinopathy, these factors may be important to consider in the treatment of athletes with significant thickening or partial tearing of the tendon, particularly those with seasonal timing considerations for treatment.

Studies of treatment outcomes have had varied results, including a randomized study in which there was no difference in outcomes between surgical and nonsurgical treatment [303]. However, treatment guidelines have been based only on symptoms (e.g., driven by Blazina or VISA scores) and imaging characteristics have not typically been quantified. When we compared the patellar tendons in the wide range of PG grading to the gold-standard Blazina grading, we found that the risk of misdiagnosing the extent of the injury was high when the symptom-based classification Blazina system was used (**Figure 7.11**). For instance, in our study, several athletes with the same symptoms and functional limitations (Blazina 3) had different PG grades (1-4); these patients may have benefited from different therapeutic approaches than those implied by the Blazina classification. Combining imaging and clinical measures to guide treatment decisions will result in more

predictable outcomes. For example, if it is known that a patient with significant symptoms has a patellar tendon thickness of > 11.5 mm or a tear of $> 50\%$ thickness, the prognosis for improvement with nonoperative treatment is worse than for someone with a smaller thickness and 25% PPTT. This prognostic information could help both the surgeon and the patient determine the length of the trial of nonoperative treatment before surgical intervention, which will improve the satisfaction of the patient with the treatment choice (e.g., the patient may consider surgery earlier if patellar tendon thickness is > 11.5 mm and PPTT is $> 50\%$). The addition of imaging characteristics in the study of patellar tendon pathology will also allow for more directed research in the outcomes of patellar tendinopathy. If researchers and, ultimately, providers can more consistently identify optimal candidates for each treatment option, outcomes of surgical and nonsurgical treatment of patellar tendinopathy and PPTTs will be improved.

The most significant limitation of this study is the retrospective nature of patient evaluation. This study collected all the patient data from the previous >15 years at our institution; hence, it was not feasible to obtain consistent patient-reported outcome measures. The only outcome measure that we could report uniformly from chart review was the Blazina score and return to previous level of activity at the time of follow-up. Prospective evaluation of tear characteristics and treatment choices in future studies will allow for a more rigorously defined progression of disease and ultimately validate the new classification system to guide treatment choices and outcomes. Despite this, the clear finding that a tear with $> 50\%$ thickness strongly correlates with the need for surgical treatment is helpful to define future study designs and for patient counseling regarding prognosis and treatment options. A second limitation was that a relatively small number of patients who required surgery because nonoperative treatment was typically successful. The third limitation was in the limited number of patients selected to do intra-rater and inter-observer variability analysis. Finally, the classification system was not tested in a population other than the one in which the system was derived. Nevertheless, this is a large study of patellar tendinopathy and PPTTs on MRI and can help guide future prospective study.

7.5 Conclusion

This chapter successfully used injury-induced architectural adaption to the patellar tendon and its insertion as a diagnostic tool to guide treatment choices and outcomes. Partial patellar tendon tears were found in the posterior and posteromedial portion of the tendon. The most sensitive predictor for the presence of a partial tendon tear was the thickness of the tendon, in which thickness >8.8 mm was strongly correlated with the presence of a tear. The proposed Popkin-Golman classification system (1-4) for PPTT can be used to help guide treatment. On the basis of these results, surgeons should consider operative treatment for patients with patellar tendon thickness >11.5 mm or tear thickness greater than 50% on axial MRI imaging who have failed nonoperative treatment for 6 months.

Chapter 8: Conclusions and future directions

8.1 Summary of the dissertation

Materials with microstructural architectures that endow them with unique mechanical functions can be found throughout nature and have recently been implemented in engineering structures [2]. However, application of this new class of materials in engineering practice is hindered by a lack of understanding on how to attach them. Nature's solution to this problem is found at the attachment ("the enthesis") of tendon and bone, two vastly different architected materials. The tendon enthesis provide joint stability and mobility and exhibits toughness across a wide range of loadings. Nevertheless, many painful and physically debilitating conditions occur at or near this interface when this architecture is compromised [127, 129]. Even with surgical intervention, natural healing processes does not restore the functional attachment unit and often fail [100, 111]. Despite progress in understanding how the enthesis achieves a strong attachment under sub-damage loading regimes [54, 67, 64, 72], it remained unclear how toughness was achieved to prevent interfacial failure. Understanding these mechanisms is critical to guide engineering and medical approaches to bimaterial attachment. Hence, the main objective of this dissertation was to define the architectural features of the enthesis that endow it with its remarkable toughness.

This dissertation first investigated architectural and compositional contributions to enthesis toughness using the mouse enthesis as a model system. A novel micro computed tomography (CT) imaging scheme was developed to enable simultaneous visualization of mineralized and unmineralized collagen across the enthesis. High-resolution microCT imaging revealed a new view of the tendon enthesis dominated by a continuous, fibrous primary insertion site. Mouse tendon entheses failed through avulsion of a bone plug when stretched to failure quasi-statically, and not at the mineralized interface within fibrocartilage where stress concentrations were predicted to occur

[54]. The healthy tendon enthesis showed a unique ability to store energy and provide resilience against attachment failures.

The enthesis is durable against the complex and repeated loadings of daily activities [149], but failure mechanisms change with loading regime and age. Avulsions and tendon mid-substance failures are common in high-impact injuries for pediatric patients [304], but rupture at the tendon end of enthesis is prominent in degenerated rotator cuffs of adult patients [96, 101]. Guided by these clinical observations, a series of experiments were conducted to quantify how fibrous networks degrade through monotonic (acute) and cyclical (degenerative) loading. Mouse supraspinatus entheses had three distinct failure modes that were dependent on the loading regime, largely mimicking what is observed in the clinic. Using interrupted mechanical testing and fluorescent microscopy successfully, we tracked molecular-scale collagen damage accumulation due to loading. These experiments uncovered that the evolution of damage through tissue failure was dependent on its loading history: under monotonic loading to failure, energy sufficient to avulse bone was stored in the enthesis with relatively little energy dissipation, while in cyclical loading, energy was absorbed by damage within the tendon and enthesis, eventually leading to failure within the unmineralized tissue. These results indicate that the enthesis contains multiscale toughening mechanisms, where fiber-level toughening mechanisms exist to resist monotonic loading and an underlying nanoscale mechanism exists to resist cyclical loading.

Tendons contain different fibrous architectures depending upon their particular function within a joint [173, 192]. Excursion and deformation differs significantly among tendons, as does ROM varies greatly from joint to joint [176]. However, it remains unclear how enthesis toughness is maintained over the staggering range of orientations necessary for joint function. In the next part of the dissertation, a series of experiments and numerical models were developed to determine the roles of architectural and positional factors on enthesis toughness. Enthesis behavior in the rotator cuff, including strength and toughness, varied with the angle of abduction. This was a surprise given the shoulder's ability to resist injury across its broad range of motion [305]. Contrast enhanced images of several joints at different positions showed that the bone ridge anatomy where

tendon attaches to bone significantly affected the orientation and engagement of tendon enthesis fibers, suggesting that fibers engaged or buckled depending on loading, consistent with previous observations in human rotator cuff injury [178, 182]. The novel position-dependent fiber kinematic model reproduced many of the trends observed in the *ex vivo* experiments, showing that normalized strength and toughness increased with decreasing abduction angle, while stiffness decreased with decreasing abduction angle. The mechanism driving this behavior was position-dependent fiber recruitment. Simulations also provided insights into why thresholds for injury differ with loading angles for each joint with varying bone ridge geometry. The positions at which soft-tissue failures are observed in the clinic coincided with the lowest respective strengths in the simulations. Taken together, the model and experiments demonstrated that the fibrous architecture of the tendon enthesis enabled its fibers to reorient, recruit, and subsequently rupture to balance strength and toughness across a wide range of motion.

The functionally graded composition of mineral and proteoglycan content at the tendon enthesis suggests an intricate balance in stiffening and toughening constituents to allow for effective load-transfer between tendon and bone [55, 61]. Previous modeling works have described a role of mineral in stiffening the tendon enthesis and mitigating stress concentrations at the interface [54, 67]. This dissertation examined the biomechanical effects of chemically removing each of these constituents, mineral and proteoglycan, on the tendon enthesis. The results showed that tendon enthesis composition, particularly the mineral content, drives enthesis strength and stiffness, but does not significantly affect its failure mode. These findings corroborate clinical observations, where loss of enthesis strength is attributed to loss of bone mineral density in the humeral head after both injury and repair [306, 132]. The role of proteoglycan content on tendon enthesis mechanics, on the other hand, remains unclear, as the only partial digestion was achieved at the enthesis in our experiments.

Musculoskeletal tissues are highly mechanosensitive, with the ability to alter tissue architecture and composition in response to loading. In this dissertation, we investigated how composition and architecture are modulated at the enthesis *in vivo* by varying the loading environment of mouse

shoulders via botulinum toxin A-induced underuse/paralysis or treadmill-induced overuse. Modifications in the loading environment achieved physiologically relevant changes to mineralization patterns at the enthesis and led to divergent changes in enthesis biomechanical and microarchitectural properties. Similar to prior studies in rats and mice [64, 129, 235], underuse decreased strength and stiffness; on the other hand, overuse increased stiffness while maintaining strength. While all specimens failed via avulsion under monotonic loading regardless of their treatment, the failure pattern was distinct depending on loading: there was a shift in fracture location and fracture quantity. The differential mechanical and failure behaviors of compromised enthesis were dictated by changes to the trabecular micro-architectural network underlying the tendon enthesis. Underloading prompted active removal of the trabecular architecture underneath the enthesis, mimicking the trabecular microarchitectural changes seen in osteoporosis [270]. On the other hand, overuse loading prompted active reinforcement and thickening of trabecular plates, resembling trabecular microarchitectural adaptations seen in osteoarthritis [20]. The trabecular micro-architecture at the tendon enthesis oriented to support and share the load (or lack of load) into orientations of relatively low enthesis strength and toughness. Pearson correlation also revealed that the entheses strength, stiffness, and failure properties correlated strongly with mineralized enthesis architecture, consistent with clinical findings [264, 265].

The strong correlation between tissue architecture and composition with its mechanical properties suggests the potential for tracking architectural changes to a tendon and its enthesis to diagnose the different stages of injury progression and prognosis. In this dissertation we showed a clinical example that applies this concept for classifying partial patellar tendon tears. Retrospective evaluation of MRI characteristics of patients with patellar tendinopathy and partial tears showed that 91% partial tears involved the posterior and posteromedial regions of the proximal tendon near its enthesis. Following what has been previously done for rotator cuff injury [107, 290, 291], we employed logistic regression and sensitivity analysis to define the relationship between tear characteristics and clinical outcome. The most sensitive predictor for detecting the presence of a partial tear was a patellar tendon thickness ratio (i.e., normalized tendon dimension per patient),

with tear thickness $>55.7\%$ predicted necessity of surgical management. A novel proposed classification system for partial tears, the Popkin-Golman classification, can be used to guide treatment decisions for patients with patellar tendinopathy and partial patellar tendon tears.

8.2 Limitations

This dissertation used a mouse model to understand how the architecture of the tendon enthesis is designed for toughness. Small animal models such as mice are increasingly being used to study the enthesis due to their low cost and relative ease of genetic manipulation. This allows for future studies examining molecular mechanisms of development or disease, which are difficult to perform in patients. We chose a mouse model to study the fundamental toughening mechanisms of the tendon enthesis because donor (patient or cadaveric) tissues have complex health histories and typically present in the late-stages of disease progression. However, the mouse enthesis is architecturally simpler than the human enthesis. Human tendon entheses are highly heterogeneous and contain complex architectural features, such as double-layered interwoven fibers between adjacent tendons [307]. It has been suggested that small animals may not have all of the hierarchical levels of humans due to their smaller sizes [37]. Several studies using larger animal models and cadaveric tissues show the presence of fiber-to-fascicle load transfer mechanisms, such as inter-fiber sliding and inter-fascicular shear transfer [36, 184, 308]. Hence, it is possible that architectural features uniquely found in larger animals may also contribute to toughening mechanisms at the enthesis. Future studies should to be conducted using large animal models or cadaveric tissues to confirm features described in the current thesis for mice and to establish additional toughening mechanism that may exist at hierarchies not seen in the mouse.

Any limitations specific to the methodologies employed for experiments and models of this dissertation are discussed in each chapter. However, a key limitation not yet mentioned is that only male mice were used for characterizing toughening mechanisms. It has been reported in both animals and humans that sex significantly affects the mechanical proprieties of tendons and ligaments [309, 310, 311]. It will be important to include female mice and consider sex as a biological

variable when conducting future studies. Furthermore, the *ex vivo* and *in vivo* experiments were conducted on young skeletally mature (12 weeks to 16 weeks aged) mice to establish putative toughening mechanisms. Clinically, many injuries to the tendon enthesis occur in elderly population [105]. Future studies should consider using aged mice to characterize whether toughening mechanisms at the tendon enthesis degrade with age.

8.3 Conclusions and outlook

This dissertation revealed architectural toughening mechanisms at the enthesis, providing guidance for implementation of biomimetic strategies for attachment of dissimilar materials (**Figure 8.1**). First, energy storage in a compliant region of the fibrous attachment was protective, precluding fracture of the intricately architected transitional tissue and instead leading to fracture of more easily regenerated bone. While counterintuitive, a tough, architected compliant material attaching two dissimilar materials occurs across nature [6], e.g., in nacre [24], tooth enamel [312], and some mollusks [313]. Compliant attachment layers in engineering have also been used in bottom-up and top-down fabrication of architecture materials, such as PMMAs (i.e., soft materials) inserted in between alumina layers [314], to absorb energy and channel crack propagation, and polymeric foams inserted into metallic foams [315].

Second, the tendon enthesis harnesses its fibrous nature for effective load transfer. Nanoscale energy absorption by collagen molecules resists fatigue loading, while milliscale network behavior enables fiber reorientation, recruitment, and load sharing for toughness across loading directions. A similar concept has been applied to topologically interlocked material panels, with failure shared across contiguous panels and localized to repairable regions [17, 198]. Distributions of fibers are further optimized at the enthesis to harness the toughness of the entire fibrous network at all loading directions, and to provide enhanced stiffness in the loading conditions for which muscle forces are highest. This relatively simple mechanism provides a principle that can be readily harnessed for engineering.

Additional features of the enthesis that will be more difficult to harness in engineering are com-

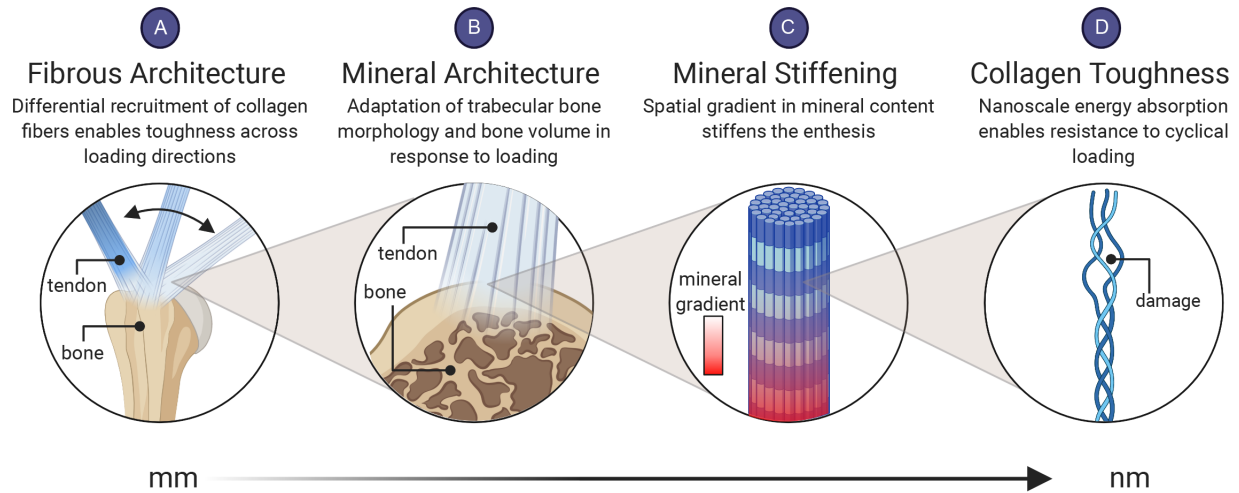


Figure 8.1: The fibrous and mineral architectures of the tendon enthesis provide multiscale toughening mechanisms for a resilient attachment between tendon and bone. At the millimeter length scale (**A**) the fibrous architecture of the tendon enthesis allows for fiber recruitment and re-orientation to optimize toughness over strength across a range of loading directions. At the micrometer length scale (**B**) the enthesis actively adapts its mineral architecture to maintain its strength along the axis of loading. At the micrometer-to-nanometer length scale (**C**) a spatial gradient in mineral across the enthesis reduced stress concentrations [64]. At the nanometer length scale (**D**) collagen damage localization protects against damage prorogating to higher length scales.

positional adaptations of architecture to physiologic loading. *In vivo* loading models revealed bony architecture actively remodeling to maintain strength along the axis of loading, while compromising overall toughness. Microstructural heterogeneity that toughens fibrous interfaces derives in part from mineral nanocrystal reorganization and reorientation [64] but controlling these factors, as well as potential mineral binding proteins such as proteoglycans [87] and osteopontin [31], is currently beyond the scope of current top-down and bottom-up manufacturing techniques.

While damage propagation and failure mechanisms vary within engineered and natural materials, there is an ultimate interest to monitor, arrest, and repair before microscopic damage (e.g., crack initiation) leads to eventual structural collapse. Many strategies have been employed for engineered materials to effectively detect damaged structures during non-destructive inspections and subsequently repaired. For example, monitoring crack length has been employed in aviation and automotive industries for monitoring and establishing service criterion for structural components subjected to alternating loading [316]. The basic principle employed in monitoring and scheduling

maintenance activities for engineered materials may be also applied in soft biological architected materials, such as in tendons, ligaments, and their entheses. This dissertation successfully applied this idea in clinical settings and developed a novel classification system for patellar tendinopathy and partial patellar tendon tears, the Popkin-Golman classification, where normalized percentage tear thickness is used as a criterion (e.g., analogous to crack length in engineered materials) to guide treatment decisions for patients. If similar diagnostic tools are built and implemented for other joints, researchers and, ultimately, providers will be able to locate and monitor sub-failure injuries, and more consistently identify optimal candidates for each treatment option. This will lead to improved outcomes of surgical and non-surgical treatment of soft-tissue musculoskeletal injuries.

In conclusion, this dissertation demonstrated how the tendon enthesis achieves a remarkable balance between strength and toughness through its architecture to resist injurious loads. The toughening mechanisms identified here for the tendon enthesis will inspire and guide strategies for optimizing architecture for tough bimaterial attachments in medicine and engineering.

References

1. Ritchie RO. The conflicts between strength and toughness. *Nature Materials* 2011;10:817–22.
2. Barthelat F. Architected materials in engineering and biology: Fabrication, structure, mechanics and performance. *International Materials Reviews* 2015;60:412–30.
3. Wegst UGK, Bai H, Saiz E, Tomsia AP, and Ritchie RO. Bioinspired structural materials. *Nature Materials* 2015;14:23–36.
4. Barthelat F, Yin Z, and Buehler MJ. Structure and mechanics of interfaces in biological materials. *Nature Reviews Materials* 2016;1:16007.
5. Liu Z, Zhang Z, and Ritchie RO. On the Materials Science of Nature’s Arms Race. *Advanced Materials* 2018;30:1705220.
6. Liu Z, Meyers MA, Zhang Z, and Ritchie RO. Functional gradients and heterogeneities in biological materials: Design principles, functions, and bioinspired applications. *Progress in Materials Science* 2017;88:467–98.
7. Jia Z, Yu Y, and Wang L. Learning from nature: Use material architecture to break the performance tradeoffs. *Materials & Design* 2019;168:107650.
8. Eder M, Amini S, and Fratzl P. Biological composites—complex structures for functional diversity. *Science* 2018;362:543 LP –547.
9. Pham MS, Liu C, Todd I, and Lertthanasarn J. Damage-tolerant architected materials inspired by crystal microstructure. *Nature* 2019;565:305–11.
10. Bouaziz O, Bréchet Y, and Embury J. Heterogeneous and Architected Materials: A Possible Strategy for Design of Structural Materials. *Advanced Engineering Materials* 2008;10:24–36.
11. Ashby MF. Hybrids to fill holes in material property space. *Philosoph. Mag.* 2005;85:3235–57.
12. Overvelde JTB, Weaver JC, Hoberman C, and Bertoldi K. Rational design of reconfigurable prismatic architected materials. *Nature* 2017;541:347–52.
13. Kaplan CN, Noorduyn WL, Li L, et al. Controlled growth and form of precipitating microsculptures. *Science* 2017;355:1395 LP –1399.

14. Raney JR, Compton BG, Mueller J, Ober TJ, Shea K, and Lewis JA. Rotational 3D printing of damage-tolerant composites with programmable mechanics. *Proceedings of the National Academy of Sciences* 2018;115:1198 LP –1203.
15. Martin JJ, Fiore BE, and Erb RM. Designing bioinspired composite reinforcement architectures via 3D magnetic printing. *Nature Communications* 2015;6:8641.
16. Kokkinis D, Bouville F, and Studart AR. 3D Printing of Materials with Tunable Failure via Bioinspired Mechanical Gradients. *Advanced Materials* 2018;30:1705808.
17. Khandelwal S, Siegmund T, Cipra RJ, and Bolton JS. Transverse loading of cellular topologically interlocked materials. *International Journal of Solids and Structures* 2012;49:2394–403.
18. Siegmund T, Barthelat F, Cipra R, Habtour E, and Riddick J. Manufacture and Mechanics of Topologically Interlocked Material Assemblies. *Applied Mechanics Reviews* 2016;68.
19. Pasternak E and Dyskin AV. Architected Materials with Inclusions Having Negative Poisson's Ratio or Negative Stiffness BT - *Architected Materials in Nature and Engineering: Archimats*. In: ed. by Estrin Y, Bréchet Y, Dunlop J, and Fratzl P. Cham: Springer International Publishing, 2019:51–87.
20. Chen Y, Hu Y, Yu YE, et al. Subchondral Trabecular Rod Loss and Plate Thickening in the Development of Osteoarthritis. *Journal of Bone and Mineral Research* 2018;33:316–27.
21. Wang Y, An B, Xue B, et al. Living materials fabricated via gradient mineralization of light-inducible biofilms. *Nature Chemical Biology* 2021;17:351–9.
22. Wang Z, Lee WJ, Koh BTH, et al. Functional regeneration of tendons using scaffolds with physical anisotropy engineered via microarchitectural manipulation. *Science Advances* 2018;4:eaat4537.
23. Mirkhalaf M, Dastjerdi AK, and Barthelat F. Overcoming the brittleness of glass through bio-inspiration and micro-architecture. *Nature Communications* 2014;5:3166.
24. Barthelat F and Espinosa HD. An experimental investigation of deformation and fracture of nacre-mother of pearl. *Experimental Mechanics* 2007;47:311–24.
25. Munch E, Launey ME, Alsem DH, Saiz E, Tomsia AP, and Ritchie RO. Tough, Bio-Inspired Hybrid Materials. *Science* 2008;322:1516 LP –1520.
26. Aizenberg J, Weaver JC, Thanawala MS, Sundar VC, Morse DE, and Fratzl P. Skeleton of *Euplectella* sp.: Structural Hierarchy from the Nanoscale to the Macroscale. *Science* 2005;309:275 LP –278.

27. Wu X, Yang M, Yuan F, et al. Heterogeneous lamella structure unites ultrafine-grain strength with coarse-grain ductility. *Proceedings of the National Academy of Sciences* 2015;112:14501 LP–14505.
28. Glimcher MJ. Bone: Nature of the Calcium Phosphate Crystals and Cellular, Structural, and Physical Chemical Mechanisms in Their Formation. *Reviews in Mineralogy and Geochemistry* 2006;64:223–82.
29. Fratzl P, Gupta HS, Paschalis EP, and Roschger P. Structure and mechanical quality of the collagen-mineral nano-composite in bone. *Journal of Materials Chemistry* 2004;14:2115–23.
30. Alexander B, Daulton TL, Genin GM, et al. The nanometre-scale physiology of bone: steric modelling and scanning transmission electron microscopy of collagen-mineral structure. *Journal of The Royal Society Interface* 2012;9:1774–86.
31. Cavelier S, Dastjerdi AK, McKee MD, and Barthelat F. Bone toughness at the molecular scale: A model for fracture toughness using crosslinked osteopontin on synthetic and biogenic mineral substrates. *Bone* 2018;110:304–11.
32. Vashishth D, Behiri JC, and Bonfield W. Crack growth resistance in cortical bone: Concept of microcrack toughening. *Journal of Biomechanics* 1997;30:763–9.
33. Koester KJ, Ager JW, and Ritchie RO. The true toughness of human cortical bone measured with realistically short cracks. *Nature Materials* 2008;7:672–7.
34. Rho JY, Kuhn-Spearing L, and Zioupos P. Mechanical properties and the hierarchical structure of bone. *Medical Engineering & Physics* 1998;20:92–102.
35. Libonati F, Gu GX, Qin Z, Vergani L, and Buehler MJ. Bone-Inspired Materials by Design: Toughness Amplification Observed Using 3D Printing and Testing. *Advanced Engineering Materials* 2016;18:1354–63.
36. Zitnay JL and Weiss JA. Load transfer, damage, and failure in ligaments and tendons. *Journal of Orthopaedic Research* 2018;36:3093–104.
37. Handsfield GG, Slane LC, and Screen HRC. Nomenclature of the tendon hierarchy: An overview of inconsistent terminology and a proposed size-based naming scheme with terminology for multi-muscle tendons. *Journal of Biomechanics* 2016;49:3122–4.
38. Svensson RB, Herchenhan A, Starborg T, et al. Evidence of structurally continuous collagen fibrils in tendons. *Acta Biomaterialia* 2017;50:293–301.
39. Eyre DR, Paz MA, and Gallop PM. Cross-linking in collagen and elastin. *Annual review of biochemistry* 1984;53:717–48.

40. Cai L, Xiong X, Kong X, and Xie J. The Role of the Lysyl Oxidases in Tissue Repair and Remodeling: A Concise Review. *Tissue Engineering and Regenerative Medicine* 2017;14:15–30.
41. Avery NC and Bailey AJ. Enzymic and non-enzymic cross-linking mechanisms in relation to turnover of collagen: Relevance to aging and exercise. *Scandinavian Journal of Medicine and Science in Sports* 2005;15:231–40.
42. Fang F and Lake SP. Multiscale Mechanical Evaluation of Human Supraspinatus Tendon Under Shear Loading After Glycosaminoglycan Reduction. *Journal of biomechanical engineering* 2017;139:710131–8.
43. Waggett AD, Ralphs JR, Kwan APL, Woodnutt D, and Benjamin M. Characterization of collagens and proteoglycans at the insertion of the human achilles tendon. *Matrix Biology* 1998;16:457–70.
44. Thorpe CT, Birch HL, Clegg PD, and Screen HR. The role of the non-collagenous matrix in tendon function. *International Journal of Experimental Pathology* 2013;94:248–59.
45. Kastelic J, Palley I, and Baer E. A structural mechanical model for tendon crimping. *Journal of biomechanics* 1980;13:887–93.
46. Lee AH and Elliott DM. Multi-Scale Loading and Damage Mechanisms of Plantaris and Rat Tail Tendons. *Journal of Orthopaedic Research* 2019;37:1827–37.
47. No YJ, Castilho M, Ramaswamy Y, and Zreiqat H. Role of Biomaterials and Controlled Architecture on Tendon/Lig. Repair and Regeneration. *Advanced Materials* 2020;32:1904511.
48. Visser J, Melchels FPW, Jeon JE, et al. Reinforcement of hydrogels using three-dimensionally printed microfibrils. *Nature Communications* 2015;6:6933.
49. Williams ML. Stress singularities resulting from various boundary conditions in angular corners of plates in extension. *Journal of applied mechanics* 1952;19:526–8.
50. Genin GM and Hutchinson JW. Failures at Attachment Holes in Brittle Matrix Laminates. *Journal of Composite Materials* 1999;33:1600–19.
51. Hutchinson JW and Suo Z. Mixed Mode Cracking in Layered Materials. *Advances in Applied Mechanics* 1991;29. Ed. by Hutchinson JW and Wu TYBTAM:63–191.
52. Linderman SW, Golman M, Gardner TR, et al. Enhanced tendon-to-bone repair through adhesive films. *Acta Biomaterialia* 2018;70:165–76.
53. Thomopoulos S, Birman V, and Genin GM. Structural interfaces and attachments in biology. 2013.

54. Genin GM, Kent A, Birman V, et al. Functional grading of mineral and collagen in the attachment of tendon to bone. *Biophysical Journal* 2009;97:976–85.
55. Genin GM and Thomopoulos S. The tendon-to-bone attachment: Unification through disarray. *Nature Materials* 2017;16:607–8.
56. Schwartz AG, Pasteris JD, Genin GM, Daulton TL, and Thomopoulos S. Mineral Distributions at the Developing Tendon Enthesis. *PLoS ONE* 2012;7. Ed. by Roeder RK:e48630.
57. Hu Y, Birman V, Demyer-Black A, Schwartz AG, Thomopoulos S, and Genin GM. Stochastic interdigitation as a toughening mechanism at the interface between tendon and bone. *Biophysical Journal* 2015;108:431–7.
58. Buehler MJ. Nature designs tough collagen: Explaining the nanostructure of collagen fibrils. *Proceedings of the National Academy of Sciences* 2006;103:12285–90.
59. Thorpe CT, Peffers MJ, Simpson D, Halliwell E, Screen HRC, and Clegg PD. Anatomical heterogeneity of tendon: Fascicular and interfascicular tendon compartments have distinct proteomic composition. *Scientific Reports* 2016;6:20455.
60. Thomopoulos S, Williams GR, Gimbel JA, Favata M, and Soslowsky LJ. Variation of biomechanical, structural, and compositional properties along the tendon to bone insertion site. *Journal of Orthopaedic Research* 2003;21:413–9.
61. Rossetti L, Kuntz LA, Kunold E, et al. The microstructure and micromechanics of the tendon-bone insertion. *Nature Materials* 2017;16:607–8.
62. Kumagai J, Sarkar K, Uthoff HK, Okawara Y, and Ooshima A. Immunohistochemical distribution of type I, II and III collagens in the rabbit supraspinatus tendon insertion. *Journal of anatomy* 1994;185 (Pt 2:279–84.
63. Schwartz AG, Long F, and Thomopoulos S. Enthesis fibrocartilage cells originate from a population of Hedgehog-responsive cells modulated by the loading environment. *Development (Cambridge, England)* 2015;142:196–206.
64. Deymier AC, Schwartz AG, Cai Z, et al. The multiscale structural and mechanical effects of mouse supraspinatus muscle unloading on the mature enthesis. *Acta Biomaterialia* 2019;83:302–13.
65. Deymier-Black AC, Pasteris JD, Genin GM, and Thomopoulos S. Allometry of the Tendon Enthesis: Mechanisms of Load Transfer Between Tendon and Bone. *Journal of Biomechanical Engineering* 2015;137:111005.

66. Saadat F, Deymier AC, Birman V, Thomopoulos S, and Genin GM. The concentration of stress at the rotator cuff tendon-to-bone attachment site is conserved across species. *Journal of the Mechanical Behavior of Biomedical Materials* 2016;62:24–32.
67. Liu YX, Thomopoulos S, Birman V, Li JSS, and Genin GM. Bi-material attachment through a compliant interfacial system at the tendon-to-bone insertion site. *Mechanics of Materials* 2012;44:83–92.
68. Boys AJ, Kunitake JAMR, Henak CR, Cohen I, Estroff LA, and Bonassar LJ. Understanding the Stiff-to-Compliant Transition of the Meniscal Attachments by Spatial Correlation of Composition, Structure, and Mechanics. *ACS Applied Materials & Interfaces* 2019;11:26559–70.
69. Gilday SD, Chris Casstevens E, Kenter K, Shearn JT, and Butler DL. Murine patellar tendon biomechanical properties and regional strain patterns during natural tendon-to-bone healing after acute injury. *Journal of Biomechanics* 2014;47:2035–42.
70. Lake SP, Miller KS, Elliott DM, and Soslowky LJ. Tensile properties and fiber alignment of human supraspinatus tendon in the transverse direction demonstrate inhomogeneity, non-linearity, and regional isotropy. *Journal of Biomechanics* 2010;43:727–32.
71. Moffat KL, Sun WHS, Pena PE, et al. Characterization of the structure–function relationship at the ligament-to-bone interface. *Proceedings of the National Academy of Sciences* 2008;105:7947 LP –7952.
72. Deymier AC, An Y, Boyle JJ, et al. Micro-mechanical properties of the tendon-to-bone attachment. *Acta Biomaterialia* 2017;56:25–35.
73. Thomopoulos S, Marquez JP, Weinberger B, Birman V, and Genin GM. Collagen fiber orientation at the tendon to bone insertion and its influence on stress concentrations. *Journal of Biomechanics* 2006;39:1842–51.
74. Liu Y, Birman V, Chen C, Thomopoulos S, and Genin GM. Mechanisms of Bimaterial Attachment at the Interface of Tendon to Bone. *Journal of Engineering Materials and Technology* 2010;133:011006.
75. Zhang L, Lake SP, Lai VK, Picu CR, Barocas VH, and Shephard MS. A coupled fiber-matrix model demonstrates highly inhomogeneous microstructural interactions in soft tissues under tensile load. *Journal of Biomechanical Engineering* 2013;135:011008.
76. Aghvami M, Barocas VH, and Sander EA. Multiscale Mechanical Simulations of Cell Compacted Collagen Gels. *Journal of Biomechanical Engineering* 2013;135.
77. Raabe D, Sachs C, and Romano P. The crustacean exoskeleton as an example of a structurally graded biological nanocomposite material. *Acta Materialia* 2005;53:4281–92.

78. Sun C and Waite JH. Mapping Chemical Gradients within and along a Fibrous Structural Tissue, Mussel Byssal Threads*. *Journal of Biological Chemistry* 2005;280:39332–6.
79. Miserez A, Schneberk T, Sun C, Zok FW, and Waite JH. The Transition from Stiff to Compliant Materials in Squid Beaks. *Science* 2008;319:1816–9.
80. Bentov S, Zaslansky P, Al-Sawalmih A, et al. Enamel-like apatite crown covering amorphous mineral in a crayfish mandible. *Nature Communications* 2012;3:839.
81. Khanarian NT, Boushell MK, Spalazzi JP, Pleshko N, Boskey AL, and Lu HH. FTIR-I Compositional Mapping of the Cartilage-to-Bone Interface as a Function of Tissue Region and Age. *Journal of Bone and Mineral Research* 2014;29:2643–52.
82. Spalazzi JP, Boskey AL, Pleshko N, and Lu HH. Quantitative Mapping of Matrix Content and Distribution across the Ligament-to-Bone Insertion. *PLOS ONE* 2013;8:e74349.
83. Ho SP, Marshall SJ, Ryder MI, and Marshall GW. The tooth attachment mechanism defined by structure, chemical composition and mechanical properties of collagen fibers in the periodontium. *Biomaterials* 2007;28:5238–45.
84. Schwartz AG, Lipner JH, Pasteris JD, Genin GM, and Thomopoulos S. Muscle loading is necessary for the formation of a functional tendon enthesis. *Bone* 2013;55:44–51.
85. Liu Y, Thomopoulos S, Chen C, Birman V, Buehler MJ, and Genin GM. Modelling the mechanics of partially mineralized collagen fibrils, fibres and tissue. *Journal of the Royal Society Interface* 2014;11:20130835.
86. Lipner J, Boyle JJ, Xia Y, Birman V, Genin GM, and Thomopoulos S. Toughening of fibrous scaffolds by mobile mineral deposits. *Acta Biomaterialia* 2017;58:492–501.
87. Schmidt MB, Mow VC, Chun LE, and Eyre DR. Effects of proteoglycan extraction on the tensile behavior of articular cartilage. *Journal of Orthopaedic Research* 1990;8:353–63.
88. Katsamenis OL, Jenkins T, and Thurner PJ. Toughness and damage susceptibility in human cortical bone is proportional to mechanical inhomogeneity at the osteonal-level. *Bone* 2015;76:158–68.
89. Ingram M and Symmons DPM. The burden of musculoskeletal conditions (MsCs). *Medicine* 2018;46:152–5.
90. Cieza A, Causey K, Kamenov K, Hanson SW, Chatterji S, and Vos T. Global estimates of the need for rehabilitation based on the Global Burden of Disease study 2019: a systematic analysis for the Global Burden of Disease Study 2019. *The Lancet* 2020;396:2006–17.

91. Jordan K, Clarke AM, Symmons DPM, et al. Measuring disease prevalence: a comparison of musculoskeletal disease using four general practice consultation databases. *The British journal of general practice : the journal of the Royal College of General Practitioners* 2007;57:7–14.
92. Yelin E, Weinstein S, and King T. *The burden of musculoskeletal diseases in the United States*. 2016.
93. Mather RCr, Koenig L, Kocher MS, et al. Societal and economic impact of anterior cruciate ligament tears. *The Journal of bone and joint surgery. American volume* 2013;95:1751–9.
94. Mather RCr, Koenig L, Acevedo D, et al. The societal and economic value of rotator cuff repair. *The Journal of bone and joint surgery. American volume* 2013;95:1993–2000.
95. Nilsson N, Nilsson Helander K, Hamrin Senorski E, et al. The economic cost and patient-reported outcomes of chronic Achilles tendon ruptures. *Journal of Experimental Orthopaedics* 2020;7:60.
96. Yamaguchi K. New guideline on rotator cuff problems. *AAOS Now* 2011;5:46–7.
97. Millar NL, Murrell GA, and McInnes IB. Inflammatory mechanisms in tendinopathy - towards translation. *Nature Reviews Rheumatology* 2017;13:110–22.
98. Killian ML, Cavinatto L, Galatz LM, and Thomopoulos S. Recent advances in shoulder research. *Arthritis Research and Therapy* 2012;14:214.
99. Khan RJ, Fick D, Keogh A, Crawford J, Brammar T, and Parker M. Treatment of acute Achilles tendon ruptures: A meta-analysis of randomized, controlled trials. *Journal of Bone and Joint Surgery - Series A* 2005;87:2202–10.
100. Galatz LM, Ball CM, Teefey SA, Middleton WD, and Yamaguchi K. The Outcome and Repair Integrity of Completely Arthroscopically Repaired Large and Massive Rotator Cuff Tears. *Journal of Bone and Joint Surgery - Series A* 2004;86:219–24.
101. Jeong JY, Min SK, Park KM, Park YB, Han KJ, and Yoo JC. Location of Rotator Cuff Tear Initiation: A Magnetic Resonance Imaging Study of 191 Shoulders. *American Journal of Sports Medicine* 2018;46:649–55.
102. Godin J. Arthroscopic Treatment of Greater Tuberosity Avulsion Fractures. *Arthroscopy Techniques* 2017;6:e777–e783.
103. Ghazanfari A, Henderson DJH, and Nourissat G. An Arthroscopic Humeral Medializing Repair of the Supraspinatus. *Arthroscopy Techniques* 2017;6:e2211–e2215.

104. Oh LS, Wolf BR, Hall MP, Levy BA, and Marx RG. Indications for rotator cuff repair: A systematic review. In: Clinical Orthopaedics and Related Research. Vol. 455. 2007:52–63.
105. Yamaguchi K, Ditsios K, Middleton WD, Hildebolt CF, Galatz LM, and Teefey SA. The demographic and morphological features of rotator cuff disease: A comparison of asymptomatic and symptomatic shoulders. *Journal of Bone and Joint Surgery Am* 2006;88:1699–704.
106. Kim HM, Dahiya N, Teefey SA, et al. Location and initiation of degenerative rotator cuff tears: An analysis of three hundred and sixty shoulders. *Journal of Bone and Joint Surgery - Series A* 2010;92:829–39.
107. Kim HM, Dahiya N, Teefey SA, Keener JD, Galatz LM, and Yamaguchi K. Relationship of tear size and location to fatty degeneration of the rotator cuff. *Journal of Bone and Joint Surgery - Series A* 2010;92:1088–96.
108. Parada SA, Dilisio MF, and Kennedy CD. Management of complications after rotator cuff surgery. *Current Reviews in Musculoskeletal Medicine* 2015;8:40–52.
109. Colvin AC, Harrison AK, Flatow EL, Egorova N, and Moskowitz A. National trends in rotator cuff repair. *Journal of Bone and Joint Surgery - Series A* 2012;94:227–33.
110. Paloneva J, Lepola V, Äärimala V, Joukainen A, Ylinen J, and Mattila VM. Increasing incidence of rotator cuff repairs - A nationwide registry study in Finland. *BMC Musculoskeletal Disorders* 2015;16.
111. Rashid MS, Cooper C, Cook J, et al. Increasing age and tear size reduce rotator cuff repair healing rate at 1 year. *Acta Orthopaedica* 2017;88:606–11.
112. Ganestam A, Kallemosse T, Troelsen A, and Barfod KW. Increasing incidence of acute Achilles tendon rupture and a noticeable decline in surgical treatment from 1994 to 2013. A nationwide registry study of 33,160 patients. *Knee surgery, sports traumatology, arthroscopy : official journal of the ESSKA* 2016;24:3730–7.
113. Soroceanu A, Sidhwa F, Aarabi S, Kaufman A, and Glazebrook M. Surgical versus nonsurgical treatment of acute Achilles tendon rupture: a meta-analysis of randomized trials. *The Journal of bone and joint surgery. American* 2012;94:2136–43.
114. Park SH, Lee HS, Young KW, and Seo SG. Treatment of Acute Achilles Tendon Rupture. *Clinics in orthopedic surgery* 2020;12:1–8.
115. Lui TH. Fixation of tendo Achilles avulsion fracture. *Foot and Ankle Surgery* 2009;15:58–61.

116. Ochen Y, Beks RB, Heijl M van, et al. Operative treatment versus nonoperative treatment of Achilles tendon ruptures: systematic review and meta-analysis. *BMJ* 2019;364:k5120.
117. Boublik M, Schlegel T, Koonce R, Genuario J, Lind C, and Hamming D. Patellar Tendon Ruptures in National Football League Players. *The American Journal of Sports Medicine* 2011;39:2436–40.
118. Dan M, Parr W, Broe D, Cross M, and Walsh WR. Biomechanics of the knee extensor mechanism and its relationship to patella tendinopathy: A review. *Journal of Orthopaedic Research* 2018;36:3105–12.
119. Lavagnino M, Arnoczky SP, Elvin N, and Dodds J. Patellar tendon strain is increased at the site of the jumper’s knee lesion during knee flexion and tendon loading: Results and cadaveric testing of a computational model. *American Journal of Sports Medicine* 2008;36:2110–8.
120. Ferretti A. Epidemiology of Jumper’s Knee. *Sports Medicine: An International Journal of Applied Medicine and Science in Sport and Exercise* 1986;3:289–95.
121. Yousef MAA. Combined avulsion fracture of the tibial tubercle and patellar tendon rupture in pediatric population: case series and review of literature. *European Journal of Orthopaedic Surgery & Traumatology* 2018;28:317–23.
122. Haskel JD, Fried JW, Hurley ET, et al. High rates of return to play and work follow knee extensor tendon ruptures but low rate of return to pre-injury level of play. *Knee Surgery, Sports Traumatology, Arthroscopy* 2021.
123. Nguyen MV, Nguyen JV, Taormina DP, Pham H, and Alaia MJ. A Comprehensive Return-to-Play Analysis of National Basketball Association Players With Operative Patellar Tendon Tears. *Orthopaedic Journal of Sports Medicine* 2018;6:2325967118800479.
124. Iannotti JP, Deutsch A, Green A, et al. Time to Failure After Rotator Cuff Repair: A Prospective Imaging Study. *JBJS* 2013;95:965–71.
125. Tashjian RZ, Hollins AM, Kim HM, et al. Factors Affecting Healing Rates after Arthroscopic Double-Row Rotator Cuff Repair. *AJSM* 2010;38:2435–42.
126. Millar NL, Hueber AJ, Reilly JH, et al. Inflammation is present in early human tendinopathy. *American Journal of Sports Medicine* 2010;38:2085–91.
127. Silva MJ, Thomopoulos S, Kusano N, et al. Early healing of flexor tendon insertion site injuries: Tunnel repair is mechanically and histologically inferior to surface repair in a canine model. *Journal of Orthopaedic Research* 2006;24:990–1000.

128. Manning CN, Havlioglu N, Knutsen E, et al. The early inflammatory response after flexor tendon healing: A gene expression and histological analysis. *Journal of Orthopaedic Research* 2014;32:645–52.
129. Abraham AC, Shah SA, Golman M, et al. Targeting the NF- κ B signaling pathway in chronic tendon disease. *Science Translational Medicine* 2019;11:eaav4319.
130. Galatz LM, Gerstenfeld L, Heber-Katz E, and Rodeo SA. Tendon regeneration and scar formation: The concept of scarless healing. *Journal of Orthopaedic Research* 2015;33:823–31.
131. Killian ML, Cavinatto L, Shah SA, et al. The effects of chronic unloading and gap formation on tendon-to-bone healing in a rat model of massive rotator cuff tears. *Journal of Orthopaedic Research* 2014;32:439–47.
132. Shah SA, Kormpakis I, Havlioglu N, Ominsky MS, Galatz LM, and Thomopoulos S. Sclerostin Antibody Treatment Enhances Rotator Cuff Tendon-to-Bone Healing in an Animal Model. *JBJS* 2017;99.
133. Killian ML, Cavinatto LM, Ward SR, Havlioglu N, Thomopoulos S, and Galatz LM. Chronic Degeneration Leads to Poor Healing of Repaired Massive Rotator Cuff Tears in Rats. *The American Journal of Sports Medicine* 2015;43:2401–10.
134. Cadet ER, Hsu JW, Levine WN, Bigliani LU, and Ahmad CS. The relationship between greater tuberosity osteopenia and the chronicity of rotator cuff tears. *Journal of Shoulder and Elbow Surgery* 2008;17:73–7.
135. Kurtaliaj I, Golman M, Abraham AC, and Thomopoulos S. Biomechanical Testing of Murine Tendons. *Journal of visualized experiments : JoVE* 2019.
136. Milz S, Rufai A, Buettner A, Putz R, Ralphs JR, and Benjamin M. Three-dimensional reconstructions of the Achilles tendon insertion in man. *Journal of anatomy* 2002;200:145–52.
137. Ganji E and Killian ML. Tendon Healing in the Context of Complex Fractures. *Clinical Reviews in Bone and Mineral Metabolism* 2018;16:131–41.
138. Sartori J, Köhring S, Witte H, Fischer MS, and Löffler M. Three-dimensional imaging of the fibrous microstructure of Achilles tendon entheses in *Mus musculus*. *Journal of Anatomy* 2018;233:370–80.
139. Sartori J and Stark H. Tracking tendon fibers to their insertion – a 3D analysis of the Achilles tendon enthesis in mice. *Acta Biomaterialia* 2020;120:146–55.

140. Howell K, Chien C, Bell R, et al. Novel Model of Tendon Regeneration Reveals Distinct Cell Mechanisms Underlying Regenerative and Fibrotic Tendon Healing. *Scientific Reports* 2017;7:45238.
141. Sherlock JP, Joyce-Shaikh B, Turner SP, et al. IL-23 induces spondyloarthritis by acting on ROR- γ + CD3+CD4-CD8-entheseal resident T cells.(cluster of differentiation). *Nature Medicine* 2012;18:1069–77.
142. Pauwels E, Van Loo D, Cornillie P, Brabant L, and Van Hoorebeke L. An exploratory study of contrast agents for soft tissue visualization by means of high resolution X-ray computed tomography imaging. *Journal of Microscopy* 2013;250:21–31.
143. Buytaert J, Goyens J, De Greef D, Aerts P, and Dirckx J. Volume Shrinkage of Bone, Brain and Muscle Tissue in Sample Preparation for Micro-CT and Light Sheet Fluorescence Microscopy (LSFM). *Microscopy and Microanalysis* 2014;20:1208–17.
144. Boyle JJ, Kume M, Wyczalkowski MA, et al. Simple and accurate methods for quantifying deformation, disruption, and development in biological tissues. *Journal of The Royal Society Interface* 2014;11:20140685.
145. Komi PV. Relevance of in vivo force measurements to human biomechanics. *Journal of Biomechanics* 1990;23:23–34.
146. Tarkin IS, Morganti CM, Zillmer DA, McFarland EG, and Giangarra CE. Rotator cuff tears in adolescent athletes. *American Journal of Sports Medicine* 2005;22:133–7.
147. Azzam MG, Dugas JR, Andrews JR, Goldstein SR, Emblom BA, and Cain EL. Rotator Cuff Repair in Adolescent Athletes. *American Journal of Sports Medicine* 2018;46:1084–90.
148. Zitnay JL, Li Y, Qin Z, et al. Molecular level detection and localization of mechanical damage in collagen enabled by collagen hybridizing peptides. *Nature Communications* 2017;8:14913.
149. Shaw HM and Benjamin M. Structure-function relationships of entheses in relation to mechanical load and exercise: Review. *Scandinavian Journal of Medicine and Science in Sports* 2007;17:303–15.
150. Tempelhof S, Rupp S, and Seil R. Age-related prevalence of rotator cuff tears in asymptomatic shoulders. *Journal of Shoulder and Elbow Surgery* 1999;8:296–9.
151. Bhatia DN, Beer JF de, and Rooyen KS van. The Bony Partial Articular Surface Tendon Avulsion Lesion: An Arthroscopic Technique for Fixation of the Partially Avulsed Greater Tuberosity Fracture. *Arthroscopy - Journal of Arthroscopic and Related Surgery* 2007;23:786.e1–786.e6.

152. Li CG, Li B, and Yang YF. Management of acute Achilles tendon rupture with tendon-bundle technique. *Journal of International Medical Research* 2017;45:310–9.
153. List JP van der and DiFelice GS. Primary repair of the anterior cruciate ligament: A paradigm shift. *The Surgeon* 2017;15:161–8.
154. Dodds AL, Halewood C, Gupte CM, Williams A, and Amis AA. The anterolateral ligament. *The Bone & Joint Journal* 2014;96-B:325–31.
155. Cech DJ and Martin ST. Chapter 6 - Skeletal System Changes. In: Functional Movement. Ed. by Cech DJ and Martin ST. Third Edit. Saint Louis: W.B. Saunders, 2012:105–28.
156. Lynch HA. Effect of Fiber Orientation and Strain Rate on the Nonlinear Uniaxial Tensile Material Properties of Tendon. *Journal of Biomechanical Engineering* 2003.
157. Haut TL and Haut RC. The state of tissue hydration determines the strain-rate-sensitive stiffness of human patellar tendon. *Journal of Biomechanics* 1997;30:79–81.
158. Zitnay JL, Jung GS, Lin AH, et al. Accumulation of collagen molecular unfolding is the mechanism of cyclic fatigue damage and failure in collagenous tissues. *Science Advances* 2020;6:eaba2795.
159. Haut RC. Age-Dependent Influence of Strain Rate on the Tensile Failure of Rat-Tail Tendon. *Journal of Biomechanical Engineering* 1983;105:296–9.
160. Woo SL, Peterson RH, Ohland KJ, Sites TJ, and Danto MI. The effects of strain rate on the properties of the medial collateral ligament in skeletally immature and mature rabbits: a biomechanical and histological study. *Journal of orthopaedic research : official publication of the Orthopaedic Research Society* 1990;8:712–21.
161. Danto MI and Woo SL. The mechanical properties of skeletally mature rabbit anterior cruciate ligament and patellar tendon over a range of strain rates. *Journal of Orthopaedic Research* 1993;11:58–67.
162. Noyes FR, DeLucas JL, and Torvik PJ. Biomechanics of anterior cruciate ligament failure: an analysis of strain-rate sensitivity and mechanisms of failure in primates. *The Journal of bone and joint surgery. American volume* 1974;56:236–53.
163. Gao J, Räsänen T, Persliden J, and Messner K. The morphology of ligament insertions after failure at low strain velocity: an evaluation of ligament entheses in the rabbit knee. *Journal of anatomy* 1996;189 (Pt 1):127–33.
164. Woo SL, Gomez MA, Sites TJ, Newton PO, Orlando CA, and Akeson WH. The biomechanical and morphological changes in the medial collateral ligament of the rabbit after immo-

- bilization and remobilization. *Journal of Bone and Joint Surgery - Series A* 1987;69:1200–11.
165. Panjabi MM, White AA, and Southwick WO. Mechanical properties of bone as a function of rate of deformation. *The Journal of bone and joint surgery. American volume* 1973;55:322–30.
 166. Wright TM and Hayes WC. Tensile testing of bone over a wide range of strain rates: effects of strain rate, microstructure and density. *Medical & Biological Engineering* 1976;14:671.
 167. Ros SJ, Muljadi PM, Flatow EL, and Andarawis-Puri N. Multiscale mechanisms of tendon fatigue damage progression and severity are strain and cycle dependent. *Journal of biomechanics* 2019;85:148–56.
 168. Andarawis-Puri N, Philip A, Laudier D, Schaffler MB, and Flatow EL. Temporal effect of in vivo tendon fatigue loading on the apoptotic response explained in the context of number of fatigue loading cycles and initial damage parameters. *Journal of Orthopaedic Research* 2014;32:1097–103.
 169. Bell R, Boniello MR, Gendron NR, Flatow EL, and Andarawis-Puri N. Delayed exercise promotes remodeling in sub-rupture fatigue damaged tendons. *Journal of Orthopaedic Research* 2015;33:919–25.
 170. Manning CN, Martel C, Sakiyama-Elbert SE, et al. Adipose-derived mesenchymal stromal cells modulate tendon fibroblast responses to macrophage-induced inflammation in vitro. *Stem Cell Research and Therapy* 2015;6:74.
 171. Veres SP, Brennan-Pierce EP, and Lee JM. Macrophage-like U937 cells recognize collagen fibrils with strain-induced discrete plasticity damage. *Journal of Biomedical Materials Research Part A* 2015;103:397–408.
 172. Screen HR, Berk DE, Kadler KE, Ramirez F, and Young MF. Tendon functional extracellular matrix. *Journal of Orthopaedic Research* 2015;33:7930799.
 173. Quigley AS, Bancelin S, Deska-Gauthier D, Légaré F, Kreplak L, and Veres SP. In tendons, differing physiological requirements lead to functionally distinct nanostructures. *Scientific Reports* 2018;8:4409.
 174. Shearer T, Thorpe CT, and Screen HR. The relative compliance of energy-storing tendons may be due to the helical fibril arrangement of their fascicles. *Journal of the Royal Society Interface* 2017;14:20170261.
 175. Thorpe CT, Klemm C, Riley GP, Birch HL, Clegg PD, and Screen HR. Helical sub-structures in energy-storing tendons provide a possible mechanism for efficient energy storage and return. *Acta Biomaterialia* 2013;9:7948–56.

176. Hamilton NP. *Kinesiology: Scientific Basis of Human Motion*. 2011.
177. Wang D, Sandlin MI, Cohen JR, Lord EL, Petrigliano FA, and SooHoo NF. Operative versus nonoperative treatment of acute Achilles tendon rupture: An analysis of 12,570 patients in a large healthcare database. *Foot and Ankle Surgery* 2015;21:250–3.
178. Huang CY, Wang VM, Pawluk RJ, et al. Inhomogeneous mechanical behavior of the human supraspinatus tendon under uniaxial loading. *Journal of Orthopaedic Research* 2005;23:924–30.
179. Bey MJ, Song HK, Wehrli FW, and Soslowsky LJ. Intratendinous strain fields of the intact supraspinatus tendon: The effect of glenohumeral joint position and tendon region. *Journal of Orthopaedic Research* 2002;20:869–74.
180. Graichen H, Englmeier KH, Reiser M, and Eckstein F. An in vivo technique for determining 3D muscular moment arms in different joint positions and during muscular activation - Application to the supraspinatus. *Clinical Biomechanics* 2001;16:389–94.
181. Newton MD, Davidson AA, Pomajzl R, Seta J, Kurdziel MD, and Maerz T. The influence of testing angle on the biomechanical properties of the rat supraspinatus tendon. *Journal of Biomechanics* 2016;49:4159–63.
182. Lindblom K. On pathogenesis of ruptures of the tendon aponeurosis of the shoulder joint. *Acta Radiologica* 1939;20:564–77.
183. Lanir Y. Constitutive equations for fibrous connective tissues. *Journal of Biomechanics* 1983;16:1–12.
184. Szczesny SE, Caplan JL, Pedersen P, and Elliott DM. Quantification of Interfibrillar Shear Stress in Aligned Soft Collagenous Tissues via Notch Tension Testing. *Scientific Reports* 2015;5:14649.
185. Barrett JM, Fewster KM, Cudlip AC, Dickerson CR, and Callaghan JP. The rate of tendon failure in a collagen fibre recruitment-based model. *Journal of the Mechanical Behavior of Biomedical Materials* 2021;115:104273.
186. Sacks MS. Incorporation of Experimentally-Derived Fiber Orientation into a Structural Constitutive Model for Planar Collagenous Tissues. *Journal of Biomechanical Engineering* 2003;125:280.
187. Biewener AA and Roberts TJ. Muscle and tendon contributions to force, work, and elastic energy savings: A comparative perspective. *Exercise and Sport Sciences Reviews* 2000;28:99–107.

188. Rack PM and Ross HF. The tendon of flexor pollicis longus: its effects on the muscular control of force and position at the human thumb. *The Journal of Physiology* 1984;351:99–110.
189. Gerber C, Snedeker JG, Baumgartner D, and Viehöfer AF. Supraspinatus tendon load during abduction is dependent on the size of the critical shoulder angle: A biomechanical analysis. *Journal of Orthopaedic Research* 2014;32:952–7.
190. Pinchbeck GL, Clegg PD, Proudman CJ, Stirk A, Morgan KL, and French NP. Horse injuries and racing practices in National Hunt racehorses in the UK: The results of a prospective cohort study. *Veterinary Journal* 2004;167:42–52.
191. Choi RK, Smith MM, Smith S, Little CB, and Clarke EC. Functionally distinct tendons have different biomechanical, biochemical and histological responses to in vitro unloading. *Journal of Biomechanics* 2019;95:109321.
192. Thorpe CT, Udeze CP, Birch HL, Clegg PD, and Screen HR. Specialization of tendon mechanical properties results from interfascicular differences. *Journal of the Royal Society Interface* 2012;9:3108–17.
193. Herod TW, Chambers NC, and Veres SP. Collagen fibrils in functionally distinct tendons have differing structural responses to tendon rupture and fatigue loading. *Acta Biomaterialia* 2016.
194. Golman M, Wright ML, Wong TT, et al. Rethinking Patellar Tendinopathy and Partial Patellar Tendon Tears: A Novel Classification System. *The American Journal of Sports Medicine* 2020;48:359–69.
195. Ouellette H, Labis J, Bredella M, Palmer WE, Sheah K, and Torriani M. Spectrum of shoulder injuries in the baseball pitcher. *Skeletal Radiology* 2008;37:491–8.
196. Razmadze D, Panyutina AA, and Zelenkov NV. Anatomy of the forelimb musculature and ligaments of *Psittacus erithacus* (Aves: Psittaciformes). *Journal of Anatomy* 2018;233:496–530.
197. Poore SO, Sánchez-Haiman A, and Goslow GE. Wing upstroke and the evolution of flapping flight. *Nature* 1997;387:799–802.
198. Carlesso M, Giacomelli R, Krause T, et al. Improvement of sound absorption and flexural compliance of porous alumina-mullite ceramics by engineering the microstructure and segmentation into topologically interlocked blocks. *Journal of the European Ceramic Society* 2013;33:2549–58.
199. Buckwalter JA and Mankin HJ. Articular cartilage: Part I. *Journal of Bone and Joint Surgery* 1997;79:600.

200. Basalo IM, Chen FH, Hung CT, and Ateshian GA. Frictional response of bovine articular cartilage under creep loading following proteoglycan digestion with chondroitinase ABC. *Journal of Biomechanical Engineering* 2006;128:131–4.
201. Ateshian GA, Warden WH, Kim JJ, Grelsamer RP, and Mow VC. Finite deformation biphasic material properties of bovine articular cartilage from confined compression experiments. *Journal of biomechanics* 1997;30:1157–64.
202. Mow VC, Holmes MH, and Lai WM. Fluid transport and mechanical properties of articular cartilage: a review. *Journal of biomechanics* 1984;17:377–94.
203. Han E, Chen SS, Klisch SM, and Sah RL. Contribution of proteoglycan osmotic swelling pressure to the compressive properties of articular cartilage. *Biophys J* 2011;101:916–24.
204. Henninger HB, Underwood CJ, Ateshian GA, and Weiss JA. Effect of sulfated glycosaminoglycan digestion on the transverse permeability of medial collateral ligament. *Journal of biomechanics* 2010;43:2567–73.
205. Dunkman AA, Buckley MR, Mienaltowski MJ, et al. The injury response of aged tendons in the absence of biglycan and decorin. *Matrix biology : journal of the International Society for Matrix Biology* 2014;35:232–8.
206. Dourte LM, Pathmanathan L, Mienaltowski MJ, Jawad AF, Birk DE, and Soslowsky LJ. Mechanical, compositional, and structural properties of the mouse patellar tendon with changes in biglycan gene expression. *Journal of orthopaedic research : official publication of the Orthopaedic Research Society* 2013;31:1430–7.
207. Lujan TJ, Underwood CJ, Henninger HB, Thompson BM, and Weiss JA. Effect of dermatan sulfate glycosaminoglycans on the quasi-static material properties of the human medial collateral ligament. *Journal of orthopaedic research : official publication of the Orthopaedic Research Society* 2007;25:894–903.
208. Fessel G and Snedeker JG. Evidence against proteoglycan mediated collagen fibril load transmission and dynamic viscoelasticity in tendon. *Matrix biology : journal of the International Society for Matrix Biology* 2009;28:503–10.
209. Fessel G and Snedeker JG. Equivalent stiffness after glycosaminoglycan depletion in tendon — an ultra-structural finite element model and corresponding experiments. *Journal of Theoretical Biology* 2011;268:77–83.
210. Rigozzi S, Müller R, and Snedeker JG. Local strain measurement reveals a varied regional dependence of tensile tendon mechanics on glycosaminoglycan content. *Journal of biomechanics* 2009;42:1547–52.

211. Andriolo L, Altamura SA, Reale D, Candrian C, Zaffagnini S, and Filardo G. Nonsurgical Treatments of Patellar Tendinopathy: Multiple Injections of Platelet-Rich Plasma Are a Suitable Option: A Systematic Review and Meta-analysis. *The American Journal of Sports Medicine* 2018;47:1001–18.
212. Zhu W, Iatridis JC, Hlibczuk V, Ratcliffe A, and Mow VC. Determination of collagen-proteoglycan interactions in vitro. *Journal of Biomechanics* 1996;29:773–83.
213. Quinn TM and Morel V. Microstructural Modeling of Collagen Network Mechanics and Interactions with the Proteoglycan Gel in Articular Cartilage. *Biomechanics and Modeling in Mechanobiology* 2007;6:73–82.
214. Carter DR. Mechanical loading histories and cortical bone remodeling. *Calcified Tissue International* 1984;36:S19–24.
215. Meakin LB, Price JS, and Lanyon LE. The contribution of experimental in vivo models to understanding the mechanisms of adaptation to mechanical loading in bone. *Frontiers in Endocrinology* 2014;5:154.
216. Sun D, Brodt MD, Zannit HM, Holguin N, and Silva MJ. Evaluation of loading parameters for murine axial tibial loading: Stimulating cortical bone formation while reducing loading duration. *Journal of Orthopaedic Research* 2018;36:682–91.
217. Miyamoto A, Shigematsu T, Fukunaga T, Kawakami K, Mukai C, and Sekiguchi C. Medical baseline data collection on bone and muscle change with space flight. *Bone* 1998;22:79S–82S.
218. Yagodovsky VS, Triftanidi LA, and Gorokhova GP. Space flight effects on skeletal bones of rats (light and electron microscopic examination). *Aviation Space and Environmental Medicine* 1976;47:734–8.
219. Warner SE, Sanford DA, Becker BA, Bain SD, Srinivasan S, and Gross TS. Botox induced muscle paralysis rapidly degrades bone. *Bone* 2006;38:257–64.
220. Grimston SK, Silva MJ, and Civitelli R. Bone loss after temporarily induced muscle paralysis by Botox is not fully recovered after 12 weeks. *Annals of the New York Academy of Sciences* 2007;1116:444–60.
221. Keaveny TM, Wachtel EF, and Kopperdahl DL. Mechanical behavior of human trabecular bone after overloading. *Journal of Orthopaedic Research* 1999;17:346–53.
222. Badieli A, Bottema MJ, and Fazzalari NL. Influence of orthogonal overload on human vertebral trabecular bone mechanical properties. *Journal of Bone and Mineral Research* 2007;22:1690–9.

223. Oftadeh R, Perez-Viloria M, Villa-Camacho JC, Vaziri A, and Nazarian A. Biomechanics and Mechanobiology of Trabecular Bone: A Review. *Journal of Biomechanical Engineering* 2015;137:010802.
224. Coates BA, McKenzie JA, Yoneda S, and Silva MJ. Interleukin-6 (IL-6) deficiency enhances intramembranous osteogenesis following stress fracture in mice. *Bone* 2021;143:115737.
225. Main RP, Shefelbine SJ, Meakin LB, Silva MJ, Meulen MC van der, and Willie BM. Murine Axial Compression Tibial Loading Model to Study Bone Mechanobiology: Implementing the Model and Reporting Results. *Journal of Orthopaedic Research* 2020;38:233–52.
226. Martinez MD, Schmid GJ, McKenzie JA, Ornitz DM, and Silva MJ. Healing of non-displaced fractures produced by fatigue loading of the mouse ulna. *Bone* 2010;46:1604–12.
227. McBride SH and Silva MJ. Adaptive and injury response of bone to mechanical loading. *BoneKEy Reports* 2012;1:192.
228. Magnusson SP and Kjaer M. The impact of loading, unloading, ageing and injury on the human tendon. *Journal of Physiology* 2019;597:1283–98.
229. Heinemeier KM and Kjaer M. In vivo investigation of tendon responses to mechanical loading. *Journal of Musculoskeletal Neuronal Interactions* 2011;11:115–23.
230. Eliasson P, Fahlgren A, Pasternak B, and Aspenberg P. Unloaded rat Achilles tendons continue to grow, but lose viscoelasticity. *Journal of Applied Physiology* 2007;103:459–63.
231. Reeves ND. Adaptation of the tendon to mechanical usage. *Journal of Musculoskeletal Neuronal Interactions* 2006;6:174–80.
232. Khayyeri H, Blomgran P, Hammerman M, et al. Achilles tendon compositional and structural properties are altered after unloading by botox. *Scientific Reports* 2017;7:13067.
233. Majima T, Yasuda K, Fujii T, Yamamoto N, Hayashi K, and Kaneda K. Biomechanical effects of stress shielding of the rabbit patellar tendon depend on the degree of stress reduction. *Journal of Orthopaedic Research* 1996;14:377–83.
234. Thorpe CT, Chaudhry S, Lei II, et al. Tendon overload results in alterations in cell shape and increased markers of inflammation and matrix degradation. *Scandinavian Journal of Medicine and Science in Sports* 2015;25:e381–e391.
235. Soslowky L, Thomopoulos S, Tun S, et al. Neer award 1999: Overuse activity injures the supraspinatus tendon in an animal model: A histologic and biomechanical study. *Journal of Shoulder and Elbow Surgery* 2000;9:79–84.

236. Spiesz EM, Thorpe CT, Chaudhry S, et al. Tendon extracellular matrix damage, degradation and inflammation in response to in vitro overload exercise. *Journal of Orthopaedic Research* 2015;33:889–97.
237. Fung DT, Wang VM, Andarawis-Puri N, et al. Early response to tendon fatigue damage accumulation in a novel in vivo model. *Journal of Biomechanics* 2010;43:274–9.
238. Tatara AM, Lipner JH, Das R, et al. The role of muscle loading on bone (re)modeling at the developing enthesis. *PLoS ONE* 2014;9:e97375.
239. Killian ML, Lim CT, Thomopoulos S, Charlton N, Kim HM, and Galatz LM. The effect of unloading on gene expression of healthy and injured rotator cuffs. *Journal of Orthopaedic Research* 2013;31:1240–8.
240. Hettrich CM, Rodeo SA, Hannafin JA, Ehteshami J, and Shubin Stein BE. The effect of muscle paralysis using Botox on the healing of tendon to bone in a rat model. *Journal of Shoulder and Elbow Surgery* 2011;20:688–97.
241. Liu XS, Sajda P, Saha PK, et al. Complete volumetric decomposition of individual trabecular plates and rods and its morphological correlations with anisotropic elastic moduli in human trabecular bone. *Journal of Bone and Mineral Research* 2008;23:223–35.
242. Birman V. *Plate structures*. 2011.
243. Couppé C, Suetta C, Kongsgaard M, et al. The effects of immobilization on the mechanical properties of the patellar tendon in younger and older men. *Clinical Biomechanics* 2012;27:1179–86.
244. Boer MD de, Maganaris CN, Seynnes OR, Rennie MJ, and Narici MV. Time course of muscular, neural and tendinous adaptations to 23 day unilateral lower-limb suspension in young men. *Journal of Physiology* 2007;583:1079–91.
245. Shin D, Finni T, Ahn S, et al. Effect of chronic unloading and rehabilitation on human Achilles tendon properties: A velocity-encoded phase-contrast MRI study. *Journal of Applied Physiology* 2008;105:1179–86.
246. Almeida-Silveira MI, Lambertz D, Pérot C, and Goubel F. Changes in stiffness induced by hindlimb suspension in rat Achilles tendon. *European Journal of Applied Physiology and Occupational Physiology* 2000;81:252–7.
247. Rumian AP, Draper ER, Wallace AL, and Goodship AE. The influence of the mechanical environment on remodelling of the patellar tendon. *Journal of Bone and Joint Surgery - Series B* 2009;91:557–64.

248. Maganaris CN, Reeves ND, Rittweger J, et al. Adaptive response of human tendon to paralysis. *Muscle and Nerve* 2006;33:85–92.
249. Dideriksen K, Boesen AP, Reitelsheder S, et al. Tendon collagen synthesis declines with immobilization in elderly humans: No effect of anti-inflammatory medication. *Journal of Applied Physiology* 2017;122:273–82.
250. Zhang J and Wang JH. The effects of mechanical loading on tendons—an in vivo and in vitro model study. *PloS one* 2013;8:e71740.
251. Fleischhacker V, Klatte-Schulz F, Minkwitz S, et al. In vivo and in vitro mechanical loading of mouse achilles tendons and tenocytes—a pilot study. *International Journal of Molecular Sciences* 2020;21:1313.
252. Soslowsky LJ, Carpenter JE, DeBano CM, Banerji I, and Moalli MR. Development and use of an animal model for investigations on rotator cuff disease. *Journal of shoulder and elbow surgery / American Shoulder and Elbow Surgeons ... [et al.]* 1996;5:79–84.
253. Thampatty BP and Wang JH. Mechanobiology of young and aging tendons: In vivo studies with treadmill running. *Journal of Orthopaedic Research* 2018;36:557–65.
254. Dirks RC, Richard JS, Fearon AM, et al. Uphill treadmill running does not induce histopathological changes in the rat Achilles tendon. *BMC Musculoskeletal Disorders* 2013;14:90.
255. Reuther KE, Thomas SJ, Evans EF, et al. Returning to overuse activity following a supraspinatus and infraspinatus tear leads to joint damage in a rat model. *Journal of Biomechanics* 2013;46:1818–24.
256. Rooney SI, Loro E, Sarver JJ, et al. Exercise protocol induces muscle, tendon, and bone adaptations in the rat shoulder. *Muscles, Ligaments and Tendons Journal* 2014;4:413–9.
257. Seynnes OR, Erskine RM, Maganaris CN, et al. Training-induced changes in structural and mechanical properties of the patellar tendon are related to muscle hypertrophy but not to strength gains. *Journal of Applied Physiology* 2009;107:523–30.
258. Reeves ND, Maganaris CN, and Narici MV. Effect of strength training on human patella tendon mechanical properties of older individuals. *Journal of Physiology* 2003;548:971–81.
259. Miller BF, Olesen JL, Hansen M, et al. Coordinated collagen and muscle protein synthesis in human patella tendon and quadriceps muscle after exercise. *Journal of Physiology* 2005;567:1021–33.
260. Langberg H, Rosendal L, and Kjær M. Training-induced changes in peritendinous type I collagen turnover determined by microdialysis in humans. *Journal of Physiology* 2001;534:297–302.

261. Dideriksen K, Sindby AKR, Krosgaard M, Schjerling P, Holm L, and Langberg H. Effect of acute exercise on patella tendon protein synthesis and gene expression. *SpringerPlus* 2013;2:109.
262. Michna H. Morphometric analysis of loading-induced changes in collagen-fibril populations in young tendons. *Cell and Tissue Research* 1984;236:465–70.
263. Ma J, Piuuzzi NS, Muschler GF, Iannotti JP, Ricchetti ET, and Derwin KA. Biomarkers of Rotator Cuff Disease Severity and Repair Healing. *JBJS reviews* 2018;6:e9.
264. Waldorff EI, Lindner J, Kijek TG, et al. Bone density of the greater tuberosity is decreased in rotator cuff disease with and without full-thickness tears. *Journal of Shoulder and Elbow Surgery* 2011;20:904–8.
265. Johnston JD, Small CF, Bouxsein ML, and Pichora DR. Mechanical properties of the scapholunate ligament correlate with bone mineral density measurements of the hand. *Journal of Orthopaedic Research* 2004;22:867–71.
266. Wren TA, Yerby SA, Beaupré GS, and Carter DR. Influence of bone mineral density, age, and strain rate on the failure mode of human Achilles tendons. *Clinical Biomechanics* 2001;16:529–34.
267. Liu XS, Zhang XH, and Guo XE. Contributions of trabecular rods of various orientations in determining the elastic properties of human vertebral trabecular bone. *Bone* 2009;45:158–63.
268. Wang J, Zhou B, Liu XS, et al. Trabecular plates and rods determine elastic modulus and yield strength of human trabecular bone. *Bone* 2015;72:71–80.
269. Zhou B, Sherry Liu X, Wang J, Lucas Lu X, Fields AJ, and Edward Guo X. Dependence of mechanical properties of trabecular bone on plate-rod microstructure determined by individual trabecula segmentation (ITS). *Journal of Biomechanics* 2014;47:702–8.
270. Liu XS, Cohen A, Shane E, et al. Individual Trabeculae Segmentation (ITS)-based morphological analysis of high-resolution peripheral quantitative computed tomography images detects abnormal trabecular plate and rod microarchitecture in premenopausal women with idiopathic osteoporosis. *Journal of Bone and Mineral Research* 2010;25:1496–505.
271. Walker MD, Liu XS, Zhou B, et al. Pre-and post-menopausal differences in bone microstructure and mechanical competence in Chinese-American and white women. *Journal of Bone and Mineral Research* 2013;28:1308–18.
272. Chiba K, Nango N, Kubota S, et al. Relationship between microstructure and degree of mineralization in subchondral bone of osteoarthritis: A synchrotron radiation μ CT study. *Journal of Bone and Mineral Research* 2012;27:1511–7.

273. Fang F, Schwartz AG, Moore ER, Sup ME, and Thomopoulos S. Primary cilia as the nexus of biophysical and hedgehog signaling at the tendon enthesis. *Science Advances* 2020;6:eabc1799.
274. Schwartz AG, Galatz LM, and Thomopoulos S. Enthesis regeneration: a role for Gli1+ progenitor cells. *Development (Cambridge, England)* 2017;144:1159–64.
275. Johnson DP, Wakeley CJ, and Watt I. Magnetic resonance imaging of patellar tendonitis. *J Bone Joint Surg Br* 1996;78:452–7.
276. Peace KAL, Lee JC, and Healy J. Imaging the infrapatellar tendon in the elite athlete. *Clinical Radiology* 2006;61:570–8.
277. Richards DP, Ajemian SV, Wiley JP, and Zernicke RF. Knee joint dynamics predict patellar tendinitis in elite volleyball players. *American Journal of Sports Medicine* 1996;24:676–83.
278. Cook J, Khan KM, Maffulli N, and Purdam C. Overuse Tendinosis , Not Tendinitis - Part 2. *The Physician and Sportsmedicine* 2000;28:31–46.
279. Visentini PJ, Khan KM, Cook JL, Kiss ZS, Harcourt PR, and Wark JD. The VISA score: An index of severity of symptoms in patients with jumper’s knee (Patellar Tendinosis). *Journal of Science and Medicine in Sport* 1998;1:22–8.
280. Karlsson J, Kalebo P, Goksor LA, Thomee R, and Sward L. Partial rupture of the patellar ligament. *American Journal of Sports Medicine* 1992;20:390–5.
281. Figueroa D, Figueroa F, and Calvo R. Patellar tendinopathy: Diagnosis and treatment. *Journal of the American Academy of Orthopaedic Surgeons* 2016;24:e184–e192.
282. Kettunen JA, Kvist M, Alanen E, and Kujala UM. Long-term prognosis for jumper’s knee in male athletes: A prospective follow-up study. *American Journal of Sports Medicine* 2002;30:689–92.
283. Khan KM, Cook JL, Taunton JE, and Bonar F. Overuse Tendinosis, Not Tendinitis. *The Physician and Sportsmedicine* 2000;28:38–48.
284. Zwerver J, Bredeweg SW, and Van Den Akker-Scheek I. Prevalence of jumper’s knee among nonelite athletes from different sports: A cross-sectional survey. *American Journal of Sports Medicine* 2011;39:1984–8.
285. Gemignani M, Busoni F, Tonerini M, and Scaglione M. The patellar tendinopathy in athletes: A sonographic grading correlated to prognosis and therapy. *Emergency Radiology* 2008;15:399–404.

286. Hansen P, Haraldsson BT, Aagaard P, et al. Lower strength of the human posterior patellar tendon seems unrelated to mature collagen cross-linking and fibril morphology. *Journal of Applied Physiology* 2010;108:47–52.
287. Blazina M, Kerlan R, Jobe F, Carter V, and Carlson G. Jumper's Knee. *The Orthopedic Clinics Of North America* 1973;4:665–78.
288. Araújo CG and Scharhag J. Athlete: A working definition for medical and health sciences research. *Scandinavian Journal of Medicine and Science in Sports* 2016;26:4–7.
289. Golman M, Padovano W, Shmuylovich L, and Kovács SJ. Quantifying Diastolic Function: From E-Waves as Triangles to Physiologic Contours via the 'Geometric Method'. *Cardiovascular Engineering and Technology* 2018;9:105–19.
290. Cofield RH. Subscapular muscle transposition for repair of chronic rotator cuff tears. *Surgery, gynecology & obstetrics* 1982;154:667–72.
291. Ellman H. Diagnosis and Treatment of Incomplete Rotator Cuff Tears. *Clinical Orthopaedics and Related Research* 1990;254:64–74.
292. Malliaras P, Cook J, Purdam C, and Rio E. Patellar Tendinopathy: Clinical Diagnosis, Load Management, and Advice for Challenging Case Presentations. *Journal of Orthopaedic & Sports Physical Therapy* 2015;45:887–98.
293. Hamilton B and Purdam C. Patellar tendinosis as an adaptive process: A new hypothesis. *British Journal of Sports Medicine* 2004;38:758–61.
294. Basso O, Amis AA, Race A, and Johnson DP. Patellar tendon fiber strains: Their differential responses to quadriceps tension. *Clinical Orthopaedics and Related Research* 2002;400:246–53.
295. Pierets K, Verdonk R, De Muynck M, and Lagast J. Jumper's knee: Postoperative assessment - A retrospective clinical study. *Knee Surgery, Sports Traumatology, Arthroscopy* 1999;7:239–42.
296. Galloway MT, Lalley AL, and Shearn JT. The role of mechanical loading in tendon development, maintenance, injury, and repair. *Journal of Bone and Joint Surgery - Series A* 2013;95:1620–8.
297. Thomopoulos S, Parks WC, Rifkin DB, and Derwin KA. Mechanisms of tendon injury and repair. *Journal of Orthopaedic Research* 2015;33:832–9.
298. Andarawis-Puri N, Ricchetti ET, and Soslowsky LJ. Rotator cuff tendon strain correlates with tear propagation. *Journal of Biomechanics* 2009;42:158–63.

299. Szczesny SE, Aeppli C, David A, and Mauck RL. Fatigue loading of tendon results in collagen kinking and denaturation but does not change local tissue mechanics. *Journal of Biomechanics* 2018;71:251–6.
300. Pang J, Shen S, Pan WR, Jones IR, Rozen WM, and Taylor GI. The arterial supply of the patellar tendon: Anatomical study with clinical implications for knee surgery. *Clinical Anatomy* 2009;22:371–6.
301. Chen TM, Rozen WM, Pan WR, Ashton MW, Richardson MD, and Taylor GI. The arterial anatomy of the Achilles tendon: Anatomical study and clinical implications. *Clinical Anatomy* 2009;22:377–85.
302. Gwynne-Jones DP and Sims M. Epidemiology and Outcomes of Acute Achilles Tendon Rupture with Operative or Nonoperative Treatment Using an Identical Functional Bracing Protocol. *Foot & Ankle International* 2011;32:337–43.
303. Bahr R, Fossan B, Løken S, and Engebretsen L. Surgical treatment compared with eccentric training for patellar tendinopathy (jumper’s knee): A randomized, controlled trial. *Journal of Bone and Joint Surgery - Series A* 2006;88:1689–98.
304. Weiss JM, Arkader A, Wells LM, and Ganley TJ. Rotator cuff injuries in adolescent athletes. *Journal of Pediatric Orthopaedics Part B* 2013;22:133–7.
305. McCully SP, Kumar N, Lazarus MD, and Karduna AR. Internal and external rotation of the shoulder: Effects of plane, end-range determination, and scapular motion. *Journal of Shoulder and Elbow Surgery* 2005;14:605–10.
306. Ditsios K, Boyer MI, Kusano N, Gelberman RH, and Silva MJ. Bone loss following tendon laceration, repair and passive mobilization. *Journal of orthopaedic research : official publication of the Orthopaedic Research Society* 2003;21:990–6.
307. Clark JM and Harryman DTn. Tendons, ligaments, and capsule of the rotator cuff. Gross and microscopic anatomy. *The Journal of bone and joint surgery. American volume* 1992;74:713–25.
308. Screen HRC, Toorani S, and Shelton JC. Microstructural stress relaxation mechanics in functionally different tendons. *Medical Engineering & Physics* 2013;35:96–102.
309. Fryhofer GW, Freedman BR, Hillin CD, et al. Postinjury biomechanics of Achilles tendon vary by sex and hormone status. *Journal of Applied Physiology* 2016;121:1106–14.
310. Morrison SM, Dick TJM, and Wakeling JM. Structural and mechanical properties of the human Achilles tendon: Sex and strength effects. *Journal of Biomechanics* 2015;48:3530–3.

311. Sarver DC, Kharaz YA, Sugg KB, Gumucio JP, Comerford E, and Mendias CL. Sex differences in tendon structure and function. *Journal of Orthopaedic Research* 2017;35:2117–26.
312. Imbeni V, Kruzic JJ, Marshall GW, Marshall SJ, and Ritchie RO. The dentin-enamel junction and the fracture of human teeth. *Nature Materials* 2005;4:229–32.
313. Marin F, Le Roy N, and Marie B. The formation and mineralization of mollusk shell. *Frontiers in Bioscience - Scholar* 2012;4:1099–125.
314. Livanov K, Jelitto H, Bar-On B, Schulte K, Schneider GA, and Wagner DH. Tough alumina/polymer layered composites with high ceramic content. *Journal of the American Ceramic Society* 2015;98:1285–91.
315. Han B, Qin KK, Yu B, Zhang QC, Chen CQ, and Lu TJ. Design optimization of foam-reinforced corrugated sandwich beams. *Composite Structures* 2015;130:51–62.
316. Beaurepaire P, Valdebenito MA, Schuëller GI, and Jensen HA. Reliability-based optimization of maintenance scheduling of mechanical components under fatigue. *Computer methods in applied mechanics and engineering* 2012;221-222:24–40.
317. McElvany MD, McGoldrick E, Gee AO, Neradilek MB, and Matsen FA. Rotator cuff repair: Published evidence on factors associated with repair integrity and clinical outcome. *American Journal of Sports Medicine* 2015;43:491–500.
318. Miller BS, Downie BK, Kohen RB, et al. When do rotator cuff repairs fail? Serial ultrasound examination after arthroscopic repair of large and massive rotator cuff tears. *American Journal of Sports Medicine* 2011;39:2064–70.
319. Dakin SG, Martinez FO, Yapp C, et al. Inflammation activation and resolution in human tendon disease. *Science Translational Medicine* 2015;7:311ra173.
320. Dakin SG, Buckley CD, Al-Mossawi MH, et al. Persistent stromal fibroblast activation is present in chronic tendinopathy. *Arthritis Research and Therapy* 2017;19:16.
321. Berglund M, Hart DA, and Wiig M. The inflammatory response and hyaluronan synthases in the rabbit flexor tendon and tendon sheath following injury. *Journal of Hand Surgery: European Volume* 2007;32:581–7.
322. Kawamura S, Ying L, Kim HJ, Dynybil C, and Rodeo SA. Macrophages accumulate in the early phase of tendon-bone healing. *Journal of Orthopaedic Research* 2005;23:1425–32.
323. Sugg KB, Lubardic J, Gumucio JP, and Mendias CL. Changes in macrophage phenotype and induction of epithelial-to-mesenchymal transition genes following acute Achilles tenotomy and repair. *Journal of Orthopaedic Research* 2014;32:944–51.

324. Adam B, Shuguang G, Sabah R, et al. Oral Ibuprofen Interferes with Cellular Healing Responses in a Murine Model of Achilles Tendinopathy. *Journal of Musculoskeletal Disorders and Treatment* 2018;4:049.
325. Connizzo BK, Yannascoli SM, Tucker JJ, et al. The detrimental effects of systemic ibuprofen delivery on tendon healing are time-dependent. *Clinical Orthopaedics and Related Research* 2014;472:2433–9.
326. Ferry ST, Dahners LE, Afshari HM, and Weinhold PS. The effects of common anti-inflammatory drugs on the healing rat patellar tendon. *American Journal of Sports Medicine* 2007;35:1326–33.
327. Gulotta LV, Kovacevic D, Cordasco F, and Rodeo SA. Evaluation of tumor necrosis factor α blockade on early tendon-to-bone healing in a rat rotator cuff repair model. *Arthroscopy - Journal of Arthroscopic and Related Surgery* 2011;27:1351–7.
328. Hayden MS and Ghosh S. NF- κ B, the first quarter-century: Remarkable progress and outstanding questions. *Genes and Development* 2012;26:203–34.
329. Ghosh S and Hayden MS. New regulators of NF- κ B in inflammation. *Nature Reviews Immunology* 2008;8:837–48.
330. Strnad J and Burke JR. I κ B kinase inhibitors for treating autoimmune and inflammatory disorders: potential and challenges. *Trends in Pharmacological Sciences* 2007;28:142–8.
331. Grothe K, Flechsenhar K, Paehler T, et al. I κ B kinase inhibition as a potential treatment of osteoarthritis – results of a clinical proof-of-concept study. *Osteoarthritis and Cartilage* 2017;25:46–52.
332. Best KT, Lee FK, Knapp E, Awad HA, and Loiselle AE. Deletion of NFKB1 enhances canonical NF- κ B signaling and increases macrophage and myofibroblast content during tendon healing. *Scientific Reports* 2019;9:10926.
333. Murata T, Shimada M, Sakakibara S, et al. Synthesis and structure-activity relationships of novel IKK- β inhibitors. Part 3: Orally active anti-inflammatory agents. *Bioorganic and Medicinal Chemistry Letters* 2004;14:4019–22.
334. Murata T, Shimada M, Kadono H, et al. Synthesis and structure-activity relationships of novel IKK- β inhibitors. Part 2: Improvement of in vitro activity. *Bioorganic and Medicinal Chemistry Letters* 2004;14:4013–7.
335. Ide J, Kikukawa K, Hirose J, et al. The effect of a local application of fibroblast growth factor-2 on tendon-to-bone remodeling in rats with acute injury and repair of the supraspinatus tendon. *Journal of Shoulder and Elbow Surgery* 2009;18:391–8.

336. Lipner J, Shen H, Cavinatto L, et al. In Vivo Evaluation of Adipose-Derived Stromal Cells Delivered with a Nanofiber Scaffold for Tendon-to-Bone Repair. *Tissue Engineering - Part A* 2015;21:2766–74.
337. Abraham AC, Shah SA, and Thomopoulos S. Targeting Inflammation in Rotator Cuff Tendon Degeneration and Repair. *Techniques in Shoulder and Elbow Surgery* 2017;18:84–90.
338. Cohen DB, Kawamura S, Ehteshami JR, and Rodeo SA. Indomethacin and celecoxib impair rotator cuff tendon-to-bone healing. *American Journal of Sports Medicine* 2006;34:362–9.
339. Rooney SI, Baskin R, Torino DJ, et al. Ibuprofen differentially affects supraspinatus muscle and tendon adaptations to exercise in a rat model. *American Journal of Sports Medicine* 2016;44:2237–45.
340. Taylor PC. Clinical efficacy of launched JAK inhibitors in rheumatoid arthritis. *Rheumatology (United Kingdom)* 2019;58:i17–i26.
341. Wilde JM, Gumucio JP, Grekin JA, et al. Inhibition of p38 mitogen-activated protein kinase signaling reduces fibrosis and lipid accumulation after rotator cuff repair. *Journal of Shoulder and Elbow Surgery* 2016;25:1501–8.
342. Swarnkar G, Zhang K, Mbalaviele G, Long F, and Abu-Amer Y. Constitutive activation of IKK2/NF- κ B impairs osteogenesis and skeletal development. *PLoS ONE* 2014;9:391421.
343. Lin TH, Pajarinen J, Lu L, et al. NF- κ B as a Therapeutic Target in Inflammatory-Associated Bone Diseases. In: *Advances in Protein Chemistry and Structural Bio.* Vol. 107. 2017:117–54.
344. Ruocco MG, Maeda S, Park JM, et al. I κ B kinase (IKK) β , but not IKK α , is a critical mediator of osteoclast survival and is required for inflammation-induced bone loss. *Journal of Experimental Medicine* 2005;201:1677–87.
345. Flick LM, Weaver JM, Ulrich-Vinther M, et al. Effect of receptor activator of NF κ B (RANK) signaling blockade on fracture healing. *Journal of Orthopaedic Research* 2003;21.
346. Glass GE, Chan JK, Freidin A, Feldmann M, Horwood NJ, and Nanchahal J. TNF- α promotes fracture repair by augmenting the recruitment and differentiation of muscle-derived stromal cells. *Proceedings of the National Academy of Sciences of the United States of America* 2011;108:837–48.
347. Mårtensson K, Chrysis D, and Säwendahl L. Interleukin-1 β and TNF- α act in synergy to inhibit longitudinal growth in fetal rat metatarsal bones. *Journal of Bone and Mineral Research* 2004;19:1805–12.

Appendix A: Enhanced Tendon-to-Bone Healing via IKK β Inhibition in a Rat Rotator Cuff Model

Portions of this **Appendix A** were previously published in: Golman M, Li X, Skouteris D, et al. Enhanced Tendon-to-Bone Healing via IKK β Inhibition in a Rat Rotator Cuff Model. *The American Journal of Sports Medicine*. 2021;49(3):780-789. doi:10.1177/0363546520985203.

A.1 Abstract

More than 450,000 rotator cuff repairs are performed annually, yet healing of tendon to bone often fails. This failure is rooted in the fibrovascular healing response, which does not regenerate the native attachment site. Better healing outcomes may be achieved by targeting inflammation during the early period after repair. Rather than broad inhibition of inflammation, which may impair healing, the current study took a molecularly targeted approach to suppress IKK β , shutting down only the inflammatory arm of the nuclear factor κ B (NF- κ B) signaling pathway. The objective of this study was to evaluate the therapeutic potential of IKK β inhibition in a clinically relevant model of rat rotator cuff repair. After validating the efficacy of the IKK β inhibitor *in vitro*, it was administered orally once a day for 7 days after surgery in a rat rotator cuff repair model. The effect of treatment on reducing inflammation and improving repair quality was evaluated after 3 days and 2, 4, and 8 weeks of healing, using gene expression, biomechanics, bone morphometry, and histology. Inhibition of IKK β attenuated cytokine and chemokine production *in vitro*, demonstrating the potential for this inhibitor to reduce inflammation *in vivo*. Oral treatment with IKK β inhibitor reduced NF- κ B target gene expression by up to 80% compared to the non-treated group at day 3, with a subset of these genes suppressed through 14 days. Furthermore, the IKK β inhibitor led to enhanced tenogenesis and extracellular matrix production, as demonstrated by gene

expression and histological analyses. At 4 weeks, inhibitor treatment led to increased toughness, no effects on failure load and strength, and decreases in stiffness and modulus when compared to vehicle control. At 8 weeks, $IKK\beta$ inhibitor treatment led to increased toughness, failure load, and strength compared with control animals. $IKK\beta$ inhibitor treatment prevented the bone loss near the tendon attachment that occurred in control repairs. In conclusion, pharmacological inhibition of $IKK\beta$ successfully suppressed excessive inflammation and enhanced tendon-to-bone healing after rotator cuff repair in a rat model.

A.2 Introduction

Rotator cuff tears are a common source of upper extremity pain and disability, leading to more than 450,000 rotator cuff surgical repairs performed annually in the United States [109, 110, 96]. Unfortunately, healing after rotator cuff repair has only shown moderate success rates. The average healing rate post rotator cuff repair at 12 months was 56% [111], with recurrent tears occurring in 20% to 94% of cases, depending on the patient population [317, 318]. The inadequate healing of rotator cuff tears contributes to lost days of work, difficulty with returning to overhead sports and recreational activities, and a substantial social and economic burden [147, 104].

Many factors have been associated with impaired rotator cuff healing after surgery, including patient age, tear size, muscle atrophy, and bone quality [111, 106, 107]. The advent of modern molecular techniques has also shed light on the contribution of inflammation to inadequate regeneration of the rotator cuff attachment site, with growing clinical and animal evidence supporting the premise that excessive inflammation post-repair leads to fibrovascular scar rather than enthesis regeneration [319, 320, 126, 97]. *In vivo* tendon injury models have revealed elevation in macrophages and pro-inflammatory factors 3 days post-operatively [321, 322, 128, 323] and poor healing between tendon and bone [130]. However, broadly suppressing inflammation through non-steroidal anti-inflammatory drugs (NSAIDs), commonly used post-operatively, is also detrimental to healing [324, 325, 326]. Therefore, a carefully balanced inflammatory response is necessary for optimal healing (e.g., by modulating inflammation at the earliest stages following repair [327]).

The canonical nuclear factor κ B (NF- κ B) pathway has been shown to be critical for many cellular responses to inflammatory stimuli, regulating cytokine production and apoptosis [328]. Binding of cytokines, such as IL-1 β and tumor necrosis factor alpha (TNF α), leads to recruitment of the inhibitor of nuclear factor kappa-B kinase (IKK) complex, composed of scaffolding protein NEMO, and catalytic subunits IKK α and IKK β (**Figure A.1A**). Activation of the IKK β subunit is essential for targeting the p50:p65 NF- κ B complex and inducing transcription of inflammatory and fibrotic mediators [329]. Manipulation of the intracellular NF- κ B pathway has been explored in treating inflammatory diseases [328, 330]. Indeed, I κ B kinase small molecule inhibitor has shown promise in clinical trial for the treatment of osteoarthritis [331].

Recent clinical investigations revealed a dramatic upregulation of the NF- κ B pathway after tendon injury and in the early phases of tendon degeneration [320, 126] and targeting this pathway enhanced flexor tendon healing in a mouse model [332]. Our recent study showed that genetic deletion of IKK β in mouse tendons improved healing outcomes after surgical repair of the rotator cuff [129]. Therefore, the objective of the current study was to evaluate the therapeutic potential of pharmacologically inhibiting IKK β in a clinically relevant model of rotator cuff repair to enhance tendon-to-bone healing. We hypothesized that oral IKK β inhibitor treatment would modulate the expression of proinflammatory factors in the early stage of healing (i.e., acute phases of inflammation), leading to improved functional outcomes.

A.3 Materials and Methods

A total of 97 adult Sprague-Dawley rats (~4 months old, ~350g, 51 males and 46 females, Envigo) were used in this study (**Figure A.1B**). All procedures were approved by the Columbia University Institutional Animal Care and Use Committee (Protocol AC-AAAZ2456).

A.3.1 Cell culture

To test the potential of the IKK β inhibitor (ACHP Hydrochloride, MedChemExpress) for preventing pro-inflammatory signaling, primary tendon fibroblasts were isolated from rat tail ten-

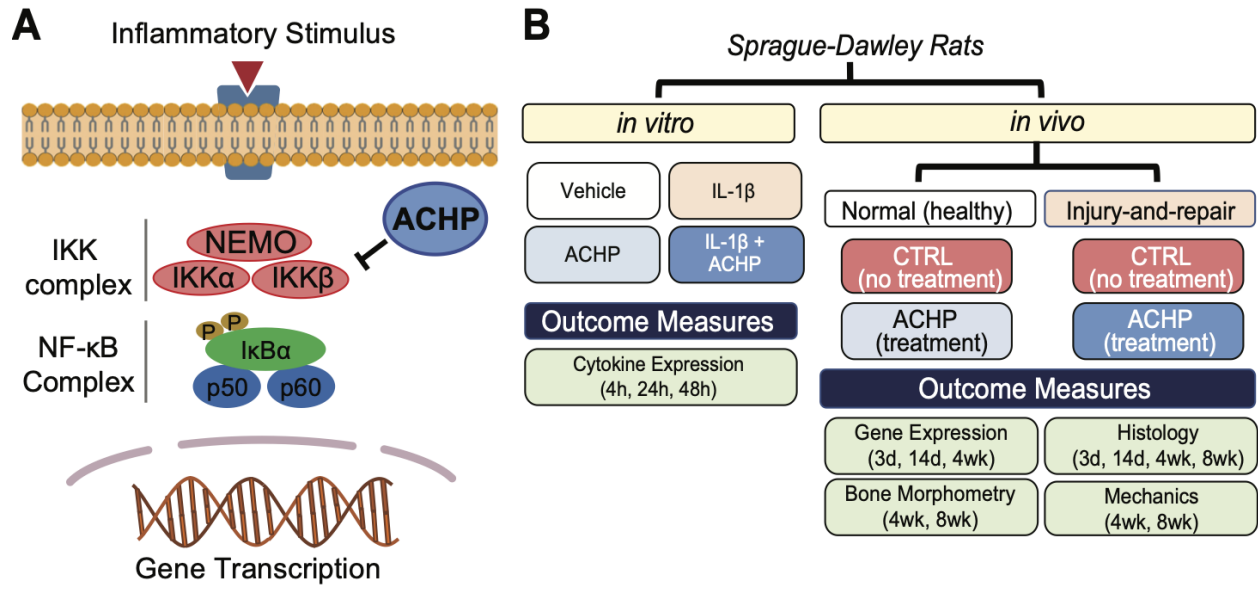


Figure A.1: (A) Schematic of NF- κ B signaling. NF- κ B signaling was modulated by targeting NF- κ B kinase subunit b (IKK β) which acts upstream of the NF- κ B complex, using IKK β small-molecule inhibitor (ACHP hydrochloride). (B) The overall study design included *in vitro* and *in vivo* methods. For *in vitro* study, rat tendon fibroblasts were treated with 1 ng interleukin-1 β (IL-1 β), 1 μ M IKK β Inhibitor, or both for 4h, 24h, 48h, and compared to vehicle-treated controls. For *in vivo* study, rats were either underwent bilateral supraspinatus tendon injury-and-repair surgery or left as normal healthy controls. Animals were either left untreated (CTRL group) or administered the IKK β inhibitor (ACHP group) orally once a day for 7 days after surgery. NF- κ B: nuclear factor κ B; CTRL: control; ACHP: ACHP hydrochloride.

dons (N=3) and cultured *in vitro* [129, 170]. Tail tendons were dissected from rats post mortem, minced, and enzymatically digested using Liberase TM (200 μ g/mL, Roche). The cells were cultured [Dulbecco's modified eagle medium (Gibco) with 10% fetal bovine serum (Crystalgen), 1% penicillin/streptomycin (Gibco)] and assessed at passage 2-3. The dose of IKK β inhibitor was determined using a cytotoxicity assay (Cell Titer Blue, Promega). Rat tail tendon fibroblasts were plated in 12-well plates at a density of 5x10⁴ cells per well with 1 ml of culture medium. Cells were adhered for 24 hours, treated with 1 ng/mL interleukin-1 β (R&D systems) to simulate inflammatory conditions, 1 μ M IKK β inhibitor, or both for 4-, 24-, and 48-hours, and compared to vehicle-treated controls. The supernatant was collected to evaluate inflammatory cytokine production using a multiplex immunoassay (ProcartaPlex Rat Th Complete Panel 14 plex, ThermoFisher) and analyzed by a Luminex multiple analyte system (Luminex 200, Luminex Corporation). All

experiments were performed using 3 biological replicates and 2 technical replicates.

A.3.2 Rotator cuff animal model

Supraspinatus tendon injury-and-repair was performed in rats bilaterally, as previously described [131]. In short, the supraspinatus tendon was sharply detached from the humeral head and repaired to its original attachment site by placing a modified Mason-Allen stitch on the tendon and passing a suture through the bone tunnel in the humeral head below the growth plate. Animals were either left untreated (CTRL group) or administered IKK β small molecule inhibitor (AHP) dissolved in 0.5% sodium carboxymethyl cellulose (Sigma). The inhibitor was delivered via oral gavage (5 mg/kg) once a day for 7 days after surgery (AHP group). This *in vivo* dosing was determined from what has been reported in the literature to have efficacy via oral administration [333, 334]. Out of 97 rats, 72 rats were injured and repaired and 25 rats were used as healthy normal controls (Normal). Of the 25 uninjured normal animals, 10 were used to study the effect of IKK β inhibitor treatment on the healthy rotator cuff (Normal:AHP) and 15 were used as healthy untreated controls (Normal: CTRL). Following acute injury and repair, animals were allowed free cage activity and sacrificed after 3 days (n=6/group), 2 weeks (n=6/group), 4 weeks (n=12/group), or 8 weeks of healing (n=12/group). Animals in the non-operatively treated control and AHP groups (Normal) were allowed free cage activity and were sacrificed at 4 weeks after the treatment started for the Normal:AHP group. As surgery was performed bilaterally and the inhibitor treatment was systemic, each animal had 2 supraspinatus tendon-to-bone units available for analysis; one shoulder was used for bone morphometry analysis and/or biomechanical evaluation and the contralateral shoulder was used for either histological analysis or gene expression analysis. Postoperatively, animals were checked daily for signs of pain or distress.

A.3.3 Gene expression

Supraspinatus tendons were dissected and snap frozen in liquid nitrogen, homogenized using a ball mill (Mikro-Dismembrator U, Sartorius), and 1 mL of TRIzol (Invitrogen) was added to

the sample. Nucleic acids were then separated from proteins using phase lock gel tubes (5PRIME phase lock gel Heavy, QuantaBio). RNA was then purified using spin columns (PureLink RNA Mini Kit, Invitrogen) with on-column enzymatic DNA digestion (DNase I, Invitrogen). Total RNA yield and sample purity were determined using a spectrophotometer (Take3, Cytation 5, Biotek). RNA concentrations were normalized to 10ng/ μ L and 100ng of total RNA was reverse transcribed to cDNA (High-Capacity RNA-to-cDNA kit, Invitrogen) using a thermocycler (ProFlex, Applied Biosystems). Quantitative real-time polymerase chain reaction was performed using SYBR (PowerUp SYBR green master mix, Invitrogen) and a real-time PCR system (Quantstudio 6 Flex, Applied Biosystems). Primers were designed using PrimerQuest (Integrated DNA Technologies, **Table A.1**). Analysis was performed using the ΔC_t method with *Gapdh* as the housekeeping gene.

A.3.4 Bone morphometry

Humerus-supraspinatus tendon-muscle specimens were dissected and scanned using micro-computed tomography (microCT) at an energy of 60 kVp, intensity of 166 μ A with Aluminum 0.25mm filter, and a resolution of 5 μ m (Skyscan 1272, Bruker). MicroCT images were evaluated using a custom segmentation algorithm to separate cortical and trabecular bone of the humeral head proximal to growth plate (CTAn, Bruker). Bone and tissue mineral density (BMD and TMD, respectively), bone volume fraction (BV/TV), trabecular number (Tb.N), trabecular thickness (Tb.Th), and trabecular spacing (Tb.Sp) were determined and compared between groups.

A.3.5 Biomechanics

After microCT scanning, the supraspinatus muscle was carefully removed from tendon and the humerus was placed into custom 3D-printed fixtures [135] and tested in saline bath at 37 $^{\circ}$ C (Electroforce 3230, TA Instruments). For repair samples, the suture was cut prior to testing. Uniaxial tension tests to failure consisted of five preconditioning cycles (2% strain, 0.2%/s), 180s recovery, and extension to failure at 0.2%/s. Strain was determined from grip-to-grip displacements

Table A.1: Names of Genes, Associated Categories and Sequences

Name	Category	NCBI Reference	Sequence
<i>Il-1β</i>	Inflammation, Cytokine	NM_031512	FWD: CTA TGG CAA CTG TCC CTG AA REV: GGC TTG GAA GCA ATC CTT AAT C
<i>Il-6</i>	Inflammation, Cytokine	NM_012589	FWD: GAA GTT AGA GTC ACA GAA GGA GTG REV: GTT TGC CGA GTA GAC CTC ATA G
<i>Ccl2</i>	Inflammation, Cytokine	NM_031530.1	FWD: GTC TCA GCC AGA TGC AGT TAA T REV: CTG CTG GTG ATT CTC TTG TAG TT
<i>Ccl12</i>	Inflammation, Cytokine	NM_001105822	FWD: GAT CCA CAT TCG GAG GCT AAA REV: GTC AGC ACA GAG CTC CTT ATC
<i>Tnf</i>	Inflammation, Cytokine	NM_012675.3	FWD: ACC TTA TCT ACT CCC AGG TTC T REV: GGC TGA CTT TCT CCT GGT ATG
<i>Cox2 (Ptgs2)</i>	Inflammation	NM_017232	FWD: GGC CAT GGA GTG GAC TTA AA REV: GTC TTT GAC TGT GGG AGG ATA C
<i>Scx</i>	Tendon	NM_001130508	FWD: CTG TGA ACA GAG AGA TGG ACA G REV: GTA GAG AGC CAG CAT GGA AAG
<i>Mmp1</i>	Matrix Metalloproteinase	NM_001134530	FWD: GGA ACA GAT ACG AAG AGG AAA CA REV: CAT GTG GGA ATC AGA GGT AGA AG
<i>Mmp3</i>	Matrix Metalloproteinase	NM_133523.3	FWD: GGA CCA GGG ATT AAT GGA GAT G REV: TGA GCA GCA ACC AGG AAT AG
<i>Mmp13</i>	Matrix Metalloproteinase	NM_001134530	FWD: GTG TGG CTG GCT TTA CAT TTG REV: TCT CCA TCT CTG TGT CCT CTA TC
<i>Rplp</i>	Housekeeping	NM_001007604	FWD: ACG GTC ACG GAG GAT AAG A REV: CCA GAG CCT TTG CAA ACA AG
<i>Hrpt1</i>	Housekeeping	NM_012583	FWD: GAC CTC TCG AAG TGT TGG ATA C REV: TCA AAT CCC TGA AGT GCT CAT

relative to the initial gauge length. Supraspinatus tendon cross-sectional area near the attachment was measured from microCT scans and used to calculate stress. Structural properties (failure load, stiffness, and work to failure [area under the curve through failure load]) were determined from load-deformation curves. Material properties (strength, modulus, resilience [area under the curve through yield], and toughness [area under the curve through failure]) were determined from stress-strain curves.

A.3.6 Histological analysis

Shoulders were dissected, fixed in 4% paraformaldehyde for 48h, decalcified in formic acid (Immunocal, StatLab), dehydrated in graded ethanol, and embedded in paraffin. 5 μ m sections were obtained and stained with pentachrome. Sections were blindly evaluated semi-quantitatively by two observers for tendon-to-bone insertion continuity, insertion organization, cell alignment, cell shape, cellularity, and collagen maturation [335, 336].

A.3.7 Statistical Analysis

Two-way analyses of variance (ANOVA) was performed to evaluate effects of time (0wk [i.e., Normal], 4wk, and 8wk) and treatment (CTRL, ACHP) (Prism 8). Bonferroni post-hoc tests were performed when the ANOVA was significant to determine CTRL vs. ACHP at each individual timepoint, and changes over the healing time period. $P < 0.05$ was considered significant. All data shown as mean \pm standard deviation.

A.4 Results

A.4.1 Cell culture model of tendinopathy

The cytotoxicity experiment showed that 1 μ M was the maximum tolerated dose of IKK β inhibitor for *in vitro* experiments, as fluorescence intensity (i.e., cell viability) decreased for tenocytes treated with IKK β inhibitor at higher than 1 μ M concentrations (**Figure A.2**). Treating tendon fibroblasts with IL-1 β significantly increased IL-6 cytokine production, while all other cytokine and

chemokines were not produced at detectable levels. Pharmacological inhibition of IKK β abrogated these effects, with IL-6 was no longer detectable (**Figure A.3**).

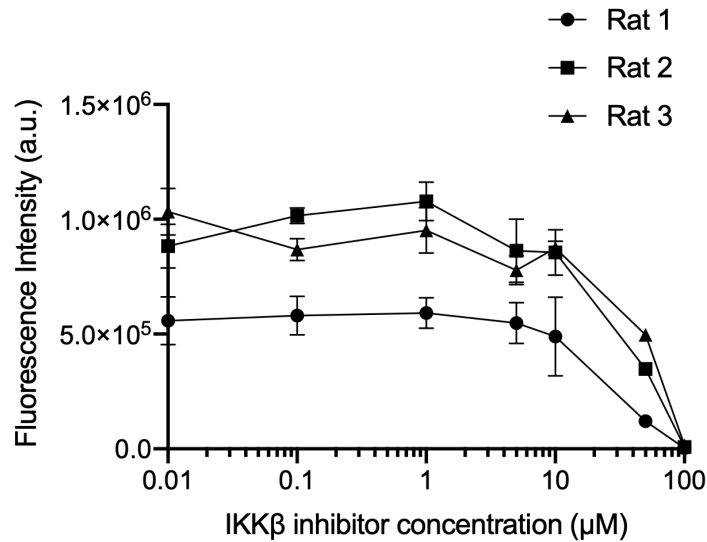


Figure A.2: *In vitro* IKK β inhibitor dose response curve for rat tail tendon fibroblasts (4 hours after treatment).

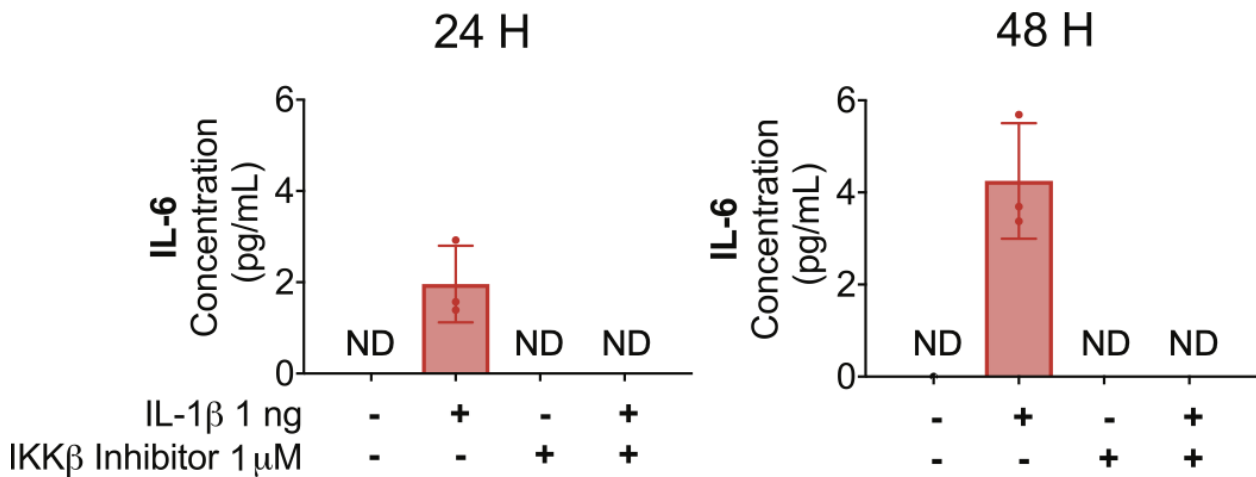


Figure A.3: A small-molecule IKK β inhibitor reduced inflammatory cytokine (IL-6) production in response to IL-1 β . ND represents that IL-6 was not detected by a multiplex immunoassay. ND: no detection

A.4.2 Gene expression

All animals tolerated the surgical procedure well without signs of distress and recovered fully. ACHP treatment significantly reduced NF- κ B target gene (*IL1 β* , *Tnf*, *Cox2*, and *Il6*) expression

by up to 80% ($p < 0.05$) compared with the non-treated group at day 3 (**Figure A.4**, $n=5/\text{group}$). Expression of matrix metalloproteinase gene (*Mmp3*) was also reduced in the presence of ACHP at day 3. The tenogenesis gene *Scx* was significantly increased by 2 weeks ($p < 0.05$) with ACHP treatment, implying enhanced repair. The expression of *Ccl2*, a chemokine related to monocyte recruitment, was not significantly affected by the treatment at any timepoint. There were significant changes in gene expression with healing time. *Scx* expression increased between 3 and 14 days and then decreased between 14 and 28 days in both groups. *IL1 β* , *Tnf*, and *Il6* expression decreased between 3 and 14 days in the CTRL group. *Cox2* expression decreased in both groups between day 14 and day 28. *Ccl2* expression did not change over time.

A.4.3 Biomechanics

ACHP treatment did not significantly alter tendon cross-sectional area after 4 or 8 weeks of healing (**Figure A.5**, $n=8-11/\text{group}$). Both injury groups, CTRL and ACHP, had significantly lower mechanical properties than the uninjured Normal group, although the ACHP group approached Normal failure load and toughness by 8 weeks. When examining the effect of ACHP treatment at 4 weeks, there was a significant increase in toughness ($p < 0.01$), no effects on failure load and strength, and a significant decrease in stiffness ($p < 0.05$) compared to CTRL. When examining the effect of ACHP treatment at 8 weeks, there was a significant increase in toughness ($p < 0.05$), and a trend towards increased failure load ($p = 0.07$) compared to CTRL. There were no effects of ACHP treatment on the mechanical properties of the uninjured Normal group. There were significant changes in mechanical properties with healing time. Failure load increased with time in both groups. Stiffness and strength increased with time in the ACHP group. Toughness increased with time in the CTRL group. The cross-sectional area and modulus did not change with time.

A.4.4 Bone morphometry

Both injury groups, CTRL and ACHP, had significant bone loss compared with the uninjured Normal group at 4 weeks of healing, with some recovery by 8 weeks of healing (**Figure A.6A**,

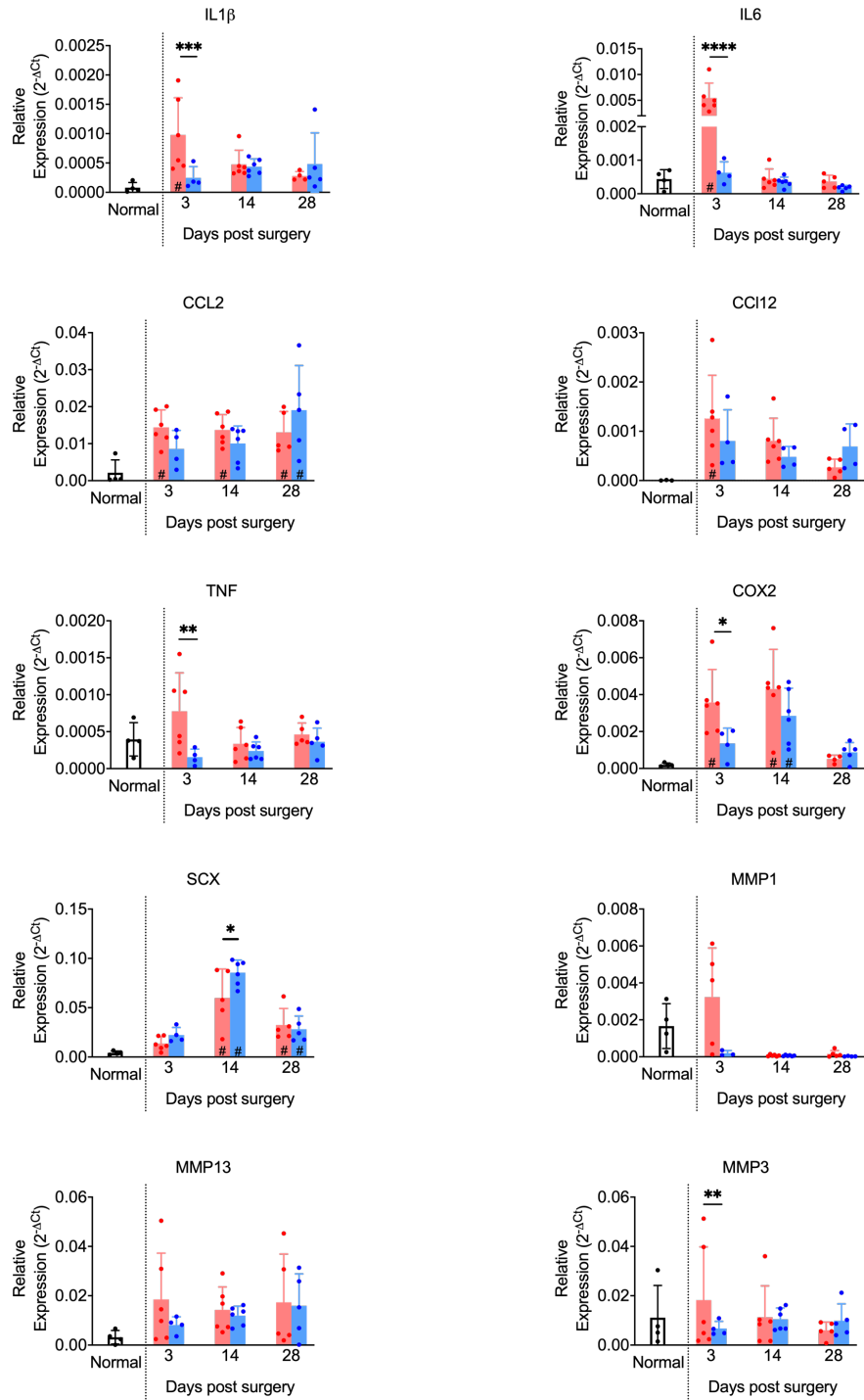


Figure A.4: Gene expression in the tendon relative to the housekeeping gene. A significant difference compared with normal is indicated by #, while a significant difference with comparing treatment to no treatment is represented by a bar (* $p < 0.05$, ** $p < 0.01$, **** $p < 0.0001$; ANOVA followed by the Bonferroni post hoc test compared with normal and the effect of treatment; a significant difference compared with normal is indicated by an “#” within a bar; a significant effect of healing time is indicated by a “t” symbol by the post surgery label)

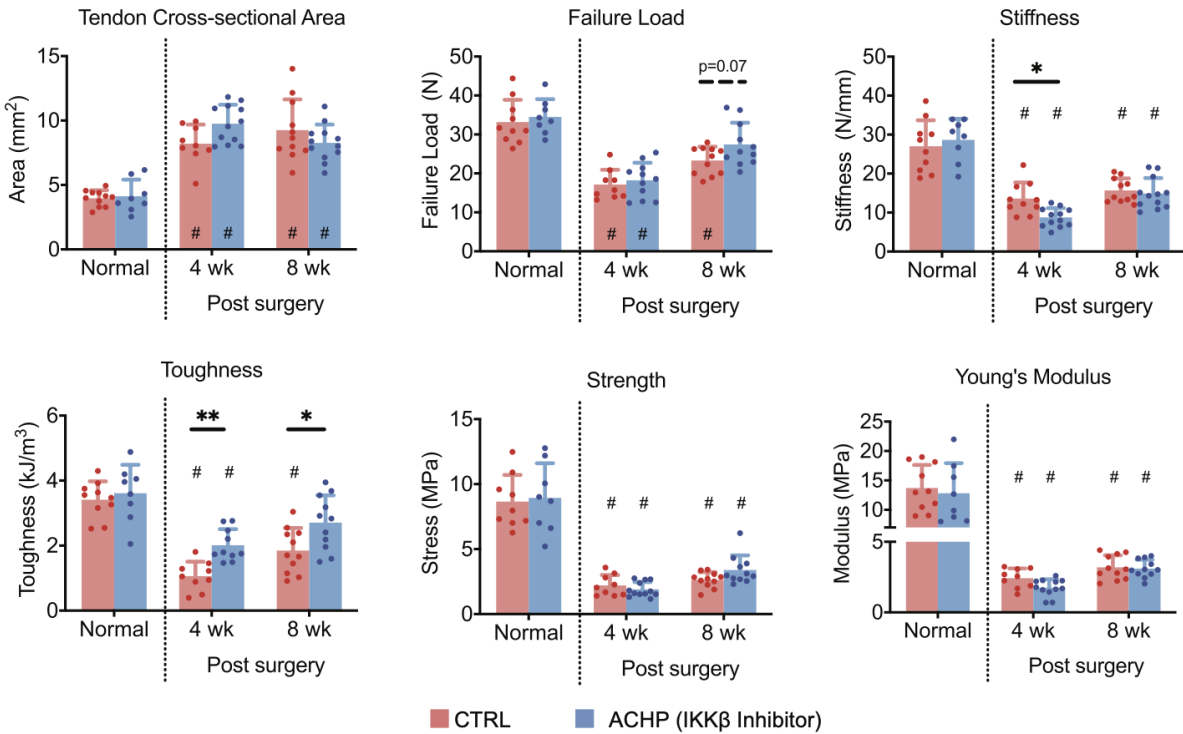


Figure A.5: Treatment with IKK β inhibitor (ACHP) had significantly increased toughness of attachment site at 4 weeks and 8 weeks of healing compared with untreated control. Treatment with ACHP also led to trend in increasing failure load and strength at 4 weeks and 8 weeks of healing, but a significant decrease in stiffness at 4 weeks of healing. The ACHP treatment did not affect mechanical properties for uninjured supraspinatus tendon-to-bone attachments. (* $p < 0.05$, ** $p < 0.01$; dashed line represent trend; ANOVA followed by the Bonferroni post hoc test compared with normal:healthy and the effect of treatment; a significant difference compared with normal is indicated by an “#” within a bar; when comparing the effect of time; a significant effect of healing time is indicated by a “t” symbol by the post surgery label).

n=8-11/group). When examining the effect of ACHP treatment, there was a significant increase in TMD at both 4-week and 8-week timepoints compared with CTRL (**Figure A.6B**). At 4 weeks of healing, cortical thickness ($p < 0.01$), BV/TV ($p < 0.001$), and trabecular thickness ($p < 0.001$) were significantly decreased, and cortical TMD ($p < 0.05$) was significantly increased in the ACHP group compared to CTRL. At 8 weeks of healing, there was a significant increase in trabecular number ($p < 0.001$) for the ACHP treatment group compared to CTRL, reaching levels comparable with those of the uninjured Normal group. There were no effects of ACHP treatment on bone morphometry of the uninjured Normal group. There were significant changes in bone morphometry with healing time. Cortical TMD, trabecular BMD, and trabecular thickness increased with

time for both groups. BV/TV increased with time for the ACHP group.

A.4.5 Histology

Pentachrome staining revealed an increase in newly formed collagen content (yellow stain) at the repair site following ACHP treatment at all time points compared to CTRL (**Figure A.7**, n=2-5/group). Semiquantitative analysis of the healing attachment showed that tendon-to-bone maturity scores improved with healing time for both groups. After 4 weeks of healing, ACHP treatment led to improved insertion organization and insertion continuity compared with CTRL (**Table A.2**). At 8 weeks of healing, ACHP treatment had a more mature tendon-to-bone attachment compared with CTRL.

A.5 Discussion

There was a dramatic increase in pro-inflammatory gene expression three days after *in vivo* rotator cuff injury and repair, consistent with previous work [321, 129, 170]. Oral treatment with IKK β inhibitor led to a significant reduction in the expression of inflammation-related NF- κ B pathway target genes. Furthermore, the IKK β inhibitor-treated group showed enhanced tenogenesis and extracellular matrix (i.e., collagen) production. These biologic changes led to a tougher repair after 8 weeks of healing compared with untreated animals.

Models of tendon injuries and tendinopathies have shown clear involvement of inflammatory signatures after injury, with increased activation of pathways such as NF- κ B [319, 126, 128, 332, 129, 337]. To address this, anti-inflammatory therapeutics such as NSAIDs are commonly used to treat tendon injuries. However, recent studies have highlighted potential detrimental effects of broadly acting NSAID treatments on healing tendon. For example, NSAIDs treatment suppressed extracellular matrix remodeling and cellular responses in a tendinopathy animal model [324, 325]. NSAIDs led to decreased [325, 338] or no effect [326, 339] on tendon mechanical properties after repair. Rather than completely suppressing the inflammatory response, small-molecule inhibitors can be used to selectively block a specific part of a pathway (e.g., the inflammatory arm of NF-

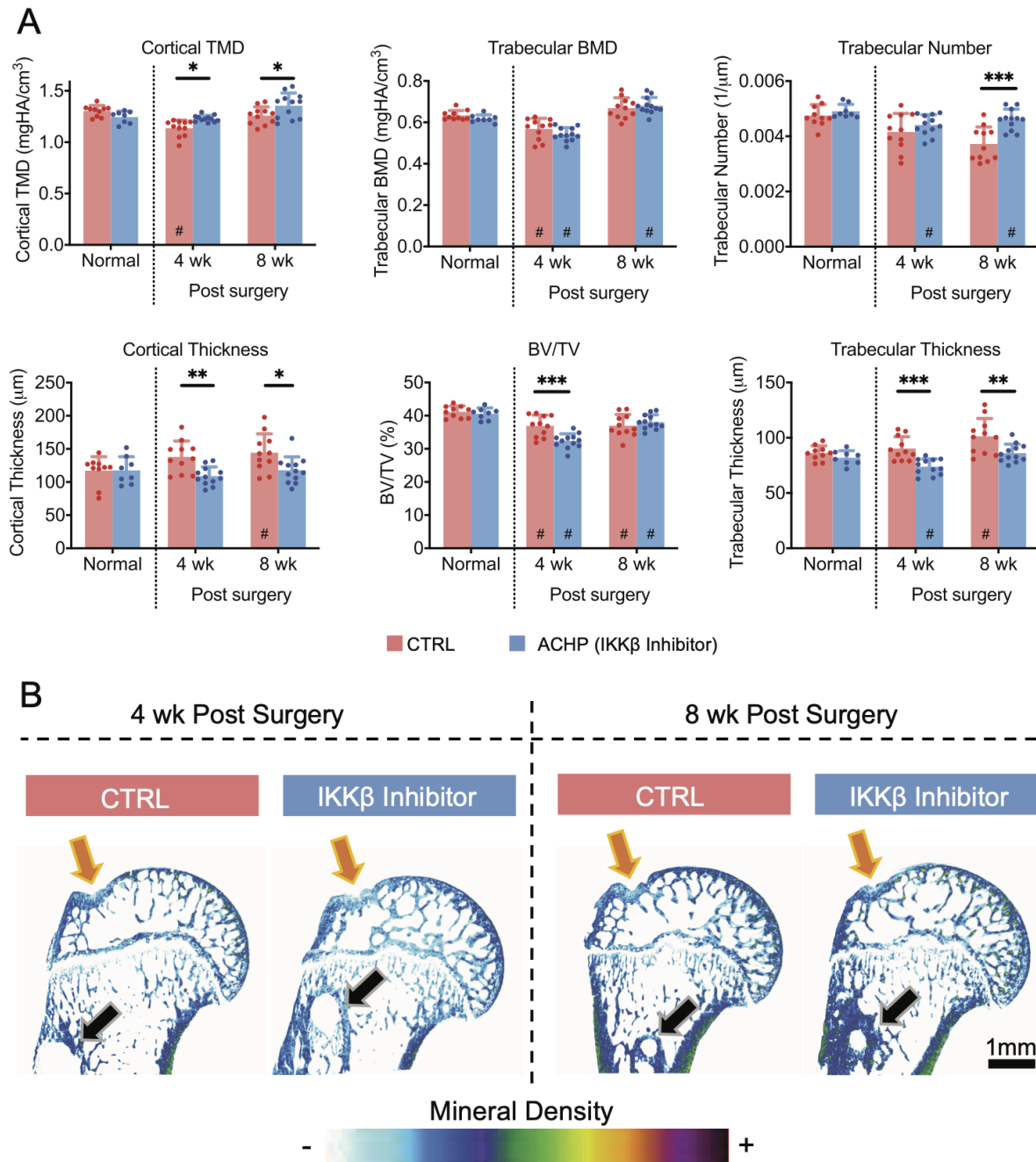


Figure A.6: (A) Treatment with ACHP led to increases in TMD and trabecular number and decreases in BV/TV, cortical thickness, and trabecular thickness. (* $p < 0.05$, ** $p < 0.01$, *** $p < 0.001$; ANOVA followed by the Bonferroni post hoc test compared with normal:healthy and the effect of treatment; a significant difference compared with normal is indicated by an “#” within a bar; a significant effect of healing time is indicated by a “t” symbol by the post surgery label). TMD: tissue mineral density; BV/TV: bone volume/tissue volume. (B) Microcomputed tomography (microCT) based two-dimensional mineral density maps for representative samples show increased mineral density in ACHP treated group. Orange arrows show the location of the attachment site and black arrows indicate bone tunnel below the epiphysis.

Table A.2: Tendon-to-Bone Histological Scores.

	4 Weeks		8 Weeks	
	CTRL	ACHP	CTRL	ACHP
Cellularity	3 (3, 4)	2 (1, 4)	3 (2, 3)	3 (2, 3)
Fibroblast shape	3 (3, 4)	3 (1, 4)	3 (2, 3)	2 (2, 3)
Matrix maturity	3 (2, 3)	2 (1, 3)	3 (2, 3)	2 (1, 2)
Cell orientation	3 (2, 4)	3 (2, 4)	3 (2, 3)	3 (2, 4)
Insertion organization	3 (2, 4)	3 (2, 4)	3 (3, 3)	3 (2, 4)
Insertion continuity	3 (2, 4)	2 (1, 3)	2 (2, 2)	2 (1, 3)
Bone quality	1 (1, 3)	1 (1, 2)	1 (1, 2)	1 (1, 2)
Overall maturity	20.0 (14.0, 22.5)	15.9 (10.5, 21.0)	17.0 (16.5, 17.5)	15.3 (13, 18.5)

Results are shown as the median (minimum, maximum). Cellularity: 1=low, 4=high; cell shape: 1=spindle shaped, 4=round; matrix maturity: 1=green, 4=yellow; cell orientation: 1=aligned, 4=random; insertion organization: 1=fibrocartilage transition, 4=fibrous/no transition; insertion continuity: 1=integrated, 4=abrupt; bone quality: 1=enthesis lamellar and underlying trabecular bone similar to healthy, 4=thin entheses lamellar bone and loss of trabecular bone; overall maturity (sum of individual scores): 7=healthy/uninjured, 28=disorganized scar tissue.

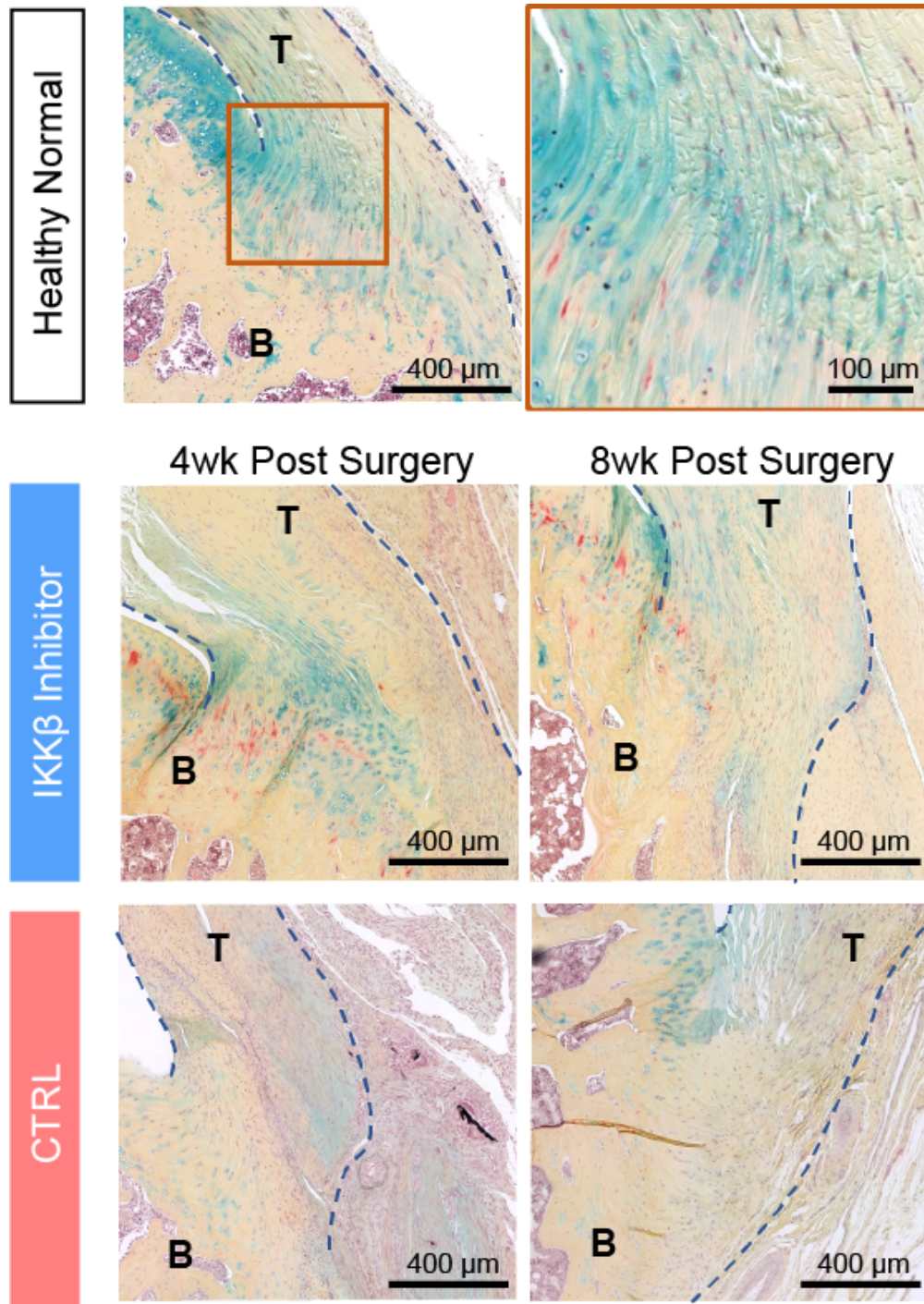


Figure A.7: Pentachrome-stained tendon-to-bone repair site. ACHP treatment ($IKK\beta$ inhibitor treatment) led to improved insertion organization and insertion continuity compared to control (yellow: new collagen; B: bone, T: tendon. Tendon-to-bone attachment is outlined with blue dotted line).

κ B) to maintain the positive inflammatory response necessary for initiating tendon healing while suppressing the detrimental effects of sustained inflammation. Such a targeted approach was recently approved for the treatment of rheumatoid arthritis [340] and cleared phase I clinical trials (safety and tolerability) for the treatment of knee osteoarthritis (I κ B kinase small molecule inhibitor for NF- κ B pathway) [331], demonstrating its potential for treating inflammation-related musculoskeletal pathologies. Several molecularly targeted approaches have also been attempted in tendinopathy models. For example, p38 inhibitors for MAPK signaling cascade reduced fibrosis and lipid accumulation after rotator cuff repair [341]. Through tendon-specific genetic deletion of *IKK β* *in vivo*, our previous work suggested the therapeutic potential of blocking *IKK β* for tendon healing [129]. In the current work, we translated this approach through small molecule inhibition after rotator cuff repair; *IKK β* inhibition successfully blocked the inflammatory *IKK β* -dependent mechanisms of NF- κ B signaling and reduced expression of related NF- κ B target genes.

Clinically, repair-site gapping or rupture after rotator cuff repairs typically occur within the first few months after surgery [318]. In the current study, targeted reduction of inflammation led to a tougher repair at both timepoints studied. High toughness (i.e., energy absorbed prior to failure) is a key feature of the healthy enthesis protecting it from damage accumulation and rupture, and would similarly protect the repair from rupture. While many studies report reduction of repair stiffness as detrimental [325, 326], the moderate reduction of stiffness in the current study contributed to the gain in toughness, a likely advantage for repair mechanics. *IKK β* inhibitor treatment increased repair toughness by increasing the displacement needed to fail the repair without affecting failure force. The histological findings further support mechanical benefit from the treatment. Histological evaluation showed improvements in collagen maturity and insertion integrity with the *IKK β* inhibitor treatment compared with controls. This is consistent with a previous report wherein expression of constitutively active *IKK β* or elevated inflammation compromised collagen expression and hindered mesenchymal function [342].

The *IKK β* inhibitor was administered orally, leading to systemic effect, which includes the effect to the humeral head bone adjacent to the healing interface. Because mineral content correlates

with tendon enthesis mechanical properties [64] and loss of mineralized tissue at the attachment site correlates with higher rates of re-tearing following surgical repair [100], we examined bone morphometry of the humeral head. While $IKK\beta$ inhibitor treatment prevented some of the mineral and trabeculae losses that are commonly seen after rotator cuff repair, systemic inhibition of $IKK\beta$ also led to decreases in overall humeral head BV/TV and cortical thickness at an earlier time point. This effect was apparent only on surgically repaired samples, implicating the necessity of active bone remodeling. Prior studies showed the complexity of canonical and non-canonical NF- κ B signaling in osteoclastogenesis and osteoblast activation [343, 344]. Furthermore, conflicting results on the temporal effect on NF- κ B signaling activation and its effect on fracture healing have been reported [345, 346, 347]. Our findings of decreases in some bone morphometry parameters at the earlier time point need further evaluation as a potential risk factor for repair site failure. Future studies will examine gene expression, as well as osteoclast and osteoblast activity, in the humeral head to understand the effect of systemic $IKK\beta$ inhibitor treatment on bone quality after repair.

There were several limitations to this study. First, the current study used an acute injury-and-repair model in young adult animals. However, most clinical rotator cuff tears occur in the elderly population after chronic tendon degeneration. Furthermore, baseline tissue inflammation increases with age and chronicity [320]. It is unknown whether the current $IKK\beta$ inhibitor treatment regime will be enough to mitigate excessive NF- κ B activation seen in tears that occur after chronic degeneration. Hence, additional studies using a chronic degeneration and repair model [131] are needed. Second, the small molecule inhibitor was delivered systemically, which may not be ideal for treatment of local inflammation at the repair site. However, there were no adverse systemic effects of the drug; specifically, there were no significant fluctuations in rat weights for both treatment and non-treatment groups post-operatively, no differences in qualitative cage activity observed among groups during daily monitoring of animals, and no differences in skin incision site healing rates. Furthermore, treatment was only applied for the first 7 days after repair to modulate NF- κ B signaling during its peak acute activity [128]. Additional studies are required to see the effect of treatment on rotator cuff healing after surgery with longer durations, dosages, and modes of delivery.

A.6 Conclusion

Pharmacological inhibition of IKK β prevented the excessive inflammation that occurs at the early crucial stages of rotator cuff tendon-to-bone healing and improved outcomes. This preclinical translational study showed the potential for modulating the NF- κ B pathway for enhanced outcomes after rotator cuff repairs in patients.

A.7 Acknowledgments

This study was funded by NIH R01-AR057836 and R01-AR072623.